Laboratory and Field Testing of Alpine and Alpine Touring Ski Equipment Retention and Release Characteristics

Jeffrey R. Campbell

A dissertation submitted in partial fulfillment of the

requirements for the degree of

Doctor of Philosophy

University of Washington

2016

Reading Committee:

Randal P. Ching, Chair
Mark Tuttle
Irving Scher

Program Authorized to Offer Degree:

Department of Mechanical Engineering

University of Washington

Abstract

Laboratory and Field Testing of Alpine and Alpine Touring Ski Equipment Retention and Release Characteristics

Jeffrey R. Campbell

Chair of the Supervisory Committee:

Research Associate Professor Randal P. Ching

Department of Mechanical Engineering

Releasable alpine ski bindings were developed and standardized in the 1970s to mitigate the risk of twisting and binding fractures of the tibia-fibula, but they have not been effective at mitigating knee injuries. They have two primary functions: 1) Retention – keep the ski attached to the skiers boot if the loads on the tibia are not dangerous and 2) Release – release the ski from the skiers boot before the loads on the tibia become injurious.

Alpine touring is a subset of alpine skiing in which skiers use specialized alpine touring (AT) bindings to ascend non-maintained trails and ski down them. The proliferation of AT bindings has exploded in the last 10 years and the changes and innovations to this sector of the binding market have far outpaced the international standards organization ability to define standardized boot-binding interface geometry or AT boot-binding performance. The relative risk of injury when using AT equipment has not been explored.

To address these issues, the objective of this research is quantify the performance of alpine and AT boot-binding systems using standardized laboratory test methods and field measurements to evaluate the risk skiers of lower leg and ACL injuries.

Laboratory measurements were performed to compare the retention and release characteristics of alpine boot-binding systems to AT boot-binding systems. When AT boots were mixed with alpine bindings, the release characteristics were altered to the degree that using such a combination would increase the risk of a lower leg injury to skiers. When testing AT bindings with AT boots from different ski boot manufacturers, significant variation in the release

characteristics was measured. Anecdotally, many skiers dis-trust the retention function of AT bindings because of this variability in performance, and some manually lock out the release mechanism of the binding, exposing themselves to a high risk of a lower leg injury.

In order to improve the performance of AT boot-binding systems, it is necessary to quantify the performance requirements of these systems, defined as the loads they must transmit from the ski to the skier. To this end, field measurements of the loads transmitted through the binding to the skier were performed. The loads at the boot-top and the knee were estimated for male and female skiers using alpine and AT bindings.

As a whole, AT and Alpine bindings transfer the same net loads to skiers. However, The toe piece of AT bindings transfers most of the load to the skiers but has a very limited ability to absorb energy, exposing a potential weakness for retention performance.

Male and female skiers generate loads that reach the release envelope of the binding. However, females generate significantly greater adduction loads at the knee, a known risk factor for ACL injuries. The lateral force at the binding toe piece was well correlated with knee loads in females but not males, indicating that a binding design could incorporate more sophisticated mechanisms at the toe to reduce peak knee loads in females. Interventions designed for female skiers may not prove beneficial for male skiers.

Acknowledgements

I would be remiss to not acknowledge the village of friends, family, and colleagues that have supported me through out my pursuit of this degree. The patience and mentorship lent to me by my advisor, Dr. Randal Ching, has been immeasurable. His ability to steer me through my constant affliction of '*paralysis by analysis*' has surely tested his patience, but has taught me to be a thoughtful and careful researcher and engineer. I am forever indebted to him for taking me under his wing.

I want to thank my doctoral supervisory committee, Dr. Mark Tuttle, Dr. Irving Scher, and Dr. Kevin McQuade for their valuable insight, and the time they devoted to supervising my research.

I cannot thank Richard and Vicki Harrington enough for their generosity and support of my research. Rich's skiing experience and insight into my sensor design was integral to my success. My lab mate Dr. Sheri Imsdahl helped me find my feet as a researcher and in the department. I am sincerely grateful for her friendship.

I have had the unique privilege of working along side some of the most talented engineers at Guidance Engineering and Applied Research for the last four years as I pursued my research. Dr. Irving Scher has been an incredible mentor, has allowed me wide birth to pursue my research interests, and has invested in me as an engineer. I thank him for his invaluable support and mentorship, and for the opportunities for growth he has provided me. Dr. Beth Suderman has been an amazing colleague and friend; it is safe to say my final chapter would not have been possible without her expertise. Dr. Lenka Stepan has been a friend, mentor, and was integral to the success of my field-testing.

My research would not have left the ground without the expertise and support of Bruce Jahnke and Dave Carpenter; thank you both for your support and friendship. I must also thank Adam Ales, Cam Shute, Matthieu Fritsch, and Massimo Pellizzier for their support. This work would not have been possible without the creative contributions of Ennio Morricone, Jose Gonzalez, Trent Reznor, Nina Simone, and John Coltrane.

My parents, Rob and Lisa, have been my unwavering cheerleaders. My in-laws, Mickey and Patty, have always been there to help keep these years in perspective. My little brothers Jonathan and Stephen have seen me at my best, and my worst. They have pushed me when I

didn’t need it, and but most importantly when I did. My grandfather Lyle imbued in me a love of all things engineering, and skiing since I was a little boy and my grandfather Rick set an unforgettable example by never letting himself be defined by his physical limitations. Thank you all.

I am most of all indebted to my lovely wife Kristin who put her career on hold to support me, and yet still managed to graduate before me. She postponed her ambitions and dreams for those that encompassed a vision we held together. She never waivered in her support over several long years. This degree is as much hers as it is mine. *Gracis por todo lo que has hecho Amor. Ahora, la vida nos espera. ¡Vamanos! - T.Q.M.*

If you feel safe in the area that you're working in, you're not working in the right area. Always go a little further into the water than you feel you're capable of being in. Go a little out of your depth. And when you don't feel that your feet are quite touching the bottom, you're just about in the right place to do something exciting.

- David Bowie

TABLE OF CONTENTS

List of Figures

List of Tables

Chapter 1. Introduction

1.1 The Etiology of Skiing and Ski Equipment

In their earliest form, skis were tools invented by humans for transportation and survival. Hunter-gatherer groups in Mesolithic Scandinavia strapped long wooden boards to their feet for flotation, speed, and efficient travel over snow-covered terrain as far back as 8,000 B.C.[1]. Humans have since improved the performance of skis used for transportation by reducing the metabolic cost of traveling on skis by two-fold[2]. In the early 1800s, skiing began to transition from a purely utilitarian mode of transportation to recreation.

From a historical perspective, the development of recreational ski equipment can be easily divided into two periods: 1) before the advent of releasable bindings in the1970s and 2) the 1970s through present day.

1.1.1 *Ski equipment and injuries before releasable bindings (pre-1970s)*

Humans have been improving the design of ski equipment for millennia for utility or recreation. In the 1800s, leather lace-up boots were affixed to wooden skis using leather straps allowing skiers to walk up hill and slide down in a semi-controlled manner. As early as 1894, ski litters were placed on ski hills to allow for the evacuation of skiers who predominantly suffered femoral fractures while skiing[3]. Downhill skiing gained significant popularity in the first half of the 20th century with the introduction of mechanical lifts used to carry skiers up the ski hill. However, the long wooden skis provided a very efficient lever for twisting ankles and legs beyond their elastic limits. Metal releasable ski bindings were developed in the 1940-1950s with the intention of preventing these injuries, however they did not reduce the high incidence of ankle sprains and fractures that were rampant in the first half of the twentieth century[3].

In the 1960s, plastic ski boots with buckles and two-piece ski bindings were introduced that allowed for better control of skis on snow. Sprains and fractures of the foot and ankle decreased significantly with the additional protection of stiff plastic boot shells[4]. It now became possible for skiers to carve on hard snow and to reach inherently higher speeds; Dr. Moritz summarized the increased risk by saying "*Whenever man attempts to move at a rapid rate of speed, over irregular terrain, among rocks and trees, he is apt to get hurt.*"[5] Although, ankle injuries

decreased, the combination of increased skier speed and stiff plastic boot cuffs resulted in a sharp increase in twisting and bending fractures of the lower leg. By the start of the 1970s, diaphyseal fractures from bending or twisting of the lower leg (Figure 1.1) accounted for 10% of all injuries with an overall injury rate for skiing of 5-8 injuries per thousand skier days[6]. Injury data from the 1940s through 1974 by Eriksson and Johnson[3] confirms this trend showing a clear increase in the prevalence of lower leg fractures in the 1960s (Figure 1.2 - A).

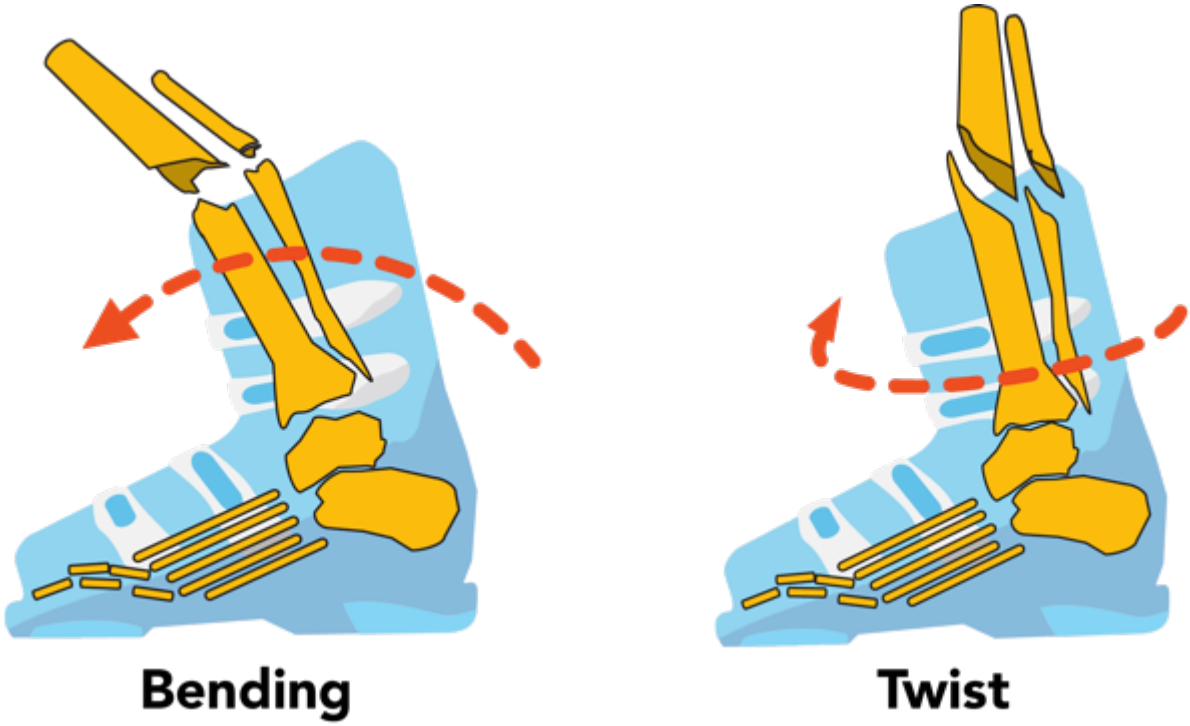

Figure 1.1. (Left) Fractures at the boot-top are commonly associated with a forward-backward lean fall resulting in bending of the tibia-fibula at the boot top cuff. (Right) Spiral fractures of the tibia-fibula are commonly associated with the ski twisting about the diaphysis of the tibia.

1.1.2 *Ski equipment and injuries after the advent of releasable bindings (post-1970s)*

The increase in lower leg injuries prompted the development of release-able ski bindings and standards for the boot-binding interface to improve the reliability and performance of these systems in the 1970s. Releasable bindings were designed with two primary functions for skier safety:

1. ***Retention*** – Hold the ski boot to the ski to allow skiers to maneuver downhill while loads transmitted from the ski to the lower leg of the skier are low enough to avoid injury.
2. ***Release*** – Release the ski from the boot when loads transmitted to the tibia of the skier approach a threshold at which they would exceed the elastic limit of the skiers' tibia, in twisting or in bending. This release removes the ski that acts as a large lever applying large torques to the tibia by bending and twisting (Figure 1.1).

The overall injury rate declined by 3-fold from 5-8 injuries per 1000 skier days (1970s) to 1.9 injuries per 1000 skier days[7] (2005). The number of skiers injured in falls where a ski does not release occurs as much as those injured when an inadvertent release of the binding occurs[8], though their injury patterns differ significantly. Injuries resulting from falls where a binding does not release typically produce lower leg injuries[9–12] while falls stemming from an inadvertent release of the binding tend to involve the head, neck, and upper extremities[8,11].

1.1.3 *Lower Leg Injuries: 1970s – Present Day*

A 34 year long prospective study by Ettlinger and Johnson[7] revealed that tibia fractures decreased when releasable bindings were introduced in the 1970s. This trend continued through 1989 when the lower leg injury rate stagnated after having initially decreased by 83% (Figure 1.2 – B, Figure 1.3). Since the early 1990s, lower leg injury rates have remained relatively stable and now account for less than 1% of overall injuries[7,10,13] (Figure 1.3). Other retrospective studies have also found the prevalence and incidence of lower leg injuries[9,14,15] have remained stable over the last two decades.

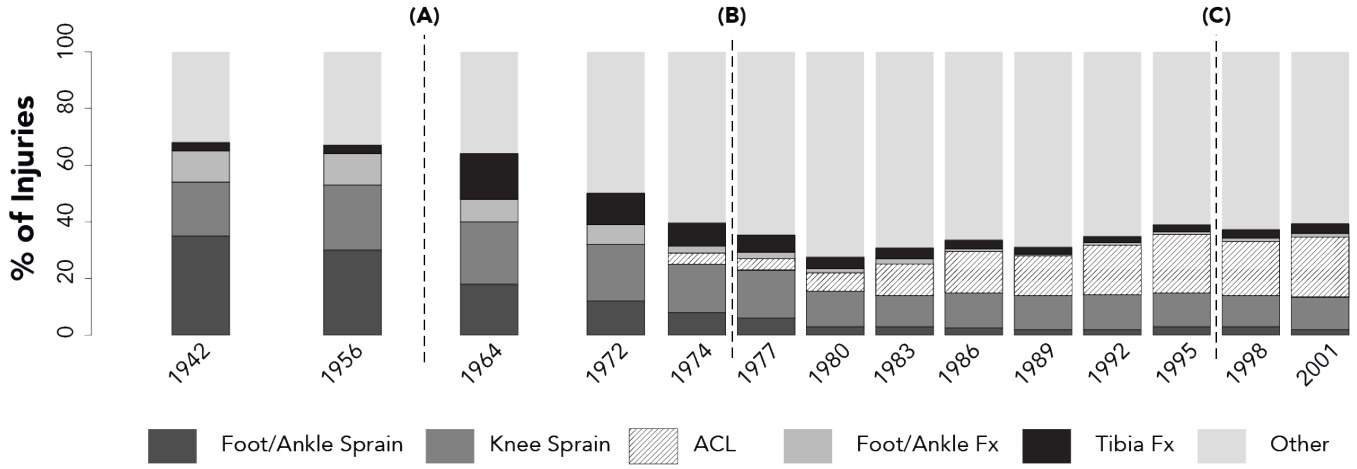

Figure 1.2: A compilation of historical prevalence of lower extremity injuries compiled from Eriksson et al.[3] (1942-1974) and Shealy et al[4] (1974-2001). Dashed lines delineate when (A) plastic ski boot shells entered the market[3,4], (B) releasable bindings were introduced, and (C) the introduction of carving skis[15].

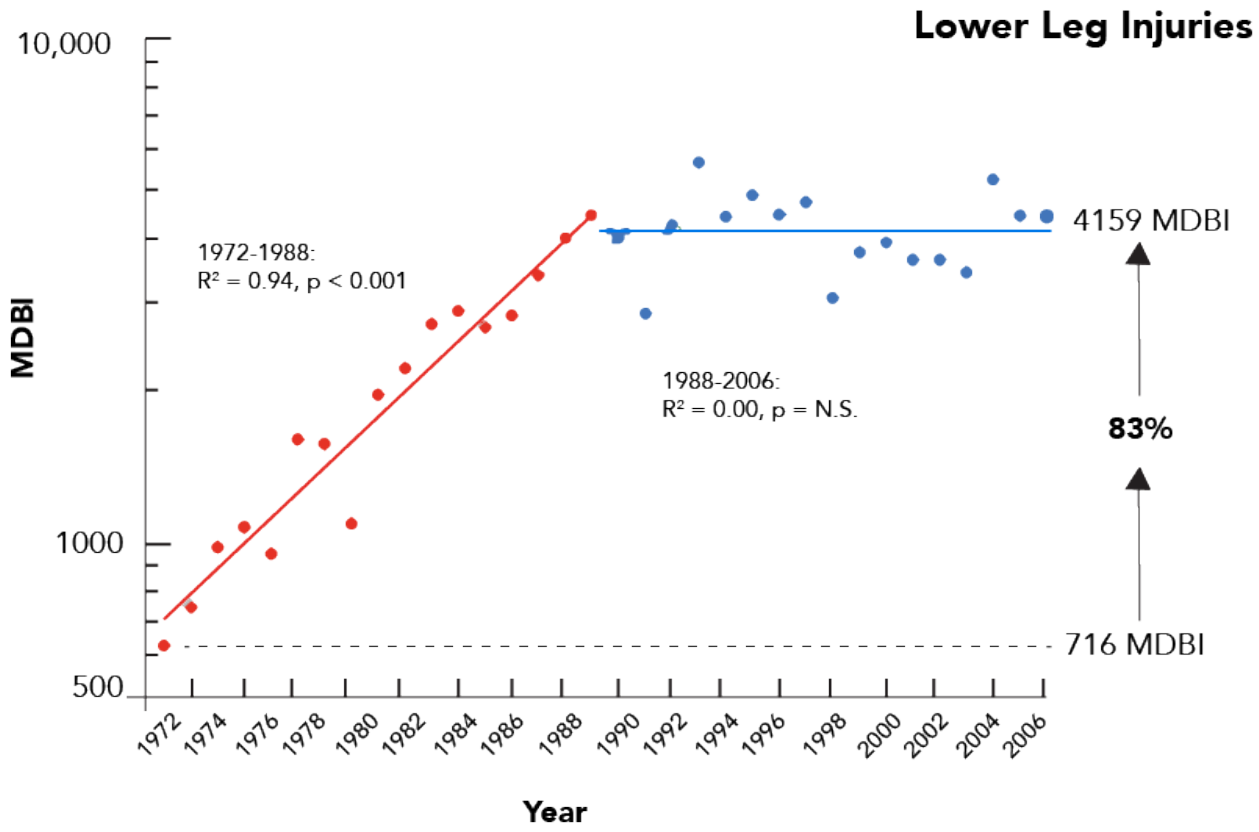

Figure 1.3: Mean Days Between Injuries (MDBI) for lower leg injuries. Reproduced from Johnson et al.[7] with permission.

1.1.4 *ACL Injuries: 1970s – Present Day*

By the 1980s, the injury rate for ACL tears had increased by 283%, accounting for 4% of overall injuries in 1972 and growing to over 20% of overall injuries by the 1990s[4]. The ACL injury rate plateaued in the 1990s and has slowly improved to 3101 Mean Days Between Injuries (MDBI) according to Johnson et al.[4,7,10,13], with an estimated 16,000 ACL injuries a year[4,6,7,13] (Figure 1.4). Other retrospective studies have found the prevalence of ACL injuries to account for 15-21% of all injuries[14,16,17], and 50% of all knee injuries[15]. Interestingly, these studies also report a disproportionate number of ACL injuries to females, 51% of all injuries, than males, 21% of all injuries[14,15]. This trend as a function of gender is present in many other sports[14].

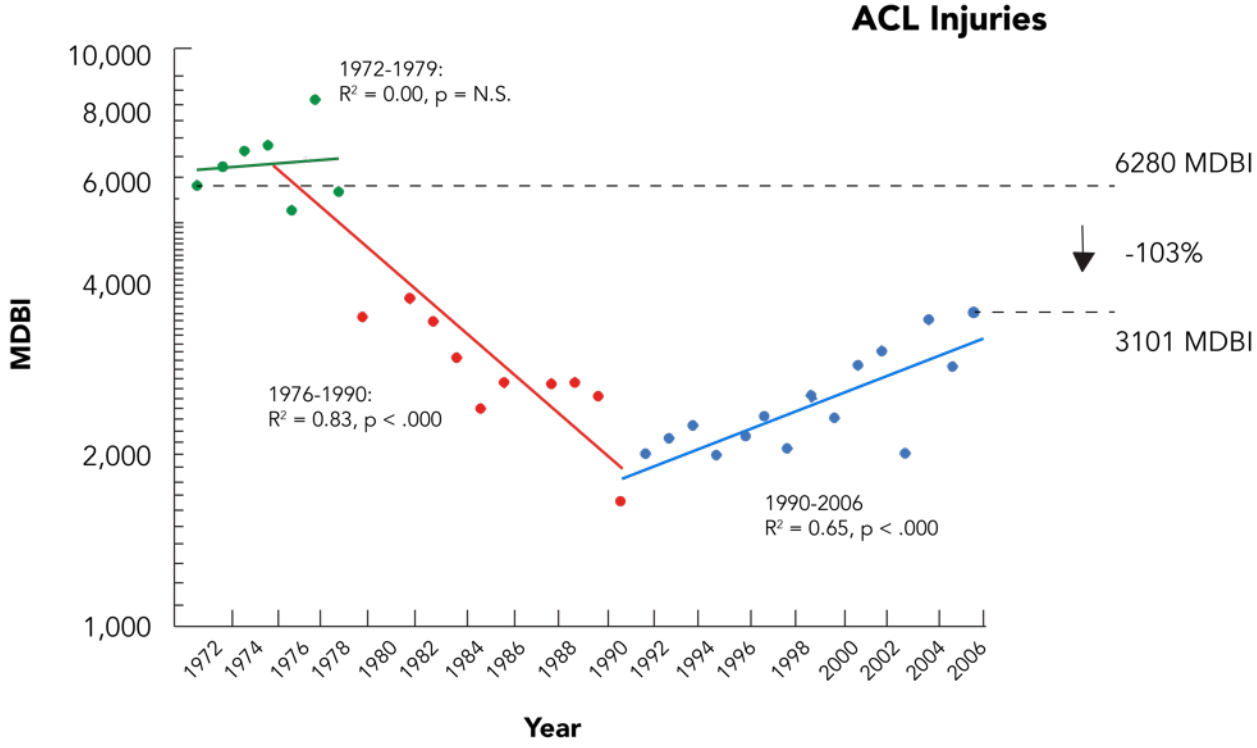

Figure 1.4: Mean Days Between Injuries (MDBI) for ACL injuries. ACL injury rates increased as lower leg fractures decreased through the 1970s and 1980s. Since 1990, ACL injury rates have slowly improved as ski lengths have decreased. Reproduced from Johnson et al.[7] with permission.

Ski shapes began to significantly change in the mid 1990s. Skis were manufactured in varying width and shapes including radii in along the length of the ski to allow for aggressive carving (Figure 1.5). However, skis with side cuts, decreasing the turning radius of the ski, were not attributed to a higher risk of injury according to Burtcher et al.[15]. Burtcher et al. reported that

between 1998-2003, when shaped skis were emerging on the market, there was actually a proportional 9% decrease in both the overall injury rate and in knee injury rates. A slight decrease in ACL injury rates was also reported by Johnson et al.[7] during this period. This may be attributed to of the length of shaped skis, which are inherently shorter than traditional straight skis.

Figure 1.5: (Left) Lyle Campbell skiing in the 1940s on early alpine ski equipment. (Right) Skiers can now carve more aggressively on modern ski equipment, and commonly ski with their feet further apart.

Lower binding release settings do not necessarily decrease the risk of an ACL injury. In a prospective epidemiological study, Deilbert et al. performed functional equipment testing on the ski equipment of injured skiers who presented with lower leg injuries, ACL injuries, and a control group of non-skiers[18]. Of the skiers presenting with lower spiral fractures of the tibia, 83% had equipment that released at a mean twisting torque 42% higher than the release torque of the control group. No association with higher release values was found with the skiers presenting with ACL injuries. Hence, Deilbert et al. concluded that lower release settings would not reduce the risk of knee injuries.

Deilbert's findings contradict a recent (2016) proposal by Ruedl et al. who cites the large disparity in ACL injury rates between males and females, and various physiologic differences between genders, as evidence for the need for lower release values for females than males[14]. Shealy et al.[4] and other researchers[18–22] have noted that protecting the knee from torque applied from the ski was never the design consideration of alpine bindings.

The use of mechatronic bindings was explored as a solution to reduce ACL injuries in the 1980s and 1990s; and, to date no such binding has been released to the market[12,23–27]. A

mechatronic binding developed by Hull et al.[28] incorporated dynamometers in the toe and heelpiece of a binding and a solenoid to activate the release mechanism. It performed comparably to mechanical bindings but there was no evidence that this mechatronic binding, or others that have been developed [26], offered any improved protection to the knee.

The primary injury mechanism for an ACL injury hypothesized to produce ACL injuries is commonly called the 'Phantom Foot'. The 'Phantom Foot' (derived its name from the combination of the tail of the ski and the stiff boot top and is caused by a backward twisting fall in which a combined axial twisting torque and a valgus torque are applied to the knee[29]. Alpine bindings were never designed to protect the knee from the loads generated by these types of falls.

1.2 Development and Function of Releasable Ski Bindings

1.2.1 *Release Values*

To achieve the retention-release function, alpine ski bindings use a spring-loaded cam mechanism such that the heelpiece breaks away in response to vertical forces at the heel that produce a bending moment at the top of the boot cuff. A forward leaning fall will produce, F_x^{Skier}, a force along the X-axis against the top of the boot-cuff as shown in Figure 1.6. In turn, a vertical resisting -F_{HEEL} force is applied the heelpiece of the binding to keep the boot attached to the ski. The force that the heelpiece of the binding is capable of overcoming $F_Z^{Heel,Binding}(k^{heel},\delta^{IV},Cam)$ is a function of the cam profile, the spring constant, k^{heel}, and the amount of preload, δ^{IV}, applied to the spring.

The sum the forces about the y-axis produces a bending moment equal to:

$$\text{(eqn 1.1)} \quad \sum M_Y = M_Y^{Binding} + M_Y^{Tibia} \text{ where,}$$

$$M_Y^{Tibia} = F_X^{Skier} L_{Boot} \text{ and } M_Y^{Binding} = F_Z^{Heel,Binding} L^{Heel}$$

In a twisting fall (such as the "Phantom Foot"), a spring loaded cam mechanism in the toe piece responds to a lateral force at the toe of the boot that produces a twisting moment about the diaphyseal axis of the tibia (Figure 1.6). The force produced by the spring-cam mechanism, $F_Y^{Toe,Binding}(k^{Toe},\delta^{IV},Cam)$, is also a function of the spring constant, the cam profile, the spring

constant, k^{Toe}, and the amount of preload, δ^{IV}, applied to the spring. The sum the forces about the z-axis produces a twisting moment equal to:

$$\text{(eqn 1.2)} \quad \sum M_Z = M_Z^{Binding} + M_Z^{Tibia} \quad \text{where,}$$

$$M_Z^{Binding} = F_Y^{Toe,Binding} L^{Toe} \quad \text{and} \quad M_Z^{Tibia} = F_Y^{Toe} L^{Toe}$$

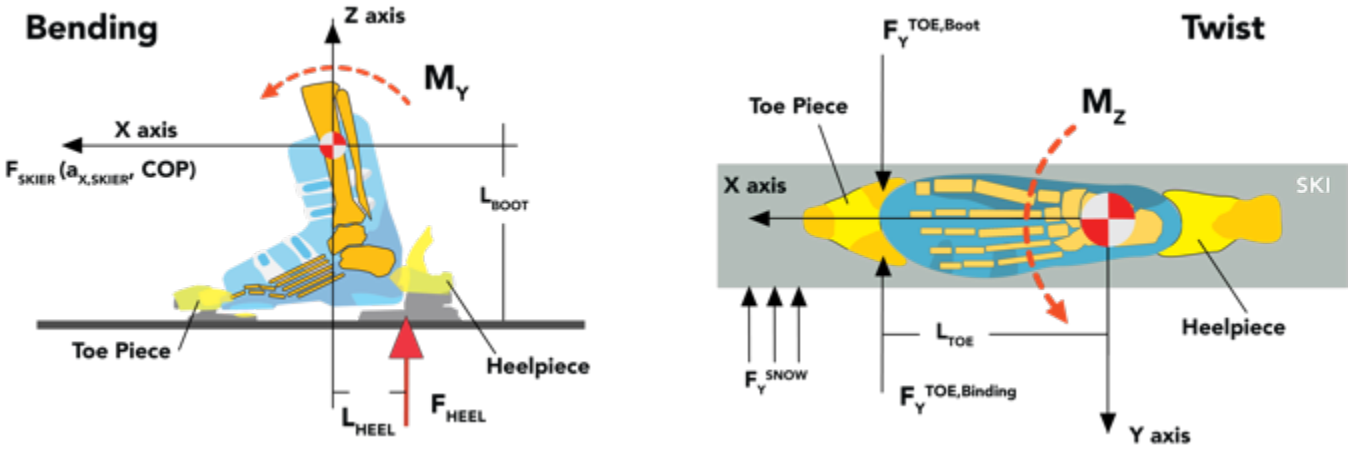

Figure 1.6: (Left) Free body diagram of the forces transmitted through the heelpiece of a binding to the tibia to produce a bending or forward lean release. (Right) Free body diagram of the forces transmitted through the toe-piece of a binding to the tibia for a twist release.

The release function of bindings during the 1970s was rudimentary, and varied significantly on the particular boot-binding combination used[4]. The simple retention-release logic of funding function was relatively simple (Eqn. 1.3); if M_Y and M_Z are less than a predetermined threshold, $\left\{\tau_Y^{Critical}, \tau_Z^{Critical}\right\}$, the binding should not release. If either M_Y or M_Z are greater than $\left\{\tau_Y^{Critical}, \tau_Z^{Critical}\right\}$ then the binding should release. At that time, no rationale had been developed for the magnitude of $\left\{\tau_Y^{Critical}, \tau_Z^{Critical}\right\}$.

$$(eqn-1.3) \sum M_Y = \begin{cases} < \tau_Y^{Crticial} & , \quad \text{Re}tention \\ \geq \tau_Y^{Crticial} & , \quad \text{Re}lease \end{cases}$$

$$(eqn-1.4) \sum M_Z = \begin{cases} < \tau_Z^{Crticial} & , \quad \text{Re}tention \\ \geq \tau_Z^{Crticial} & , \quad \text{Re}lease \end{cases}$$

In the early 1970s, several research groups in concert with the American Standards for Testing and Materials (ASTM), Industry Applications Standards (IAS), and International Standards Organization (ISO) began to propose various criteria for the determination of the thresholds at which bindings should release, $\left\{\tau_Y^{Critical}, \tau_Z^{Critical}\right\}$.

One school of thought was to select release values based on the elastic limit of the tibia. Using destructive twist and bending tests on cadaveric tibia, Asang[19,20] found the elastic limit of the tibia correlated well with the medial-lateral width of the tibial plateau. Using this correlation as a release threshold criterion, the 'IAS Tibia Head' method[21] was introduced. It was necessary for the medial-lateral width of a skier's tibial plateau to be measure to properly determine the appropriate release value for a particular skier. Correction factors had to be employed to correct for variations in soft tissue from measurements taken on females[4].

A more conservative method for selecting release torque values developed by Shealy and Ettllinger[30]. They performed field trials to determine empirically what minimum release requirements (MRR) were sufficient for skiers to ski without an inadvertent release of the binding, and then correlating those values with skier parameters. Skier weight was found to be the single best predictor for determining an appropriate release torque value for the MRR and resulted in predicted release values $\left\{\tau_Y^{Critical}, \tau_Z^{Critical}\right\}$, 15-20% lower than the tibia head method[30], thus providing additional protection to the skier. Crawford and Mote[31] later found that the MRR for a given skier was well correlated to skier weight, leg length, and was not correlated to skier ability.

The MRR method was eventually adopted in the international standards ASTM F939[32] and later in ISO 8061:2015[33] as the recommended lower limit for release torque values. Other international standards for standardizing the boot-binding interface (ISO 5355:2006[34]), frictional requirements, and performance requirements (ISO 9462:2006[35]) of the retention-release function of the boot-binding system were also introduced. The sharp decrease in lower leg injuries between the 1960s through 1989 was a direct result of the development and optimization of releasable ski bindings, the standardization of their release values, and of the boot-binding interface.

1.2.2 *Selection and Adjustment of Ski Binding Release Settings*

International standards normalized release torque values for forward lean and twist releases. Skiers of different height, weight, and boot sole lengths require different release torque values. The Z-Scale, refereed to in this study as the Indicator Value (IV) (most commonly but erroneously referred to as a DIN setting), was developed to allow easy adjustment of a skiers binding to the appropriate release value. The Z-Scale is a numerical scale on the toe and heel piece of the binding that mechanically corresponds to an increasing level of preload applied to the spring-cam mechanism in the toe and heelpiece. The release torque vs. Indicator Value (IV) relationship for Forward Lean and Twist releases is standardized in ISO 9462:2006(E)[35] and is shown in Figure 1.8.

Manufacturers commonly provide a chart to ski shops that allows for the easy and reliable selection of the appropriate IV for a particular skier. These charts use information from the skier such as self-selected skier type, skier height, skier weight, age, and boot sole length as criteria for determining the appropriate release value[4].

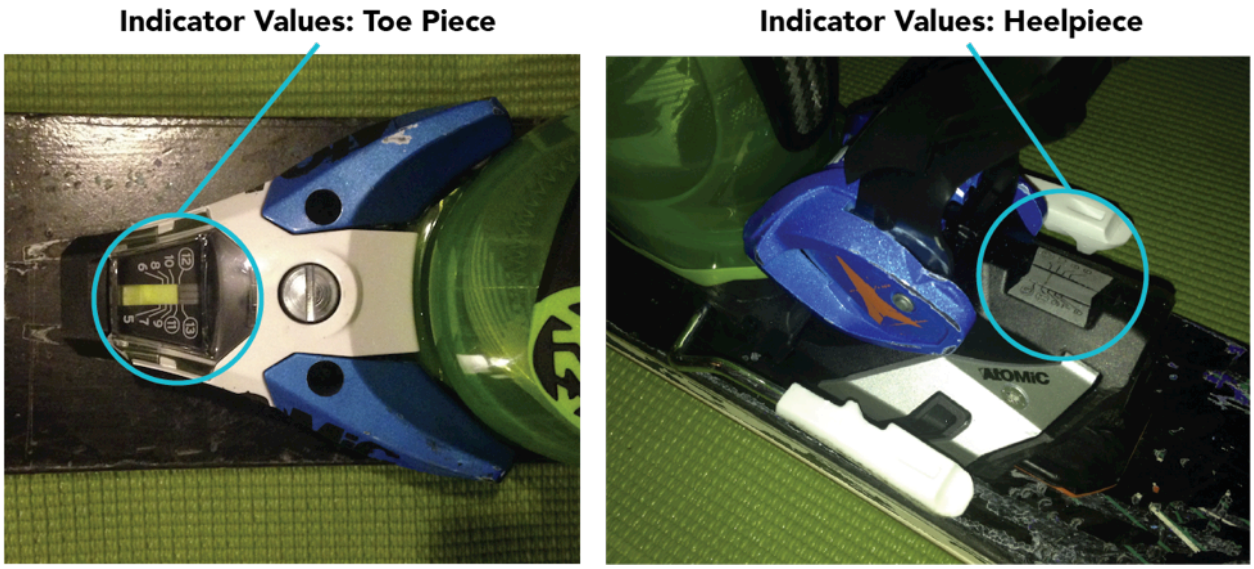

Figure 1.7: An alpine ski binding with the Z-Scales highlighted showing the indicator settings for the toe piece (Left) and the heelpiece (Right).

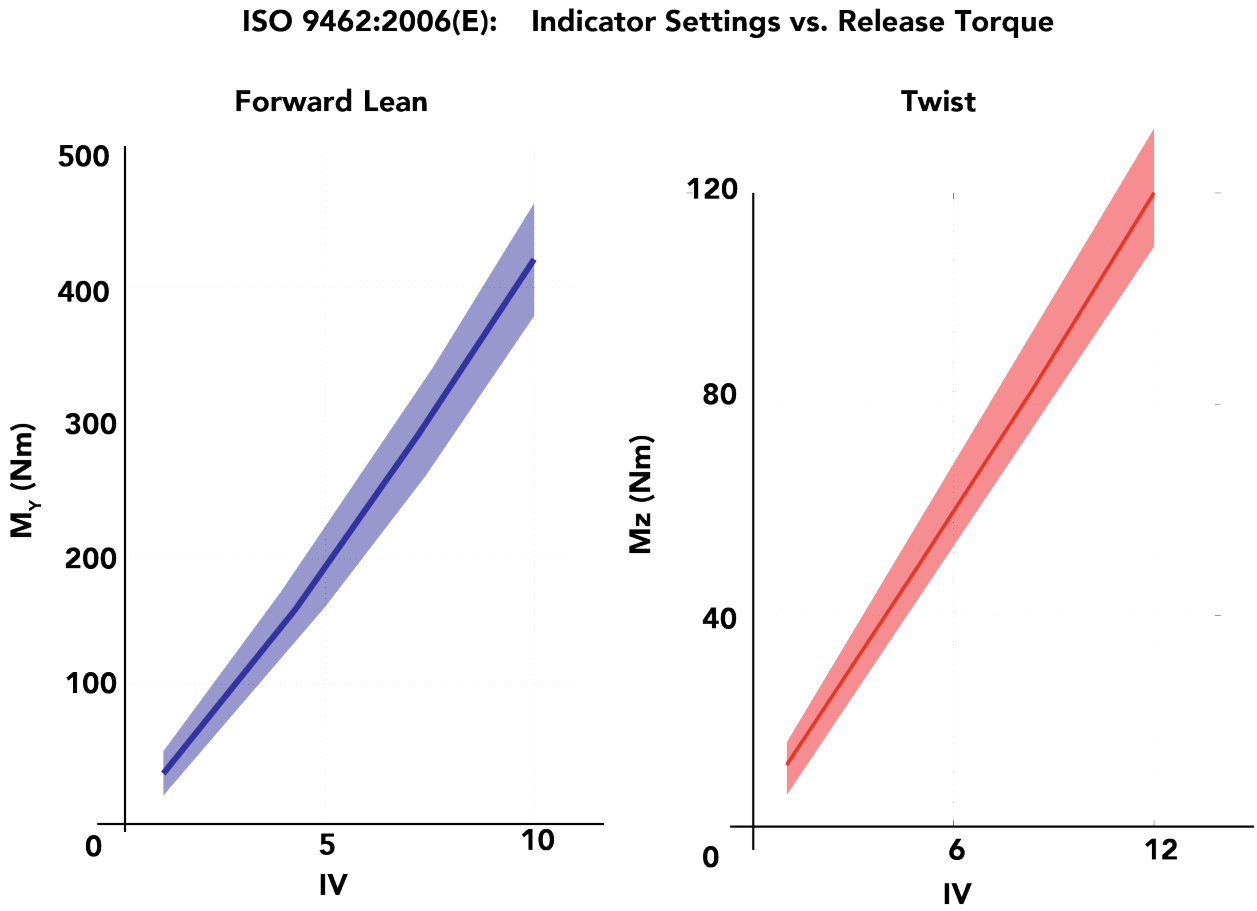

Figure 1.8: Release torque values (solid line) and tolerances for release torque (shaded region) standardized by ISO 9462:2006(E) corresponding to the binding indicator settings for a forward lean release (Left) and a twist release (Right).

1.3 Alpine Touring

Alpine Touring (AT) is a sub-discipline of skiing in which skiers use specialized boots and bindings to ascend, traverse, and descend snowy terrain away from the maintained trails found in ski resorts. AT boots and bindings are specifically designed to allow for the boot heel to separate from the ski to allow skiers to ascend snowy terrain (walk mode) and to also enable the boot heel to be rigidly affixed to the ski to ski down hill (ski mode) (Figure 1.9). There are two types of AT bindings, AT frame bindings and Tech/Pin bindings (Figure 1.9). AT frame bindings closely resemble alpine bindings that are mounted on a hinged chassis that can be released for walking. Tech/Pin bindings interface with the boot via metal inserts molded into the toe of the boot. In the walk mode of Tech/Pin bindings, the heelpiece is disengaged from the boot, but the toe piece remains engaged, and the boot pivots about the pins in the toe piece.

The interface geometry of AT boots with AT frame bindings was recently standardized by ISO9523:2008[36]. These standards were an extrapolation of standards from alpine equipment standards intended to ensure the fit of AT boots with AT bindings. AT frame bindings do not utilize any novel technology unique to AT equipment; rather they simply have more adjustability to accommodate the large variation in dimensions found in AT boots (Figure 1.10Figure 1.10). The functional retention-release values for AT bindings were adopted from alpine binding standards (Figure 1.8) and is replicated in ISO 13992:2006[37], with additional provisions for testing the walk mode function. The indicator settings for AT Frame bindings are adjusted in the same manner as alpine bindings.

Tech/Pin bindings interface with AT boots via metal inserts molded into the boot shell; unfortunately, the geometry of these inserts has not been standardized. AT boots with inserts are often referred to as Randonee boots, a French work for 'a walk'. However, few Tech/Pin bindings currently on the market are able to satisfy the functional requirements of ISO 13992:2006. In contrast to alpine bindings and AT Frame bindings, Tech/Pin bindings currently on the market, the release torque for both Forward Lean and Twist releases is controlled and adjusted on the heelpiece (Figure 1.11). The preload on the toe piece is not adjustable. The relationship of Tech/Pin binding indicator values to release torque will be discussed in Chapter 5.3.1.

Figure 1.9: (Left) AT Bindings in ski mode, with the boot heel connected to the ski. (Right) AT bindings in walk mode, with the boot free to pivot in the binding about the toe for ascending snowy slopes.

Figure 1.10: Alpine boots (left) differ from AT boots (center). AT/Randonee boots (right) are similar to AT boots and have metal inserts molded into the toe and heel to interface with Tech/Pin bindings.

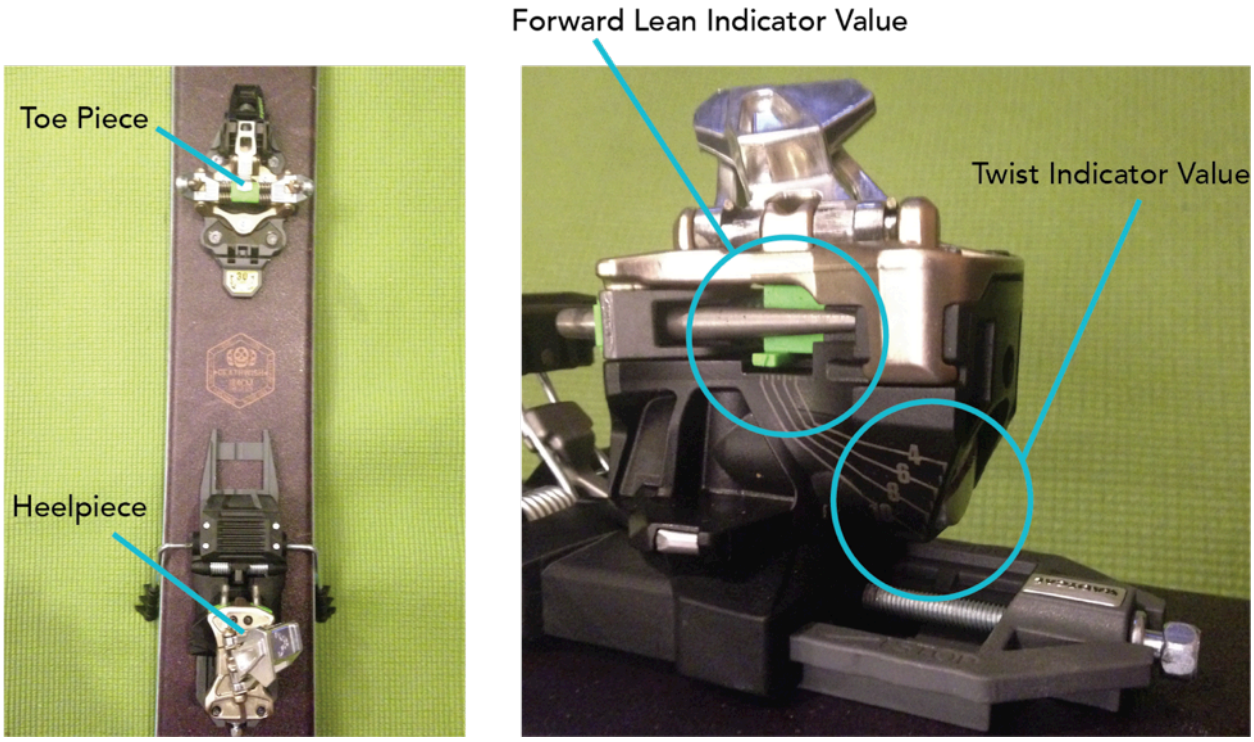

Figure 1.11: Tech/Pin Bindings do not have adjustable indicator settings in the toe piece (Left). The Forward Lean and Twist release settings are both located on the heelpiece (Right).

1.4 Significance

The current challenges facing the alpine and AT ski equipment fundamentally differ as a function of the potential risk of injuries. For example, Alpine boots and bindings are unable to protect skiers from ACL injuries. And, AT boots and bindings may not offer the protection against lower-leg injuries that skiers are accustomed to from their alpine ski equipment.

1.4.1 *The Future for Alpine Equipment*

The decrease in overall skiing injury rates during in the 1970s and 1980s was a direct result of the development and implementation of international standards for the boot-binding interface, the retention-release function of the boot-binding system, and the implementation of shop practices to verify proper function of the boot-binding system for consumers. These standards ensured that consumers could purchase boots and bindings from different manufacturers and while not increasing their risk of injury.

In the 25 years since lower leg injury rates plateaued, there have not been any significant improvements in the retention-release function of ski equipment. Knee injuries are still the most prevalent injury among skiers, with ACL injuries being the most common and severe. ACL injury rates have not shown any significant improvement in nearly 25 years, and approximately 15,000-17,000 skiers per year still suffer an ACL injury in the United States[7,14].

Little information exists regarding forces acting on the knee while skiing. Several studies in the 1980s-1990s[25,27,38] mounted six-axis dynamometers under the toe and heel piece of alpine bindings and measured the ground reaction forces and knee flexion-extension of skiers. Both Quinn[39] and Scher[27] reported on reaction forces at the tibia while Maxwell[25] reported knee loads in 1989. Scher[27] reported that the maximal measured forced generated by approximately two-thirds of the skiers was significantly lower than the allowable minimum retention release (MMR) values dictated. Rotation and varus-valgus angular displacement of the knee, the two components hypothesized to cause ACL injuries, were not documented in these studies.

Recent studies have attempted to calculate knee loads using pressure insoles or, more broadly, using Inertial Measurement Units (IMUs) and differential Global Positioning Satellite Systems (dGPSS) to calculate knee loads using a pendulum model[40–42]. However these models

cannot fully resolve the six-axis load components acting on the knee as they only directly measure compression on the boot sole and do not measure the other five load components.

Skis have changed significantly since the 1970s and now come in a wide variety of widths, lengths, flexural stiffness, and side cut radii. Similarly, the technique skiers use to carve down slopes has also changed significantly with a wider stance and higher speeds (Figure 1.5). However, little has changed in alpine binding technology in 25 years. Since alpine bindings were never originally intended to protect the knee from injury; no real improvement in knee injury rates is expected with current binding technology. Current lower-leg injury rates do not imply that the MRR values determined in the 1970s-1980s are not applicable to skiers using modern alpine equipment, as have been suggested by studies that claim ACL injuries are related to release settings of alpine binding[14].

The forces and torques acting on the knee while skiing must be fully quantified, before ski equipment can be specifically designed to protect the knee. The effect of risk factors for ACL injuries such as gender, leg dominance, and snow condition to knee loads must also be quantified.

The forces and torques acting on the knee while skiing must be fully quantified, before ski equipment can be specifically designed to protect the knee. The effect of risk factors for ACL injuries such as gender, leg dominance, and snow condition to knee loads must also be quantified.

1.4.2 *The Future for Alpine Touring Equipment*

It is not possible to elucidate establish injury rates associated with the use of AT ski equipment. Most skiers using AT equipment do so outside of ski resorts in the backcountry. Skiers in the backcountry with minor injuries typically self extricate without the assistance of ski patrol, and these injuries therefore go unreported. If a skier suffers an injury in the backcountry, that would normally require ski patrol assistance, Search and Rescue teams are often dispatched and the injured skiers typically bypass ski-area clinics to receive medical care elsewhere. However, anecdotal evidence from manufacturers of AT equipment suggests that lower-leg injuries are on the rise, particularly among younger children and teenagers using AT equipment.

AT/Randonee equipment was the fastest growing market in the snowsports industry in

2013/14, growing 8% in both dollars and units sold[1]. AT boots accounted for 12% of units sold and 16% of dollars spent on ski boots. Generally, ski area visits are used as a metric for participation and have remained relatively flat at approximately 60 Million/year in the U.S. for several decades (Figure 1.12)[2]. The percentage of visits by alpine skiers is slowly growing as snowboarding has plateaued or declined. However, they do not capture the growing participation of backcountry users. As a result, traditional alpine skiing equipment may actually be losing market share to the growing AT sector than is indicated by ski area visits. The AT boot market grew 27% and was worth nearly $43 Million[1] in the U.S.

The rate of development of AT equipment has far outpaced the ability of the international standard organizations to address new changes to equipment and keep such standards relevant. As such, the retention-release characteristics of AT equipment may not offer as much protection from lower-leg injuries as skiers have become accustomed to with their alpine ski equipment.

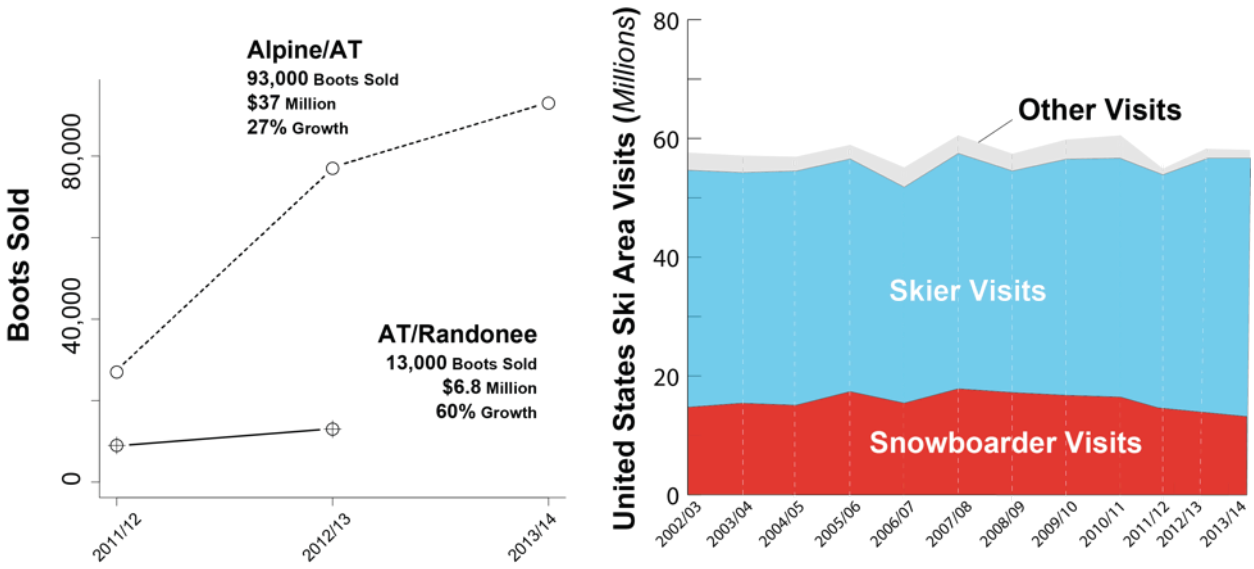

Figure 1.12: (Left) Sales of Ski boots with Alpine Touring Functionality are growing rapidly and taking market share from Alpine skiing. (Right) Skier visits to United States Ski Areas have remained relatively flat for more than a decade.

Although widely used by backcountry skiers, the retention-release performance of AT equipment has not been studied at all. The risk of injury to skiers resulting from the use of AT equipment will be a function of how closely AT equipment can mimic the retention-release

[1] SIA Reports 2012/13 & 2013/14
[2] NSAA National Demographic Study 2013/14

function of alpine bindings. If AT equipment cannot adequately match the retention-release function of alpine bindings, the risk of a lower-leg injury will be higher. Even if AT bindings can match the function of alpine bindings, there is still no guarantee that AT bindings pose less of a threat to knee injuries than alpine bindings.

The effect of AT equipment on the loads transmitted to the lower leg and knee have not been measured and must be quantified to identify potential risk factors or injury mechanisms.

1.5 Dissertation Objectives & Hypotheses

The purpose of this dissertation research is to quantify the retention-release performance of modern alpine and AT boot-binding systems using both laboratory bench tests and on-snow field measurements. The performance of alpine and AT equipment from laboratory testing will be compared to performance metrics established by international standards ISO 9462:2008 and ISO 13992:2006.

The on-snow performance of alpine and AT equipment will be quantified using instrumentation developed and compiled to measure 1) ground reaction forces transmitted from the ski to the skier and 2) whole body kinematics of skiers skiing on alpine and AT equipment. Using this instrumentation, an inverse dynamics model will be used to calculate 1) leg loads at the top of the ski boot cuff and 2) knee loads.

This dissertation research is designed to test these specific hypotheses:

1.5.1 *Hypotheses from laboratory testing:*

- H_1: The retention-release performance of modern alpine boot-binding systems, quantified through laboratory tests, will fall within the specified minimum and maximum lower and upper release torque limits of ISO8061:2008.
- H_2: The retention-release performance of modern AT boots in modern alpine binding systems, quantified through laboratory tests, will exceed release torque values specified by ISO8061:2008.
- H_3: The retention-release performance of AT boots and Tech/Pin bindings in modern alpine binding systems, quantified through laboratory tests, will fall within the specified release torque limits of ISO8061:2008.

1.5.2 *Hypotheses from on-snow testing:*

- H_4: The MRR values, established by international standards, will not exceed the maximal leg loads generated by skiers using alpine equipment while skiing on groomed maintained slopes.
- H_5: The MRR values, established by international standards, will not exceed the maximal leg loads generated by skiers using AT equipment while skiing on groomed maintained slopes, but may exceed forces generated by skiers using AT equipment off-piste (on non-maintained slopes).
- H_5: The maximal leg loads generated by males will not be different from females.
- H_6: The maximal knee loads generated by males will be different from females.
- H_7: The maximal knee loads generated by skiers will be higher on their dominant leg than their non-dominant leg.

1.6 **Organization/Research Outline**

The proposed hypotheses H_1-H_3 will be tested through a series of two studies in a laboratory setting:

- Study 1 – Retention release performance of AT boots in Alpine bindings (Chapters 2-3)
- Study 2 – Interactions of Tech/Pin Bindings with AT Boot Inserts (Chapters 4-5)

Hypotheses H_4-H_7 will be tested in on snow:

- Study 3 – Measurement of leg and knee loads for male and female skiers in alpine and AT equipment. (Chapters 9-10)

Currently Studies 1-2 (Chapters 2-5) have been completed, and submitted in the form of four manuscripts for peer review to the Journal of Experimental Medicine and Biology. They are presented here in their manuscript form.

The methodology and development of low-profile six-axis dynamometers to be used in Study 3 is described in Chapters 6-7. An introduction of the XSENS MVN Biomechanics Suit, used to measure skier kinematics is presented in Chapter 8. Finally, Chapter 9 provides a description of the proposed research for Study 3. [Update this...]

Chapter 2. Release Characteristics of Alpine Touring Boots in Alpine Bindings

2.1 Introduction

Before the 1980s, alpine (or downhill only) skiing had a reputation for being a dangerous sport, with the most prevalent injuries being ankle and tibia/fibula fractures. Releasable ski bindings were developed to reduce the likelihood of lower leg injury. In order to work effectively, ski bindings have two functional requirements: (1) retention – to hold firmly the boot to the ski during controlled skiing maneuvers when the likelihood of injury is low; and (2) release – to release the boot from the ski when the likelihood of lower leg injury is high. The result of releasable ski/boot/binding systems has been a significant reduction in the incidence of skiing-related lower leg injuries decreasing from 8 injuries per 1000 skier days in the 1970s to 3 ski injuries per 1000 skier days in the 1990s[6,43]. Overall the incidence of below the knee ski injuries decreased 58% between 1972-2008[7]. This reduction may also be attributed to the development and adoption of international standards for the ski binding release setting values (visual indicator values), standardized geometry and materials (particularly hardness) of ski boot soles, and establishing minimum performance characteristics of ski bindings (for example, *ISO 5355*[34]*, ISO 9462*[35]*,* and *ASTM F1063*[44]). Natri et. al.[10] attributed the injury rate decrease to these international standards. The international standards for ski boots and bindings have assured consumers that any alpine ski boot could be used appropriately in any alpine ski binding.

Alpine touring (AT) is a sub-discipline of skiing in which the skier uses the skis to ascend, traverse, and descend snow-covered terrain, typically in the backcountry where trails are not maintained. Alpine touring bindings and boots differ from conventional alpine skiing equipment. Alpine touring bindings allow for the free movement of the AT boot's heel for climbing or traversing[37]. For traditional downhill skiing, the bindings are set to hold firmly the boot heel to the ski (similar to alpine ski equipment). Although AT boots look similar to alpine ski boots, they are different. AT boots typically have a different geometry[36], softer boot soles, and metal inserts at the toe and heel to accommodate special AT bindings (Figure 2.1). Because AT boots are generally more comfortable and make walking/climbing easier, some skiers are using AT boots as their primary boots for downhill skiing in alpine bindings. Despite

international standards for AT boots, at the current time there are few boots that have been manufactured that meet those standards. Furthermore, there is no universal reference sole for AT binding tests representative of the AT boots that are on the market currently.

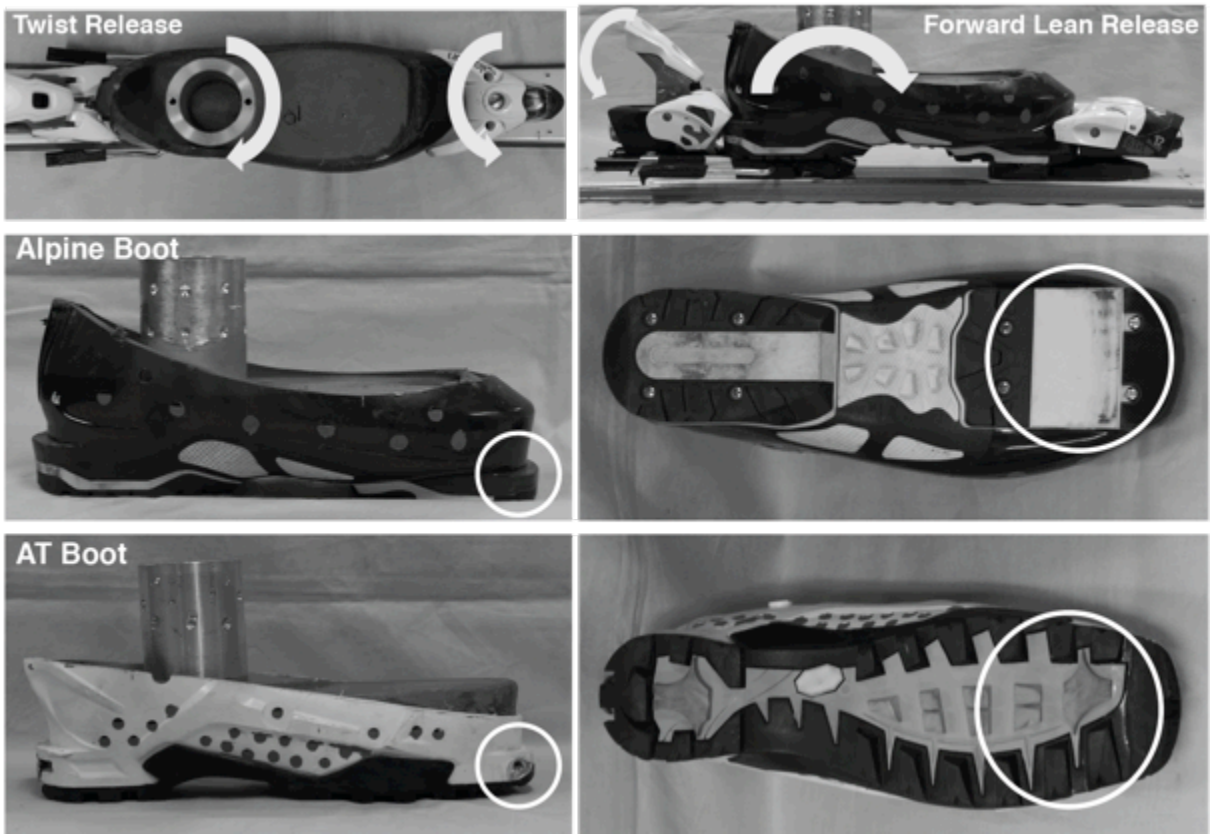

Figure 2.1: Features of Alpine Bindings, Alpine ski boots, and Alpine Touring ski boots. Alpine bindings have two release modes: Twist (1a) and Forward Lean (1b). Alpine boot toes (1c) and AT boots toes (1d) differ both in the geometry and shape of the toe. AT boots (1d) commonly employ metal inserts in the toe. Alpine boot soles have a hard smooth gliding surface (1e) to interface with the anti-friction device (AFD) on Alpine bindings. AT boot soles (1f) have soft rubberized tread to maximize traction when walking.

Although most AT boots can often fit into alpine ski bindings, manufacturers do not generally recommend this combination. Nevertheless, skiers are using AT boots in alpine bindings. In a small ad-hoc survey of local ski patrollers in Western Washington, we found that 27% of ski patrollers reported using AT boots in alpine ski bindings for almost 50% of their time spent skiing. There are no published studies available that show that the combination of AT

boots and alpine ski bindings can provide the retention and release characteristics needed to meet the international standards and that have been shown to reduce significantly the lower leg injury rates[9]. Mixing alpine and AT equipment, could increase the likelihood of a ski/boot/binding system not releasing as intended, and thus increase the risk of leg injury[45,46].

International standards specify methods for boot and binding adjustment and testing by trained professionals to ensure proper ski/boot/binding performance[44]. In a ski shop, ski/boot/binding systems are tested using a pure twisting release for the toe piece and a pure forward lean release for the heel piece. It is unknown whether the system testing conducted in a ski shop would be sufficient to determine if an AT boot in an alpine binding would perform as desired in fall, especially a fall in which the skier is loading the fore-body or tail of the ski. To this end, we compared the retention-release characteristics of AT boots to alpine ski boots in alpine ski bindings using laboratory testing in accordance with the ASTM F504-05 standard[47]. We hypothesize that using an AT boot, instead of an alpine ski boot, in an alpine ski/boot/binding system will alter significantly the release/retention characteristics.

2.2 **Methods**

The release and retention characteristics of ski/boot/binding systems were tested in a laboratory setting using a lower leg surrogate that conformed to standards ISO 9462:2012 Appendix B[35] and ASTM F504-05[47] (Figure 2.2). Eight (8) models of alpine ski bindings were selected for testing as representative of the general release mechanisms and features currently on the market. Each binding was mounted to its own test ski; all test skis were the same make, model, and length 167cm (AMP Rx, K2 Sports, Seattle, USA). Five (5) models of alpine ski boots and ten (10) models of AT boots with boot sole lengths between 306 and 310 mm were acquired for testing. In order to measure the effect of boot design features, it was necessary to create a rigid coupling between the portion of the boot that interacts with the ski binding and a torque transducer. To this end, each test boot shell was cut below the pivot point of the upper shell and an aluminum adapter plate was secured to the foot area by filling the empty space with aluminum-filled epoxy (Rencast® 4037, Huntsman, The Woodlands, TX) (Figure 2.3).

Ski/boot/binding systems were rigidly affixed to a transducer located in a lower leg surrogate via the adapter plate mounted in the boot; torque was applied to the ski using a system of motors, cables, pulley and pneumatics which is measured by the transducer about the axial

and transverse axes, as defined in ISO 9462-2012 [5] (Figure 2.2). The range of the load cell was ±400 Nm (resolution: 0.29 Nm) and ±700 Nm (resolution: 0.17 Nm) along the axial and transverse axes. The load cell was calibrated against a calibrated, NIST-traceable six-axis load cell (Model 4526, Humanetics, Plymouth, MI) and had less than 0.5% error at full scale.

Six string potentiometers (L-Series, Unimeasure, Corvalis, OR) were attached to the test skis at the toe and heelpiece of the binding to measure the angular displacement (resolution: 0.03º) of the ski binding relative to the boot in the mid-sagittal and transverse planes during release. The data were collected at 1,000 Hz using a 16-bit data acquisition system (Model 6210-USB, National Instruments, Austin, TX) with a 200 Hz low-pass, anti-aliasing filter. Labview 14.0 software (National Instruments, Austin, TX) was used to collect and filter digitally the data using with a four pole, zero phase shift, low-pass Butterworth filter with a cut-off frequency of 10 Hz.

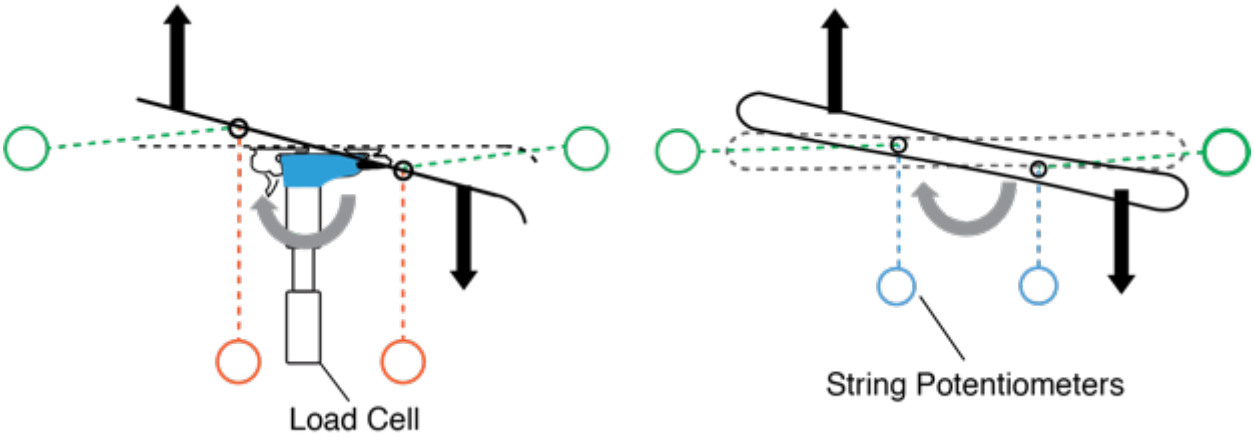

Figure 2.2: Schematic of test apparatus that conforms to ISO 9462-2012: Appendix B and ASTM F504-05. The system applied forces (black arrows) and torques (grey arrows) to the ski using a motor-driven system of cables and pulleys. A load cell measured the torque on the simulated leg along the axial and transverse axes. String potentiometers measured angular deflection of the ski relative to the fixed boot.

Figure 2.3: Preparation of ski boots for testing. Preparation of test boot soles required a metal adapter plate (left) to be fixed inside a cut boot shell using tooling compound (right). A custom jig was used to maintain proper alignment of the adapter plate-load cell interface relative to the boot.

2.2.1 *Testing Protocol*

Based on test standard ASTM F504-05 [15], four independent load scenarios were applied to each boot-binding system: (1) *Pure Forward Lean* – a bending moment was applied along the transverse axis of the ski (Figure 2.4a); (2) *Pure Twist* – an axial twisting moment was applied to the ski (Figure 2.4b); (3) *Front Preload Twist* – a vertical preload force was applied to the fore-body of the ski prior to the application of a lateral force on the ski 45 cm in front of the toe piece, to simulate a skier having their weight over the fore-body of the ski during a forward, twisting fall (Figure 2.4c); and, (4) *Rear Preload Twist* – a preload force was applied to the rear of the ski prior to the application of a lateral force 45 cm behind the heelpiece on the ski, to simulate a skier having their weight over the tail of the ski during a backward, twisting fall (Figure 2.4d). As required by the international standards, the testing system applied forces and pure torques quasi-statically to the ski and the system kinematics and simulated leg loads were measured until the bindings released. Unless the ski binding was damaged in the testing, each test was repeated three times in dry conditions and at ambient temperature. 120 unique combinations of boots and bindings were tested (8 bindings x 15 boots) and a total of 1,440 tests conducted (120 x 4 tests x 3 trials).

Each ski binding was set to visual indicator setting of 7½, the median value calculated from the range of the eight bindings tested. A reference alpine ski boot that conformed to standard ISO 5355 was used to verify that the bindings released at the appropriate torques. If the release torque was not within 2% of the median torque (Table 2.1), the setting was adjusted iteratively until it complied. The angular displacement at boot release was also measured during the setting verification.

Table 2.1: Minimum, Median, and Maximum allowable release torque values for the four loading scenarios tested.

Loading Scenario	Min (Nm)	Median (Nm)	Max (Nm)
Pure Forward Lean	248	276.5	305
Pure Twist	60	67	74
Front Preload Twist	60	80.0	99.9
Rear Preload Twist	60	76.3	92.5

Pilot testing showed that the AT boots could damage the alpine ski bindings; therefore, all of the alpine ski boots were tested before the AT boots in each binding. The order of testing for AT boots was randomized. Before testing, the boots and bindings were cleaned to remove silicon grease from contact points and the ski binding forward pressure was adjusted. If a binding had an adjustable height anti-friction device (AFD), it was set per the manufacturers specifications to the boot being tested. Some alpine ski bindings did not have the ability or range to accommodate properly the AFD height of each AT boot, but the boots were tested if it was possible to place the boot into the bindings.

2.2.2 *Data Processing*

For each boot, the torque transducer was set to zero with only the boot on the transducer. Angular displacement data were zeroed before the start of each test to obtain the relative angular displacement from the start of each test to release of the binding. From the time-history data, the maximum torque at release and the corresponding angular displacement were recorded for each test. For each boot-binding combination in each loading scenario, the means and 95% confidence intervals for the release torque and angular displacement were calculated.

The means (and 95% confidence intervals) were compared to the ranges of desired release torque for each load scenario based on the settings and international standards: Forward Lean (248 - 305 Nm), Pure Twist (60 - 76 Nm), Front Preload Twist (60 - 94 Nm), and Rear Preload Twist (60 - 102 Nm). A limit on the angular displacement at release was included because some AT boots released at significantly higher angular displacements than the reference alpine boot (Figure 2.5). The desired angular displacement at release for AT boots was defined as 300% of the angular displacement at release of the reference alpine boot for each specific binding and load case. Because the angular displacement at release for the reference alpine boot varied by binding model and load scenario, the desired range for angular displacement at release for AT boots also varied by binding model and load scenario; see Table A.1 in Appendix A. The angular displacement means (and confidence intervals) were compared to the desired angular displacement for each binding in each load case.

For each load scenario, the AT boot - alpine binding combination performed as desired if the confidence intervals fell within the desired release ranges for both the torque and angular displacement at release. The overall release function of a specific AT boot – alpine binding combination was deemed acceptable when the combination performed as desired for all load scenarios.

Unpaired, Bonferroni-corrected t-tests were performed to test for differences between alpine and AT boots in release torque and angular displacement for each load case, but not across load cases, with a significance level of 0.05.

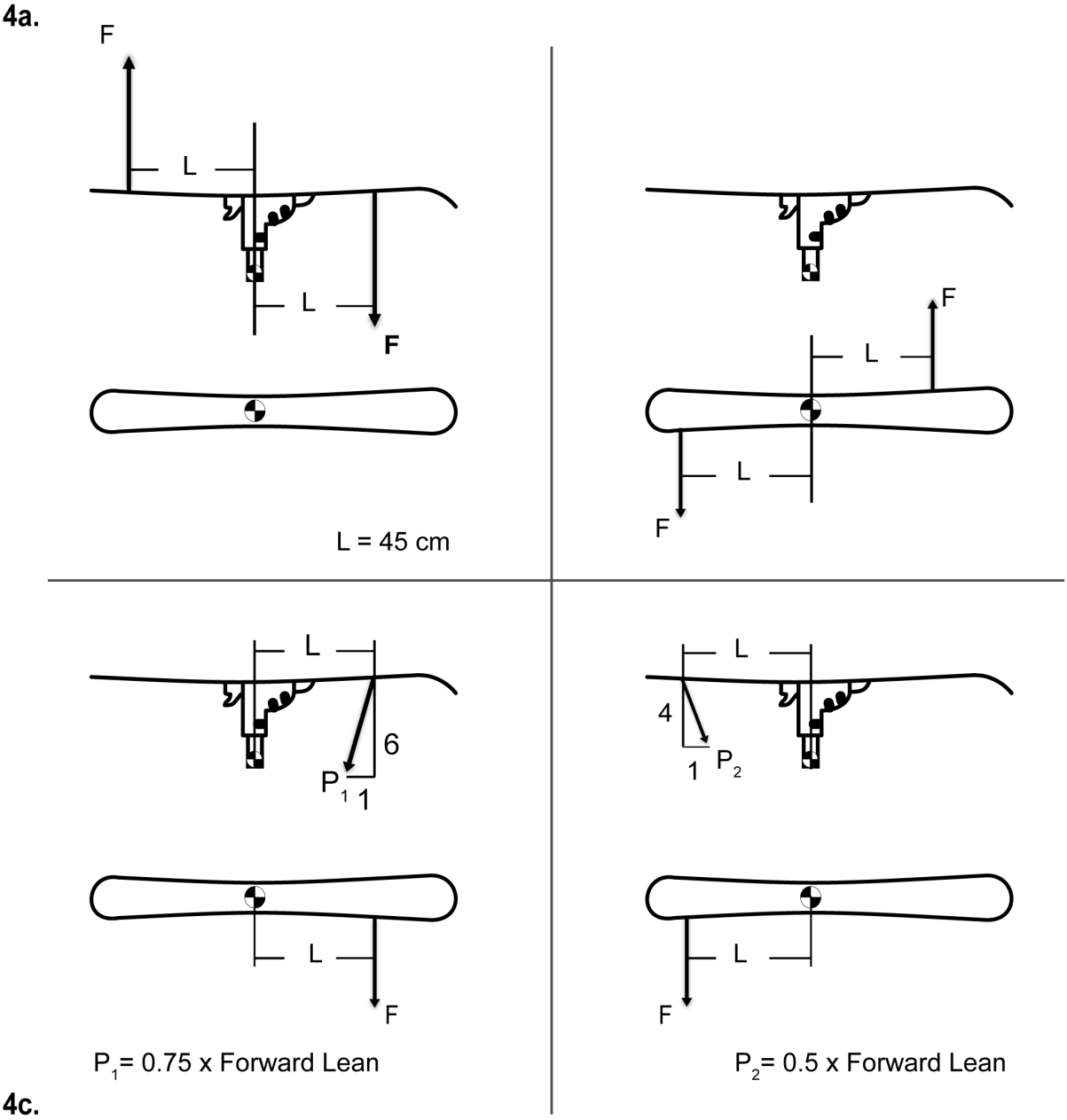

Figure 2.4: Boot-binding systems were tested in four loading scenarios. (1) Pure Forward Lean – (4a); (2) Pure Twist (4b); (3) Front Preload Twist (4c); (4) Rear Preload Twist (4d).

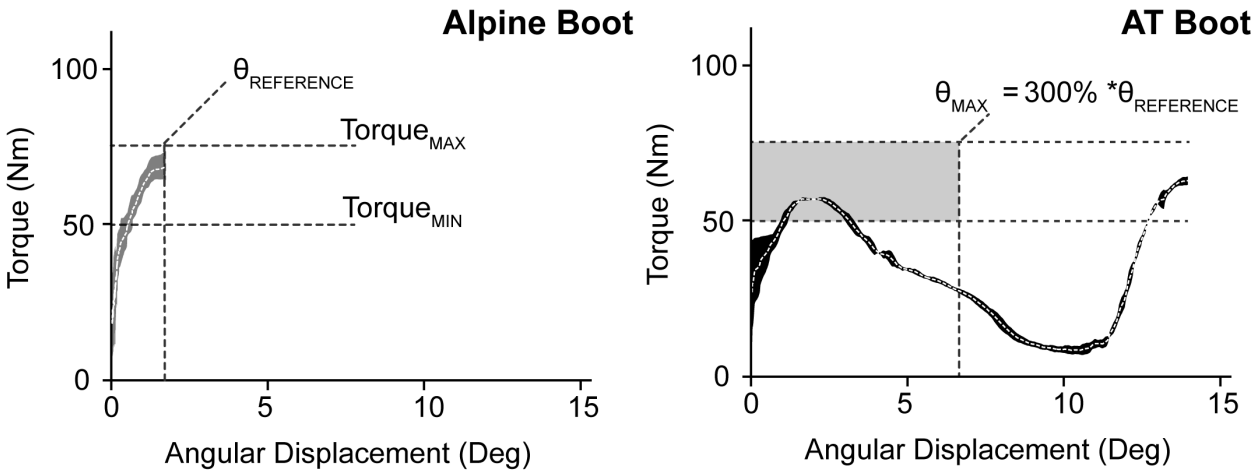

Figure 2.5: Exemplar Torque-Angular displacement curves from a Front Preload Twist release. The average and standard deviation (shaded curve) of three trails for an alpine boot (left) and an AT boot (right) are shown. The minimum and maximum allowable release torque values were determined by the indicator setting used in this study and boot sole length. $\Theta_{reference}$ *is the angular displacement at which the reference alpine boot released from each alpine binding. The maximum desired angular displacement for the AT boot was defined as 300% of the* $\Theta_{reference}$ *value. The shaded region is the acceptable release envelope for the AT boot.*

2.3 **Results**

All alpine boots released within the torque and displacement ranges with all alpine bindings in each load case. Of the 80 combinations of AT boot-alpine binding systems tested, 28.8% produced the desired release characteristics (that is, the release torque and angular displacement were within the desired ranges for all load scenarios); see Table 2.2. When considering the individual load scenarios, the Pure Twist and Front Preload Twist tests performed the lowest rate of releases in the desired ranges, 27.5% and 46.3%. When examining the data with respect to individual alpine binding performance with AT boots, one alpine binding released within the desired torque and displacement ranges with all AT boots tested and two bindings did not release within the desired torque and displacement ranges for any AT boot tested. When using AT boots in alpine bindings, 43% of the alpine ski binding models were damaged during a Pure Twist or Front Preload Twist test.

Table 2.2: AT boot-alpine binding combinations that released in the desired range for the torque and angular displacement.

	Forward Lean	Pure Twist	Forward Preload Twist	Rear Preload Twist	Overall
Torque	96.3%	53.8%	57.5%	85.0%	41.3%
Angular Displacement	100.0%	73.8%	88.8%	98.8%	67.5%
Combined	96.3%	27.5%	46.3%	85.0%	28.8%

Table 2.3: Maximum, average, and standard deviation values for the torque and angular displacement to release for alpine and AT boots in for each of the four load cases tested. p-values presented indicate significant or non-significant differences between Alpine and AT Boots within each test.

		Alpine Boots		AT Boots		
		Max	MN ± SD	Max	MN ± SD	*p*
Torque (Nm)	Forward Lean	307	281.9 ± 14.9	459	278.7 ± 27.3	0.056
	Pure Twist	67	60.6 ± 4.1	136	77.3 ± 17.7	< .001
	Front Preload Twist	92	67.1 ± 8.6	154	97.1 ± 19.9	< .001
	Rear Preload Twist	99	74.6 ± 10.4	138	84.8 ± 16.8	< .001
Angular Displacement at Release (Deg)	Forward Lean	5	3.1 ± 1.0	6	2.7 ± 0.2	0.005
	Pure Twist	5.2	2.2 ± 0.9	8.7	2.5 ± 1.4	0.007
	Front Preload Twist	3	1.4 ± 0.7	10.6	3.5 ± 3.0	< .001
	Rear Preload Twist	5.1	2.6 ± 1.0	5.1	2.5 ± 1.1	0.192

Significant differences were found between the release torque of Alpine and AT Boots in Pure Twist ($p<0.001$), Front Preload Twist ($p<0.001$), and Rear Preload Twist ($p<0.01$) but not Forward Lean; see Table 2.3. In addition, significant differences in the angular displacement at release were found in Forward Lean ($p = 0.005$) Pure Twist ($p = 0.007$) and Front Preload Twist tests ($p<0.001$) between AT and alpine boots.

When considering only the tests that would be performed in a by a ski shop technician (Pure Twist and Pure Forward Lean), the release torque of 33.8% percent of the AT boot and

alpine combinations were within the ranges required by the standards (Table 2.2). However 22.5% of these combinations released outside the angular displacement criterion in pure twist and 11.3% did not release within the performance envelope for either torque or displacement under combined loading (Front Preload Twist and Rear Preload Twist).

2.3.1 *Discussion*

In this study, we compared the retention and release characteristics of alpine touring (AT) boot with (typical) alpine ski boots when used an alpine ski binding in a laboratory setting. In this study, all alpine ski bindings released as expected (within the specifications found in ISO 9462-2012[35]) when used with the alpine boots. Only 29% of AT boot-alpine binding combinations released as desired. Unlike alpine ski boots, 69% of the AT boot and alpine ski binding combinations either required too much torque to release (59%) or released at much higher angular displacements than the alpine ski boot counterparts (32%). Each of these problems is cause for concern, as it increases the likelihood of a lower leg injury during a fall or accident. In some cases, using an AT boot in a alpine binding created significantly larger release torques than alpine boots; the highest twisting release torque with AT boots exceeded the desired torque range by more than 110%; this would increase significantly the risk of a lower leg injury, as the torque transmitted to the leg from the ski may reach or even exceed the injury threshold. Though most AT boots functioned poorly in alpine bindings, one alpine binding released appropriately with all of the AT boots tested.

Based on these results, we believe that binding designs are likely very sensitive to the several significant geometric and frictional differences between AT boots and alpine ski boots. The soles of alpine and AT boots are designed for conflicting purposes. AT boot soles are designed for maximum traction during walking on unmaintained trails and rough terrain, while alpine ski boot soles are designed to minimize friction between boot and alpine ski bindings at the contact points[44]. When used in alpine ski bindings, several features of AT boots introduce additional friction when compared the alpine ski boots and this additional friction can significantly alter the boot-binding behavior[48]. We hypothesize that the friction and geometric differences between boots created the performance differences between AT boots and using alpine ski boots.

Injury rates have been shown to decrease when consumers have their ski equipment adjusted professionally and tested by trained technicians in ski shops[48]. Other studies have shown indirect effects of having bindings adjusted by ski shops versus having ski bindings adjusted without professional advice or test equipment[45]. Ski shops assess the retention and release function of a boot-binding-ski combination by measuring the release torque while performing Pure Twist and Pure Forward Lean release tests; they do not measure angular displacement nor do they simulate other release scenarios that are more likely to occur during normal skiing (including Front Preload Twist and Rear Preload Twist).

It would be logical for consumers to also have their AT boots tested in their alpine bindings by a ski shop to assess the release and retention characteristics of their equipment. In our tests, approximately one-third of AT boot and alpine ski binding combinations functioned as desired in the Pure Twist and Pure Forward Lean tests (that is, those tests that are similar to ski shop tests), but released outside of the desired range in the Front Preload Twist and Rear Preload Twist tests. If one of these combinations were tested in a shop, the ski shop technician would likely conclude that the system performed adequately, even though the system could allow forces, torques, and displacements beyond what is desired. It is unlikely that a shop technician would reliably be able to determine which combinations of AT boots and alpine ski bindings would provide the retention and release characteristics desired by a typical alpine ski system. This type of "false positive" result could lull the consumer into believing that a particular combination would preform as desired even though it could increase the likelihood of a lower leg injury in a forward or backward twisting fall.

Anecdotally, skiers have reported altering the visual indicator settings when using AT boots in alpine bindings in an effort to maintain the same retention and release characteristics as alpine ski boots in alpine bindings. In an ad hoc analysis to determine the effect of altering the visual indicator setting, each alpine ski binding was tested with one representative alpine boot and one representative AT boot during a set of Front Preload Twist tests in which the visual indicator settings were varied. When examining the potential relationship between visual indicator settings and release torque, a significant linear regression for alpine boots was found ($F(1,16) = 45.2,\ p < .001$). This correlation suggested that binding settings accounted for approximately 74% of the variation in release torque ($R^2 = .739,\ Adjusted\ R^2 = .722$). The AT boots in alpine bindings did not produce the same relationship; the linear correlation ($F(1,16) =$

7.916, p = .012) suggested that the visual indicator setting accounted for only ~33% of the variation in release torque (R^2 = *.331, Adjusted* R^2 = *.289*). In 45% of the cases, the representative AT boot released at the same torque and very large displacements regardless of the visual indicator setting; see Figure 2.6. For the remaining 55% of bindings, the visual indicator setting had a small affect on the release torque were still significantly higher than the allowable release torque defined by international standards.

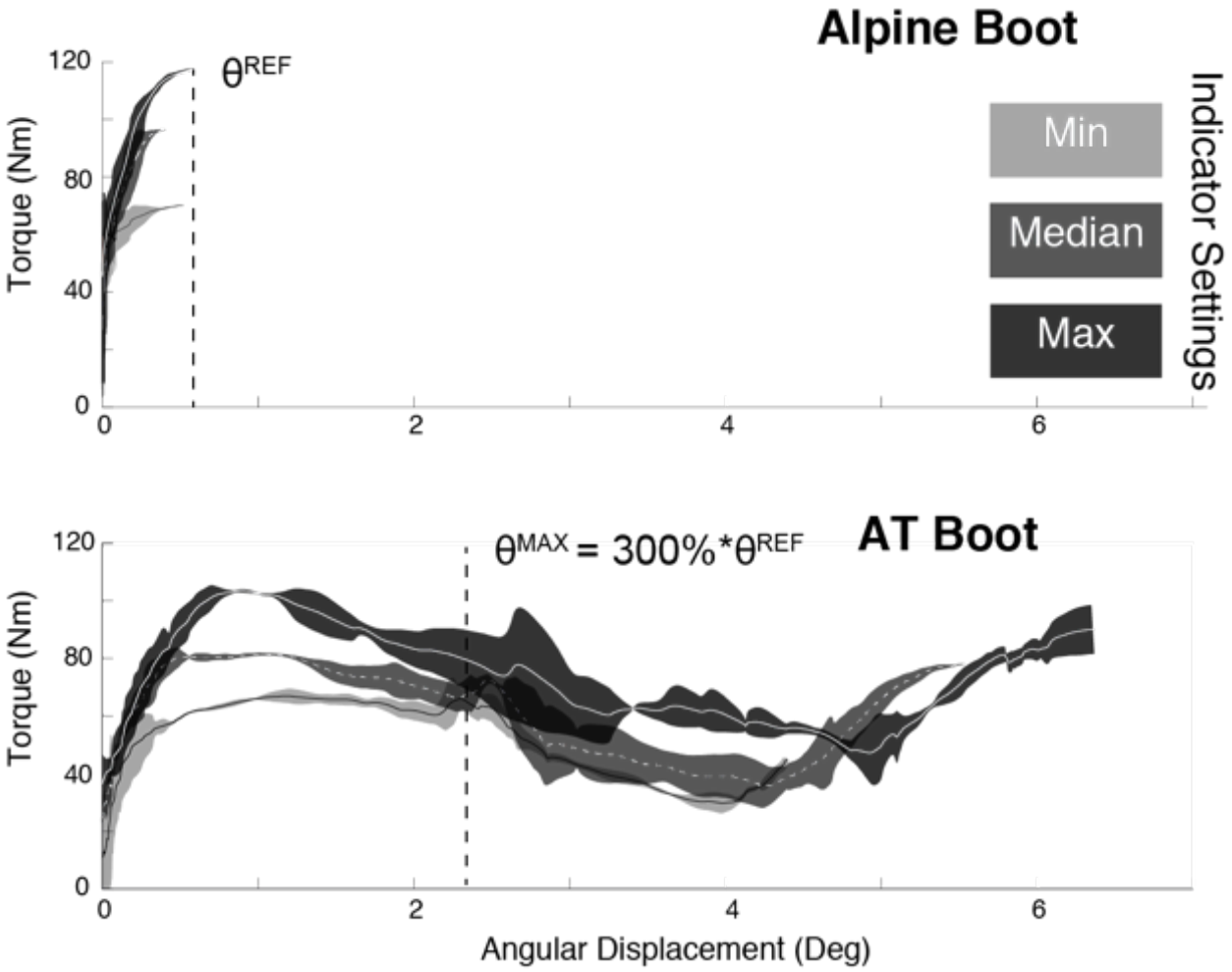

Figure 2.6: Effect on release torque of changing the visual indicator settings in bindings. The release torque was altered for an alpine boot in an alpine binding (left); however this had little to no effect on the release torque of an AT boot used in an alpine binding (right) in a Front Preload Twist test.

For skiers whose indicator settings fall on the lower end of the range, based on their height and weight, the release torque of AT boots from alpine bindings would be higher than the

allowable release torque based on international standards. A comparison of the allowable release torque per international standards, and the release torque for a representative alpine and AT boots from the same representative binding shown in Figure 2.6, is shown in Figure 2.7. The release torque for the AT boot-alpine binding does not change proportionally with the indicator setting as the alpine boot-alpine binding does.

The maximum allowable release torque per international standards for a BSL = 305mm and an indicator setting = 3 is 45 Nm. Using data reported on the quasi-static strength of the tibia the estimated the probability of tibia failure for a normal population with an applied twisting torque of 45 Nm to the tibia, was estimated to be ~ 1 in 44 tibias would fracture, given a normal distribution by Mote[12]. Even with the binding indicator setting = 3 the AT boot released at a value of 70.8 ± 5.1 Nm. Using Mote's estimates ~ 1 in 6 tibias would fracture with this applied load. Indicator settings are predetermined by a skier's height, weight, and aggressiveness; higher indicator settings are reserved for taller, heavier, more aggressive skiers. Indicator settings on the lower end of the scale would be reserved for small, lightweight skiers that have a much lower injury threshold for the tibia than larger skiers. Therefore the risk of a tibia fracture to these smaller skiers will be significantly higher.

Based on this ad hoc analysis, adjusting the visual indicator setting will not likely produce the desired release and retention characteristics and is not a reliable method to overcome the problems created by using an AT boot and in an alpine binding.

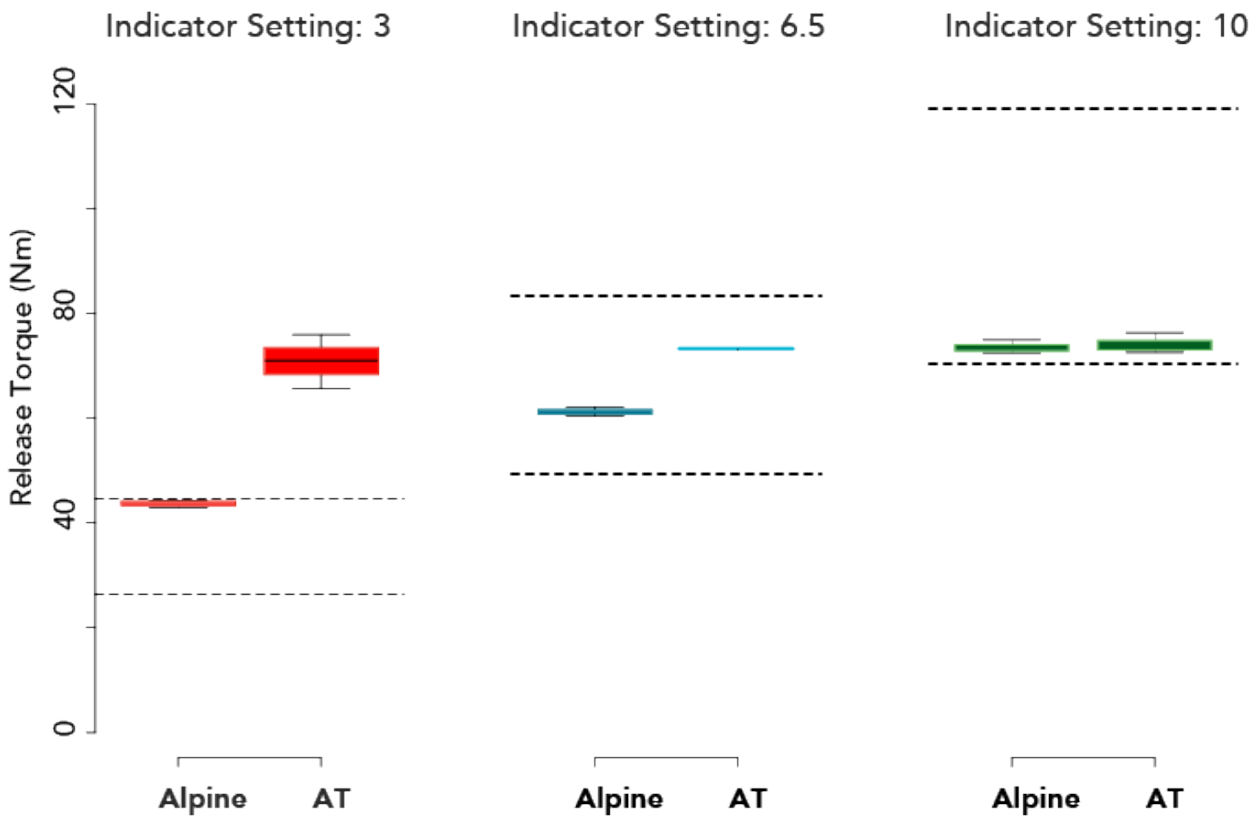

Figure 2.7: Comparison of release torque from alpine and AT boots to the values specified by international standards, denoted by the dashed lines.

Testing ski equipment at room temperature in a dry laboratory setting is a limitation of the current study. In wet and cold conditions similar to those found when skiing, it is possible that AT boot-alpine binding systems may perform better as the AT boot sole hardness would increase. This study was intended to examine the worst-case scenario for use of these systems. Shop technicians also perform binding adjustment and testing at room temperature and in dry conditions. Therefore the results presented here have significant relevance to the conditions in which boot-binding systems are evaluated for consumers.

2.3.2 *Conclusion*

Alpine ski boots and bindings for downhill skiing comply with international standards and provide reliable release and retention characteristics. Alpine touring (AT) boots do not provide the same reliable retention and release characteristics when used with alpine ski bindings. While some AT boots fit geometrically into alpine ski bindings, the release function of the ski/boot/binding system can be compromised severely and increase the risk of a lower leg injury. The results of our testing indicate that it is unlikely that ski shop test equipment could reliably detect whether a given AT boot and alpine ski binding combination will perform properly. This potential 'false-positive' could misinform consumers into believing their equipment will function properly when the likelihood of an injury could be increased significantly. Based on these results, it is not recommend that skiers use AT boots in alpine ski bindings, as they currently exist on the market. The development of international standards for AT boot test soles, representative of AT boots currently on the market, could help improve alpine binding designs to function properly with AT boots.

Chapter 3. Release Characteristics of Alpine Touring Ski Boots in Alpine Ski Bindings: A Case Study of Binding Features

3.1 Introduction

Alpine touring (AT) is a sub-discipline of skiing in which the skier uses skis to ascend, traverse, and descend snow covered backcountry terrain where trails are not maintained or do not exist. AT boots have unique geometry and soft boot soles[36] with rubberized tread for maximum traction and metal inserts at the toe and heel interface with special AT bindings[49]. Many consumers currently use AT boots in alpine bindings for comfort though alpine bindings are not generally marketed as compatible with AT boots. However, the lines between AT and alpine ski equipment for consumers are blurring quickly with the rapid pace of new AT products brought to market each season, and it is increasingly common for consumers to use AT boots in their alpine bindings while downhill skiing at ski resorts (Chapter 2).

In a previous study, the retention-release characteristics of 80 AT boot – alpine ski binding combinations were tested, of which, 71% did not release appropriately (Chapter 2). One alpine binding released appropriately for all alpine and AT boots tested; the remaining alpine bindings performed appropriately for only 40% of the boots or less. Two bindings did not release appropriately for any of the AT boots tested. While most AT boots geometrically fit into alpine bindings, we found that the functionality of the ski-boot-binding system was compromised severely. It was hypothesized that frictional and geometric differences created the performance differences between AT boots and alpine boots when used in alpine bindings.

A broad spectrum in the release performance between alpine bindings, when used with AT boots, serves as the motivation for this study: to identify differences in features of AT boots and alpine bindings, and/or combinations thereof, which are critical to optimizing the release function of alpine bindings with AT boots for future product design and consumer safety. These features and their effect on the release characteristics of boot-binding systems are identified through the utilization of linear multivariate regression models

3.2 **Methods**

The retention-release characteristics were tested in a previous study from five models of alpine ski boots and ten models of AT boots in eight representative models of alpine ski bindings; 120 unique combinations of boots and bindings were tested (*Chapter 2*).

To briefly summarize the four independent load scenarios used in the previous study, the release characteristics of each boot-binding combination was tested per the requirements of test standard ASTM F504-05 in: (1) *Pure Forward Lean* –a bending moment applied along the transverse axis of the ski; (2) *Pure Twist* – an axial twisting moment applied to the ski; (3) *Front Preload Twist* –a vertical preload force is applied to the fore-body of the ski prior to the application of a lateral force on the ski 45 cm in front of the toe piece, to simulate a skier having their weight over the fore-body of the ski during a forward, twisting fall; and, (4) *Rear Preload Twist* –a preload force was applied to the rear of the ski prior to the application of a lateral force 45 cm behind the heelpiece on the ski, to simulate a skier having their weight over the tail of the ski during a backward, twisting fall.

The release torque from these four loading conditions in the previous study were used in the present case study to identify boot and binding features predictive of the boot-binding performance results from our previous study. In each of the four loading conditions tested, the absence or presence of static preload forces imposed one of three unique boundary conditions on the boot-binding system before the start of each test:

- Boundary Condition 1 (BC_1): Pure Forward Lean and Pure Twist tests only comprise of internal forces of the boot-binding system acting on the boot-binding interface (Figure 3.1A).
- Boundary Condition 2 (BC_2): Front Preload Twist applies a static preload force in the vertical direction to the fore-body of the ski (Figure 3.1B).
- Boundary Condition 3 (BC_3): Rear Preload Twist applies a static preload force in the vertical direction to the aft-body of the ski (Figure 3.1, Figure 3.1C).

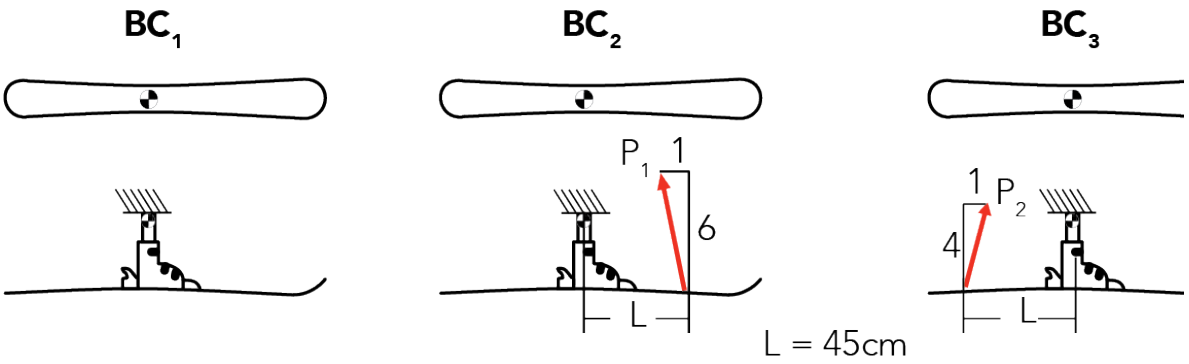

Figure 3.1: (A) Boundary Condition 1 (BC_1, left), (B) Boundary Condition 2 with P_1 (BC_2, center), and (C) Boundary Condition 3 with P_2 (BC_3, right).

For BC_1, several constraining forces were hypothesized to affect the release torque of a ski boot from an alpine binding including: the boot sole hardness (Figure 3.2), interference of the tech inserts with the binding (Figure 3.3), the type of anti-friction device (AFD), forward pressure of the binding (Figure 3.3), and the contact pressure at the AFD-boot interface (Figure 3.2 & Figure 3.6).

When external forces are applied to the system in BC_2 and BC_3, other parameters such as bending stiffness (EI) of the ski-boot-binding system (Figure 3.4) and additional degrees of freedom of the binding can influence or compound the effect of frictional forces already present from BC_1. These constraints were quantified for each boot, binding, and boot-binding combination tested in our previous study. Each constraint is thoroughly defined below and also summarized in Table 3.1 for clarity.

3.2.1.1 Boot Constraints

***Boot Dimensions**:* Dimensions were measured using digital calipers (Model No. CD-6" CSX, Mituyo, resolution: 0.01mm) (Figure 3.2).

***Boot sole hardness**:* Sole Hardness (Shore D) was measured per ASTM D2240-05[50] for alpine and AT boots in the region that contacted the AFD (Figure 3.2).

Tech Inserts: Boots with tech inserts were coded ***Tech = 1***; boots with no tech inserts were coded ***Tech = 0*** (Figure 3.2).

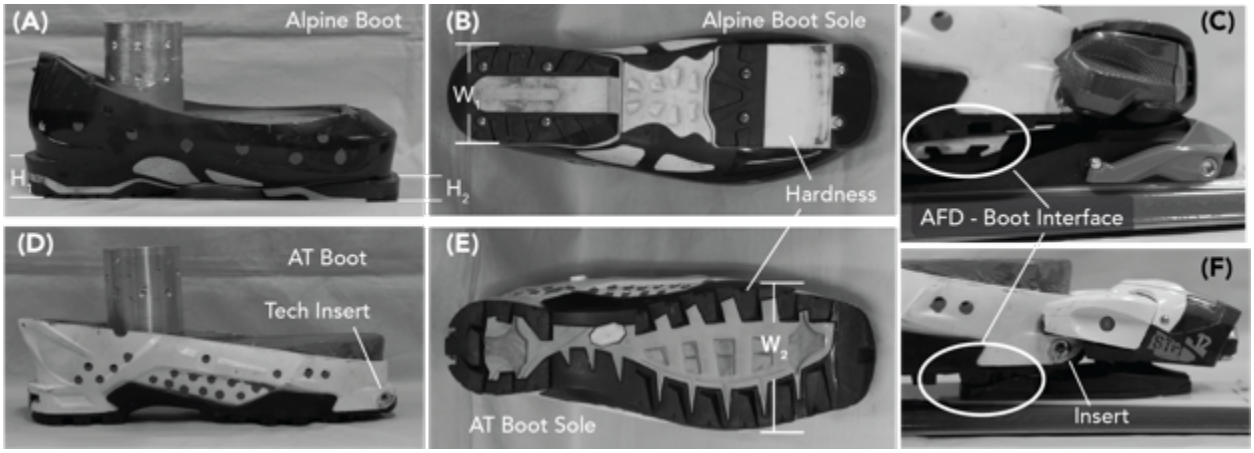

*Figure 3.2: Boot features recorded included: (A) Heel Height, **H_1**, and Toe Height, **H_2**, (B) Heel Width, **W_1** and Toe Last Width **W_2**, and boot sole hardness, Shore D (B & D). The presence of tech inserts and their interface location with the inserts, low (C) or high (D) was recorded. Contact pressure between the boot and the binding was measured at the AFD-Boot Interface (B & F).*

3.2.1.2 Binding Constraints

Forward Pressure (FP): The toe and heelpieces of alpine bindings apply a forward pressure (FP), or compressive force (with units of Newtons), to the boot along the longitudinal axis of the ski. Elastic travel of the heelpiece helps to maintain a constant compressive force to prevent the boot from releasing from the binding during ski flexion and extension. The magnitude of the FP not standardized; therefore the FP was measured for each binding using rigid aluminum alpine boot toe and heel blocks connected in series with a load cell (Model 31, Honeywell, Columbus, OH, resolution 0.87 N) (Figure 3.4).

Bending Stiffness (EI): The bending stiffness in the transverse plane, or equivalent 'EI', where EI is the combination of the composite modulus of elasticity, *E*, and the bending moment of inertia for the ski, *I*. The EI was measured using a custom fixture that applied a 222N ± 44N three-point bending load to the ski through the center of an ISO 5355 boot-test boot sole placed in each ski binding and the outside bending supports were located ±0.69m from the point of load application. The radius of curvature was calculated by measuring the vertical defection of the ski (µMaxµm, Mahr, Göttingen, Germany, resolution =10 µm) in discrete 76mm increments

between the two outside supports. The radius of curvature of was used to calculate equivalent EI of the boot-binding-ski system using beam theory (Figure 3.4).

AFD: Anti-friction devices on the binding toe pieces provide a low-friction support for the ski-boot sole. Mechanical AFDs consist of a sliding, spring loaded plate that slides with the boot as it releases in pure twist. Static AFDs are a low-friction surface, often made from Teflon. Bindings with mechanical AFDs, were coded AFD = 1, and AFD = 0 for static AFDs.

Degrees of Freedom (DoF): Alpine binding toe pieces react to a lateral force at the toe and a vertical force at the heel and are considered to have two degrees of freedom (Figure 5). Several bindings have a 'mobile' toe considered to have a third degree of freedom (Senner, 2013) that allows for an upward release of the toe and were coded DoF = 1, otherwise they were coded DoF = 0.

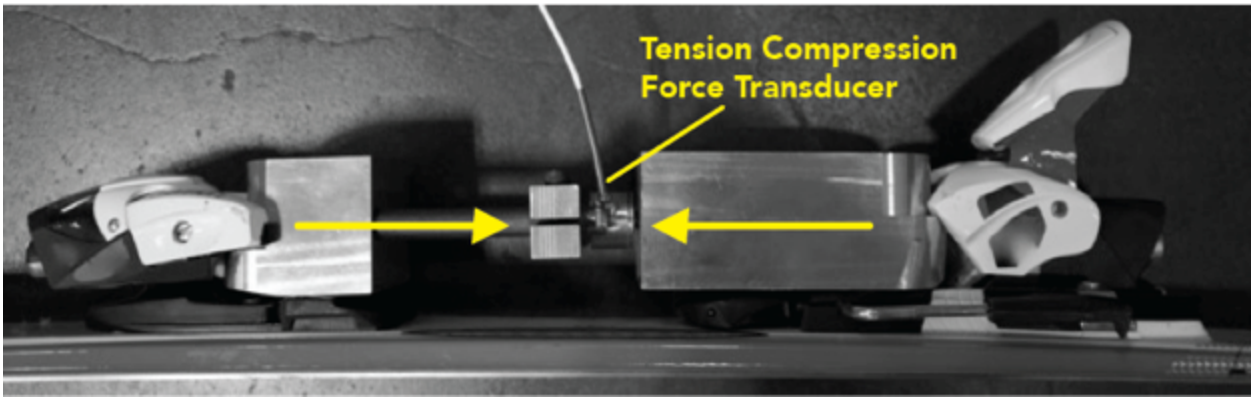

Figure 3.3: Forward Pressure measurement fixture placed in an alpine binding.

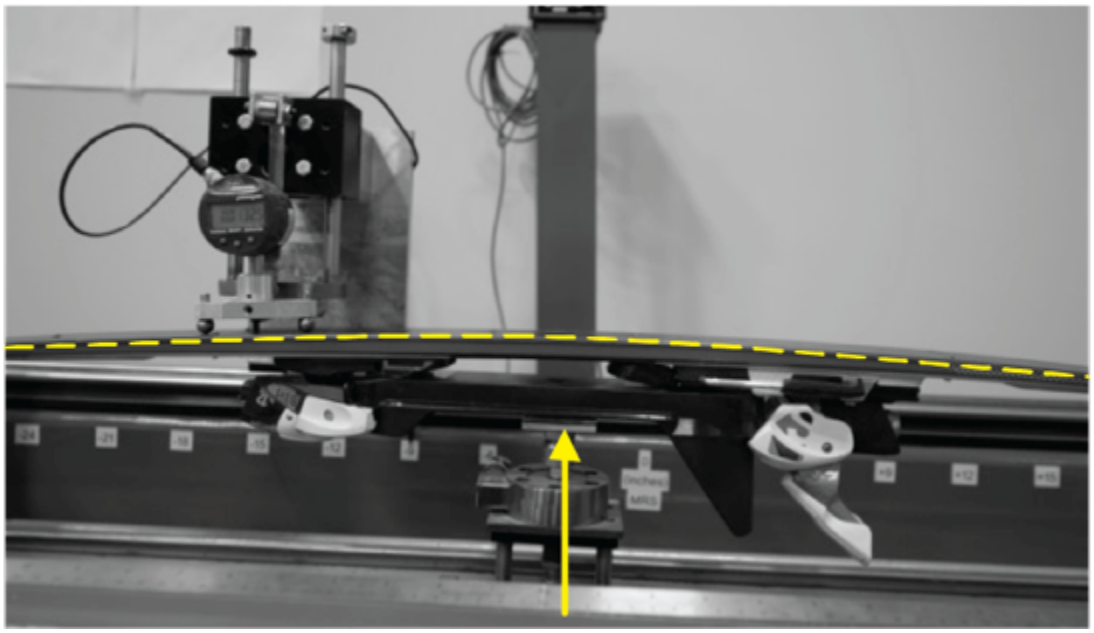

Figure 3.4: Bending Stiffness (EI) measurement fixture with a load applied to a test sole in the ski binding inducing the three-point bending load.

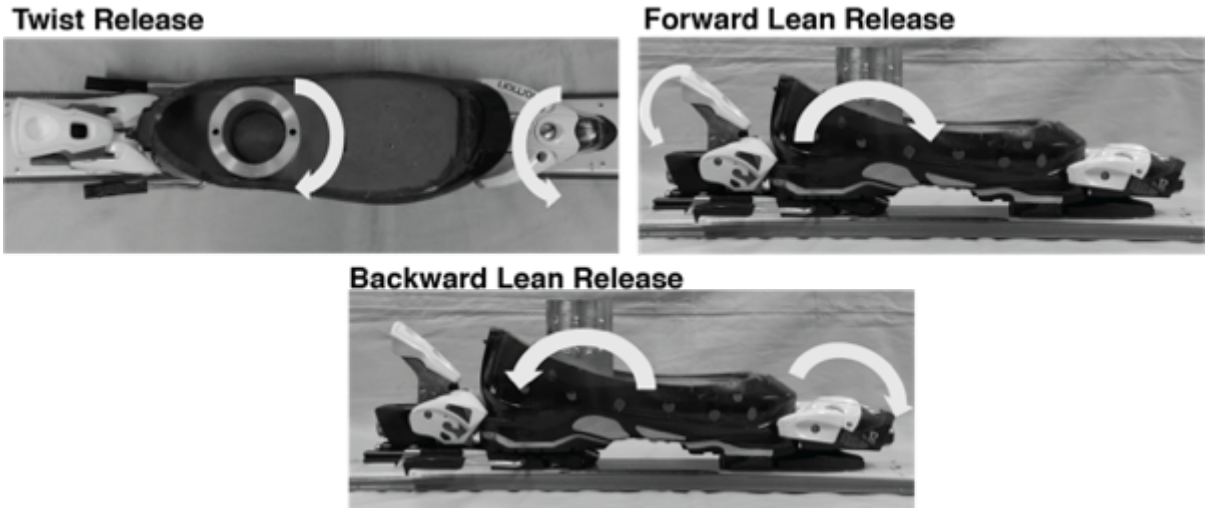

Figure 3.5: Motions of the ski boot and binding heel and toe pieces in a Twist Release Mode (top left), Forward Lean Release Mode (top right), and Backward Lean Release showing the toe piece allowing upward displacement of the toe (bottom center).

3.2.1.3 Boot-Binding Interface Constraints

3.2.1.3.1 Tech Insert Interference

The ***Toe*** interface region of the binding with tech inserts was coded as ***Toe = 1*** for the high region and ***Toe = 0*** for the low region (Figure 3.2).

3.2.1.3.2 Contact Pressure at the AFD-Boot Interface

Pressure sensitive film (Fujifilm Prescale, Bedford, MA) was inserted between the boot sole and AFD for the three boundary conditions, BC_1, BC_2, and BC_3 to measure the contact pressure for 80 combinations of AT boots and alpine bindings, and 40 combinations of alpine boots and alpine bindings; a total of 360 pressure measurements were taken. Films covering three ranges of pressure 0.17 – 0.59 MPa (resolution = 0.03 MPa), 0.48 – 2.41 MPa (resolution = 0.21 MPa), and 2.41- 9.65 MPa (resolution = 0.48 MPa) were calibrated using an MTS material testing machine (Eden Prairie, ME) and a load cell (Model 4526, Humanetics, Plymouth, MI)[51–53].

The height of the toe piece on some binding models was adjustable; toe height for these binding models was adjusted per manufacturers' specifications to accommodate the toe height of each boot. No extra height was added to accommodate for the films' thickness, 0.3 ± 0.05mm, in order to not bias measurements from bindings with no toe height adjustment. Samples were digitized after a 50-hour development period[52] using a digital scanner (Laserjet 3020, Hewlett-Packard, Palo Alto, CA) at a resolution of 300 dpi. Digitized images were converted to contact pressure, ***AFD P,*** using calibration data in Matlab (Mathworks, Natick, MA) (Figure 3.6). Contact area, ***AFD A***, and applied normal force, ***AFD F***, were calculated from the pressure measurements.

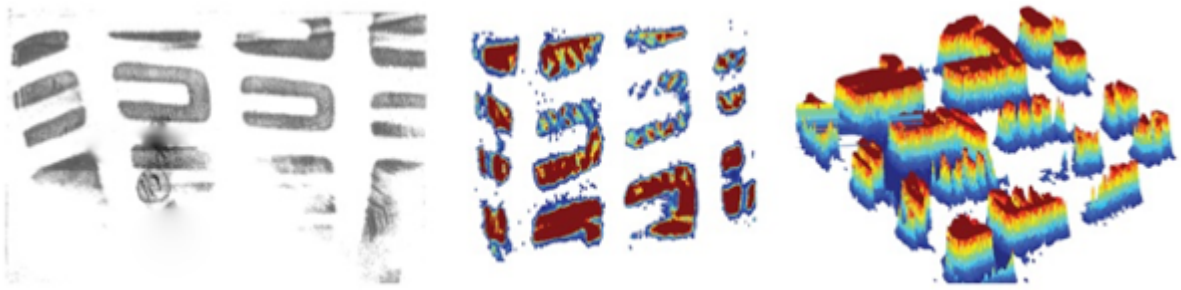

Figure 3.6: Representative scanned image of contact pressure, force, and area recorded on Fujifilm Prescale (left) and transformed to contact pressure in a 2-D (center) and a 3-D view (right).

3.2.2 *Statistical Analysis*

Unpaired, Bonferroni-corrected t-tests and two-way ANOVAs were employed to test for statistical differences in constraints between alpine and AT boots, with $\alpha = 0.05$.

3.2.2.1 Multiple Linear Regression (MLR) Analysis

Independent variables quantified from boot-binding constraints were used predict release torque in multiple linear regression (MLR) models (***R***, *Foundation for Statistical Computing, Vienna, Austria, Fox, 2003*). MLR models were developed for Pure Twist, Front Preload Twist, and Rear Preload Twist. No significant difference in release torque between alpine and AT boots was found in Forward Lean release torque, so it was excluded from the MLR analysis. To obtain a baseline MLR model, the release torque for alpine boot tests were modeled first. New MLR models were then developed using AT boot release torque data pooled with alpine boot data to predict the release torque based on the differences in constraints and features between alpine and AT boots. Boot and binding parameters and their coding used in the MLR analysis are tabulated in Table 3.1.

Table 3.1: Summary of boot-binding constraints, their abbreviations and nomenclature, and units or binary designators.

	Predictor Variable	***Abr.***	**Units or Binary Designator**
Boots	Linear Dimensions	*(see Fig 3.2)*	(mm)
	Hardness	*H*	Shore D Scale
	Tech Inserts	*Tech*	Boots with no Inserts [Tech = 0] Boots with Inserts [Tech = 1]
Bindings	Forward Pressure	*FP*	(N)
	Bending Stiffness	*EI*	(MNm^2)
	AFD	*AFD*	Static [AFD = 0] Mechanical [AFD = 1]
	Degrees of Freedom	*DoF*	No upward release of the toe piece, DoF = 0 Bindings with an upward release of the toe piece, DoF = 1
Boot-Binding Interface Constraints	Tech Insert Interference	*Toe*	Low region, Toe = 0 High region, Toe = 1
	AFD Pressure	*AFD P*	(Pa)
	AFD Contact Force	*AFD F*	(N)
	AFD Contact Area	*AFD A*	(mm^2)

Data were centered about their mean and scaled by one standard deviation. The Kolmogorov-Smirnov test was employed to test for skewness. Transformations were performed on Pure Twist (exponentiated), Front Preload Twist (log), and Rear Preload Twist (log) release torque data from AT boots pooled with alpine boots to reduce skewness.

MLR analyses were used to predict release torque based on unique combinations of independent variables for each load case. The likelihood ratio test compared models using different independent variables and tested for interactions between independent variables. Variance inflation factors (VIF > 5) were used to identify regressors with high collinearity[54]. Regressors were not used if they were not significant contributors to the model, with a significance level of 0.05, or if they were redundant.

3.2.2.2 Relative Contribution of Regressors to MLR models

The percent contribution to variation in release torque of each regressor in the MLR models was calculated using the *lmg* metric from the *relaimpo* statistical package in ***R***[55]. The *lmg* metric normalizes R^2 to 100 percent and the contribution of each regressor is calculated as a

percentage of the R^2 from the linear model. The variance of percent contribution was calculated by bootstrapping the MLR models at 1000 bootstrap intervals, holding the regressors fixed and bootstrapping the residuals. The 95% bootstrap confidence intervals for regressors are reported.

3.2.2.3 Assessing MLR Model Validity

Using the coefficients from the MLR models, predicted release torque values were calculated using the regressors for each combination of boots and bindings tested. Simple linear regressions were performed using torque predictions as independent variables to quantify how well the predicted values matched the measured release torque values using the R^2 metric.

3.3 **Results**

3.3.1.1 Boot Constraints

Alpine boot dimensions were significantly different from AT boot dimensions in every dimension measured except heel width, W_1 ($p < 0.001$). Alpine boot sole hardness (M = 69.5. SD = 4.5) was significantly greater than AT boots (M = 29.5, SD = 17.5) $t(10.9) = 6.85, p<.001$. No alpine boots had tech inserts; and nine of the ten AT boots had tech inserts.

3.3.1.2 Binding Constraints

Forward Pressure, FP, of the alpine bindings was 173.8±35 N. The EI of the bindings was 181.3 ± 24.2 MNm^2. Five bindings had static AFDs and three had mechanical AFDs. Two bindings had fixed toe pieces, DoF = 0, and six bindings had mobile toe pieces allowing of an upward release at the toe piece, DoF = 1.

3.3.1.3 Boot-Binding Interface Constraints

Four binding toe pieces interfaced with *low* the region of AT boots with tech inserts, Toe = 0, and four interfaced with *high* the region of AT boots above the tech inserts, Toe = 1. The results of a two-way analysis of variance indicated that AFD pressure was significantly greater for AT boots than alpine boots in each boundary condition $F(1,939) = 516.14, p < .001$ (Table 2). Boundary conditions significantly affected AFD pressure, $F(2,939) = 173.4, p < .001$. The effect of boot type, alpine or AT, had a significantly reduced effect on AFD pressure for BC_2 ($\beta = -1.16, SE = 0.26, p < 0.001$) and BC_3 ($\beta = -1.62, SE = 0.26, p < 0.001$) because the

contribution of the applied preloads contributed similar amounts of pressure on, or off, the AFD in those two boundary conditions $F(2,939) = 21.2, p < .001$.

A post hoc Tukey test showed AFD pressure was significantly different between all boundary conditions ($p < .001$) for alpine boots; for AT boots, AFD pressure was significantly different between $BC_2 - BC_3$ ($p < .001$) and $BC_1 - BC_3$ ($p < .001$) but not between $BC_1 - BC_2$ ($p = .81$). AFD pressure was poorly correlated to release torque for both Alpine and AT boots in all three boundary conditions (Figure 3.7, Table 3.2).

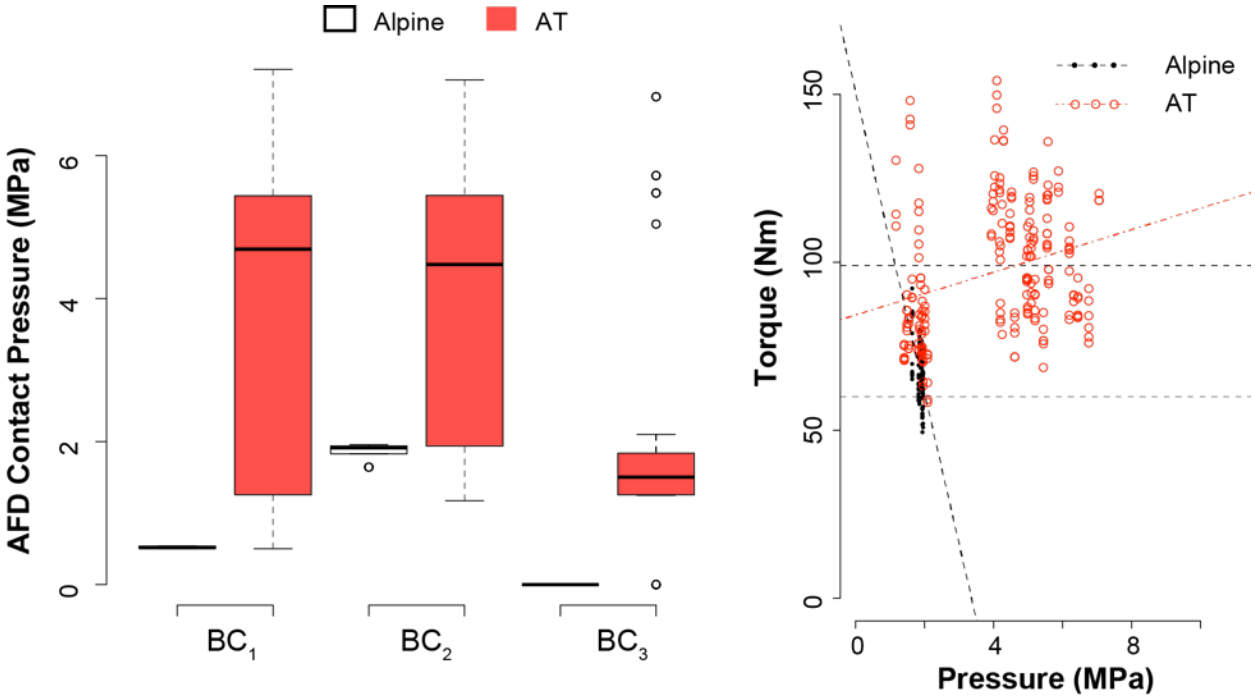

Figure 3.7: AFD pressure was significantly different between alpine and AT boots, and between boundary conditions except for BC_1-BC_2 in AT boots (left). AFD pressure was poorly correlated to Release Torque for all load cases including Front Preload Twist (right).

Table 3.2: AFD Contact Pressure for Alpine and linear regression on AFD pressure versus Torque. Note: The variance of AFD Contact pressure was zero, $\sigma = 0$, for all Alpine boot combinations under BC_3; a linear regression was could not be calculated for this condition.

AFD Contact pressure (MPa), Linear Regression: Pressure versus Torque

	Alpine Boots (MN ± SD), Linear Reg.		AT Boots (MN ± SD), Linear Reg.	
BC_1	0.5 ± 0.01	$R^2 = 0.04$, $p < 0.001$	3.8 ± 0.1	$R^2 = 0.12$, $p < 0.001$
BC_2	1.9 ± 0.01	$R^2 = 0.28$, $p < 0.001$	4.0 ± 1.8	$R^2 = 0.10$, $p < 0.001$
BC_3	0.0 ± 0.0	-	1.7 ± 1.6	$R^2 = 0.02$, $p = 0.03$

3.3.2 *Predicting Release Torque from boot-binding constraints: Alpine Boots*

MLR models were developed to predict how features of boots and bindings contribute to variation in release torque. Significant MLR models were found for predicting release torque with alpine boots for Pure Twist ($F(5, 99) = 25.6$, $R^2 = .566$, Adjusted $R^2 = .542$, $p < .001$*) (Table 3.3), Front Preload Twist (*$F(6, 98) = 50.52$ $R^2 = .756$, Adjusted $R^2 = .741$, $p < .001$*) (*

Table 3.4), and Rear Preload Twist tests (*$F(5, 99) = 95.2$ $R^2 = .828$, Adjusted $R^2 = .819$, $p < .001$*) (Table 3.5). Standardized regression coefficients, their standard errors, and *p-values* testing the null hypothesis that their effects, $\beta n = 0$, are shown in Appendix B, Table B1.

Alpine boot sole hardness had the largest contribution to release torque in Pure Twist, 74.8% [54.2, 95.8], and Front Preload Twist releases 45.9% [30.9, 61.8] (Table 7). An additional degree of freedom at the toe, coded DoF = 1, had the strongest effect on release torque in Rear Preload Twist tests 41.4% [35.0%, 48.7%] (Table 3).

3.3.3 *Predicting Release Torque from boot-binding constraints: Alpine & AT Boots*

A significant MLR model was found (*$F(14, 300) = 29.4$, $p < .001$*) that accounted for approximately 58% of the variance of Pure Twist release torque of alpine and AT boots in Pure Twist (*$R^2 = .578$, Adjusted $R^2 = .558$*, Appendix B, Table B2). AFD contact pressure, 19.5% [14.5, 25.9], and boot sole hardness, 18.6% [12.8, 25.3] had the strongest effect on Pure Twist release torque (Table 3.3). AFD type had a significant interaction with AFD contact pressure, meaning the effect of AFD contact pressure on release torque was effected by whether a binding had a static or mechanical AFD; this contributed 9.9% [4.9, 16.3] to release torque variation. In Pure Twist releases, static AFDs produced higher release torque in Pure Twist (*$\beta = 0.266$, $SE = 0.046$, $p < 0.001$*).

A significant regression model was found (*$F(10, 304) = 74.9$, $p < .001$*) that accounted for approximately 71% of the variance of Front Preload Twist release torque of Alpine and AT boots (*$R^2 = .711$, Adjusted $R^2 = .702$, Appendix B, Table B2*). Boot sole hardness, 31.6% [26.3, 36.6], and tech inserts, 22.1% [17.4, 27.5], had the strongest effect on release torque in Front Preload Twist releases (

Table 3.4). AFD contact pressure, 13.7% [11.3, 16.8], had a smaller contribution in a Front Preload Twist release compared to a Pure Twist release 19.5% [14.5, 25.9]. Static AFDs were

associated with lower release torque values ($\beta = -0.126, SE = 0.034, p < 0.001$), and mechanical AFDs produced higher release torque for Front Preload Twist releases; this is a reversal for the effect of AFD type from the Pure Twist.

A significant regression model was found ($F(13, 301) = .767, p < .001$) that accounted for approximately 77% of the variance of Rear Preload Twist release torque of Alpine and AT boots ($R^2 = .767$, *Adjusted* $R^2 = .756$, Appendix B, Table B2). Similar to Alpine boots, an upward release of the toe, DoF = 1, had a strong effect on release torque, 19.5% [15.7, 23.8], but FP was the strongest contributor, 22.2% [17.1, 27.5] (Table 3.5). Other constraints such as FP's effect interacting with flexible ski-binding combinations, or lower EI values, FP|EI, 20.7% [15.9, 26] were had largest effect on Rear Preload Twist release torque.

Table 3.3: *Percent relative contribution of boot-binding constraints to release torque variation for Pure Twist releases.*

Regressors		Pure Twist: % Relative Contribution	95% CI [LL, UL]
		Alpine	**AT**
Boots	Tech	-	6.9% [4.1, 11.1]
	Hardness	**74.8% [54.2, 95.8]**	18.6% [12.8, 25.3]
Bindings	AFD	-	2.2% [1.3, 4.3]
	DoF	-	5.8% [2.3, 10.8]
	EI	9.4% [3, 19.1]	5.6% [2.2, 10.4]
	FP	4.2% [0.8, 15]	9.1% [4.8, 14.8]
	EI|FP	-	3.4% [0.9, 7.6]
	Toe	-	1.9% [0.7, 4.6]
	Tech | Toe	-	-
Boots-Bindings	AFD Area	-	-
	AFD Force	-	7.2% [5.4, 10.1]
	AFD Pressure	8.3% [1.7, 20.8]	**19.5% [14.5, 25.9]**
	AFD | Hardness	-	-
	AFD P | Hardness	3.3% [0.2, 9.6]	-
	AFD | AFD P	-	9.9% [4.9, 16.3]
	AFD F| DoF	-	2.3% [0.7, 6]
	AFD F | Hardness	-	2.3% [0.7, 6]
	FP | Tech	-	4.2% [1.2, 8.8]
Model Fit	**F**	*F(5, 99) = 25.6*	*F(12, 302) = 30.0*
	R^2	0.564	0.543
	p	< .01	< .01

Table 3.4: Percent relative contribution of boot-binding constraints to release torque variation for Front Preload Twist releases.

Regressors		Front Preload Twist: % Relative Contribution 95% CI [LL, UL]	
		Alpine	**AT**
Boots	Tech	-	22.1% [17.4, 27.5]
	Hardness	**45.9% [30.9, 61.8]**	**31.6% [26.3, 36.6]**
Bindings	AFD	5.7% [2.7, 11.7]	2.8% [1.6, 4.6]
	DoF	-	-
	EI	11.9% [5.6, 21.8]	5.3% [2.9, 8.5]
	FP	0.8% [0.4, 3.7]	2% [0.6, 4.3]
	EI|FP	-	6.7% [3.5, 10.4]
	Toe	-	6.2% [3.2, 10.2]
	Tech | Toe	-	0.8% [0.1, 2.4]
Boots-Bindings	AFD Area	-	-
	AFD Force	-	9.8% [7.7, 12.8]
	AFD Pressure	27.5% [14.6, 40.8]	13.7% [11.3, 16.8]
	AFD | Hardness	-	-
	AFD P | Hardness	-	-
	AFD | AFD P	-	1.3% [0.3, 3.2]
	AFD F| DoF	-	-
	AFD F | Hardness	-	3.4% [1.4, 6.3]
	FP | Tech	-	-
Model Fit	**F**	*F(6, 98) = 50.5*	*F(8, 306) = 81.1*
	R^2	0.756	0.68
	p	< .01	< .01

Table 3.5: Percent relative contribution of boot-binding constraints to release torque variation for Rear Preload Twist releases.

Regressors		Rear Preload Twist: % Relative Contribution 95% CI [LL, UL]	
		Alpine	**AT**
Boots	Tech	-	0.7% [0.5, 1.5]
	Hardness	-	4.7% [3, 6.9]
Bindings	AFD	-	2.1% [2, 2.6]
	DoF	**41.4% [35.0%, 48.7%]**	19.5% [15.7, 23.8]
	EI	0.7% [0.5, 2.4]	0.6% [0.3, 1.6]
	FP	35.6% [25.2, 46.8]	**22.2% [17.1, 27.5]**
	EI|FP	-	20.7% [15.9, 26]
	Toe	23.8% [16.6, 32.5]	7.7% [5.2, 10.6]
	Tech | Toe	13.3% [7.4, 22.1]	0.2% [0.1, 0.7]
Boots-Bindings	AFD Area	-	13.7% [10.2, 17.6]
	AFD Force	-	-
	AFD Pressure	-	2.6% [1.9, 3.8]
	AFD | Hardness	-	4.4% [2.3, 7.1]
	AFD P | Hardness	-	1% [0.2, 2.5]
	AFD | AFD P	-	-
	AFD F| DoF	-	-
	AFD F | Hardness	-	-
	FP | Tech	-	-
Model Fit	**F**	*F(5, 99) = 95.2*	*F(11, 303) = 69.2*
	R^2	0.828	0.715
	p	< .01	< .01

3.3.4 *Validity of MLR Models*

Significant regression equations were found for each load case modeled in data sets with only alpine boot data, and data which included both alpine and AT boots (Table 4). Regression equations for MLR models using alpine boot data and AT boot data pooled with alpine boot data predicted slopes, βn, equal to unity indicating a strong one-to-one relationship between the predicted and measured release torque values. Intercepts passed slightly below zero indicating a slight bias of ranging from 1-3.5 Nm for MLR models using AT boot data pooled with alpine boot data compared to MLR models using only alpine boot data (Table 3.6).

MLR models predicted the measured release torque better for alpine boot data alone compared to models developed from the pooled alpine and AT boot data. The addition of AT boot data to the models increased RMSE values and 95% confidence intervals (Table 3.6, Figure 3.8). However, the 95% CIs are narrower than the release torque tolerances, ± 30%, specified by international standards (*ISO 9462-2012*) for in-use range of alpine bindings, indicating that the models are at least as precise, if not slightly more so, as the requirements of the systems they are modeling.

Table 3.6: Simple linear regression on measured release torque vs. predicted release torque from the MLR models.

MLR Model Metrics	Boots	β	Intercept	F	R^2	RMSE	95% CI
Pure Twist	Alpine	1	< 0.00	F(1,133)=133	0.564	2.7	12.2
	Alpine & AT	1.06	-0.99	F(1,313)=630	0.667	10.9	19.9
Front Preload Twist	Alpine	1	< 0.00	F(1,103) = 191	0.65	10.1	14.4
	Alpine & AT	1.06	-3.46	F(1,313)=439	0.651	13.1	29.5
Rear Preload Twist	Alpine	1	< 0.00	F(1,103) = 495	0.828	2.7	11.3
	Alpine & AT	1.04	-2.7	F(1,313)=1112	0.780	8.3	15.2

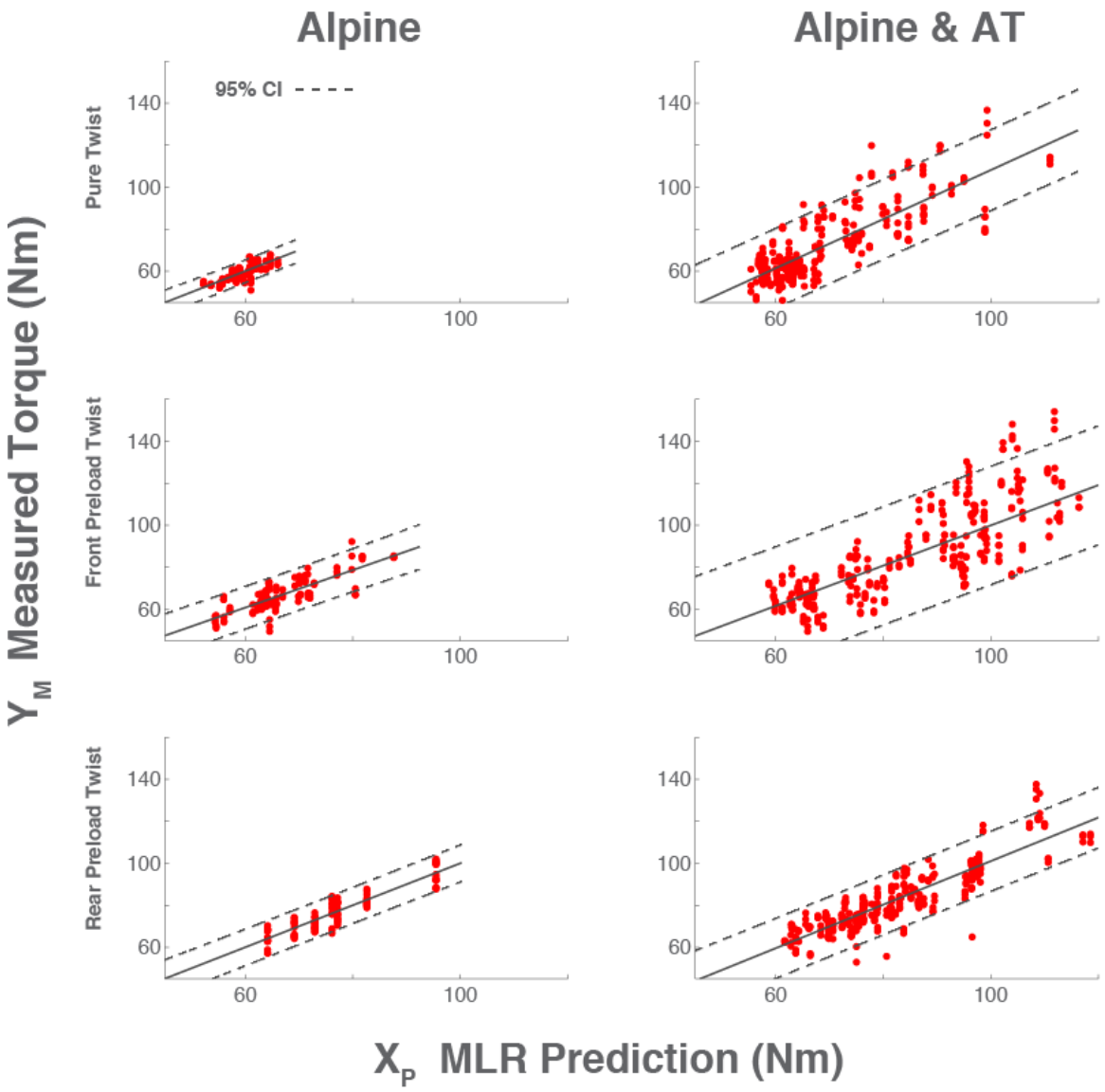

Figure 3.8: Measured release torque (Y_M) for Alpine Boots (Left Column) and Alpine and AT boots combined (Right Column) for Pure Twist (Top row), Front Preload Twist (Center row), and Rear Preload Twist (Bottom row) plotted against the MLR model predictions, (X_P) for each boot-binding tested.

3.3.5 *Static vs. Mechanical AFDs*

In the previous study, AFDs were damaged in 43% of AT boot-alpine binding combinations. Every binding model with a mechanical AFD was damaged; one static AFD, out of five, was damaged (Figure 3.9). Bindings with mechanical AFDs ranked as the lowest performing bindings with AT boots (Table 3.7).

Alpine bindings with AT boots were predicted to be 50% less sensitive to changes in indicator settings than with alpine boots. A significant linear regression model found (*$F(1, 4) = 40.0$, $p = .003$*) that accounted for approximately 90% of the variation in release torque as a function of indicator settings for AT boots in alpine bindings with static AFDs (*$R^2 = .909$, Adjusted $R^2 = .886$*, Figure 3.10). Other boot-binding described above often caused AT boots in alpine bindings with static AFDs to release at higher torque values than allowed by international standards; however, changes in indicator settings resulted in the same proportional changes in release torque between AT boots in alpine bindings with static AFDs as alpine boots in alpine bindings.

In contrast to static AFDs, AT boots used in alpine bindings with mechanical AFDs alter release characteristics so severely that a linear regression analysis shows that indicator settings are not correlated with the release torque in anyway (*$F(1, 10) = 1.43$, $p = .26$, $R^2 = .125$, Adjusted $R^2 = .037$*); release torques corresponding to the minimum, median, and maximum indicator settings often fell within ±3% (Figure 3.10). The three lowest performing bindings with AT boots incorporated mechanical AFDs (Table 3.7).

The worst load case for mechanical AFDs occurs in Front Preload Twist releases, when a preload is applied to the fore-body of the ski significantly increasing the pressure between the soft AT boot sole and AFD. As a lateral load is applied to the ski, softer AT boot soles stick to mechanical AFD as the binding moves away. During this phase, the spring-loaded cam in the toe piece, which normally controls release torque, is overcome. Here the boot settles into a local minima 5-10° past the point when an Alpine boot would have released (Figure 3.10). Internal friction retains the boot in the ski and the boot must overcome a second energy barrier to finally release. This final energy barrier is simply a function of the internal friction of the system and is no longer controlled by the spring-loaded cam intended to control the release torque.

Figure 3.9: One static AFD was damaged (Left); every binding with a mechanical AFD was frequently forced beyond the limit of their elastic travel and damaged (Right).

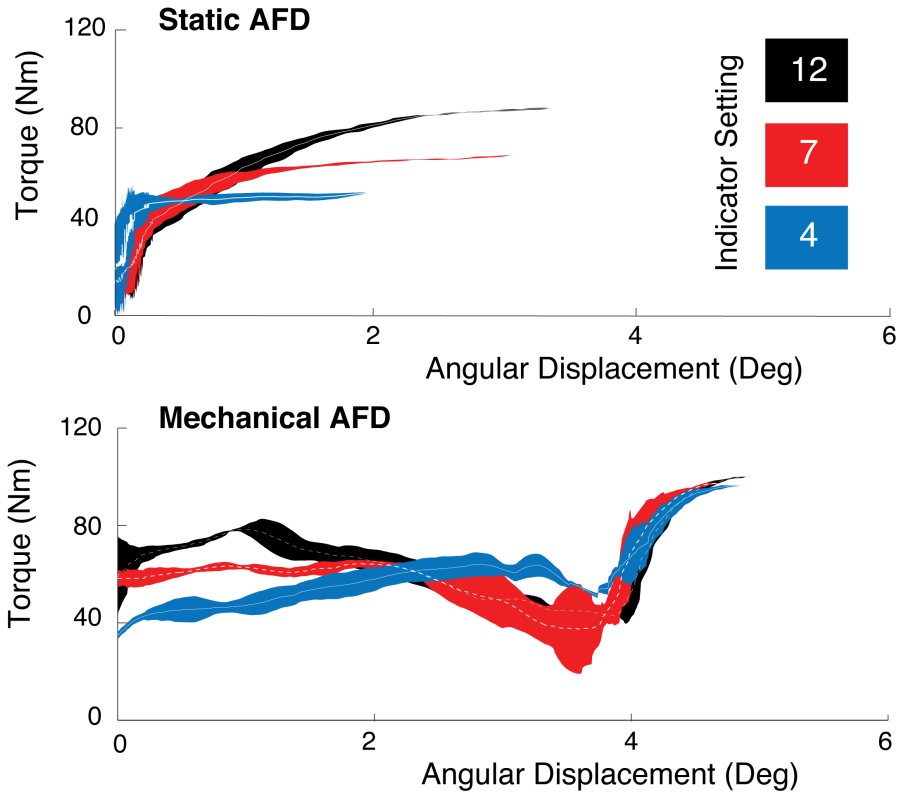

Figure 3.10: Release torque and angular displacement during a Front Preload Twist release for three different indicator settings for an AT boot in one representative alpine binding with a static AFD (Top) and one representative alpine binding with a mechanical AFD (Bottom). Dashed lines are the average of three trials; the shaded regions denote one standard deviation.

*Table 3.7: Comparison of binding features for the single binding which released appropriately for all AT boots tested versus the averages of binding features of the ten bindings tested. *Pass rate from the percentage of the N = 10 AT boots that passed the testing with each binding. See Chapter 3.2.1.1-3.2.1.3 for definitions of the coding used in the table below.*

Binding Parameters		AFD	Toe	FP	EI	DoF	AFD P		
							BC1	BC2	BC3
MN ± SD, or No. of Bindings		5 3	6 2	173±33	181±22	2 6	3.8±2.2	4.0±1.8	1.7±1.6
Units or Coding		0 1	0 1	0	(MNm^2)	0 1	(MPa)	(MPa)	(MPa)
1	100%	0	1	206	175.4	1	.5 ± 0.0	1.9 ±0.2	0.0 ± 0.0
2	40%	0	0	179.4	174	1	2.9 ± 2.3	3.8 ±1.6	1.1 ± 0.9
3	30%	0	0	177	172.5	1	2.9 ± 2.6	3.8 ±1.7	0.9 ± 0.8
4	20%	0	1	135.4	193.9	1	3.1 ± 2.5	2.9 ±1.5	1.7 ± 2.2
5	20%	0	1	197.6	141.2	1	2.7 ± 2.3	3.7 ±1.6	1.0 ± 0.8
6	10%	1	0	206	220.6	1	3.2 ± 2.4	3.7 ±2.1	1.5 ± 1.8
7	0%	1	0	175.4	190.4	0	3.5 ± 2.5	3.3 ±2.0	1.8 ± 2.0
8	0%	1	0	213	190.4	0	.53 ± 0.0	1.7 ±0.1	0.0 ± 0.0
Binding No.	% Pass Rate*								

3.4 **Discussion**

Alpine and AT boots and bindings are designed functionally for very different purposes. Alpine bindings are designed to minimize the frictional and geometric interference constraints at the interface the alpine boot sole and alpine bindings. AT boots are designed to maximize friction between boot soles and walking surfaces and interface with special AT bindings. Several features of AT boots examined in this study that were strong predictors of high release torque in alpine bindings, such as soft boot soles and tech inserts, explicitly do comply with international standards that govern how alpine ski boots should interface and perform with alpine bindings (ISO 5355-2005). Tech inserts do not comply with any current international AT boot standards such as ISO 9523-2006).

In our previous study, all 10 AT boots released appropriately from one alpine binding model (out of the eight models studied). Two bindings did not release appropriately with any AT boot. Such a large variation in binding performance indicates that boot-binding systems are very

sensitive to how they interface and how their constraints change across different boundary conditions.

Features of the single binding that passed testing with 100% of the boots have been shown to be predictive of lower release torque and displacement in the statistical analyses reported in this study. Acceptable release performance was achieved for only 40% of the AT boots, or less, in the seven remaining alpine bindings. Some of these bindings had some features in common with the most successful binding, but no other bindings shared the specific combination of features with the highest performing binding that released appropriately with all AT boots tested.

AT boot-alpine binding systems are highly sensitive to the interactions (e.g. combinations) of boot-binding features that can have a multiplicative affect on release torque. Sometimes the effects of these interactions can be reversed by changes in boundary conditions, as is the case with static and mechanical AFDs. Overall, bindings with mechanical AFDs ranked as the lowest performing bindings with AT boots (Table 7).

A governing paradigm in the ski industry is that a boot will function properly in a binding if it "fits"; and, it is therefore assumed that the fit of AT boots in alpine bindings should be correlated with proper function. AFD contact pressure measurements were able more accurately quantify how well a given boot *fit* into a binding toe piece. Higher AFD contact pressure values are predictive of a tighter fit and higher frictional forces; lower AFD contact are predictive of a normalized fit resulting adjustable toe height or boots conforming to international standards (*ISO-5355-2012*). AFD contact pressure was a strong predictor of release torque for the Pure Twist release but its' effect was much smaller in combined loading releases (Front Preload Twist, Rear Preload Twist). Table 3.7 indicates that the highest performing alpine binding and the lowest performing binding both had nearly equivalent AFD contact pressure. In other words, AT boots *fit* into both the highest and lowest performing bindings equally well but performed significantly differently. These results show that the interaction of AT boots and alpine bindings is significantly more complicated than just fit and AT boots fail to perform properly in bindings that can be adequately adjusted to fit the larger linear dimensions of AT boots.

In the analyses presented here, statistical models have only been reported for boot-binding features controlling release torque. However, many of the features predictive of higher

release torque are indicative of larger angular displacement of the ski relative to the boot, but are not reported here for brevity.

3.5 Conclusions

Features of alpine touring (AT) boots and alpine bindings that cause the boot-binding systems to not release appropriately include soft boot soles and tech inserts; both are ski boot features that explicitly do not comply with alpine ski boot and alpine ski binding international standards intended to maintain reliable and predicable binding release function to lower the risk of lower leg injuries to skiers. A combination of binding features unique to one alpine binding was shown to allow AT boots to release with in the allowable torque limits specified by international standards. Other bindings that did not release from AT boots appropriately shared some features, but not all with the highest performing binding. How well an AT boot fit into an Alpine binding was not indicative of proper release performance; rather, significant consideration much be given to the constraint forces produced by features of the boot, the binding, and how they interact as a system.

Caution should be utilized to ensure that if alpine bindings are intended for use with AT boots, such designs are driven by empirical data rather than industry paradigms. As they currently exist on the market, most alpine bindings cannot reliably function properly with AT boots, even if they appear to fit. However this work demonstrates that a specific combination of features exists that can provide reliable binding release function.

Chapter 4. The Effect of Alpine Touring Ski Boot Toe Inserts on Release Characteristics of the Tech Binding Toe Piece

4.1 Introduction

Conventional alpine boots and bindings rigidly couple the skiers boot to the ski to allow skiers to perform maneuvers while skiing down hill, and to release the ski from the boot before loads to the lower leg become injurious. Alpine touring (AT) is a sub-discipline of skiing in which the skier uses the skis to ascend, traverse, and descend snow-covered terrain in the backcountry on unmaintained trails and sometimes rough terrain. Conventional alpine skiing equipment lacks functionality to allow skiers to ascend slopes under their own power during alpine touring. As a result, ski boot and binding manufacturers have developed specialized alpine touring equipment.

AT boots and bindings as a system have two functional modes:

- **Downhill (Ski) mode:** the toe and heel of the boot are both rigidly fixed to the ski by the binding to allow the skier to perform maneuvers as they ski down snow slopes.
- **Uphill (Walk) mode:** the binding allows the heel of the boot to be decoupled from the ski, and the toe of the boot is free to pivot to allow the skier to walk up hill on skis, providing both flotation in deep snow and efficiency.

4.1.1 *Alpine Touring Bindings*

There are currently two alpine touring binding designs on the market, AT Frame Bindings and Tech/Pin bindings. AT Frame bindings are extrapolations of established alpine binding technology that incorporates an alpine binding toe piece and heelpiece that are mounted on a chassis. The chassis has a locking mechanism that locks the chassis to the ski for skiing and unlocks it for walking uphill. A hinge at the toe of the chassis allows the binding to pivot on the ski. The functional interface of AT frame bindings with AT boots is nearly identical to alpine bindings. AT frame bindings typically have release value settings that are controlled on the toe piece for twist and heelpiece for forward lean of the binding. These bindings are defined here for clarity but not the subject of the current study. Tech/Pin bindings were developed by Fritz Barthell in the 1980's but were not widely adopted by AT skiers until the mid-2000s. Since the

expiration of Barthell's patent in 2005, the growth in the AT boot sector has been explosive. Their name is derived from Barthell's first model, the 'Low-Tech' bindings. The boot-binding interface and retention-release mechanisms of these bindings function on completely different principles from alpine and AT frame bindings.

Commonly referred to as 'mouse-trap bindings', Tech/Pin bindings have two stable equilibrium positions, open or closed (Figure 4.1). The toe and heelpiece of the binding interface with metal inserts molded into the toe and heel of AT boots (Figure 4.2). The toe-piece commonly consists of a spring-loaded cam mechanism that has two conical pins that clamp into the inserts of the boot toe. For downhill skiing, the heelpiece commonly has two pins that engage into slots in the heel of the boot. For walking, the heelpiece pins can be retracted or rotated 90 degrees such that the rear pins do not engage the boot heel and the boot pivots about the toe-piece to allow the skier to walk uphill (Figure 4.2). With the exception of one or two models, the toe-piece does not have any release value adjustment and only in the last year or two have models begun to incorporate other features from alpine bindings such as forward pressure. The twist and forward lean release values are generally controlled on the heelpiece of nearly all Tech/Pin models.

4.1.2 *The State of Alpine Touring Equipment*

Skiing is not a new concept; Mesolithic humans are estimated to have begun using skis for locomotion over snowy terrain as far back as 9,000 BC[1,2]. However, AT is still in its infancy as a recreational sport compared to its alpine skiing counterpart. AT equipment is continually evolving in an effort to meet consumer demands for light-weight equipment that allows efficient uphill performance, while simultaneously providing reliable retention and release functionality skiers have come to expect from their conventional alpine ski equipment. However, the release-retention performance of many of these systems is a secondary design function to their uphill and downhill performance.

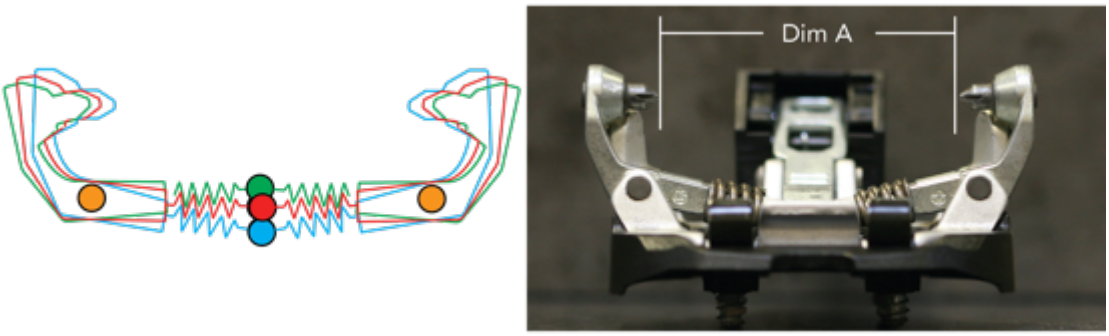

Figure 4.1: (Left) Open and closed equilibrium positions of the Tech/Pin binding toe-piece. (Right) Dim A is denoted as the pin-to-pin dimension when the binding is closed.

Figure 4.2: (A) Heel Inserts (B) Toe inserts molded into ski boots (C) Tech/Pin binding-boot in ski model, with the toe and heel of the boot engaged (D) Heel of the boot engaged (E) Toe of the boot engaged (F) Walk mode with the heelpiece disengaged and only the toe-piece of the binding engaged with the boot.

Safety standards have long been established for alpine ski equipment and have been proven to be effective in reducing the incidence of skiing-related lower leg injuries since the 1980's [34,35,43]. It wasn't until the early 2000's that international standards began to address the safety considerations of AT equipment with standards adapted from alpine ski equipment for AT equipment. The rapid pace of development of AT equipment has quickly outpaced the

international standards organization's ability to address many new issues presented by evolving equipment designs. The interface geometry of AT boot soles with AT Frame bindings was standardized by ISO 9523:2006 and the retention-release requirements of AT bindings were defined by ISO 13992:2006 [36,37]. However, these standards were largely derived from alpine boot-binding standards and have little bearing on how Tech/Pin boot-binding systems function.

No standard currently exists for the interface geometry or properties of AT boots with Tech/Pin bindings. A strong perception among consumers is that Tech/Pin bindings suffer notoriously from inadvertent releases, which occur when a binding releases prematurely, when loads transferred from the ski to the skier are not at risk of injuring the lower leg. Consequently, many consumers ski with the toe piece of their Tech/Pin bindings in walk mode, which effectively locks out any release capability of the toe piece mechanism. In the event of a skiing fall with the toe piece in walk mode, the likelihood of the binding releasing is virtually non-existent which has been shown to triple the likelihood of a lower leg injury [9,45,46].

There are no known epidemiological studies for injury rates using AT equipment. However, examining injury rates in alpine skiing, inadvertent releases cause slightly less injuries than those caused by bindings not-releasing, 0.89% vs. 1.15% of all injuries respectively [8]. Manufacturers have begun to recommend use of their boots with specific bindings and not others based on inter-manufacturer differences in boot geometry to address consumer perceptions of inadvertent releases. If consumer's perceptions are correct, then the risk of injury from an inadvertent release or from a non-release because the toe-piece is locked out, is a concession of safety that must be addressed. To our knowledge, no previous work exists addressing the retention-release characteristics of AT boot-binding systems.

The purpose of the current study is to examine parameters critical to the retention-release performance of the AT boot-Tech/Pin bindings system and quantify the amount of inter-manufacturer variability in AT boot geometry and Tech/Pin binding performance. It is hypothesized that the dimensions of the boot inserts will be the largest s of release torque variability. From this analysis we hypothesize that several parameters can be identified for standardization to improve the reliability of the retention-release performance of Tech/Pin boot-binding systems.

4.2 Methods

When an AT boot is inserted into the toe-piece of a Tech/Pin binding, the pins of the toe piece engage and come to rest at the inner most conical point of the inserts, defined as *Dim A* for the purposes of this study (Figure 4.1 & Figure 4.3). As load is applied to the ski, the pins of the toe-piece will move apart, and the overall distance between them will increase until the toe-piece snaps open.

4.2.1 *Boot Measurements*

Two linear dimensions, *Dim A* and *Dim B*, were measured three times each from the inserts on one pair of boots from nine boot models from seven manufacturers (Table 1) using a micrometer fitted with conical tips (Mitutoyo, Resolution ± 0.001mm). *Dim A* is defined as the inner most point between the two inserts (Figure 4.3). Dim A is defined as the largest distance, in the horizontal plane, of the insert on the anterior most position of the insert (Figure 4.1). A third dimension, *Dim C* was calculated as the difference between *Dim A* and *Dim C*.

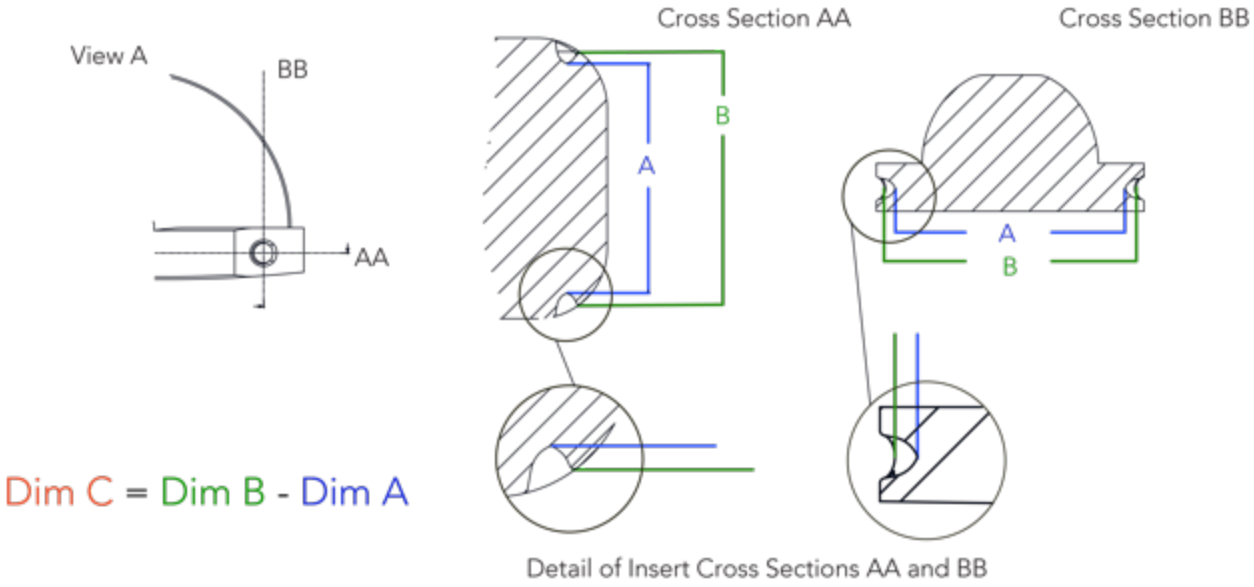

Figure 4.3: AT boot dimensions measured at the toe inserts. View (A) is looking at a boot toe from the side. Cross section (AA) is a horizontal cut through the plane of the insert and boot sole. Cross section (BB) is a cut through the vertical plane of the boot toe; the view is towards the boot toe.

4.2.2 *Binding Measurements*

The force-displacement of the toe-piece was measured using a custom force-displacement transducer (Figure 4.4). The transducer incorporated a custom strain gage based compression load cell (Range: 300 N, Resolution .3N ± 0.1N) and custom linear displacement transducer (Range 12mm, Resolution 0.1mm ± 0.01mm) (J2A-06-S047G-350/SP62 Strain Gages, Vishay Measurements Group, Raliegh, NC). The custom force transducer was calibrated against a NIST-traceable six-axis load cell (Model 4526, Humanetics, Plymouth, MI) and the custom linear displacement transducer was calibrated using a micrometer (Mitutoyo, Resolution ± 0.001mm). The force-displacement transducer incorporated a forcing screw mechanism to push the pins of the toe-piece from the closed to open position while measuring the corresponding force-displacement relationship (Figure 4.4). Force-displacement was measured on a total of 10 pairs of bindings from five manufacturers using a 16-bit data acquisition device while data were sampled at 250 Hz (SLICE NANO, Diversified Technical Systems, Seal Beach, CA). Tests were repeated six times on each binding toe-piece.

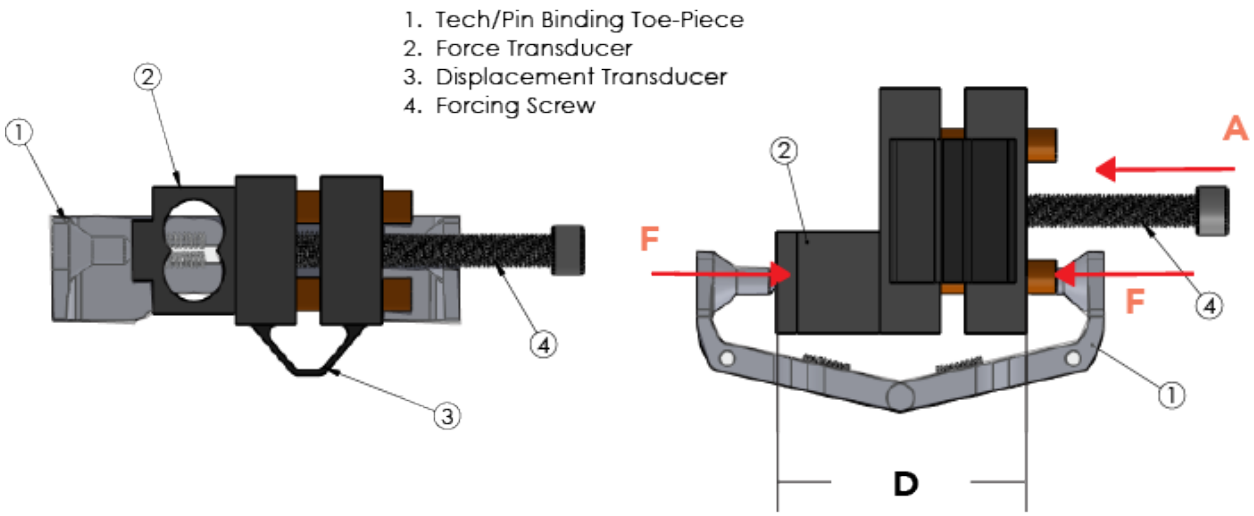

Figure 4.4: Force-Displacement transducer for measuring the clamping force-displacement curve of toe-pieces. (A) The direction of the forcing bolt. (F) Arrows show the resulting compressive clamping force measured by the force transducer. (D) The linear displacement of the binding pins measured by the displacement transducer.

4.2.3 *Release Torque Measurements*

The release characteristics of Tech/Pin boot-binding systems were tested in a laboratory setting using a lower leg surrogate that conformed to standards ISO 9462:2012 Appendix B [5] and ASTM F504-05[47] (Figure 4.5). The ten models of Tech/Pin bindings measured in section 2.2 was mounted to its own test ski; all test skis were the same make, model, and length 167cm (AMP Rx, K2 Sports, Seattle, USA). Five models of AT boots measured in section 4.2.1 (Models A1, B1, C2, D1, E1 from

Table 4.1) with boot sole lengths between 306 and 310 mm were prepared for testing. In order to measure the effect of boot design features, it was necessary to create a rigid coupling between the portion of the boot that interacts with the ski binding and a torque transducer. To this end, each test boot shell was cut below the pivot point of the upper shell and an aluminum adapter plate was secured to the foot area by filling the interstitial space with aluminum-filled epoxy (Rencast® 4037, Huntsman, The Woodlands, TX) (Figure 4.5).

Ski/boot/binding systems were rigidly affixed to a transducer located in a lower leg surrogate via the adapter plate mounted in the boot; torque was applied to the ski using a system of motors, cables, pulley and pneumatics which is measured by the transducer about the axial and transverse axes, as defined in ISO 9462-2012 (Figure 4.5). The range of the load cell was ±400 Nm (resolution: 0.29 Nm) and ±700 Nm (resolution: 0.17 Nm) along the axial and transverse axes. The load cell was calibrated against a NIST-traceable six-axis load cell (Model 4526, Humanetics, Plymouth, MI) and had less than 0.5% error at full scale. The data were collected at 1,000 Hz using a 16-bit data acquisition system (Model 6210-USB, National Instruments, Austin, TX) with a 200 Hz low-pass, anti-aliasing filter. Labview 14.0 software (National Instruments, Austin, TX) was used to collect and filter digitally the data using with a four pole, zero phase shift, low-pass Butterworth filter with a cut-off frequency of 10 Hz. A pure twisting couple, or torque, was applied to the ski with only the toe-piece engaged in the ski position. Tests were performed dry, at 70 degrees F.

4.2.4 *Statistical Analysis*

Two-way ANOVAs were employed to test for statistical differences in constraints between bindings and boots, with a significance level of 0.05.

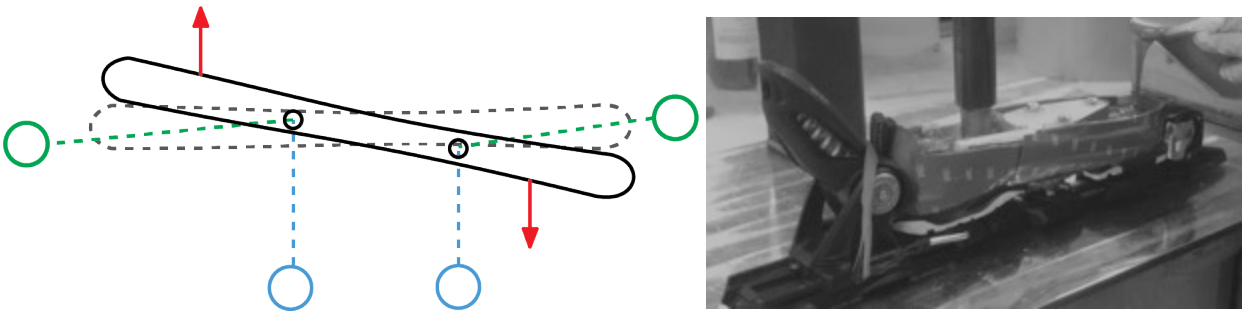

Figure 4.5: Schematic of test apparatus that conforms to ASTM F504-05. The system applied forces (red arrows) to the ski using a motor-driven system of cables and pulleys. A load cell measures the torque on the simulated leg along the axial and transverse axes.

4.2.5 *Multiple Linear Regression (MLR) Analysis*

Independent variables quantified from boot-binding constraints were used predict release torque in multiple linear regression (MLR) models (***R***, *Foundation for Statistical Computing, Vienna, Austria, Fox, 2003*). Data were centered about their mean and scaled by one standard deviation. The Kolmogorov-Smirnov test was employed to test for skewness [56]. MLR analyses were used to predict release torque based on unique combinations of independent variables for each load case. The likelihood ratio test compared models using different independent variables and tested for interactions between independent variables. Variance inflation factors (VIF > 5) were used to identify regressors with high collinearity [54]. Regressors were not used if they were not significant contributors to the model, with a significance level of 0.05, or if they were redundant.

4.2.6 *Relative Contribution of Regressors to MLR models*

The percent contribution to variation in release torque of each regressor in the MLR models was calculated using the *lmg* metric from the *relaimpo* statistical package in ***R*** [55]. The *lmg* metric normalizes R^2 to 100 percent and the contribution of each regressor is calculated as a percentage of the R^2 from the linear model. The variance of percent contribution was calculated by bootstrapping the MLR models at 1000 bootstrap intervals, holding the regressors fixed and bootstrapping the residuals. The 95% bootstrap confidence intervals for regressors are reported.

4.3 **Results**

4.3.1 ***Boots***

Descriptive statistics for measured dimensions of AT boot inserts are tabulated in

Table 4.1. The distribution of measurements of *Dim A*, *Dim B,* and *Dim C* were positively (*Dim A*: 0.849) and negatively skewed (*Dim B*: -0.147, *Dim C*: -1.12), respectively (Figure 4.6). However, skewness was not significant enough to require data transforms according to the Kolmogorov-Smirnov tests. The variation in *Dim A*, ± 0.24 mm, and *Dim B*, ± 0.51 mm, appeared to contribute to tolerance stacking as the standard deviation in the *Dim C* dimension, ±0.63 mm, is approximately equal to the sum of the standard deviations of *Dim A* and *Dim B*.

Table 4.1: *Descriptive statistics for three linear boot dimensions.*

Manufacturer	**Model**	**Dim A (mm)**	**Dim B (mm)**	**Dim C (mm)**
A	A1	58.13 ± 0.07	63.80 ± 0.38	5.15 ± 0.36
B	B1	58.17 ± 0.03	63.24 ± 0.20	5.07 ± 0.22
	B2	58.13 ± 0.03	63.69 ± 0.01	5.45 ± 0.04
C	C1	57.97 ± 0.06	63.91 ± 0.07	5.94 ± 0.13
	C2	58.09 ± 0.00	64.24 ± 0.02	6.15 ± 0.02
D	D1	58.47 ± 0.13	62.24 ± 0.23	3.95 ± 0.10
E	E1	57.85 ± 0.20	63.66 ± 0.28	5.81 ± 0.08
F	F1	57.85 ± 0.20	63.37 ± 0.13	5.52 ± 0.32
G	G1	57.60 ± 0.02	63.15 ± 0.02	5.55 ± 0.00
MN ± SD		58.03 ± 0.24	63.45 ± 0.51	5.42 ± 0.63
[Min, Max]		[57.58, 58.56]	[62.25, 64.25]	[3.89, 6.17]

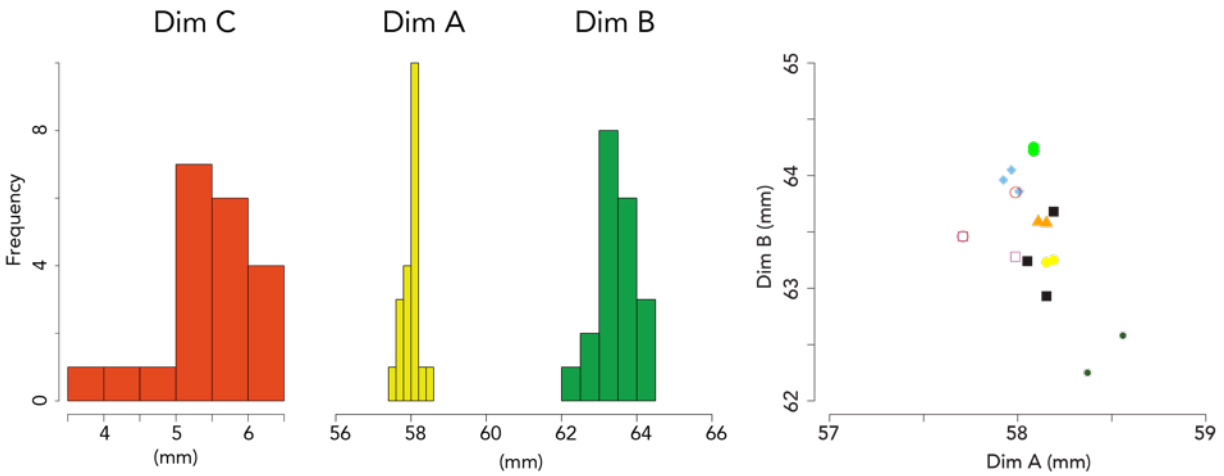

Figure 4.6: Histogram of the distribution of Dim A, Dim B, and Dim C. Dim A vs. Dim B from nine boot models (right). No trend or scaling of Dim A vs. Dim B is apparent, meaning Dim C varies across manufacturers.

4.3.2 ***Bindings***

Force-displacement curves were generated for ten binding models from five manufacturers. Each curve showed significant variation in magnitude (Figure 4.7A). Three representative clamping force-displacement curves are shown in Figure 4.7 with the standard deviation from six repeated measurements of the force displacement curve. The peak clamping force each binding was capable of generating varied significantly between models, ranging from 125N up to 225N.

4.3.3 ***Boot-Binding Clamping Force***

In Figure 4.7B (*curve A*) the points corresponding to *Dim A* for all boots measured lie on the uphill side of the force-displacement curve. Their location on this curve represents the amount of initial clamping force holding the boot in the binding. The steepness of the curve results in differences in preload applied to different boots, depending on the value of *Dim A* for a given boot. These corresponding clamping forces are shown in Figure 4.7 A & B. To release from the toe piece, these loads transmitted from the ski to the boot must overcome the energy barrier that corresponds with the peak of the force-displacement curve.

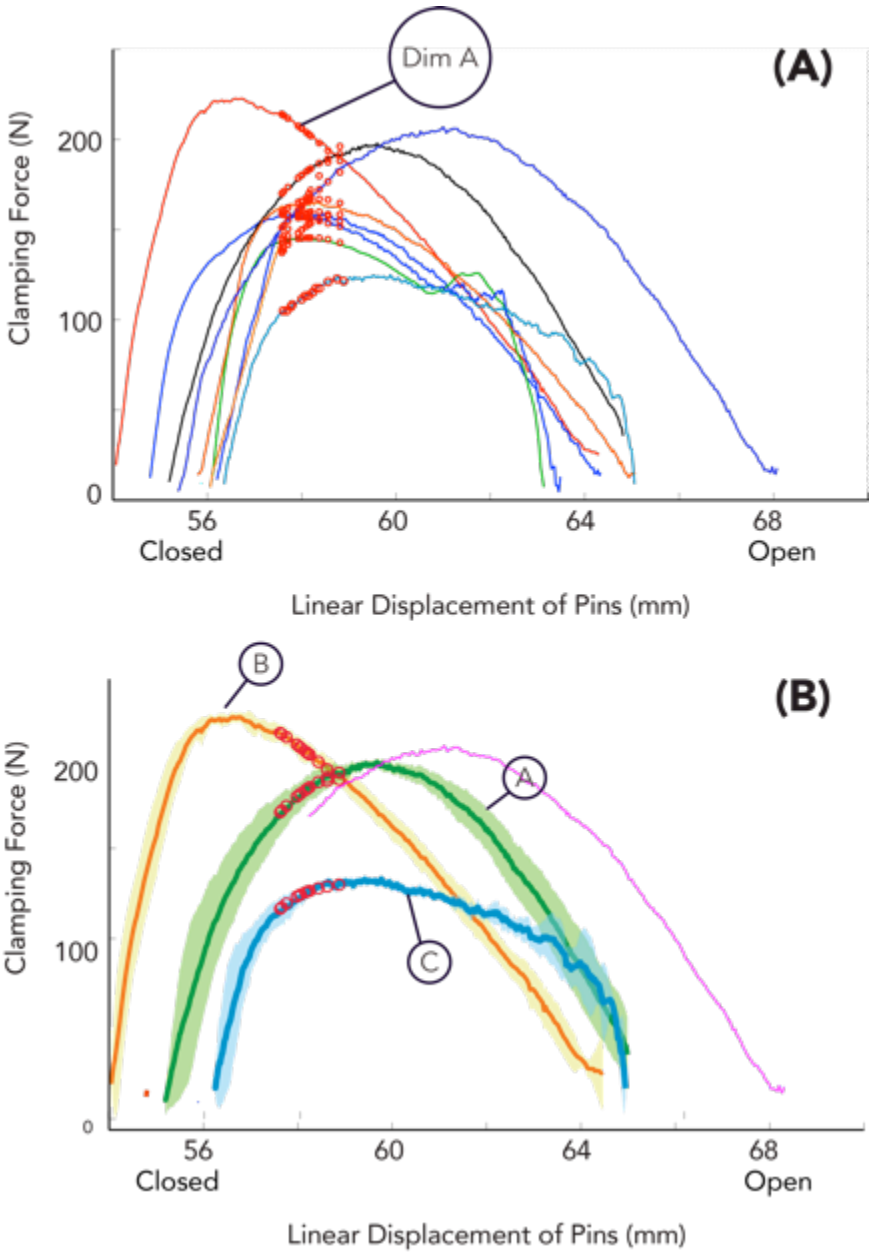

Figure 4.7: (A) Force displacement curves from all toe-pieces measured. Red circles annotate Dim A from the nine boots measured, and where they lie on each force-displacement curve. (B) Clamping force-displacement curves for three representative binding toe pieces. Shaded region indicates the standard deviation of six measurements of the force-displacement curve.

The curve for another binding shown in Figure 4.7B (*curve B*) is significantly different; its shape indicates that the toe-piece closes on all boots at points along the curve that are already past the energy barrier. As the pins of the toe-piece open in response to loads transmitted from

the ski to the boot, the binding toe-piece will apply a smaller and smaller compressive force until the toe-piece snaps open.

The curve for another binding shown in Figure 4.7B (*curve C*) is also significantly different from the other two; it's shape indicates that the toe-piece closes on all boots at points along a relatively flat curve that does not have a large energy barrier. As the pins of the toe-piece open in response to loads transmitted from the ski to the boot, the binding toe-piece will apply a more constant compressive force until the toe-piece snaps open.

An analysis of variance on the clamping force yielded significant variation between bindings, $F(9,170) = 80.69$, $p < 0.001$. A post hoc Tukey test showed significant differences between all but 39 of the clamping forces generated by five of the binding toe-pieces were significantly different from the remaining five (*two-way ANOVA, Tukey's Post Hoc Test, $p < 0.001$,* Figure 4.8).

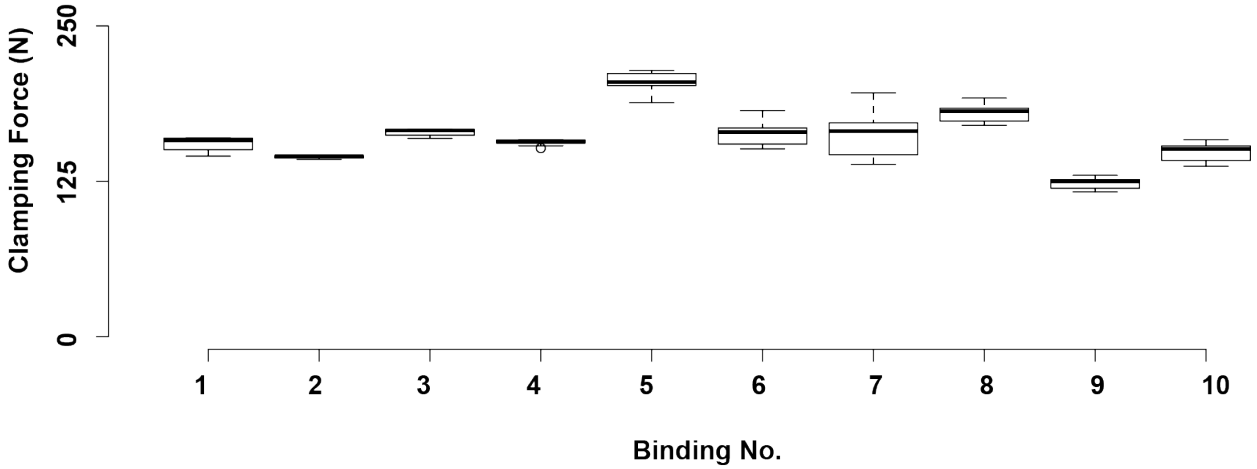

Figure 4.8: The initial clamping force that 10 bindings apply to 10 different boots. The variation in clamping force results from variation in Dim A. These initial clamping force values correspond to their location on the force-displacement curve of each binding (see Figure 4.7B).

4.3.4 *Twisting Release Torque: Toe Piece Only*

An analysis of variance on the release torque yielded significant variation among boots and bindings, $F(39,140) = 12.94$, $p < 0.001$. A post hoc Tukey test showed significant differences in release torque in all but three boots (Figure 4.9). A post hoc Tukey test also revealed the

release torque from one binding toe piece to be significantly different from six other bindings (Figure 4.9).

4.3.4.1 Predicting Release Torque from boot-binding constraints:

With independent variables of clamping force and boot dimensions, *Dim A* and *Dim C*, a significant MLR model was found for all binding toe-pieces ($F(4,175) = 22.55$) that accounted for approximately 34% of the variance in release torque for all bindings (*Multiple-*R^2 *= 0.340, Adjusted-*R^2 *= 0.325,* $p < 0.001$). However, significant MLR models were found for each individual binding toe-piece that accounted for approximately 84.7% ± 19.1% of the variance of Pure Twist release torque (Appendix C, Table C.1).

The MLR models predicted the boot dimensions, *Dim A* and *Dim C* control ~ 85% of the variability in release torque in each binding toe-piece (Table 4.2, *Figure 4.10*). In contrast the clamping force exerted by the binding on the boot accounts for only ~ 15% of the variability in release torque. A significant interaction between the starting positions of the pins, Dim A, and the amount of displacement required to release in twist, *Dim C*, was found 20.4% [8.8%, 32%]. Finally, the clamping force from the binding contributed the least amount to variance in release torque 14.9% [13.1%, 16.7%]. Results from the MLR predict that increases in *Dim A* will decrease the release torque and increases in *Dim C* will increase release torque (Appendix C, Table C.2).

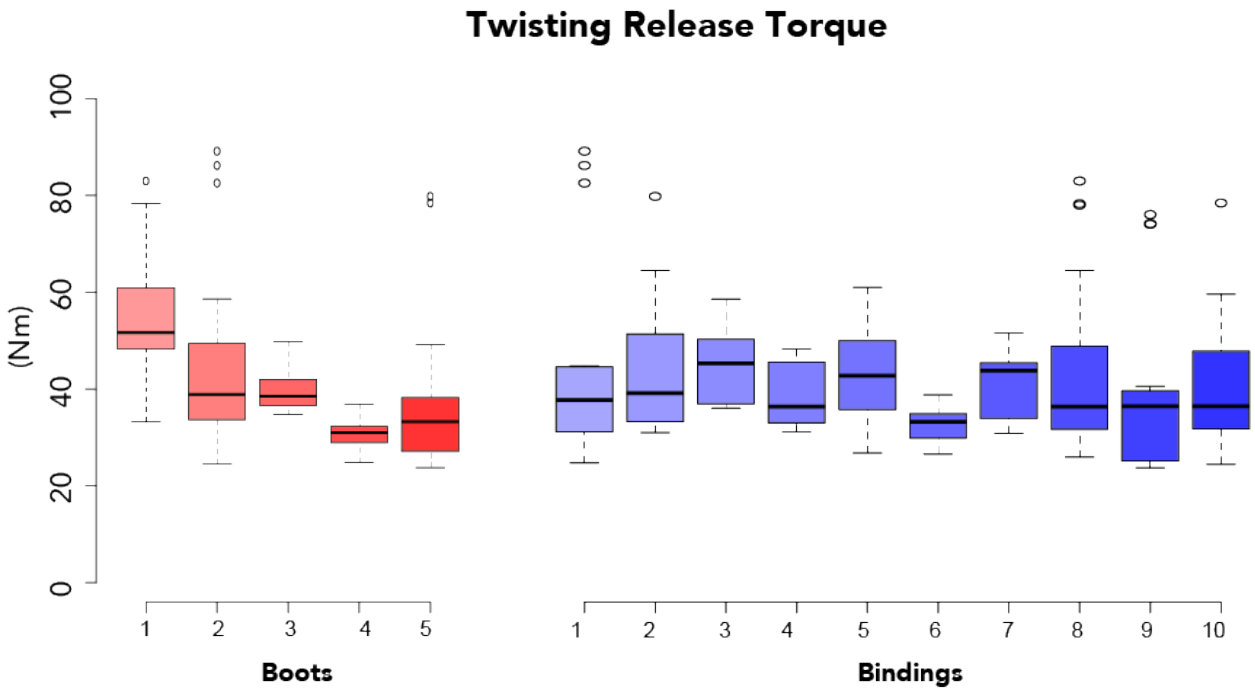

Figure 4.9: Boxplots of release torque of the toe-piece of bindings grouped by boots (L) and bindings (R). The median is denoted by the solid line through the box. The box represents the lower and upper quartile of data. Whiskers represent the minimum and maximum data values except when outliers (circles) are present.

Table 4.2: *Percent relative contribution and the 95% CIs [LL, UL] of boot-binding constraints to release torque variation for pure twist releases.*

Binding	Dim A	Dim C	DimA | DimC	Clamping Force	R^2	*p*
1	22.2% [20.9, 23.7]	18.8% [17.8, 19.9]	9.9% [8.7, 11.1]	48.7% [47, 50.8]	0.995	< 0.001
2	26.2% [23.6, 28.1]	35.4% [31.7, 38.4]	10.5% [7.2, 13.7]	28% [24, 31.1]	0.976	< 0.001
3	25.4% [23.5, 27.9]	44.0% [39.1, 50.2]	4.6% [1.7, 9.9]	21% [16.2, 27.8]	0.930	< 0.001
4	33.9% [33.1, 34.8]	46.1% [44.7, 47.6]	7.7% [6.6, 8.8]	12% [11, 13.4]	0.996	< 0.001
5	33.1% [26.2, 44.2]	33.5% [25.4, 44.7]	10.4% [4.3, 20.5]	11.7% [8.6, 18.6]	0.841	< 0.001
6	8.2% [5.6, 11.8]	9.3% [6.3, 13.3]	66.4% [60.2, 72]	13.3% [11.6, 16]	0.961	< 0.001
7	22.9% [18.6, 28.0]	37.5% [29.2, 46]	5.9% [1.2, 14.1]	7.4% [4.3, 14.8]	0.709	< 0.001
8	31.4% [30.8, 32.1]	53.1% [52, 54.3]	8.4% [6.7, 10.1]	6.7% [6.3, 7.3]	0.995	< 0.001
9	26.4% [25.9, 26.9]	58.3% [57.1, 59.6]	8.4% [6.9, 10.1]	6.5% [6, 7.1]	0.600	< 0.001
10	28.1% [8.4, 49.7]	12.8% [4.9, 25.5]	16.6% [1.2, 44.4]	4.5% [1.1, 25]	0.467	< 0.001

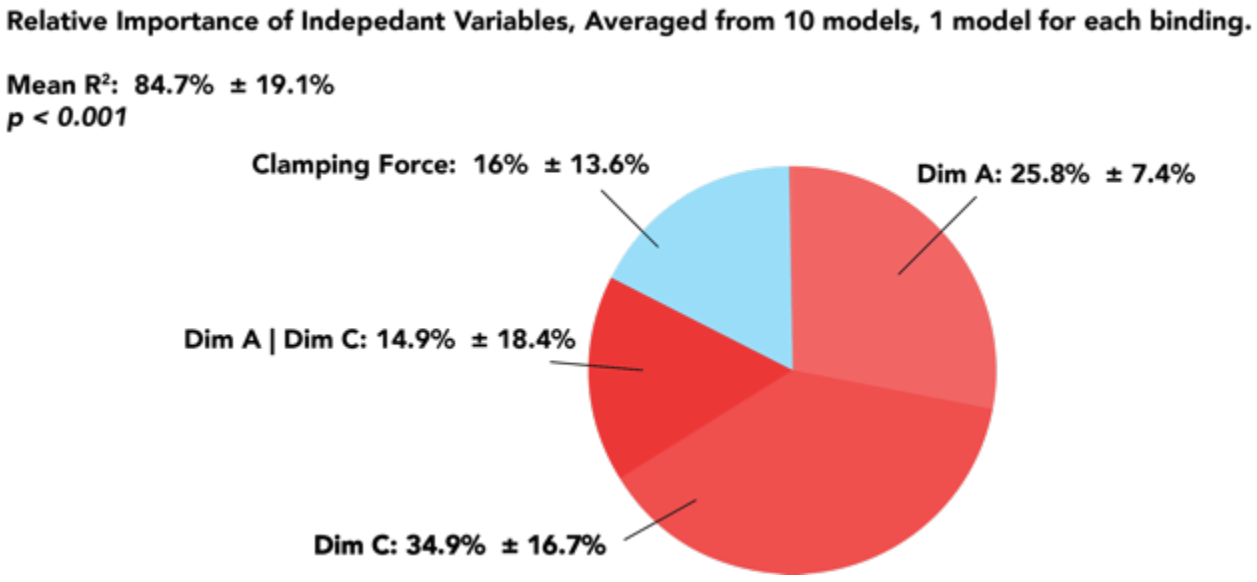

Figure 4.10: Average relative importance of independent for the 10 models from each binding.

The clamping force for a given boot-binding combination controlled ~15% of the variation in release torque of the toe-piece. Depending on the slope of the force-displacement curve, the initial clamping force is also controlled by *Dim A* of the boot. However, the effect of the shape of the force-displacement curve has not been captured by the MLR models reported here. The toe-piece with the highest clamping force (Figure 4.7B, *curve A*) is very symmetrical and has a peak at a specific displacement value such that the values of *Dim A* lie on the positive slope of the curve.

In contrast, no matter what boot is used in the binding corresponding to curve B in Figure 4.7B, there is no energy barrier to resist an inadvertent release, and curve C in B is relatively flat. It follows that the available energy dissipation from each of these bindings is significantly different. These force-displacement curves from Figure 4.7B are shown individually in Figure 4.11 with the maximal available energy to release, starting at the average value for *Dim A* and ending at the average value for *Dim B*, designated by the darker shaded regions. It is apparent that not only is the available energy, the area under each curve, very different, but the variation in geometry found across all boots will alter considerably, the amount of energy a binding has to dissipate energy and prevent an inadvertent release.

4.4 Discussion

International standards for alpine and AT boot geometry specify the geometry and tolerances for key inter-face dimensions to provide repeatable retention-release characteristics even as consumers mix and match boots and bindings from different manufacturers. Allowable deviations from standardized dimensions according to international standards range between 0.5mm - 2mm [34,36] .

Compared to these tolerances, the variation measured in *Dim A*, *Dim B*, and *Dim C* between boots from 10 manufacturers was relatively small, ± 0.25mm, ±0.55mm, and ±0.73mm respectively. However, these small variations significantly altered the release torque of boots from the toe-piece in twist. For example, in Figure 4.9, mean release torque of Binding 2 from a sample of 10 boots was 36.5 Nm, but the maximum torque recorded from a boot was 78.44 Nm, a 215% increase in release torque resulting from the use of different boots in the same binding. The MLR models predicted that 85% of this variability is a product of the small variations in boot geometry. These results highlight *Dim A* and *Dim B* as dimensions that highly influence the behavior of Tech/Pin boot-binding systems and that if standardized across manufacturers, a significant portion of the variation in release torque could be reduced. However, if a standard were to be developed for the insert geometry, the dimensions would likely require significantly tighter tolerances than what manufacturers are accustomed to.

The amount of variation in release torque found between boots and bindings may give credence to the perception among consumers that the release torque of Tech/Pin binding-boot systems is variable and unpredictable, underscoring why many lock out the release mechanism of the toe-piece while skiing. If the variability in release torque found in this study is an indicator of retention-release function of Tech/Pin bindings under skiing conditions, consumers may be at a higher risk of injury than they are accustomed to when using typical alpine skiing equipment, whether they lock out the release mechanism or not [8].

This study was limited to an examination of the interactions of the boot-binding interface with the toe inserts of the boot and toe-piece of the binding. The goal of this study was to understand the fundamental parameters of the toe-piece behave. However, the heelpiece is always engaged when skiing and likely assists the toe-piece in energy dissipation. Future studies will examine the relative contributions of both the toe and heelpieces to variation in release torque. Other than a pure twisting release, the current study did not examine any other load

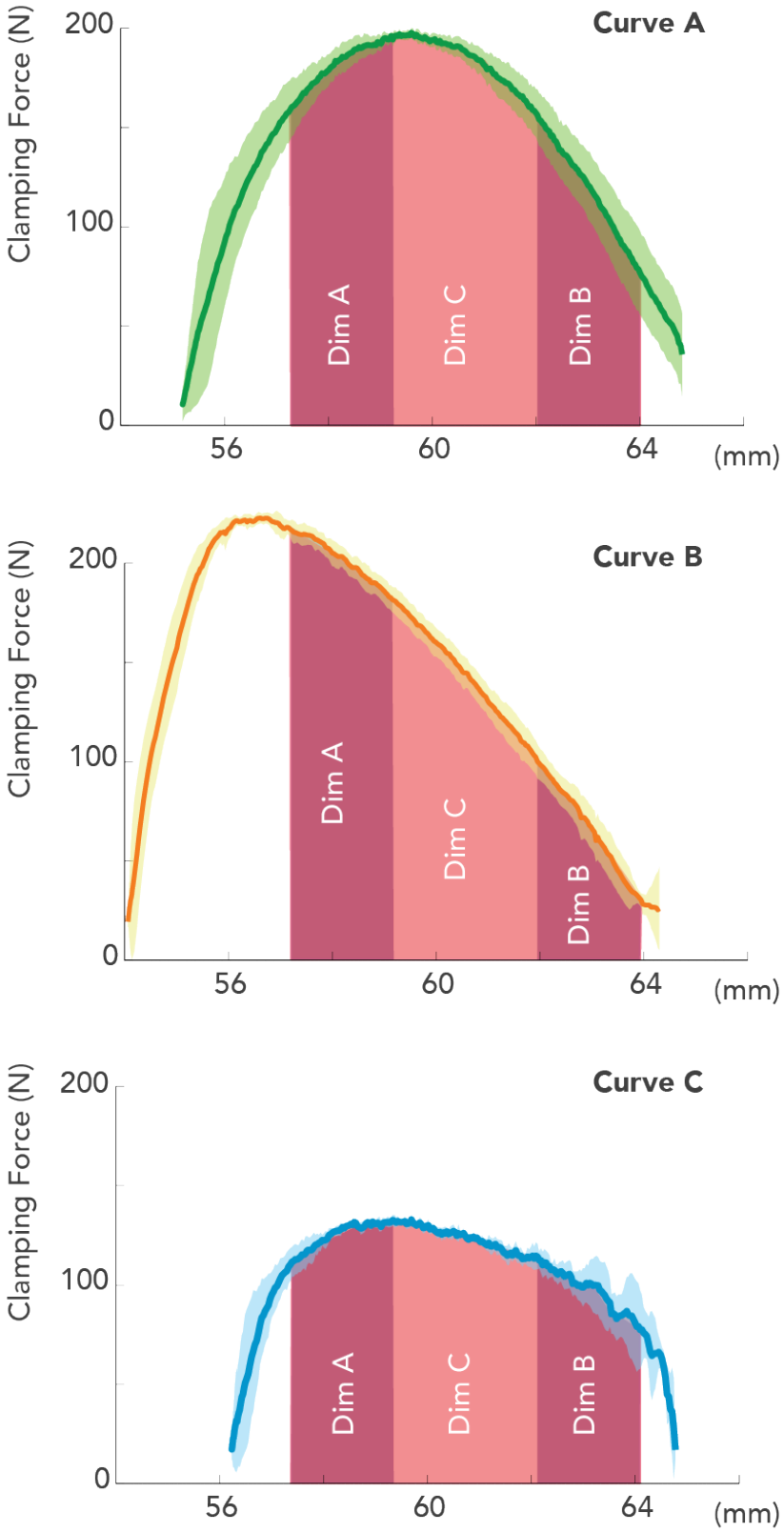

Figure 4.11: The Maximum available energy from three binding toe-pieces is highlighted in the shaded area below the force-displacement curve. Darker shaded regions denote the range of values measured for ***Dim A*** *and* ***Dim B*** *on boots from ten different boot manufacturers.* ***Dim C*** *is labeled as the maximum possible distance the toe-piece pins could displace.*

cases. Future studies will also examine how the contributions of boot dimensions affect variations in release torque under other loading scenarios simulating forward and backward twisting falls. Pilot data indicated that in a twisting release the total linear pin displacement of the toe-piece is significantly less than *Dim C* and varies as a function of boot insert geometry and toe-piece design. Therefore, future testing will focus on the amount of pin displacement necessary for release and on what the maximum available dissipative energy for various boot-binding combinations might be. Possible values for what the upper bounds of that energy might be are illustrated in Figure 4.11.

4.5 **Conclusion**

Anecdotally, skiers have reported locking the release mechanism of the binding toe-piece due to a consumer perception that Tech/Pin boot-binding systems have unreliable retention performance. However, this exposes skiers to a higher risk of injury in the event of a fall when the binding should release from the boot. The consumer perception may have some merit since large variations in release torque were measured in this study. These large variations stem from the differences in boot insert geometry between manufacturers. If boot insert geometry were standardized across all manufacturers, the variation in release torque would decrease significantly.

Chapter 5. Sensitivity of Tech Bindings to changes in AT Boot geometry, and challenges for optimization.

5.1 Introduction

Alpine touring (AT) is a sub-discipline of skiing in which the skier uses skis to ascend, traverse, and descend snow-covered terrain in the backcountry on unmaintained trails for which ski boot and binding manufacturers have developed specialized alpine touring equipment. However, international standards have not yet been developed for the interface geometry of a subset of AT equipment, called Tech/Pin boot-binding systems. In a companion study (Chapter 4) the relationship between variations in the interface geometry between the boot and binding toe-piece, the resulting variations in release torque by quantifying the amount of variation in interface geometry, and constraint forces of the binding were explored. A twisting release torque was applied to the ski-boot-binding system with only the toe-piece of the binding engaged with the boot. The amount of variation in boot geometry and binding constraint forces between manufacturers significantly affected the release torque of these systems. The geometry of these inserts are not defined in international equipment standards[36]. This study found that ~85% of the variation in release torque between AT boots from different manufacturers could be attributed to difference in two critical dimensions of the boot geometry, namely *Dim A* and *Dim C* (Figure 5.1). The other ~15% of variation was a result of differences in the amount of clamping force the toe-piece of the binding imposed on the boot.

This initial study provided a foundation for examining features critical for understanding the variation in release torque of Tech/Pin boot-binding systems. However it was limited to the performance of the toe-piece and serves as the motivation for the current study; to measure the effect of differences in boot-binding features on the variation in release torque of Tech/pin boot-binding systems as a whole, with the toe and heel pieces are engaged.

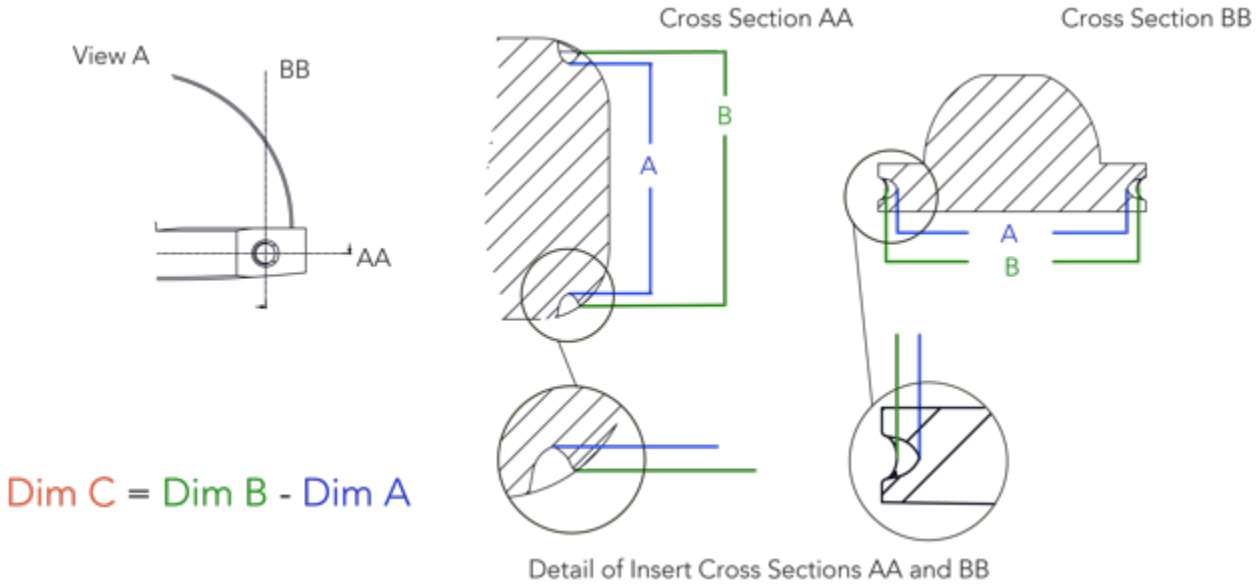

Figure 5.1: AT boot dimensions measured at the toe inserts. View (A) is looking at a boot toe from the side. Cross section (AA) is a horizontal cut through the plane of the insert and boot sole. Cross section (BB) is a cut through the vertical plane of the boot toe, the view is towards the boot toe.

5.2 **Methods**

The release characteristics of Tech/Pin boot-binding systems were tested in a laboratory setting using a lower leg surrogate that conformed to standards ISO 9462:2012 Appendix B [35] and ASTM F504-05 [47]. For a complete description of the test methods and setup, please refer to Chapter 4.2. Three models of Tech/Pin ski bindings were selected for testing as representative of the principal toe-piece mechanism currently on the market. Each binding was mounted to its own test ski; all test skis were the same make, model, and length 167cm (AMP Rx, K2 Sports, Seattle, USA). Five models of AT boots with boot sole lengths between 306 and 310 mm were acquired for testing. A pure twisting couple, or torque was applied to the ski-binding-boot system with the binding in four configurations tabulated in Table 5.1. Each configuration was tested three times. Tests were performed dry, at 70° F.

Table 5.1: *A pure twisting torque was applied to the ski in four test configurations shown below. IV = indicator value setting on the heelpiece of the minding.*

Test Configuration	**1**	**2**	**3**	**4**
Toe-piece Setting	Ski Mode	Ski Mode	Ski Mode	Ski Mode
Heelpiece Setting	Not Engaged	IV = Min	IV = Median	IV = Max
Binding 1	0	IV = 5	IV = 8.5	IV = 12
Binding 2	0	IV = 4	IV = 7	IV = 10
Binding 3	0	IV = 5	IV = 7.5	IV = 10

5.2.1 *Multiple Linear Regression (MLR) Analysis*

Independent variables, boot dimensions *Dim A* and *Dim C* and the clamping force associated with each boot-binding combination, were quantified in the previous study and used predict release torque in multiple linear regression (MLR) models for each binding and configuration listed in Table 5.1 (***R**, Foundation for Statistical Computing, Vienna, Austria, Fox, 2003*). Data were centered about their mean and scaled by one standard deviation. The Kolmogorov-Smirnov test was employed to test for skewness. MLR analyses were used to predict release torque based on unique combinations of independent variables for each test configuration. The likelihood ratio test compared models using different independent variables and tested for interactions between independent variables. Variance inflation factors (VIF > 5) were used to identify regressors with high collinearity [54].

5.2.2 *Relative Contribution of Regressors to MLR models*

The percent contribution to variation in release torque of each regressor in the MLR models was calculated using the *lmg* metric from the *relaimpo* statistical package in ***R*** [55]**.** The *lmg* metric normalizes R^2 to 100 percent and the contribution of each regressor is calculated as a percentage of the R^2 from the linear model. The variance of percent contribution was calculated by bootstrapping the MLR models at 1000 bootstrap intervals, holding the regressors fixed and bootstrapping the residuals. The 95% bootstrap confidence intervals for regressors are reported.

5.2.3 *MLR Coefficients*

Coefficients from the MLR models were rescaled to observe how the sensitivity of the boot-binding to the independent variables changed as the binding heelpiece settings were increased.

5.3 Results

5.3.1 *Release Torque*

Release torque for configuration 1 (IV = 0, toe-piece only) varied significantly between Binding 1 and Binding 3 (two-way Anova, Tukey's Post Hoc Test, $p < 0.001$). The release torque for the other test configurations with the heelpiece at the minimum, median, and maximum settings increased linearly for all three bindings. However they did not increase proportionally at the rate defined by international standards. A boxplot of the release torque from the three bindings and five boots in all four test configurations is shown in Figure 5.2. The shaded region defines the minimum-maximum release torque envelope for a given IV setting per ISO 13992:2006 [37]. The indicator settings of all three bindings do not increase the release torque at the same proportional rate as prescribed by international standards. A linear regression on the release torque vs. Indicator Value (not including test configuration 1, IV = 0), revealed that torque for Bindings 1, 2, and 3 increased at 35.4%, 55.9%, and 84.7% the rate prescribed by international standards, respectively (Appendix D, Table D1).

The largest variance in release torque for Binding 1 was with the heelpiece setting at the maximum IV. Bindings 2 and 3 both had the largest variation in release torque when the heelpiece was not engaged (toe-piece only). However, across the five boots tested in each binding, the variation in release torque at each indicator setting with the heelpiece engaged exceeded the minimum-maximum variation prescribed by the envelope shown in Figure 5.2.

5.3.2 *Predicting Release Torque from boot-binding constraints*

Using independent variables of clamping force and boot dimensions *Dim A* and *Dim C*, significant MLR models were found for each binding and configuration tested (*Appendix D, Table D.2*). The relative contribution of each independent variable is reported in Table D.2 and shown graphically in Figure 5.3. The relative contribution of each independent variable is

dependent on the heelpiece. As the indicator setting is increased, the heelpiece contributes more resistance to the release torque and the toe-piece dynamics change. The relative contribution to the variance in Torque of each independent variable was scaled to its contribution to the standard deviation, and the overall standard deviations with the absolute contribution of each boot-binding parameter is overlaid in Figure 5.4.

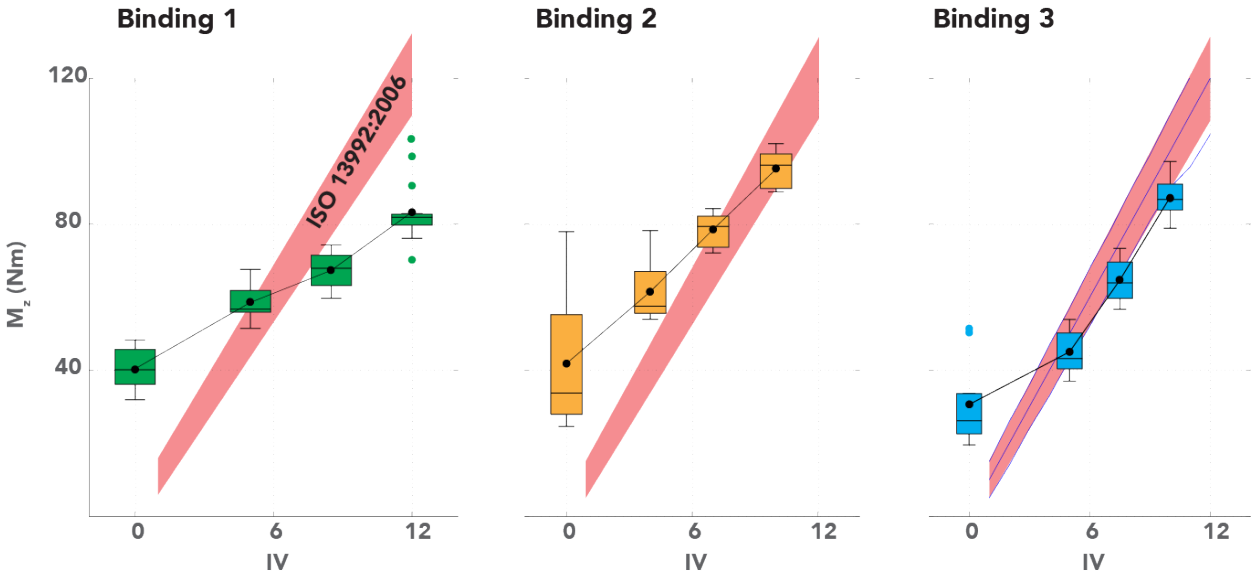

Figure 5.2: Boxplots of the release torque of three bindings for configurations 1-4 overlaid with the minimum-maximum release envelope defined by ISO 13992:2006 for a twisting release torque. Boxplots at IV = 0 correspond to tests performed without the heelpiece engaged (toe-piece only). Other plots are located on the x-axis corresponding to their IV setting (minimum, median, or maximum) for the heelpiece of each binding. Each boxplot shows the median value by the solid band, the upper and lower quartile ranges of the data on each side of the median, and 95% CI LL and UL are indicated by the lower and upper whiskers. Circles outside of the whiskers designate outliers. The black line connecting each box plot intersects each boxplot at the algebraic mean for each test.

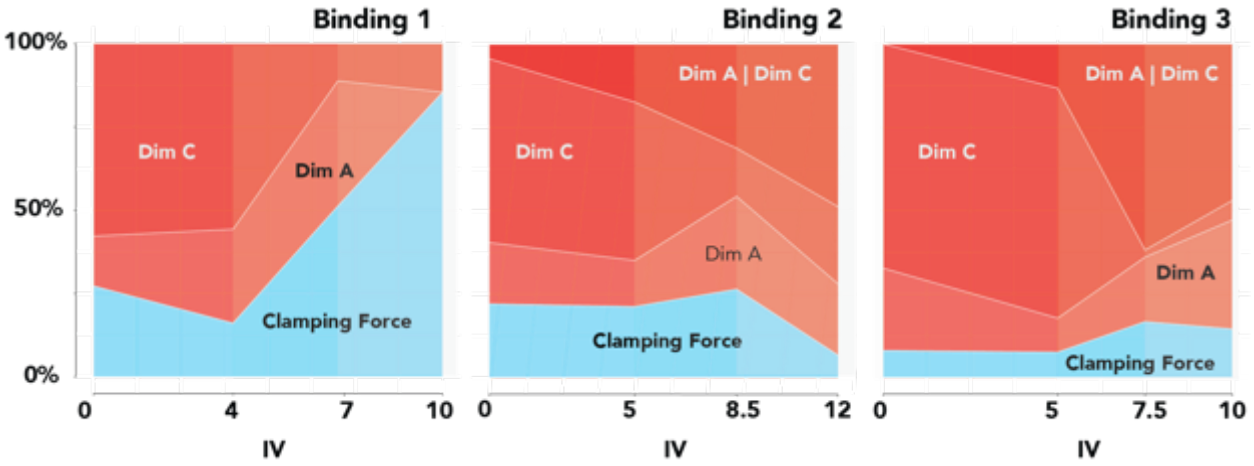

Figure 5.3: The relative contribution of each independent variable to the total variance in release torque for each configuration scaled to 100%.

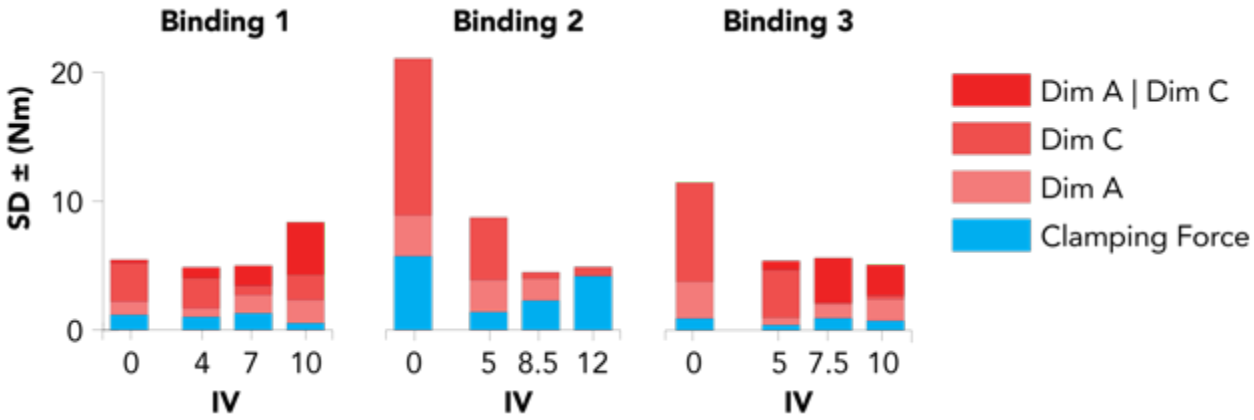

Figure 5.4: The standard deviation from each binding tested in each configuration, toe only (IV = 0), followed by IV = [Min, Median, Max] for each binding. The relative contribution of boot dimensions and the clamping force of each binding shown in Figure 5.3 are scaled and plotted for each configuration.

5.3.3 *Binding sensitivity to boot-binding features*

The effects or sensitivities from the MLR models are designated by the symbol β_n, of each linear fit correspond to how the change in release torque, *dT*, is affected as a function of the change in each independent variable *dDimA*, *dDimC*, *dF*. The β_n's of each MLR are describe

sensitivity of the release torque to changes in each of the parameters the coefficients are derived from. Figure 5.5 shows an exemplar MLR for the independent variables *Dim A*, *Dim C*, and *Clamping Force* regressing on the twisting release torque for all four test configurations for Binding 3. Each β_n outlined in equations (5.1) – (5.3) represents the slope of the linear fit of the independent variable and response variable, torque.

$$\beta_{DimA} = \frac{dT}{dDimA} \qquad \text{Eqn. 5.1}$$

$$\beta_{DimC} = \frac{dT}{dDimC} \qquad \text{Eqn. 5.2}$$

$$\beta_{F} = \frac{dT}{dF} \qquad \text{Eqn. 5.3}$$

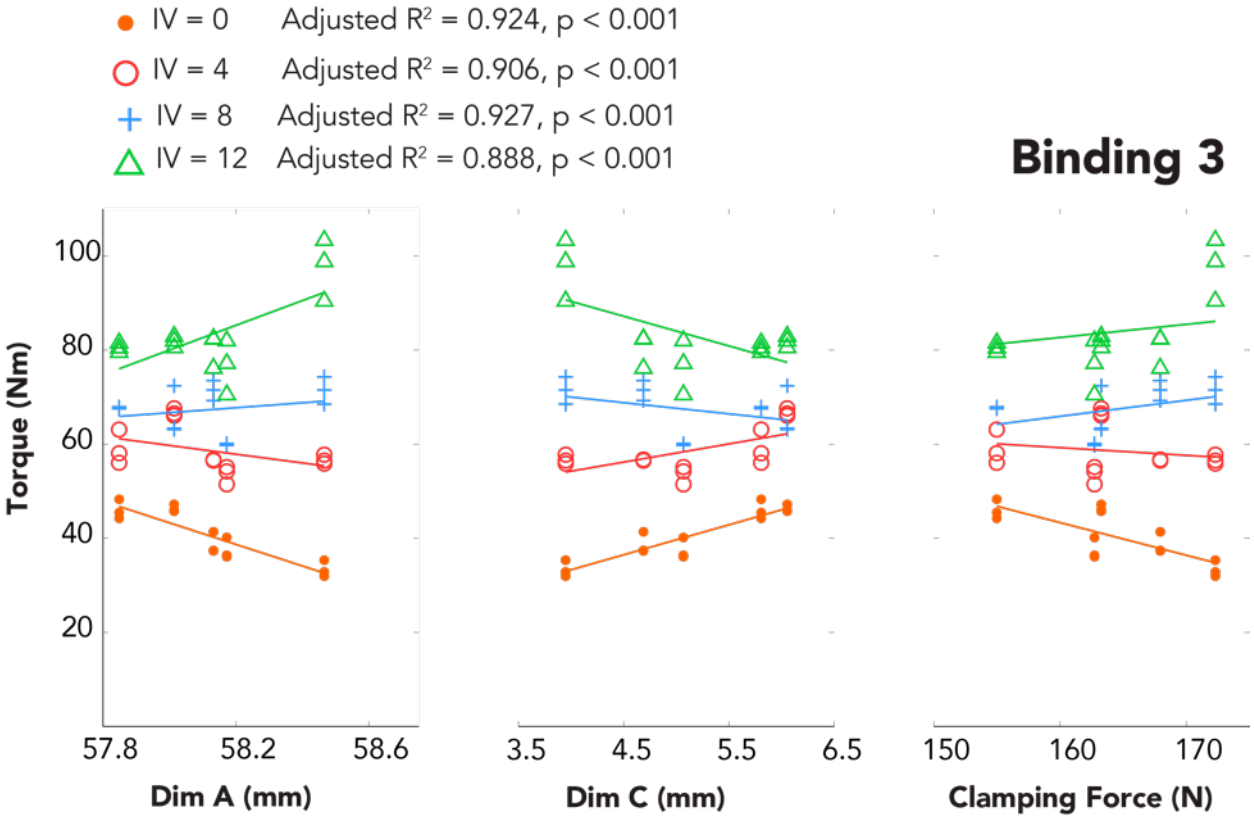

Figure 5.5: An MLR for Binding 3, with independent variables Dim A (left), Dim C (center), and clamping force (right) regressing on the twisting release torque for all four test configurations. Fit metrics for the four MLR models corresponding to each IV setting are given in the legend.

Of particular interest is the change in each β_n as the IV values were increased on the heelpiece. In Figure 5.5, β_{DimA} is plotted against β_{DimC} for each test configuration and each binding. The origin of each plot represents the point at which the release torque of a binding would be invariant to changes in *Dim A* or *Dim C*, in other words the slope β_n would equal zero. Figure 5.6 shows that as the IV of the heelpiece increases, the overall sensitivity to changes in boot geometry decreases. In fact, for Binding 1, the sensitivity curve between IV = 5 and IV = 8.5 passes through the origin at IV = 7.5, assuming a linear relationship. Theoretically, at this discrete value of IV = 7.5, any of the five boots tested would all release at the same release torque value from Binding 1. However for any settings above IV = 7.5, the variation in *Dim A* and *Dim C* will have the opposite effect on release torque since the sensitivity curve passes from the upper left quadrant to the lower right quadrant. This could explain why the largest variation in release torque for Binding 1 was at the highest IV setting (Figure 5.4).

Extrapolating these observations to the plots for Binding 2 and Binding 3, the sensitivities of both bindings decrease and trend towards the origin, but do not intersect the origin at any point. The sensitivity curve for Binding 2 remains in the upper left quadrant but approaches the origin. Similarly for Binding 3, the sensitivity curve actually circles close to the origin, but never intersects it. Therefore, the variation in release torque will not be as significant between boots at higher IV settings for Binding 2 and 3.

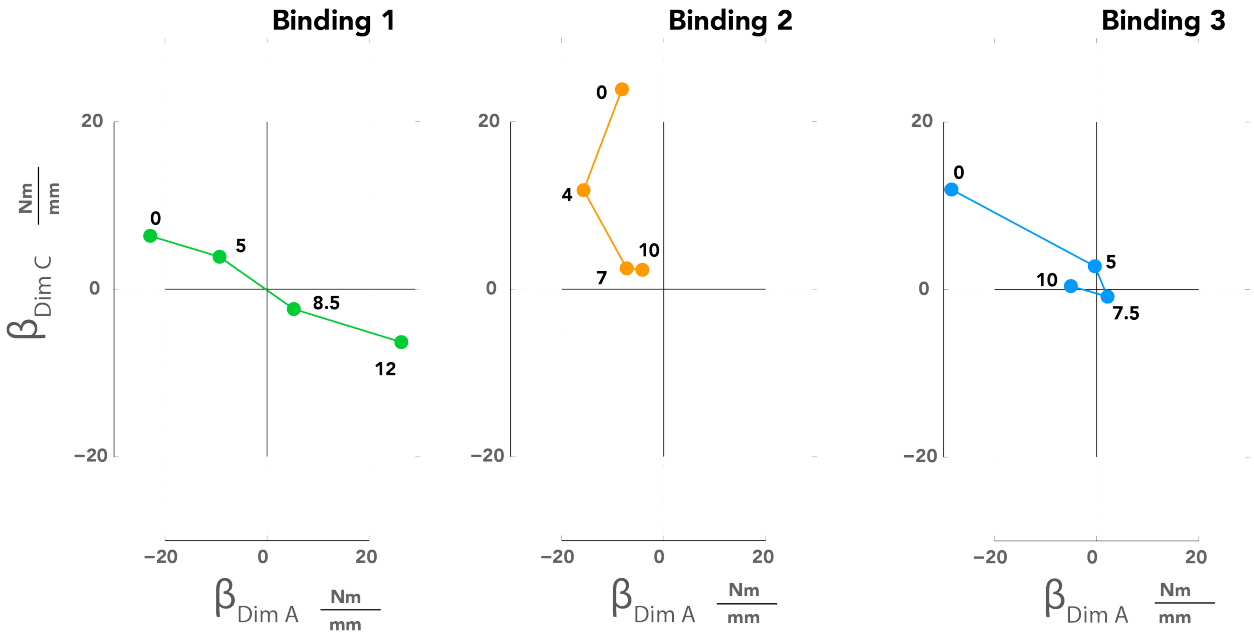

Figure 5.6: The MLR coefficient β_{DimA} (x-axis) is plotted against β_{DimC} (y-axis) for each of the three bindings. The numbers aside each point indicate the corresponding Indicator Value of the binding (IV). IV = 0 indicates a test performed without the heelpiece engaged (toe-piece only). Other numerical values represent the IV setting (minimum, median, or maximum) for the heelpiece of each binding.

5.4 **Discussion**

Consumers perceive that Tech/Pin boot-binding systems have unreliable retention characteristics and often react by locking out the release function of their bindings. Given the amount of variation in release torque between boots shown in Figure 5.1 and Figure 5.3, this perception might have some merit. Injury rates stemming from an inadvertent release of a binding are slightly lower than rates associated with no-release of a binding during a fall [8]. However, both options (an inadvertent release or non-release) are considered to increase the risk of injury than if the release function of a binding adheres to international standards [10].

The purpose of this two-part study aimed quantify the amount of inter-manufacturer variability in release torque and determine specific parameters of the Tech/Pin boot-binding system that could possibly be optimized to reduce inter-manufacturer variability.

Part one (Chapter 4) of this study identified two boot measurements, *Dim A* and *Dim C*, as well as the clamping force from the binding that are strong predictors of release torque

variability of the toe-piece, but that boot dimensions are responsible for most of the variation in release torque from the toe-piece alone.

This pilot study has shown that while the boot parameters are still responsible for the bulk of the variability in release torque when the heelpiece of Tech/Pin bindings is engaged with the boot, the effect of these parameters changes as the indicator values on the heel are changed.

The sensitivities of the bindings to differences in boot dimensions complicate an otherwise simple optimization problem due to the fact that the sensitivities themselves did change as a function of binding settings (Figure 5.6). The lack of adjustability in most Tech/Pin binding toe-pieces would limit the effectiveness of an optimization routine that identified values for *Dim A* and *Dim C* (among other possibilities) undertaken to reduce the amount of variation in release torque. If only boot dimensions are to be considered, one set of boot dimensions found to be optimal for lower IV settings would not be optimal for higher IV settings.

It is hypothesized that for Tech/Pin boot-binding systems to have retention-release characteristics similar to alpine ski boot-binding systems, improvement on current designs or new mechanisms for the toe-piece will be necessary. There are currently two models of Tech/Pin bindings that utilize different mechanisms than the majority of bindings that incorporate indicator settings into the toe-piece as well as the heelpiece. These designs are new do not have significant market share, and one of them utilizes different heel inserts than other bindings. Therefore they were not considered by the authors to be representative of a sample of bindings on the market, and the authors do not speculate on their performance. However, it is likely that some ability to adjust the clamping force preload of the toe-piece, the release load of the toe-piece, and the dynamics of the toe-piece based on the corresponding heelpiece dynamics will be necessary to reduce the variation in release torque in Tech/Pin boot-binding systems.

This study has not examined the effect of material hardness or loading conditions other than a pure twisting release. It is possible that other boot dimensions and binding features studied here are critical in other release modes or loading conditions. Furthermore, it will likely be impossible to optimize these systems until reaction forces transmitted from the ski to the boot through Tech/Pin bindings is directly measured such that the functional retention-release requirements of Tech/Pin boot-binding systems is clearly defined.

5.5 Conclusion

In summary, Tech/Pin boot-binding systems have variations in release torque that exceed the minimum-maximum allowable release envelope prescribed by international standards. These variations stem from using boots from different manufacturers in a given binding. The indicator settings in these bindings do not change the release torque at the same proportional rate as other AT and alpine ski equipment. Skiers should not assume that Tech/Pin bindings will provide the same retention-release characteristics as alpine ski equipment, nor that the numerical indicator settings on alpine bindings are equivalent to Tech/Pin bindings. Homogenizing boot geometry would reduce the amount of variation in release torque from these boot-binding systems, but would not eliminate the problem completely, and could exacerbate the problems for users on one far end of the binding setting scale or the other.

Chapter 6. Development of a Low-Profile Six Axis Force Sensor for Measuring Ground Reaction Forces of Skiing

6.1 Introduction

6.1.1 *Measurement of Leg and Joint Loads while skiing*

Little information exists regarding forces acting on the knee while skiing. Several studies in the 1980s-1990s[12,25,27,39] mounted six-axis dynamometers under the toe and heel piece of alpine bindings (Figure 6.1). They measured the ground reaction forces at the toe and the heelpiece and knee flexion-extension angle of skiers. Maxwell[25] reported knee loads in 1989 and in the 1990s, Quinn[39] and Scher[27] reported on reaction forces on the leg. Scher[27] reported that maximal leg loads generated by two-thirds of skiers measured were still significantly lower than their minimum retention release values (MRR). Rotation and varus-valgus angular displacement of the knee, the two components hypothesized to cause ACL injuries, were not measured in these studies.

More recent studies have attempted to calculate knee loads using pressure in-soles or more broadly, using Inertial Measurement Units (IMUs) and differential Global Positioning Satellite Systems (dGPSS) to calculate knee loads using a pendulum model[40–42]. However these methods only measure or calculate the compressive force acting on the boot of the skier and cannot fully resolve the six load components acting on the knee.

Before ski equipment can be designed to protect the knee, the forces and torques acting on the knee while skiing must be fully quantified. The effect of risk factors for ACL injuries such as gender, leg dominance, and snow condition must also be quantified for knee loads while skiing. It is necessary to measure the six load components acting on the toe and heelpiece of the ski binding to understand what forces the toe and heelpiece are not capable of reacting to, and which of those loads are critical to protecting the knee. The forces and torques under the toe and heelpiece can be summed about a point projected onto the ski from the longitudinal axis of the tibia, **Point O** (Figure 6.1). Using the forces and torques summed about Point O, an inverse solution can be utilized to determine the forces that produce a particular joint.

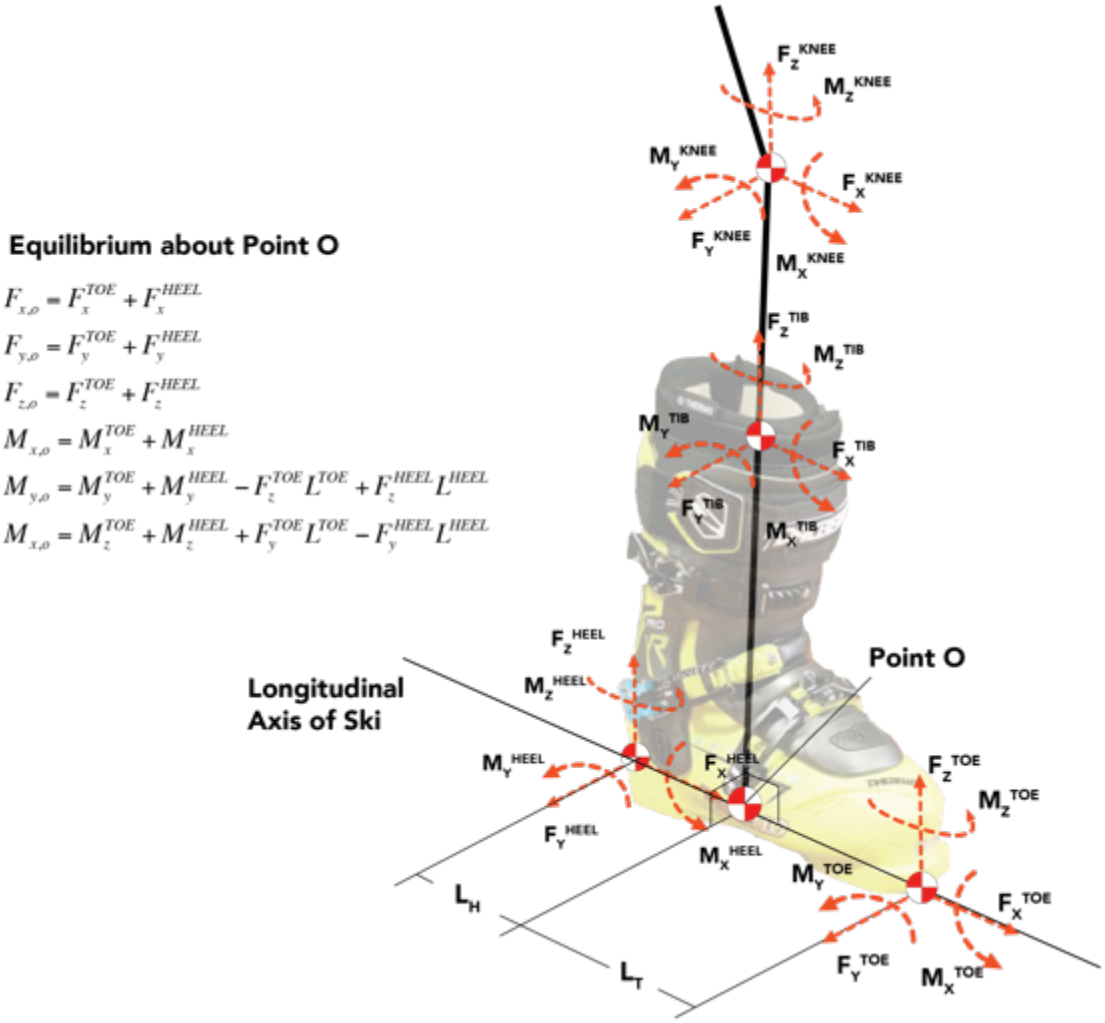

Figure 6.1: The use of six-axis force sensors under the toe and heelpiece of the binding can be utilized to measure ground reaction forces necessary for calculating leg and knee loads.

6.1.2 *Six Axis Force Sensor Design*

Strain gage based force transducers are commonly designed using spring elements instrumented with foil strain gages that convert the elastic deflection of the spring element into a change in voltage proportional to the change in the load being applied to the spring element. The design of force transducers increases in complexity if a sensor is to measure force and torque in all three axes of a Cartesian coordinate system, namely $\{F_X, F_Y, F_Z, M_X, M_Y, M_Z\}$. The structural design of such a transducer requires that the sensitivity to each individual load component be decoupled mechanically[57–59].

Various geometrical structures have been used in the design of six-axis force sensors including columns [59–62], tri-spokes[63–65], steward platforms [58,66,67], multi-column[68,69], and maltese cross [57,66,70–73]. While each structure has particular strengths and weaknesses for different applications, the maltese-cross can be designed to have significantly lower thickness compared to other designs such as column-type transducers, but their full-scale range can be limited. The other difficulty inherent in the design of maltese-cross sensors lies in their susceptibility to cross-sensitivity; if a pure moment, M_x or M_y, is applied to the sensor, and the design is not mechanically decoupled, the sensor will measure an extraneous shear force, F_y or F_x respectively, or vice versa. To address the issues of cross-sensitivity, several studies have adapted tri-spoke and maltese-cross sensor designs by incorporating bearings or other sliding elements to alter the boundary conditions which can produce large cross sensitivity between shear and torque axes[57,64,66]. However, bearings and other sliding surfaces can degrade over-time and introduce hysteresis into the sensing unit. Other studies have utilized holes in sensing arms to improve sensitivity of one or both of the horizontal or vertical axes [66,68,74].

The crux of making any physical measurement is inserting a measurement device into a physical system such that it does not significantly alter the behavior or characteristics of the system, or subject, being measured. For the purposes of measuring the ground reaction forces transmitted from skis to skier through the bindings, it is necessary to place a multi-axis force transducer in the load paths under the toe and heelpieces of the ski binding. An increase in height of the ski boot off the snow can affect how a skier performs maneuvers on snow. To minimize this effect, the functional requirements of the sensors dictate that they must have minimal thickness and weight but relatively large full scale limits given their size. The purpose of this study was to identify or develop a low profile, high range six axis force-torque transducer for the purpose of measuring ground reaction forces between alpine skis and ski bindings while human subjects perform ski maneuvers.

6.2 **Methods**

After a review of the literature, a novel configuration sensor design was explored to satisfy the design requirements and constraints (presented below). The proposed geometry was modeled using Finite Element Analysis (FEA) to optimize the sensors cross sensitivity response as well as to include overload protection into the sensor. A virtual calibration of the sensor using

the FEA model was used to optimize sensor performance before the physical sensor was built using the dimensions determined from the optimization routine.

6.2.1 *Design Requirements for measuring ground reaction forces in skiing*

The intended use of this sensor not only necessitates the overall height of the sensor be minimized, but that the sensor have sufficient range to measure the anticipated range of forces and torques. An estimate of the full scale range required of the six axis transducer to be designed was approximated from a brief analysis of data collected and shared by Scher[27] and Quinn[38,39], who measured ground reaction forces under the toe and heelpiece of ski bindings in the 1990s. From their data, maximal values for each of the six load components at the toe and heel-piece of ski bindings were identified (Table 6.2).

Several other studies[75,76] have collected ground reaction forces on skiers in the past as well, but only measured the ground reaction forces at a single point below the binding making it difficult, if not impossible to elucidate the full scale range required of sensors to be mounted separately under the toe and heel-piece of bindings. A compilation of the full-scale range, height, and weight of previous studies that have directly measured ground reaction forces of skiing is tabulated in Table 6.2. With consideration given to the full scale ranges of sensors used in past studies and the maximal values they report[27,39,75,76] as well as the changes in ski equipment including stiffer ski boots and wider skis, it is anticipated that the full-scale ranges tabulated in Table 6.1will be necessary for the proposed testing.

An extensive review of the literature did not result in any sensor design that satisfied the full-scale range requirements and the height constraints.

Therefore, the motivation of this study is to design and optimize a six-axis force transducer that meets the function and performance criteria. In addition to meeting the full scale range requirements listed in Table 6.3, the primary functional constrain of the sensor design under consideration is to have an overall height less than 30 mm. Other functional constraints include the mounting footprint of the sensor on the ski, overload protection, sensitivity, environmental protection, and accuracy which will be described in Chapter 6.2.5.3.

Table 6.1: Maximal ground reaction forces measured by either the toe or heel piece sensor measured by Scher[27] from six adult skiers. Data reproduced with permission.

F_X (N)	F_Y (N)	F_Z (N)	M_X (Nm)	M_Y (Nm)	M_Z (Nm)
355±78.9	25.3±9	309±82.3	25.9±14.6	40±21.2	64.7±35.3

Table 6.2: Comparison of the full scale ranges, height, and weight of multi-axis transducers designed to measure ground reaction forces of skiing and snowboard to the proposed sensor design.

	F_X (kN)	F_Y (kN)	F_Z (kN)	M_X (Nm)	M_Y (Nm)	M_Z (Nm)	Height (mm)	Weight (kg)
MacGregor[24] (1985)	-	270	580	-	82	82	25	-
Quinn[20] (1990)	1.7	2.1	5.1	132	124	102	39	1.73
Kiefmann[25] (2005)	1	2	6	60	280	85	-	-
Moyer[27] (2005)	-	-	2.7	-	204	-	38	2
Strickter[26] (2010)	1.5	1	4	-	-	-	36	0.9
Kruger[22] (2011)	1.5	1.5	6	175	175	175	31	1.6

Table 6.3: Minimum full-scale range requirements of the new sensor design being considered.

$F_{X,Y}$ (kN)	F_Z(kN)	$M_{X,Y}$ (Nm)	M_Z (Nm)
$\geq \pm 2$	$\geq \pm 5$	$\geq \pm 180$	$\geq \pm 130$

6.2.2 ***Proposed Design***

Maltese-cross and tri-spoke style transducers were initially explored but could not meet strength requirements without exceeding the maximum height requirement. Therefore an adaptation of the maltese-cross was considered, comprising of four radial sensing arms, one arm in each quadrant of the horizontal X-Y plane (Figure 6.2). Each radial arm incorporates two Wheatstone bridges. Similar to traditional maltese-cross sensors, one bridge measures normal strain resulting from the vertical deflection of the arm while another bridge measures normal strain resulting from the horizontal deflection of the arm (Figure 6.3, Figure 6.4). Strain gages are placed on each side of the beam to measure strain resulting from bending. This also adds the benefit of temperature compensation for each bridge.

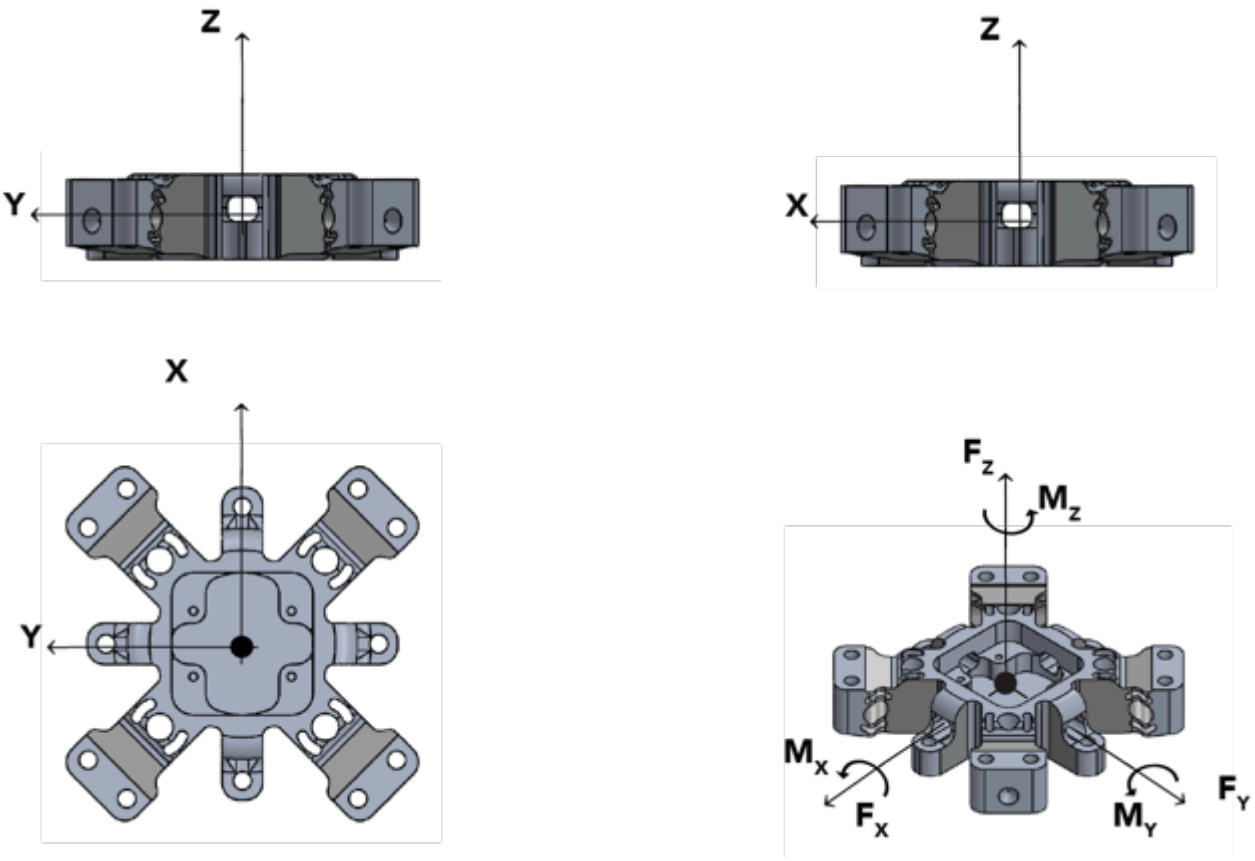

Figure 6.2: Each radial arm is located in one of the quadrants of the XY plane. The XY principal axes of the sensor coordinate system are defined 45 degrees from the arms.

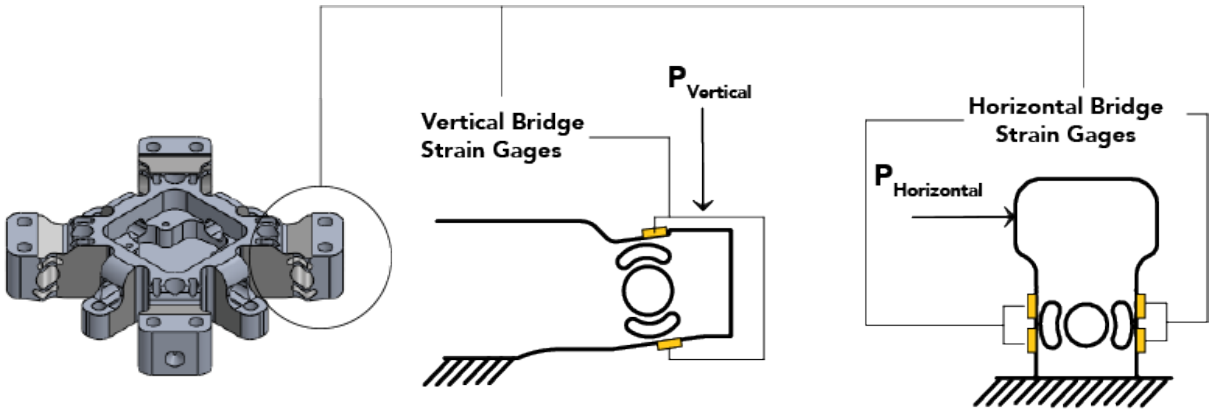

Figure 6.3: Each radial arm is instrumented with two strain gage bridges. The Vertical Bridge is placed to respond to loads that cause a vertical deflection of the arm. The Horizontal Bridge is place to response to loads that cause a horizontal deflection of the arm.

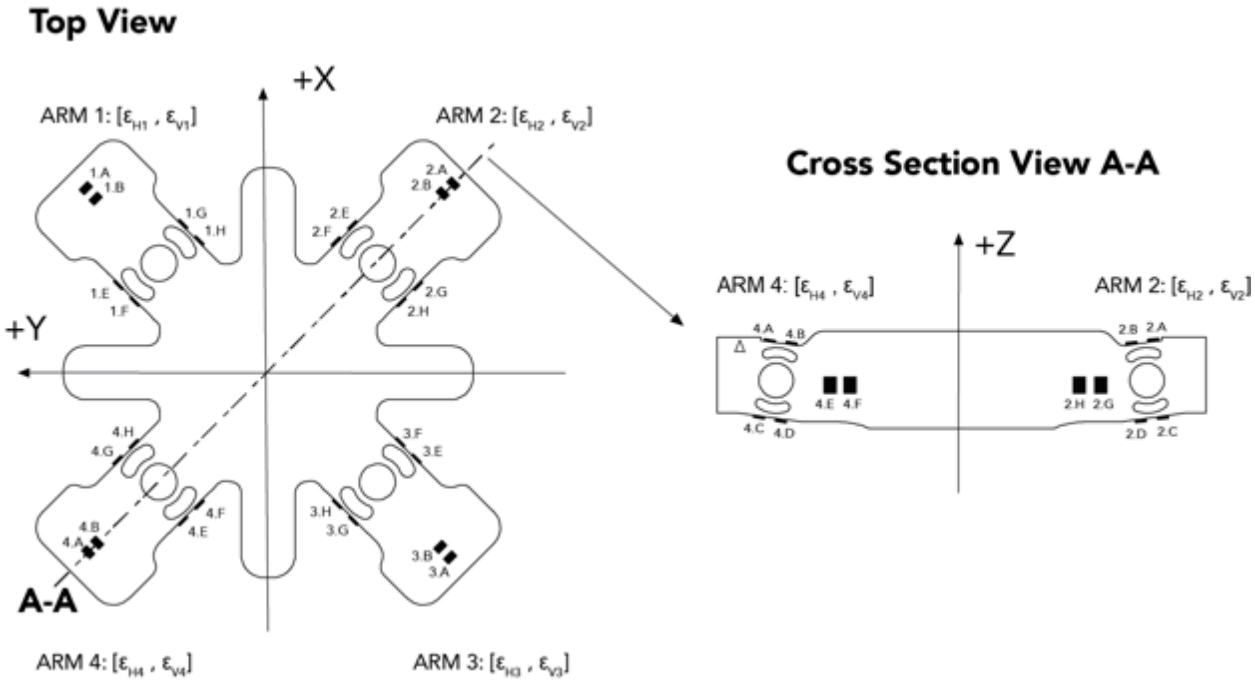

Figure 6.4: The sensor design considered incorporates four radial arms positioned at 45 degree increments from the principal X-Y axes of the sensor (Top). Each arm is instrumented with two Wheatstone bridges sense deflection of their respective arm in two directions; the vertical bridge senses the deflection of it's respective arm in the Z plane and the horizontal bridge senses horizontal deflection of it's respective arm in response to forces normal to it's longitudinal axis. Approximate gage locations are shown above.

The overall structural limit of the sensor can be increased along the principal axes of the sensor by rotating the principal X-Y axes of the transducer 45 degrees from the arms of the transducer such that the principal axes of the sensor do not align with the long axis the arms. In some applications this may not be advantageous; however, when measuring the ground reaction forces of skiing or snowboarding, the ski or snowboard acts as a large lever. If the X or Y axis of the proposed sensor is aligned with the longitudinal axis of the ski or snowboard, the largest forces and torques acting on the sensors will act along the principal axes of the ski or snowboard(Figure 6.1).

Each of the four radial arms is instrumented with one vertical deflection-sensing bridge, $\varepsilon_{V1\text{-}V4}$, and one horizontal deflection-sensing bridge, $\varepsilon_{H1\text{-}H4}$. The responses of these eight bridges are summed and transformed to fully resolve the six-load components acting on the sensing body

using equations (6.1-6.7). Define $\bar{F}$ as a 1-D force vector with *n* force and torque components. $\bar{\varepsilon}_o$ is the 1-D measured strain vector taken from *m* bridges on the sensor. An *m*x*n* compliance matrix $\bar{C}$ relates the measured $\bar{\varepsilon}_o$ vector to the force vector $\bar{f}$ acting on the sensor. In general, $m \geq n$; for the proposed sensor, $m=8$ which produces an *8x1* $\bar{\varepsilon}_o$ vector and a non-square, *8x6* compliance matrix. To produce a square compliance matrix, an additional transformation matrix, $\bar{K}$ (eqn 6.2), is used to transform $\bar{\varepsilon}_o$ into a *6x1* strain vector, $\bar{\varepsilon}$. The transformation matrix, $\bar{K}$, sums the strain response of all four arms into a single strain component corresponding to a specific load component (eqn. 6.3). This produces a square 6x6 compliance matrix $\bar{C}$. The force vector $\bar{F}$ is determined by multiplying the transformed strain vector by the pseudo-inverse of the compliance matrix $\bar{C}$ (eqn. 6.7). The compliance matrix is constructed by performing a least squares fit to the applied uniaxial forces and the measured response of each bridge (eqn. 6.5).

(eqn 6.1) $$\bar{\varepsilon}_o = \begin{bmatrix} \varepsilon_{H1} & \varepsilon_{H2} & \varepsilon_{H3} & \varepsilon_{H4} & \varepsilon_{V1} & \varepsilon_{V2} & \varepsilon_{V3} & \varepsilon_{V4} \end{bmatrix}^T$$

(eqn 6.2) $$\bar{K} = \begin{bmatrix} 1 & 1 & -1 & -1 & 0 & 0 & 0 & 0 \\ 1 & -1 & -1 & 1 & 0 & 0 & 0 & 0 \\ 0 & 0 & 0 & 0 & 1 & 1 & 1 & 1 \\ 0 & 0 & 0 & 0 & 1 & -1 & -1 & 1 \\ 0 & 0 & 0 & 0 & 1 & 1 & -1 & -1 \\ 1 & 1 & 1 & 1 & 0 & 0 & 0 & 0 \end{bmatrix}$$

(eqn 6.3) $$\bar{\varepsilon} = \bar{\varepsilon}_o \bar{K} = \begin{bmatrix} \varepsilon_{Fx} \\ \varepsilon_{Fy} \\ \varepsilon_{Fz} \\ \varepsilon_{Mx} \\ \varepsilon_{My} \\ \varepsilon_{Mz} \end{bmatrix} = \begin{bmatrix} \varepsilon_{H1} + \varepsilon_{H2} - \varepsilon_{H3} - \varepsilon_{H4} \\ \varepsilon_{H1} - \varepsilon_{H2} + \varepsilon_{H3} - \varepsilon_{H4} \\ \varepsilon_{V1} + \varepsilon_{V2} + \varepsilon_{V3} + \varepsilon_{V4} \\ \varepsilon_{V1} - \varepsilon_{V2} - \varepsilon_{V3} + \varepsilon_{V4} \\ \varepsilon_{V1} + \varepsilon_{V2} - \varepsilon_{V3} - \varepsilon_{V4} \\ \varepsilon_{H1} + \varepsilon_{H2} + \varepsilon_{H3} + \varepsilon_{H4} \end{bmatrix}$$

(eqn 6.4) $$\bar{F} = \begin{bmatrix} F_X & F_y & F_z & M_X & M_y & M_z \end{bmatrix}^T$$

(eqn 6.5) $$\overline{C} = \begin{bmatrix} C_{11} & C_{12} & C_{13} & C_{14} & C_{15} & C_{16} \\ C_{21} & C_{22} & C_{23} & C_{24} & C_{25} & C_{26} \\ C_{31} & C_{23} & C_{33} & C_{34} & C_{35} & C_{36} \\ C_{41} & C_{42} & C_{43} & C_{44} & C_{45} & C_{46} \\ C_{51} & C_{52} & C_{53} & C_{54} & C_{55} & C_{56} \\ C_{61} & C_{62} & C_{63} & C_{64} & C_{65} & C_{66} \end{bmatrix} \quad where,\ C_{ij} = \frac{d\varepsilon_i}{dF_j}\ for\ i,j = 1,....6$$

(eqn 6.6) $$\overline{C}\overline{F} = \overline{\varepsilon} = \overline{\varepsilon}_o \overline{K}$$

(eqn 6.7) $$\overline{F} = \overline{\varepsilon_o}\,\overline{K}\,\overline{C}^{-1}$$

6.2.3 ***Sensor FEA Model***

The baseline geometry of the sensor was developed using Computer Aided Design (CAD) Software (Solidworks, Waltham, MA). A static structural finite element analysis model of the sensor was developed for optimization and to enable a virtual calibration of the sensor before a prototype sensor was manufactured.

The CAD model of the sensor was imported into the Static Structural Module of ANSYS v16.0 (ANSYS, Canonsburg, PA) where strain gages were modeled in the Design Modeler module. The 32 strain gages shown in Figure 6.4 were modeled as surface bodies with dimensions 1.9mmx2.54mm to match sensing foil grid of the strain gages to be used on the physical sensor (Part No. J2A-13-S047D-350-SP62, Gage Factor, K = 2.11, Vishay, Shelton, CT). Three materials were considered for Material properties were defined to match the slightly orthotropic properties of three four alloys Direct Metal Laser Sintered Inconel 718 heat treated per AMS 5664 (Table 6.4).

The geometry model, including both the CAD and strain gage geometry, was passed to the Static Structural Module in ANSYS. Strain Gages were modeled as surface bodies with the elements of type 181 and meshed with one element along each side of the rectangular gage body. This allowed them to be modeled with an elastic stiffness equal to zero. The average normal strain could then be calculated under the mounting area of each gage. The sensor body and housing were meshed with hexagonal elements (Figure 6.5, Figure 6.6). Uniaxial forces and pure

moments {Fx Fy Fz Mx My My} are applied to the top of the sensor while the bottom was modeled as bolted a fixed foundation. The contact surfaces of the interface between the housings and the sensing body were modeled as frictional contacts with a coefficient of friction of 0.34. The interface between the bottom housing and the base support was also modeled as frictional with a coefficient of friction of 0.34.

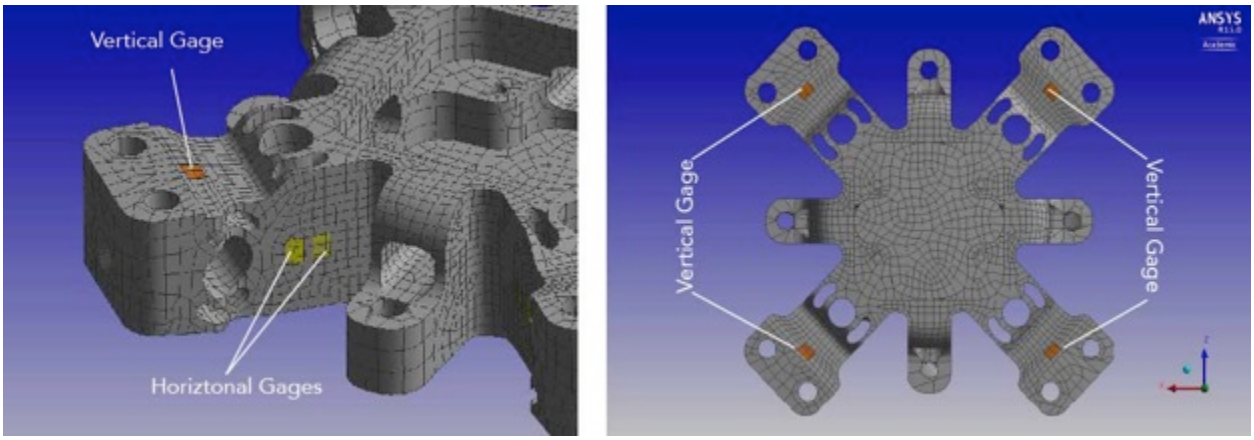

Figure 6.5: 32 strain gages modeled as surface bodies with the same physical dimensions as the specified strain gage foil grid.

Table 6.4: Material properties and design restrictions of various alloys considered for the prototype and full-scale sensors[77–79]. Strength was given the primary consideration before density, accuracy, and wall thickness.

Alloy		Aluminum, AlSi10mg[77]	Inconel, IN-718[78]		Titanium, Ti-6AL-V4[79]
Heat Treatment		NA	NA	AMS 5664	NA
Density (g/cm^3)		2.67	8.15	8.15	4.41
Wall Thickness (mm)		0.3-0.4	0.3-0.4	0.3-0.4	0.3-0.4
Accuracy (±μ m)		100	40-60	40-60	50
σ_{UTS} (MPa)	XY	460	1060	1060	1230
	Z	460	980	1380	1200
σ_{Yield} (MPa)	XY	270	780	780	1060
	Z	240	634	1240	1070
E (GPa)	XY	75	160	160	110
	Z	70	160	170	110

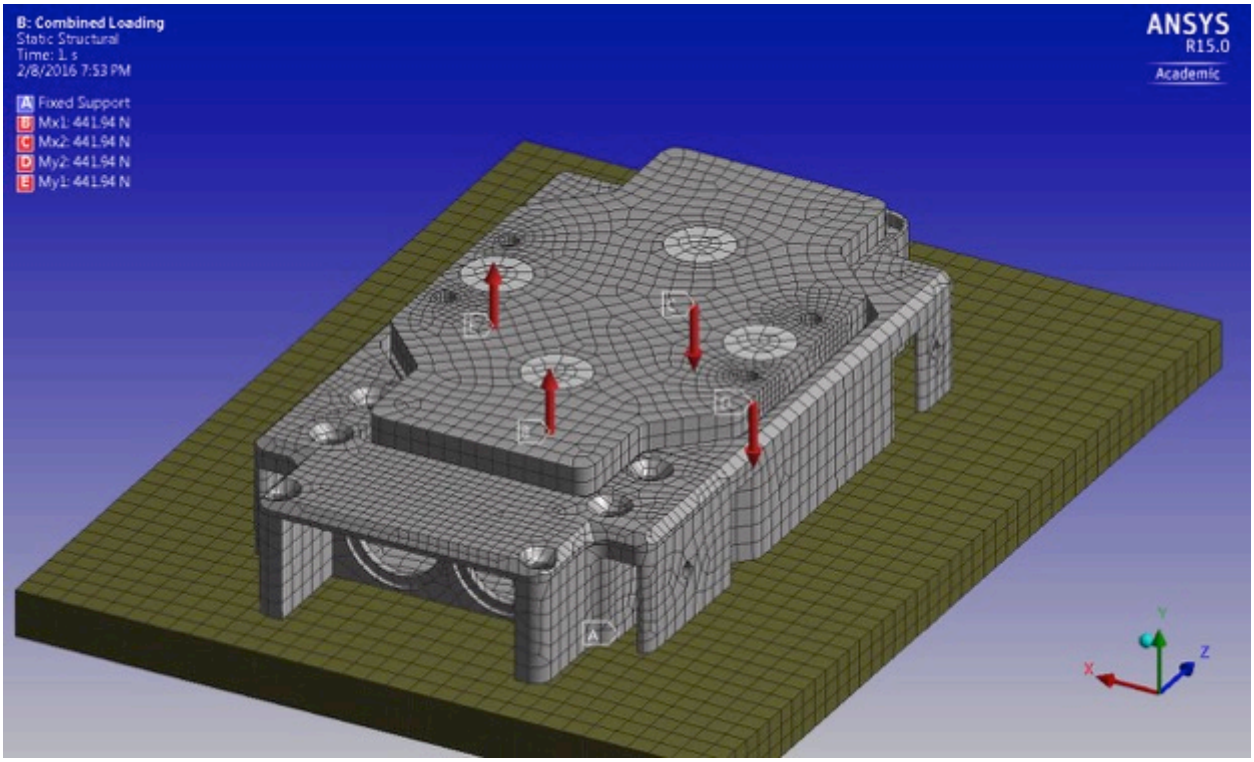

Figure 6.6: The CAD model shown with the generated mesh of hexagonal elements, with a total of 77,168 elements and 247,013 nodes. The boundary conditions are shown applying a combined M_X and M_Y load.

6.2.4 ***Processing FEA Model Results***

ANSYS has limited ability to post process its own results, and cannot perform simple arithmetic on the strain values predicted from different strain gages modeled. Therefore, Matlab (Natick, MA) was used to post-process the strain results. The strain results from the 32 strain gages modeled in ANSYS were imported into Matlab for each load step (Figure 6.7B). In Matlab, the strain gages were summed into the corresponding bridges (Figure 6.4) to form an nx8 strain vector, $\bar{\varepsilon}_o^{FEA,raw}$, where n = the number of load steps applied in the FEA model (Figure 6.7C). The transformation matrix, $\bar{K}$, (eqn. 6.2) is used to transform the strain vector into an nx6 vector, $\bar{\varepsilon}_o^{FEA}$. From the applied load vector and the strain vector, a linear regression is performed to calculate each element of the compliance matrix, $\bar{C}^{FEA}$ (Figure 6.7D).

To evaluate the performance of the compliance matrix, the applied loads, and the nx6 strain vector are used to calculate the applied loads, $\bar{F}_{FEA}$ (Figure 6.7E). Finally the RMSE between the applied loads and calculated loads can be calculated (Figure 6.7F).

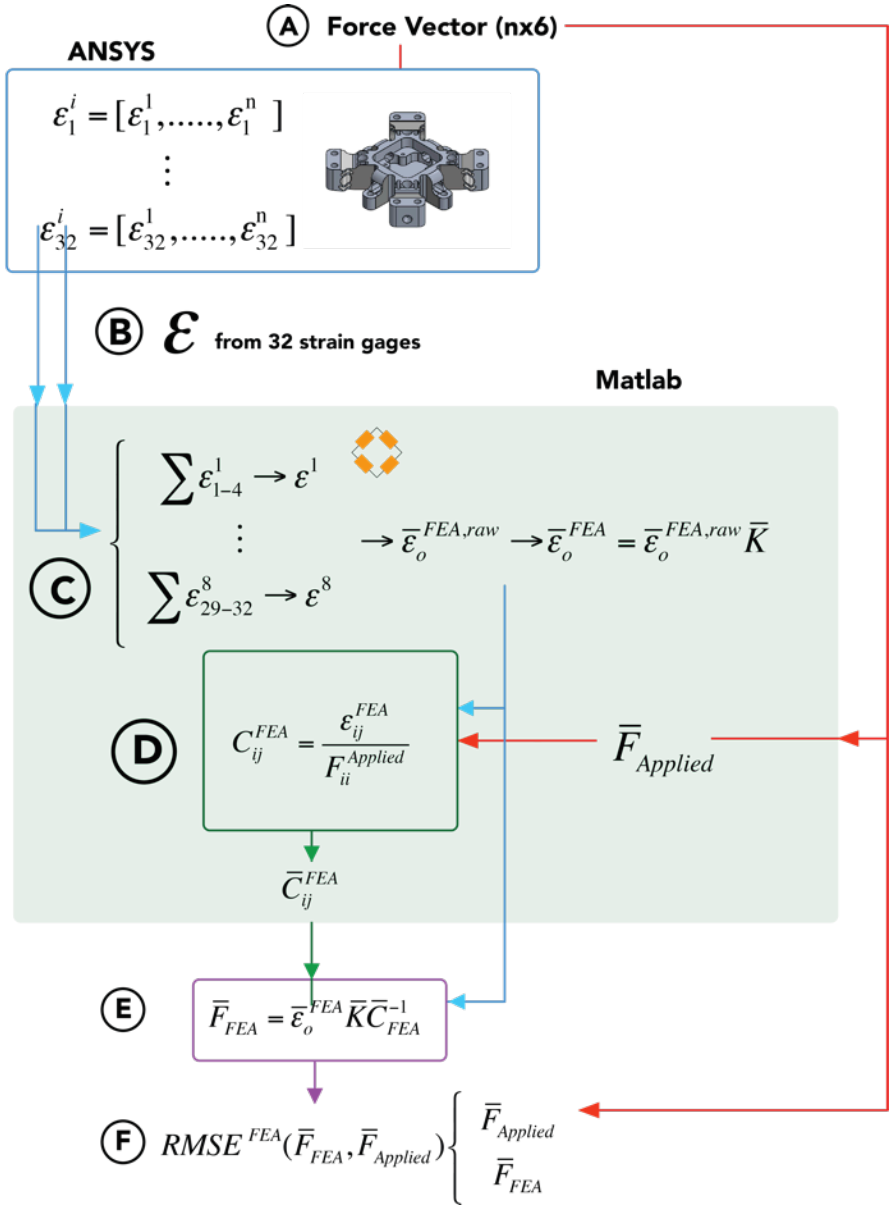

Figure 6.7: A schematic of the sensor model comprising of the FEA model and the processing of strain values from the FEA model in Matlab: A. Uniaxial loads are applied to the sensor body. B. The strain response from the 32 strain gages are exported from ANSYS and imported into Matlab. C. The strain response from the 32 strain gages is summed into each of the eight wheat stone bridges. The matrix, $\bar{K}$, is used to sum the eight bridges into six strain vectors. D. The compliance matrix is calculated. E. Using the summed strain response vector, $\bar{\varepsilon}_o^{FEA}$, and the calculated compliance matrix, $\bar{C}_{ij}^{FEA}$, the applied loads are calculated. F. The RMSE between the applied loads and the loads calculated using the strain vector and compliance matrix are calculated.

6.2.5 *Sensor Optimization*

After the baseline CAD model development of the sensor, several design variables including geometry dimensions and wheat-stone bridge configurations for the vertical and horizontal bridges required optimization to achieve the necessary functional design constraints.

Given the large number of design variables and optimization criteria to be minimized, the Parameter Space Investigation (PSI) method was employed which is particularly well suited to the solution of multi-criteria optimization problems[64,80] including that of multi-axis sensors[64].

6.2.5.1 Parameter Space Investigation

The PSI method for solving multi-criteria optimization problems described by Statnikov[80] is briefly described here using the author's notation. The PSI method requires a model that can accurately calculate the performance of a system, in this case the six-axis force transducer design being considered. The model is used to predict sensor performance by varying *r* design variables, $\boldsymbol{\alpha}_{\mathbf{l}} = \{\alpha_1, \ldots \alpha_r\}$. Design variables create a, *r*-dimensional solution space, $\prod(\alpha)$, and are given upper and lower bounds such that:

$$C_l^* \le f(\alpha) \le C_l^{**}, l = 1,....,t \qquad \text{(eqn. 6.8)}$$

Functional constraints, $f(\alpha)$, such as maximum allowable stress, are often a function of the design variables. They define a subset G $(\alpha, f(\alpha))$ of $\prod(\alpha)$, such that $G \subset \prod$ and are also given upper and lower bounds:

$$\Phi_V \le \Phi_V^{**} \qquad \text{(eqn. 6.9)}$$

Optimization criteria $\Phi(\alpha)$ are typically responses of the system that are used as a measure of system performance. The goal of any optimization routine is typically to find a solution such that:

$$\Phi(P) \le \min(\Phi(\alpha)) \qquad \text{(eqn. 6.10)}$$

P is the Pareto optimal point at which the optimization criteria are minimized. The PSI method first calculates the system for the entire solution space $\prod(\alpha)$, and then the feasible solution set $G(\alpha, f(\alpha))$ is defined through functional constraints $f(\alpha)$ (Figure 6.8). Interaction from the expert is necessary to decide the maximum acceptable values for $\Phi(\alpha)$ such that:

$$\Phi(\alpha) \le \Phi_V^{**} \qquad \text{(eqn.6.11)}$$

The feasible solution set $D(\alpha, f(\alpha), \Phi(\alpha))$ can then be defined using Φ_V^{**} and the Pareto optimal point can be found as defined by equation 6.10.

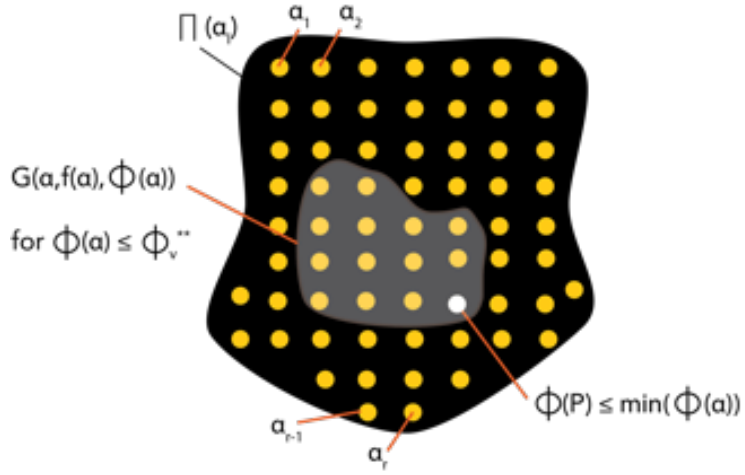

Figure 6.8: *The solution space $\prod(\alpha)$ comprising of system solutions resulting from every α_r. G $(\alpha, f(\alpha))$ is defined as the solutions with in $\prod(\alpha)$ that satisfy the functional relations $f(\alpha)$. Φ_V^{**} is then used to define the feasible set, $D(\alpha, f(\alpha)\, \Phi(\alpha))$. Then $\Phi(P) \leq \min(\Phi(\alpha))$ can be solved*

6.2.5.2 Design Variables: α_l

Geometry affecting the sensitivity, size, and location of the strain fields where the strain gages are to be placed must be carefully designed. Maltese cross sensors of the past have utilized circular holes to improve sensitivity [74] or used bearings to alter the boundary conditions of the arms [57,66]. The sensor under consideration required geometry more sophisticated to reduce the cross sensitivity of the sensor. Several shape factors were explored including non-concentric holes, triangular holes, and other shape factors. The shape factor shown in Figure 6.3, consisting of two concentric circular slots with a central hole provides a constant strain field on the sensing surface while providing sufficient structural integrity to meet the strength requirements of the sensor.

Lower and upper constraints for design variables are tabulated in Table 6.5. Dimensions α_3-α_4 and α_7-α_8 in Figure 6.9 control the location of the strain field and correspondingly, the optimal location of the strain gages. Due to the geometric constraints, the locations of the gages along the radial dimension of the sensor are relatively fixed; therefore α_3-α_4 and α_7-α_8 are centered in a location that focuses the maximum strain fields under the sensing matrix of the gages. The other dimensions control the sensitivity and cross-sensitivity of each Wheatstone bridge.

A twelfth design variable, α_{12}, was used to determine the optimal bridge configuration. Three variations of full and half bridge configurations were considered for the vertical bridge, and two variations were considered for the horizontal bridge (Figure 6.10). In total, six combinations of the various options for the vertical and horizontal bridge configurations were considered (Table 6.6).

Table 6.5: Design Variables, $\boldsymbol{\alpha_l}$, to be optimized tabulated with their upper and lower constraints.

α (mm)	α_1	α_2	α_3	α_4	α_5	α_6	α_7	α_8	α_9	α_{10}	α_{11}
α_l*	4.00	0.50	0.50	4.00	3.50	0.50	0.50	4.00	3.00	10.75	12.00
α_l**	5.15	1.25	0.75	7.00	5.00	1.00	1.00	6.00	α_{10} - 3	15.00	15.00

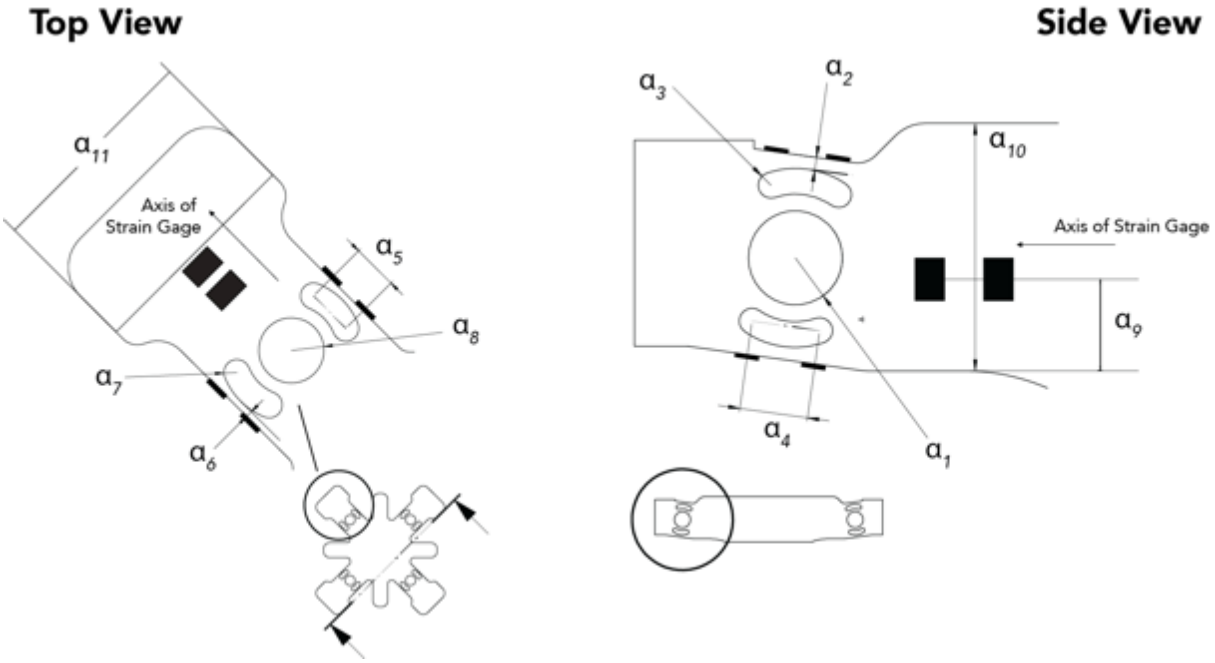

Figure 6.9: Design Variables, $\boldsymbol{\alpha_r}$, considered for optimization that control the sensitivity and cross-sensitivity of the sensor to applied loads.

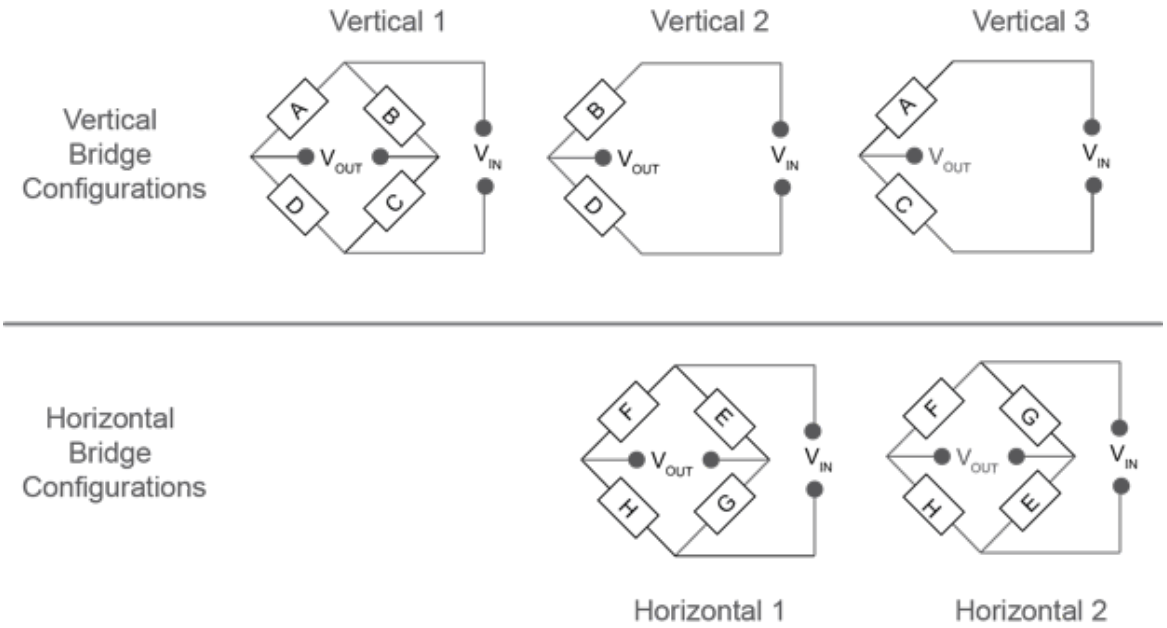

Figure 6.10: Five possible bridge configurations were explored for vertical and horizontal bridges. Table 6.6 tabulates the six combinations of these five bridges that were explored as design variable α_{12}*. Letters designating each gage match the location of the gages shown in Figure 6.4.*

Table 6.6: Design variable α_{12} *incorporated six combinations of the five possible bridge configurations shown in Figure 6.10 were explored.*

Design Variable	Bridge Configuration	Vertical Bridge	Horizontal Bridge
$\alpha_{12,n}$	1	1	1
	2		2
	3	2	1
	4		2
	5	3	1
	6		2

6.2.5.3 *Functional Constraints:* $f(\alpha_l)$

Functional constraints necessary for using the sensor under consideration for measuring forces while skiing are tabulated in Table 6.7. Functional constraints are not intended to be maximized or minimized so long as the proposed design does not violate each constraint.

Table 6.7: Functional constraints considered in the sensor design, though not all were utilized in the PSI analysis such as Environmental Protection.

Functional Constraints: $f(\alpha_i)$	
Height	$\leq$ 30mm
Width	$\leq$ 85mm
Length	$\leq$ 150mm
Maximum Allowable Von-Mises Stress: $\{F_X,F_Y,F_Z,M_X,M_Y,M_Z\}$	$\leq$ 50% σ_y
Minimum Wall Thickness	$\geq$0.5mm
Overload Protection: $\{F_X,F_Y,F_Z,M_X,M_Y,M_Z\}$	$\geq$ 2x Full Scale Range
Error: $\{F_X,F_Y,F_Z,M_X,M_Y,M_Z\}$	$\leq$ 2.5% Full Scale
Environmental Protection	IP-65 equivalent water resistance
Natural Frequency: ω_n	> 2 kHz

6.2.5.4 Optimization Criterion: $\phi_v(\alpha)$

The compliance matrix of a six-axis sensor that is decoupled well will have numerical values along the diagonal that are much larger than the off-diagonal terms. The condition number of a matrix gives a measure of how diagonal it is. For example, the identity matrix has a condition number equal to unity. The less diagonal a matrix is, the larger its condition number becomes. Many studies have used the condition number of the compliance matrix for a sensor as a measure of sensor accuracy and as an optimization criteria for solving objective functions to optimize sensor performance[57–59,74]. Many of these studies perform this optimization using analytical models of the sensor with simple geometry. This criterion requires calculating the full *6x6* compliance matrix of each design iteration, which can be computationally expensive with complex designs. The FEA Model of the proposed sensor comprised of 77,168 elements and 247,013 nodes, which necessitates a more efficient optimization criterion.

Kang et. al.[73] recently proposed a novel optimization criterion for Maltese cross sensors in which the optimization criteria focuses on minimizing two specific terms of the compliance matrix, assuming the sensor is symmetric about the X and Y axes. Decoupling a pure shear force F_i applied to the sensor, from a signal response in torque on the orthogonal axis, M_j is a the most computationally expensive task during the optimization of maltese-cross sensors. The criterion proposed by Kang et. al.[73] utilizes the metric of percent Cross Sensitivity, defined as the relative

magnitude of the off-diagonal terms relative to the corresponding diagonal term of each row as shown in equation (6.12). F_Z and M_Z are easily decoupled from the other four components and do not require significant computational effort to optimize.

$$\text{(eqn 6.12)} \quad \%CrossSensitivity = \frac{C_{ij}}{C_{ii}} * 100$$

Therefore, the optimization criterion was utilized to minimize the terms $\boldsymbol{C_{15}}$, $\boldsymbol{C_{24}}$, $\boldsymbol{C_{42}}$, and $\boldsymbol{C_{51}}$ terms of the compliance matrix $\boldsymbol{C}$ in equation (6.5) which correspond to the sensor's response in shear under an applied torque and the sensor's response in torque under and applied shear load. From symmetry, this can further be reduced to minimizing either pair of coefficients, $\{\boldsymbol{C_{15}}, \boldsymbol{C_{42}}\}$ or $\{\boldsymbol{C_{24}}, \boldsymbol{C_{51}}\}$. This reduces the number of times the FEA model must be solved per permutation of each design variable, α_r, during the optimization routine from six, if using the condition number criterion, to two. To fully define the optimization criteria, equations 6.13 -6.15 are used:

$$\text{(eqn 6.13)} \quad \phi_1 = \frac{C_{25}}{C_{22}} \le \phi_{V1}^{**}$$

$$\text{(eqn 6.14)} \quad \phi_2 = \frac{C_{14}}{C_{44}} \le \phi_{V1}^{**}$$

$$\text{(eqn 6.15)} \quad \phi_3 = \sqrt{\phi_1^2 + \phi_2^2} \le \phi_{V1}^{**}$$

Furthermore, the secondary design objective, after meeting the necessary accuracy requirements, is to minimize the overall sensor height, design variable α_{10}. Therefore, $\phi_4(P) = \min(\phi(\alpha_{10}))$ is defined as a final criterion, resulting in the performance criteria vector, $\bar{\phi}_v = \begin{bmatrix} \phi_1 & \phi_2 & \phi_3 & \phi_4 \end{bmatrix}$. Equation (6.16) defines $\overline{\phi_v^{**}}$, a vector defining the maximum permissible values for the performance criteria vector $\bar{\phi}_v$.

$$\text{(eqn 6.16)} \quad \overline{\phi_v^{**}} = \begin{cases} \phi_{v1}^{**} = 2.5\% & v = 1,...3 \\ \phi_{v2}^{**} = 16mm & v = 4 \end{cases}$$

The overall objective of the optimization routine is to find the Pareto optimal set, such that each performance criterion and pseudo criterion in $\bar{\phi}_v$ is minimized, such that

$\overline{\phi(P)} = \min(\phi(\alpha))$. The solution, $\overline{\phi(P)}$, may be non-unique for the original solution space, which has been constructed by equally spaced permutations in the design variables. Additional solutions may also lie outside the initial upper and lower bounds set for the design variables. Therefore, the expert may define 'soft' constraints for the upper and lower limits of the design variables, as well as the interval of permutation of relevant design variables to expand the solution space, or improve it's resolution, to include interesting solutions that are potentially better than the initial solution $\overline{\phi(P)}$.

Using this criterion, the optimization routine shown in Figure 6.11 was performed. A total of 176 combinations of the r = 12 design variables were modeled in CAD. Each CAD model was passed to through FEA routine that applied a shear load and torque load in discrete load steps to define the $\prod(\alpha)$ solution space. If the results of the FEA analysis met the functional criteria, $f(\alpha)$, the strain response from the modeled strain gages was exported to MATLAB (Waltham, MA) where the performance criteria vector, $\bar{\phi}_V = \begin{bmatrix} \phi_1 & \phi_2 & \phi_3 & \phi_4 \end{bmatrix}$, was calculated for each unique combination of design variables. From the $\bar{\phi}_V$ vectors calculated, the feasible solution set, $D(\alpha_r, f(\alpha), \bar{\phi}_V)$ is constructed and the Pareto optimal set can be identified.

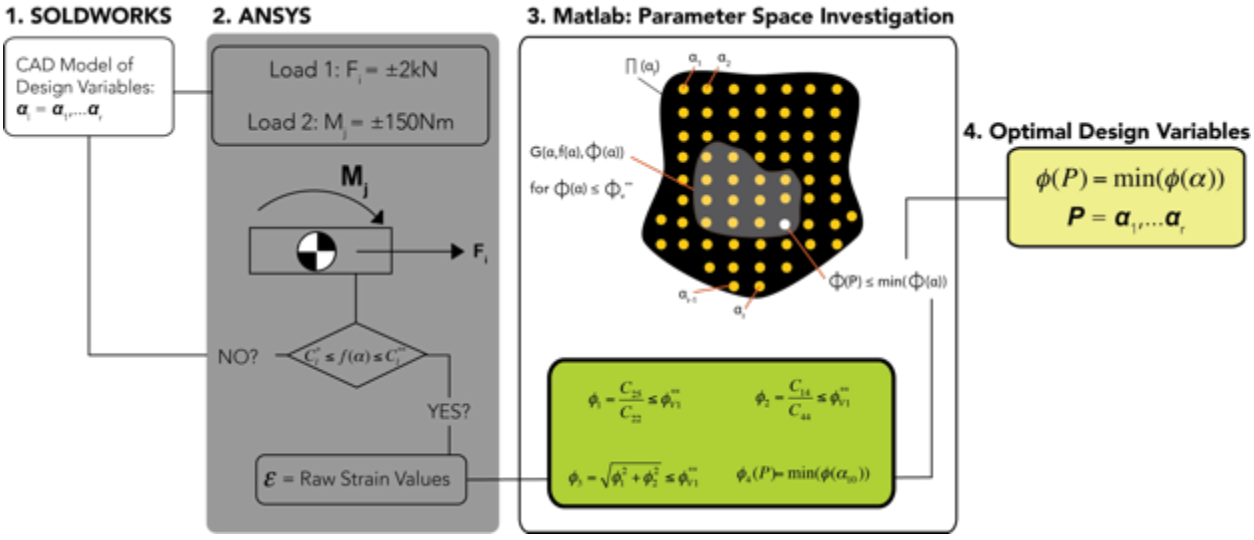

Figure 6.11: Optimization Routine (1) Sensor Geometry is defined in CAD and imported into ANSYS (2). A uniaxial shear load, F_i, and a uniaxial Moment, M_j, were both applied to the sensor in the FEA model. If the design variables, α_r, meet the functional constraints, $f(\alpha)$, for both the shear and moment uniaxial loads, the sensor response is passed to Matlab (3) to calculate the performance criteria vector $\bar{\phi}_V$ and the corresponding α_r is included in the feasible solution set, $G(\alpha,f(\alpha))$. The Pareto optimal set is then identified along with the corresponding optimal design variables (4).

6.2.6 *FEA Sensor Calibration*

Once the optimization criterion was met, the FEA model geometry was updated with the optimal design variables. All six-load components were applied to the sensor, one at a time, after which the strain response was exported and used to define the full *6x6* compliance matrix for the sensor, as modeled in the FEA software. To quantify the accuracy of the calculated compliance matrix, varying magnitudes of all six-load components were applied simultaneously to the sensor for 20 load steps. The individual response of each strain gage to each load step was exported, processed, and used to back-calculate the loads applied to the sensor. The predictions from each bridge configurations were compared to the actual applied loads calculating the Root Mean Squared Error (RMSE) for each channel of the sensor model (Figure 6.7). A final optimization criterion (eqn 6.17) was defined as:

(eqn 6.17) $$\phi_5^{**} = RMSE = \sqrt{\frac{\sum\left(F_i^{Calculated} - F_i^{Applied}\right)^2}{\sum\left(F_i^{Applied} - \overline{F_i^{Applied}}\right)^2}} \le 5\% \text{ for } i = 1\text{-}6.$$

6.2.7 *Overload Protection*

To protect the sensor from plastic deformation should it undergo deflections greater than it's elastic limit, hard stops were designed into the base housing of the sensor to restrict the maximum amount of vertical deflection each arm could sustain (Figure 6.12). The FEA model was used to test several load cases considered to be the most critical overload protection. In particular, load cases that had the potential to focus the load along the axis of the arms rather than allow the load to be shared between all four arms along the principal axes were considered. The largest defections of the arms were produced when F_Z and $M_X = M_Y$. The hard-stops were designed to limit the deflection of the arms such that the equivalent Von-Mises Stress, $\sigma_{VonMises}$, did not exceed 80% of the yield stress σ_y, $\sigma_{VonMises} \le 0.8 \cdot \sigma_y$.

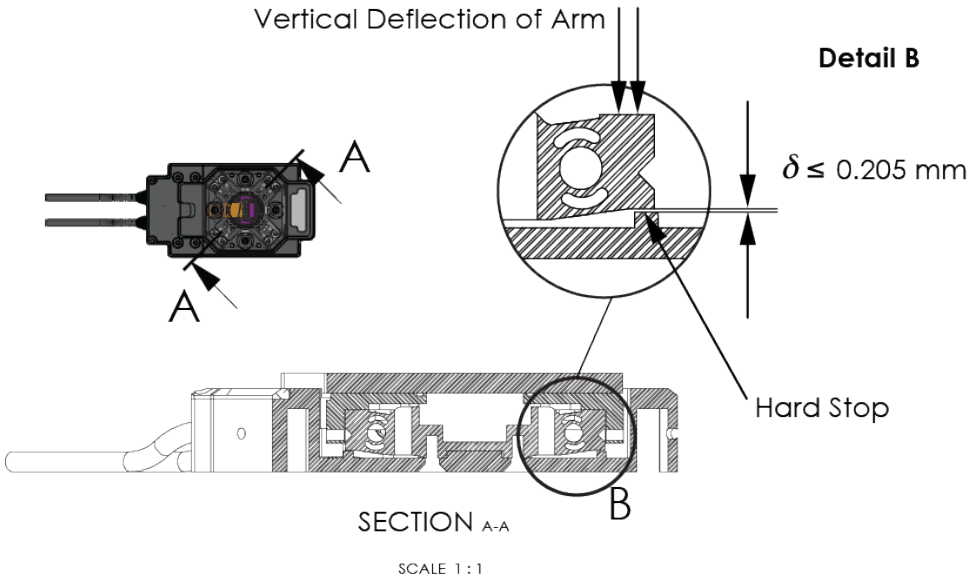

Figure 6.12: Hard stops designed into the sensor housing to limit the vertical elastic travel of each sensing arm to provide overload protection.

6.3 Model and Optimization Results

6.3.1 *Sensor Design and FEA Results*

The predicted full-scale range of the sensor, calculated as the maximal uniaxial load required to produce $\sigma_{VonMises} = 0.8\sigma_y$, are tabulated in Table 6.8. The predicted maximal uniaxial loads are twice that of the design requirements (Table 6.7). The FEA model calculated a focused and uniform strain field over which strain gages may be placed (Figure 6.13 and Figure 6.14) for both the horizontal and vertical bridges. The overall sensor body dimensions are 78mm x 78mm x 13.74mm. When installed in the IP-66 protective housing, the final sensor dimensions are 85mmx150mmx29.5mm.

Table 6.8: Predicted Full Scale Range of the sensor from the FEA model, calculated as the maximal uniaxial load applied for $\sigma_{VonMises} = 0.8\sigma_y$.

Predicted Full Scale Range	**F_X**	**F_Y**	**F_Z**	**M_X**	**M_Y**	**M_Z**
	±19kN	±19kN	±9kN	±280Nm	±280Nm	±250Nm

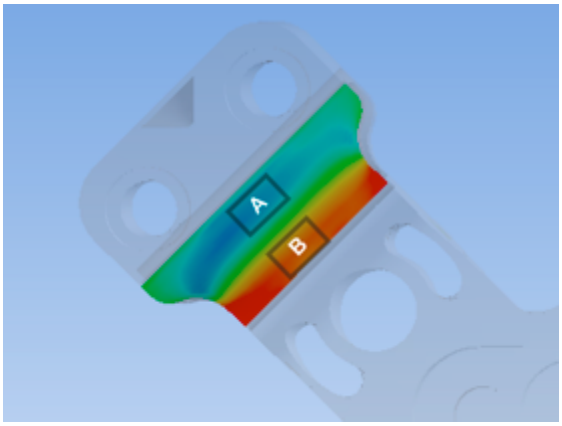

Figure 6.13: The normal strain field for the mounting surface for the vertical bridges in response to a compressive load {F_Z}. The gradient of the normal strain field under gages A & B are relatively homogenous, and equal and opposite in magnitude.

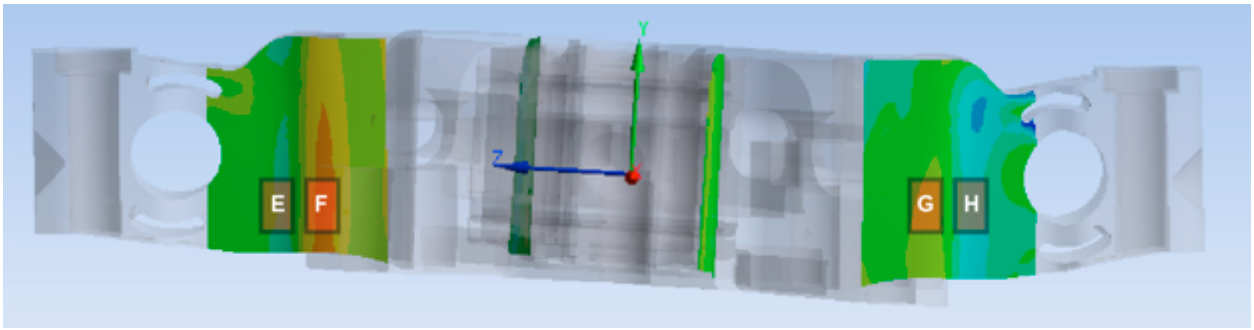

Figure 6.14: The normal strain field for the mounting surface for the horizontal bridges in response to a Shear Load {$F_{X,Y}$}. The gradient of the normal strain field below gages E-F & G-H are homogenous. However, the strain field is approximately the same width as the gage sensing matrix, therefore proper gage alignment is critical. Deformation shown not to true scale.

6.3.2 *Optimization Results*

The PSI method was able to find a solution to the multi-criteria optimization problem from 176 combinations of 12 design variables. Soft design constraints were utilized to explore viable solution space that was not initially included. The optimization routine was able to identify a Pareto optimal point that satisfied the performance criteria. Performance Criteria ϕ_1 and ϕ_2 are plotted for the feasible solution set *D(α,f(α),ϕ(α))* (Figure 6.15 *A)*. All points plotted meet the functional constraints, *f(α)*. For each point corresponding to the performance criteria ϕ_1 and ϕ_2 a surface is fit to the corresponding pseudo-criterion, ϕ_4 (Sensor Height). From the feasible solution set, the Pareto Optimal Set, ϕ(P) = min(ϕ(α)), is found by finding the minimum sensor height within the constraints of $\boldsymbol{\phi_1,\phi_2} \leq \boldsymbol{\phi_v}^{**}$. Here, $\phi(P)$ is designated by the red dashed lines, and circle. Table 6.9 tabulates the four performance criteria for three possible choices for the Pareto optimal point, shown in Figure 6.16. The design variables corresponding to the optimal solution are tabulated in Table 6.10.

*Table 6.9: Performance Criteria from the three points that satisfy the $\boldsymbol{\phi}^{**}_{v,max}$ criteria. Point A was selected as the Pareto Optimal Point **ϕ(P)** from the additional ϕ(P) = min($\boldsymbol{\phi}^{**}_{v}(\alpha)$).*

Points	ϕ_1	ϕ_2	ϕ_3	ϕ_4
P_1	**0.49%**	**0.27%**	**0.56%**	**13.75 mm**
P_2	0.68%	2.12%	2.21%	13.27 mm
P_3	1.68%	0.41%	1.73%	14.51 mm

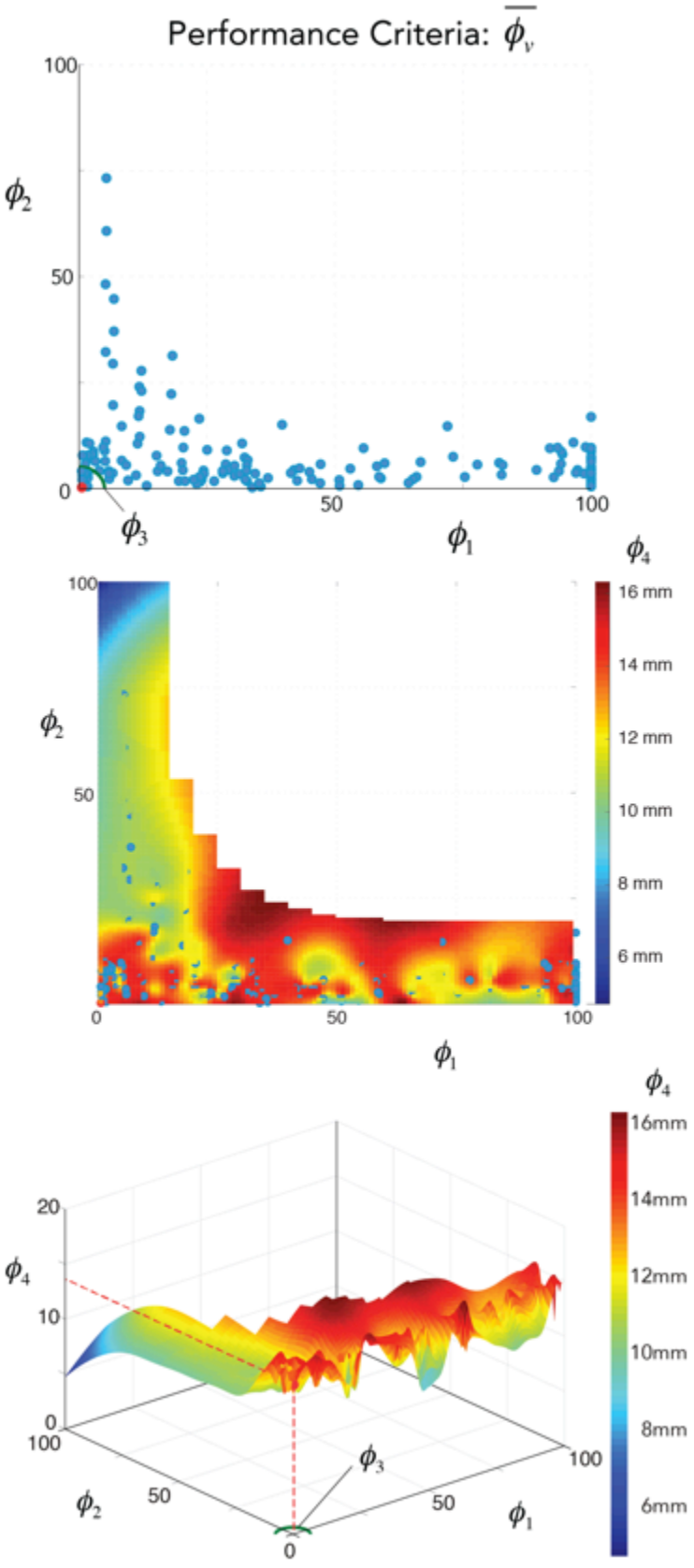

Figure 6.15: ***(A)*** *Performance Criteria* $\boldsymbol{\phi_1}$ *vs.* $\boldsymbol{\phi_2}$ *are plotted for the feasible solution set D(α,f(α),ϕ(α)). All points plotted meet the functional constraints, f(α). The boundary for* $\boldsymbol{\phi_3}$ *is denoted by the green radius near the origin.* ***(B)*** *For each point corresponding to the performance criteria* $\boldsymbol{\phi_1}$ *and* $\boldsymbol{\phi_2}$ *a surface is fit to the corresponding pseudo-criterion,* $\boldsymbol{\phi_4}$ *(Sensor Height).* ***(C)*** *From the feasible solution set, the Pareto Optimal Set, ϕ(P) = min(ϕ(α)), is found by finding the minimum sensor height,* $\boldsymbol{\phi_4} \leq \boldsymbol{\phi_{v2}}^{**}$ *within the constraints of* $\min(\boldsymbol{\phi_1},\boldsymbol{\phi_2},\boldsymbol{\phi_3}) \leq \boldsymbol{\phi_{v1}}^{**}$. *Here,* $\phi_v(P)$ *is designated by the red dashed lines, and* $\boldsymbol{\phi_3}$ *by the green circle.*

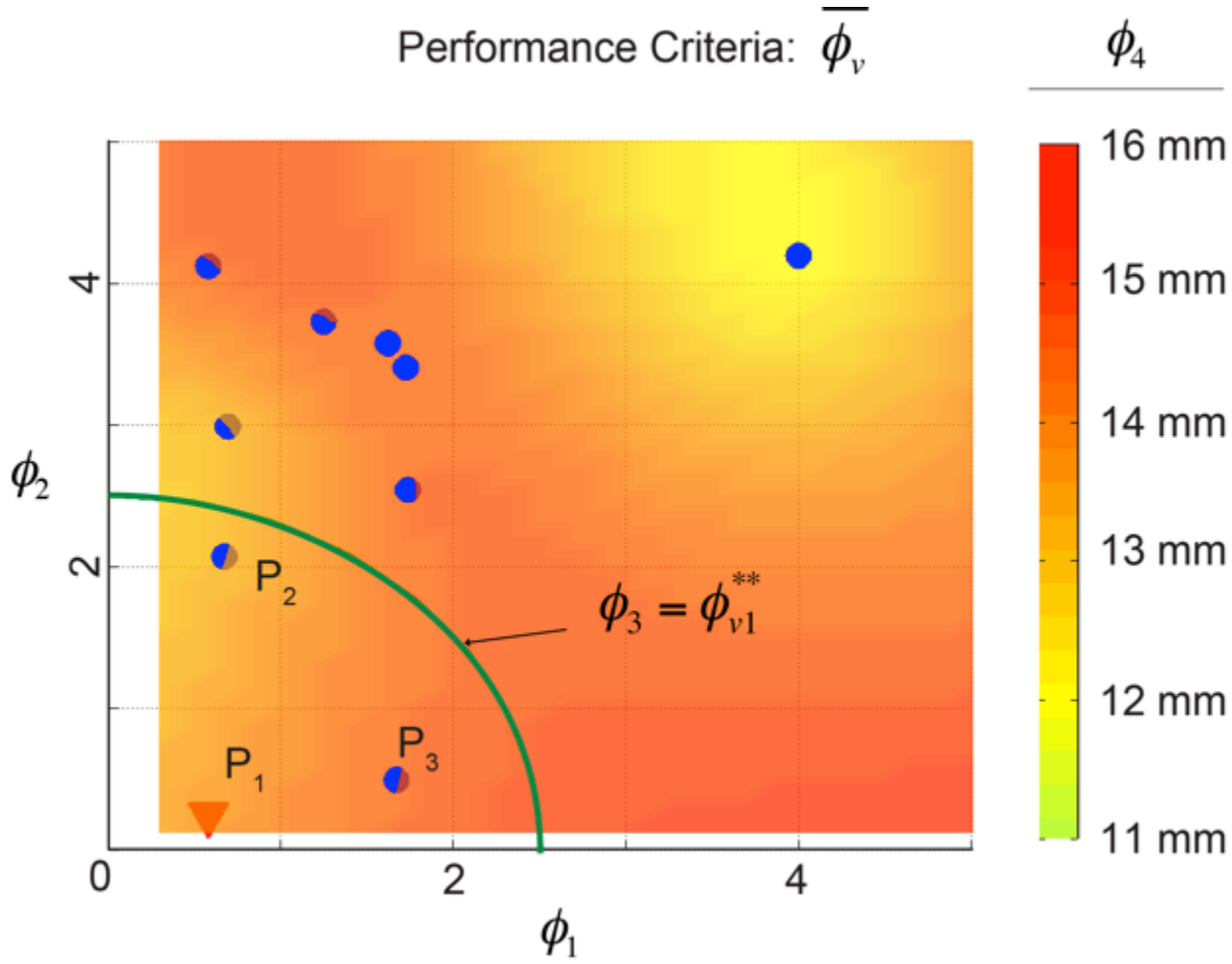

Figure 6.16: Performance Criteria, $\boldsymbol{\phi_v}$, plotted showing the Pareto Optimal Point (P_1) and two other points (P_2 & P_3) that met the $\boldsymbol{\phi}^{**}_{v,max}$ criteria. Point P_2 and P_3 corresponded with a lower value for $\boldsymbol{\phi_4}$ but a larger value for $\{\boldsymbol{\phi_1}, \boldsymbol{\phi_2}, \boldsymbol{\phi_3}\}$. Therefore Point P_1 was chosen as the Pareto Optimal Point.

Table 6.10: Pareto Optimal set $\phi(P_1)$ values for design variable α_l. They are reported to the nearest 0.05mm, which is reflective of the accuracy of the DMLS Manufacturing process used to manufacture these sensors.

α	α_1	α_2	α_3	α_4	α_5	α_6	α_7	α_8	α_9	α_{10}	α_{11}	α_{12}
(mm)	5.15	0.75	0.75	5.5	3.5	0.5	0.75	6.0	7.15	13.75	14	n 5

Lower values for ϕ_4 were able to meet the functional constraints for allowable Von-Mises Stress, but not performance constraints ϕ_{1-3}. Figure 6.17 shows the effect on of decreasing sensor height, design variable α_{10}, on the normal strain field where the strain gages are placed for measuring $\{F_X,F_Y,M_Z\}$ components. Figure 6.17 shows that edge effects resulting from vertical loading of each sensor arm translate into the normal strain field. From the optimization procedure, these edge effects are sensed by the strain gages for $\alpha_{10} < 13.75$mm.

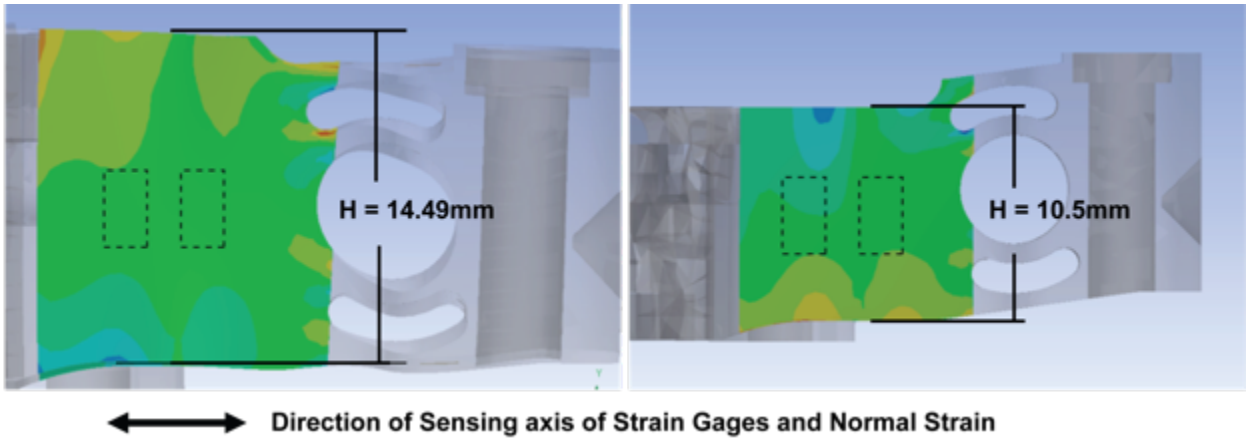

Figure 6.17: Normal strain from an applied M_Y plotted on the horizontal sensing surfaces along the sensing axis of the gages under an applied M_X or M_Y. The larger value of dimension α_{10} prevents the edge effects from overlapping with the strain gage (left). For values of $\alpha_{10} < 13.75$mm, the edge effects begin to overlap under the sensing area of the strain gage (right) and increases the cross sensitivity of the sensor.

6.3.3 *FEA Calibration*

Under uniaxial calibration loads, the response of each bridge was linear and proportional to the applied load. The response of the individual strain gages for an applied M_Z is shown in Figure 6.18. The individual bridge responses, and their transform using equations (6.1-6.3) from each calibration load step are shown in Figure 6.19 along with the mechanical decoupling of the sensor for each load component.

The full calibration matrix of the sensor calculated from the FEA model using uniaxial loads of all six-load components and the strain response of each individual strain gage (Table 6.11). The magnitude of the off-diagonal terms did not exceed 2.69% of the diagonal term in

each corresponding row. The condition number of the calibration matrix was 192.5. The optimization criterion used by Kang. et. al.[73] was used rather than the condition number, so no acceptable criterion for the condition number was defined.

The RMSE error for each bridge configuration is listed in Table 6.12 and shown in Figure 6.20. Similar to what was indicated in the optimization results, Strain Gage Bridge Configuration 5 had the lowest RMS Error out of the six possible bridge configurations.

Table 6.11: Calibration matrix calculated from strain output from the FEA Model.

$$\overline{C_{FEA}} = \begin{bmatrix} 3.1547 & -0.0522 & 0.0006 & -0.0003 & 0.0004 & -0.0002 \\ 0.0107 & -2.7963 & -0.0007 & 0.0004 & 0.0000 & -0.0002 \\ 0.0113 & -0.0018 & 0.5356 & 0.0001 & -0.0001 & 0.0000 \\ -0.0013 & -0.0014 & 0.0026 & 0.0156 & 0.0003 & 0.0000 \\ 0.047 & -0.0029 & 0.0015 & 0.0001 & -0.0164 & 0.0000 \\ 0.0157 & -0.0011 & -0.0011 & 0.0000 & 0.0000 & -0.0164 \end{bmatrix} \frac{\mu\varepsilon}{EU}$$

$$Cond(C_{FEA}) = 192.8$$

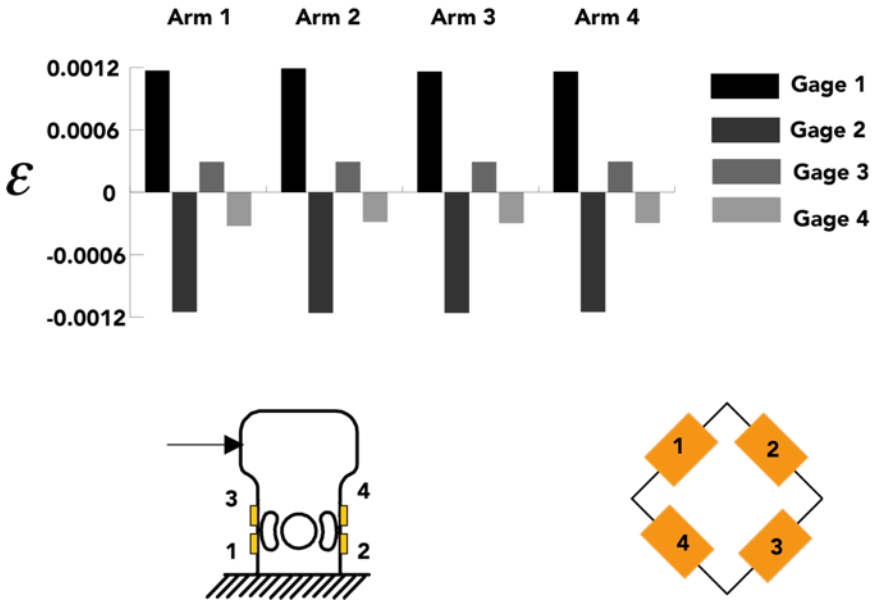

Figure 6.18: The raw strain values measured by each of the gages for the horizontal bridges on arms 1-4 in response to an applied M_Z. Gage locations on the arm are shown, and their wiring schematic is shown at the bottom. These are the values exported from ANSYS, and imported into MATLAB (Figure 6.7 B).

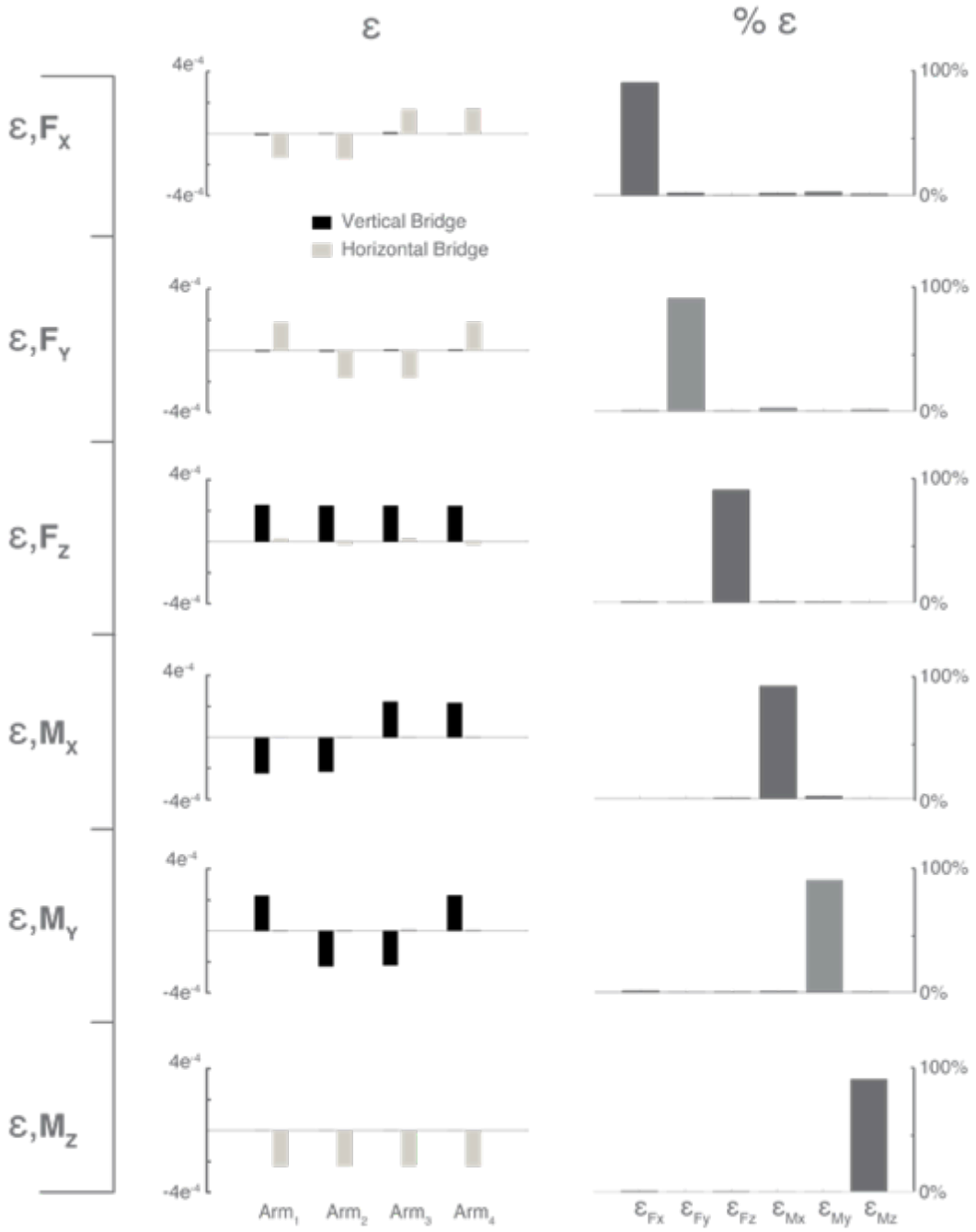

Figure 6.19: Strain response from each vertical and horizontal bridge in each arm (Left Column) and the normalized summed strain response summed $\bar{\varepsilon} = \bar{\varepsilon}_o \overline{K}$ *(eqn. 6.3). (Right Column) in response to an applied uniaxial loads {F_X, F_Y, F_Z, M_X, M_Y, M_Z}. The bridge response on the left is the equivalent strain response that the data acquisition unit would measure.*

Table 6.12: Calculated RMSE of the applied combined loads and corresponding loads calculated from the FEA model of the optimized sensor.

RMSE	F_X (N)	F_Y (N)	F_Z (N)	M_X (Nm)	M_Y (Nm)	M_Z (Nm)
FEA	0.2	0.2	0.05	0.015	0.015	0.015

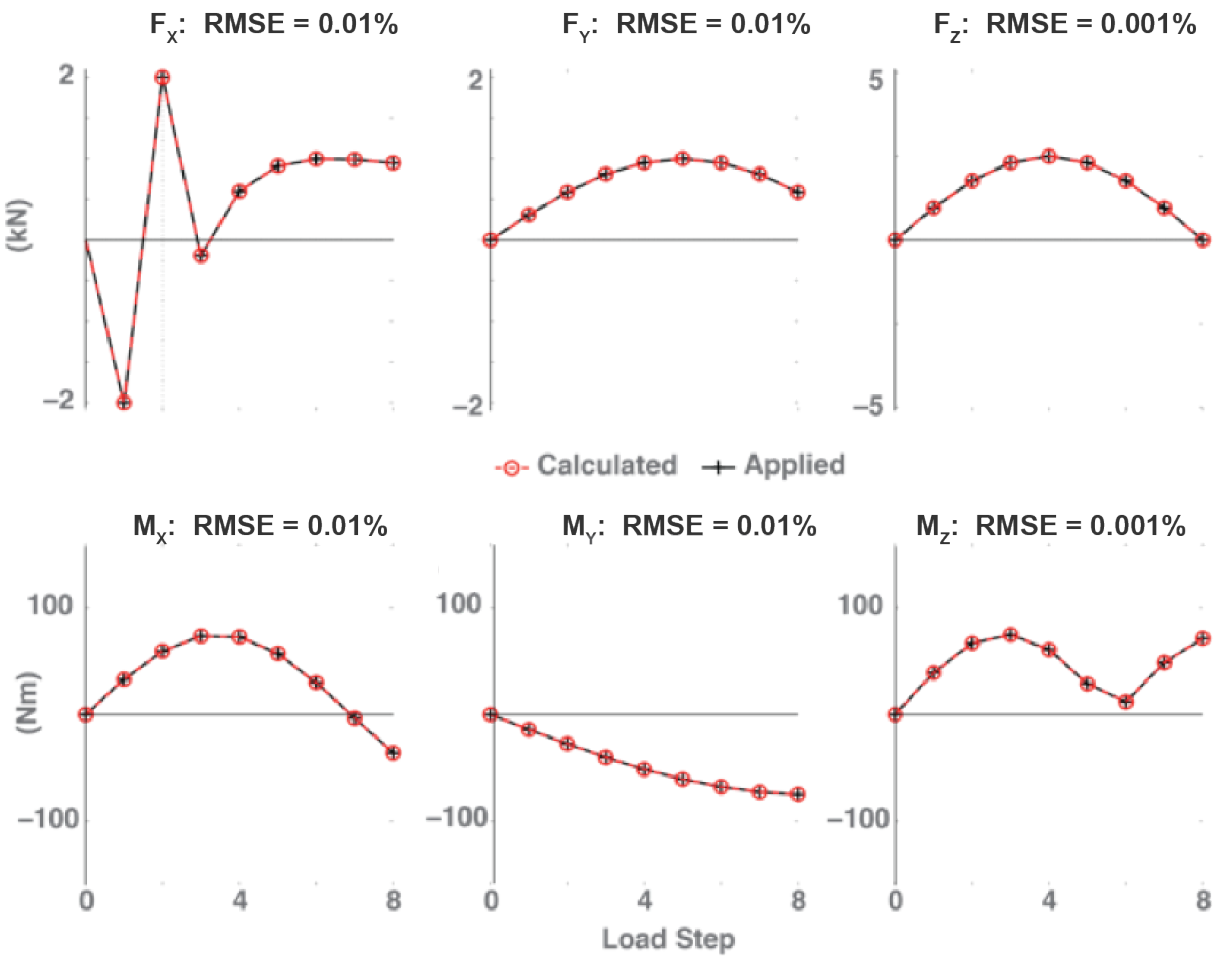

Figure 6.20: Root Mean Square Error calculated from an exemplar trial of combined loads applied to the FEM Model and calculated from the strain response and the calibration matrix

6.4 **Discussion**

The PSI method was able to find a solution to the multi-criteria optimization problem from 176 combinations of 12 design variables. It is possible this solution found is non-unique; soft design constraints were utilized to expand the solution space to include higher resolution for permutations on design variables. After expanding the solution space on several occasions with marginal gains, $\phi(P)$ was accepted as the optimal solution that satisfied the optimization criteria. Examination of Figure 6.16 shows that the surface fit to the optimization criteria for minimized sensor height, ϕ_4^{**}, is fairly homogeneous within the boundary defined by the other criteria ϕ_{1-3}^{**}. The surface fit indicates that the minimum sensor height that can be achieved is 12.9mm, which comes at a cost of 2% cross talk. Given the marginal gains of minimizing height compared to the computational expense of solving the FEA model for each permutation, $\phi(P)$ was accepted as the optimal solution. Using the optimization criterion of minimizing the cross-sensitivity terms of the calibration matrix, as proposed by Kang et. al.[73], was significantly more efficient than using the condition number criteria as suggested by multiple other studies[57–59,74,81–83]. From the combined loading analysis, the RMSE values are well below the maximum allowable error of 5%.

The FEA model predicts that the optimized sensor design shown here will have a full-scale range of each load component was predicted to be twice the designed requirement or greater (Table 6.13) and significantly higher than other sensors used by past researchers. The FEA model also predicts that the optimized sensor design will meet the other performance and functional requirements for accuracy and minimal height and weight.

Table 6.13: *Comparison of the uniaxial full-scale ranges, height, and weight, of multi-axis transducers designed to measure ground reaction forces of skiing and snowboard to the proposed sensor design without the overload hard stop protection.*

	F_X (kN)	F_Y (kN)	F_Z (kN)	M_X (Nm)	M_Y (Nm)	M_Z (Nm)	Height (mm)	Weight (kg)
MacGregor[39] (1985)	-	0.27	0.58	-	82	82	25	-
Quinn[41] (1990)	1.7	2.1	5.1	132	124	102	39	1.73
Kiefmann[75] (2005)	1	2	6	60	280	85	-	-
Moyer[84] (2005)	-	-	2.7	-	204	-	38	2
Strickter[85] (2010)	1.5	1	4	-	-	-	36	0.9
Kruger[86] (2011)	1.5	1.5	6	175	175	175	31	1.6
Proposed Sensor	19	19	9	280	280	259	29	0.75

6.5 **Conclusion**

A strain gage based multi-axis force transducer was modeled in an FEA model. The FEA model was used to optimize the sensor geometry for accuracy and to minimize the height of the sensor. The strain output from the model was used to calculate a calibration matrix that predicted accurately various combinations of forces and torques. The optimized solution satisfies the necessary functional and performance constraints and criteria. A prototype sensor will be constructed to validate the FEA model and verify the accuracy of the optimized sensor design.

Chapter 7. Construction and Calibration of the Optimized Six-Axis Force Sensor

7.1 Introduction

A low-cost prototype six-axis force sensor was constructed based on the results from the sensor design optimization routine reported previously (Chapter 6). The purpose of the prototype was to validate the sensor model before the full-scale transducers were constructed. Given the complex geometry of the sensor design, additive manufacturing (i.e., 3-D printing) methods were explored in lieu of traditional subtractive (machining) methods. The prototype sensor was calibrated and an error analysis of the prototype sensor relative to both a reference measurement system and the FEA model was performed.

7.1.1 *Construction of a Prototype Sensor*

7.1.1.1 Material Selection

The FEA optimization routine was performed using material properties for Inconel IN-718 heat treated per ASM 5665[84] (Table 6.4). Other materials were explored for the prototype and construction of the full-scale sensors (Table 6.4). The FEA model confirmed that both IN-718 heat-treated per AMS 5664 and Ti-6AL-V4 would satisfy the strength and sensitivity requirements of the sensor (Table 6.3). Therefore, the cost and difficulty of manufacturing became the primary criterion to choose between IN-718 and Ti-6AL-V4 alloys for the full-scale sensors.

7.1.1.2 Manufacturing Methods

Direct Metal Laser Sintering (DMLS) is an additive manufacturing process which deposits thin layers, 20-40μm, of metal powder that is sintered using a precise laser to fuse the metal powder particles in the desired geometry[85,86]. Layer-by-layer complex geometries, which are impossible to be made by traditional subtractive manufacturing techniques, can be achieved with material density < 99%. Electron beam melting (EBM) is a competing additive manufacturing process that uses a similar methodology to that of the DMLS process, but with an electron beam to melt powdered metal layer by layer to form a desired geometry. EBM has been

shown to produce parts with lower residual stresses stemming from the cooling rate post-sintering relative to DMLS parts[87]. However, with proper heat treatment of DMLS parts, the residual stresses can be relieved, but can produce greater orthotropic material properties between the horizontal and vertical (sintering) plane (Table 6.4) [77–79,84,87–89].

Several design limitations must be considered when designing a component to be manufacturing using the DMLS process. To produce cantilevered structures, supporting structures for the cantilevered structures during the sintering process must be utilized and then removed post-sintering. If supporting structures are not used, the formation of cantilevered features can sag or become warped depending on the wall thickness[77–79] and sintering temperature required for the material being used. Further more, the surface finish produced by the DMLS process is very rough for certain applications, such as bearing surfaces or the application of strain gages, requiring secondary-machining processes achieve the proper surface finish requirements[77–79].

In the context of manufacturing the sensor body using the DMLS process, the cantilevered arms themselves require supporting structures that would be removed post-sintering. The thin walls and cantilevered geometry of the hole and concentric slots shown in Figure 7.1 are perpendicular to the Z-sintering plane. These would require supporting structures and secondary machining processes such as Wired Electron Discharge Machining (EDM), to remove them to achieve the specified manufacturing tolerances if IN-718 or Ti-6AL-V4 were used. Prior to the construction of the prototype, a considerable degree of uncertainty existed regarding the ability of the DMLS process to hold the necessary tolerances for features A-C in without any supporting structures. Additionally, IN-718 requires wire EDM processing to achieve the necessary surface finish for strain gage application.

Due to the uncertainty of the DMLS process to hold the tolerances for features A-C in Figure 7.1 without supporting structures, a low-cost prototype of the optimized sensor geometry was made using a DMLS aluminum alloy ALSi10mg because of its lower sintering temperature compared to Inconel (Table 6.4). The lower sintering temperature, an aluminum sensor would not require supporting structures. Additionally, the aluminum alloy would allow for the strain gage surfaces to be ground down by in-expensive methods for strain gage application.

The objective of constructing the aluminum prototype was to provide a validation of the sensor design and FEA model at a low cost (~$1500) relative to the full-scale sensors made from Inconel or Titanium (~ $5500).

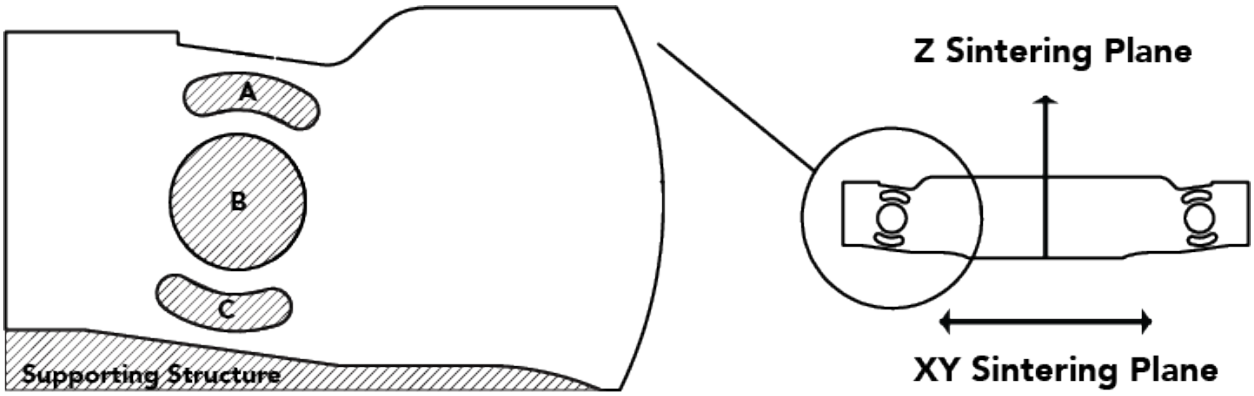

Figure 7.1: The DMLS process deposits thin layers of a metal alloy in powder form. A laser sinters each thin layer to the previous layer in the Z-plane and in the geometry specified for each layer.

7.2 Construction of the Sensor Assembly

Transducer class strain gages (Part No. J2A-13-S047D-350-SP62, 350Ω, Vishay, Shelton, CT) were selected for their small footprint, accuracy, and stability. Gages were applied to sensing surfaces using transducer class adhesive (M-Bond AE-10, Vishay, Shelton, CT) (Figure 7.2). The sensor body was enclosed in a two-part housing were made from Aluminum 7075-T6 Alloy with tensile σ_{yield} = 500 MPa and was hard coat anodized Type III (Apex Anodizing, Portland, OR). The housing was designed to allow the sensor to be mounted to a ski and bindings, provide overload protection to the sensor body, and to be sealed with a water-ingress rating of IP-66. Two printed circuit boards (PCBs) (OSHPark, Portland, OR) (Figure 7.3) were designed for intermediate bridge connections between gages and to interconnect the PCBs to IP-67 rated connectors (HEN.2F.319.XLNP, LEMO, Rohnert Park, CA) used to connect the sensor to a cables leading to the data acquisition system (Figure 7.4). A custom designed flexible printed circuit provided the interconnecting signal bridge between the two PCBs.

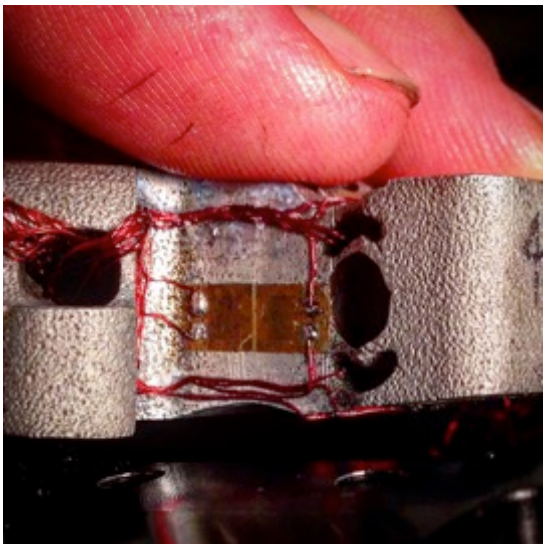

Figure 7.2: Installed strain gages were wired using 134-AWP solid wire coded in polyurethane enamel.

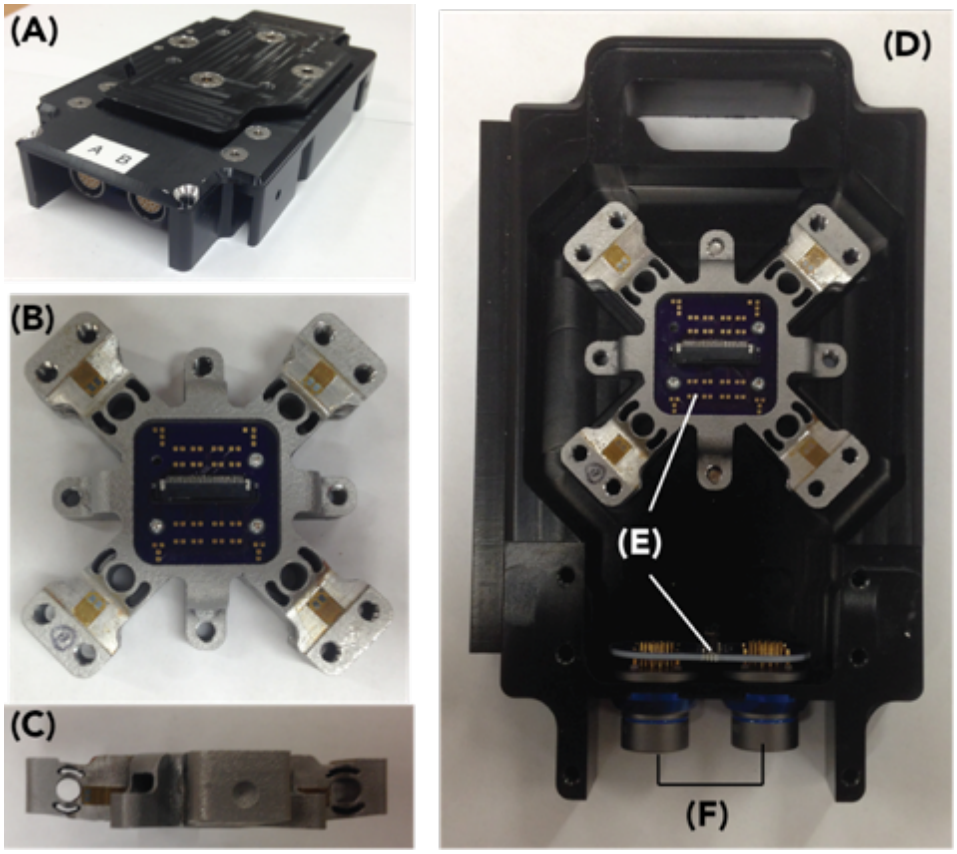

Figure 7.3: (A) Assembled sensor including the IP-66 housing. (B) Top view of sensor body with strain gages and center PCB installed. (C) Side view of sensor body with strain gages installed. (D) Sensor body in the base housing with the interconnecting PCBs (E) and IP-67 receptacles.

7.2.1 *Data Acquisition, Signal Conditioning, and Data Processing*

A Diversified Technical Systems (DTS) Nano Slice 16-bit data acquisition unit is used to provide bridge excitation, signal conditioning, A-D conversion, and data logging (Figure 7.4) (Diversified Technical Systems, Seal Beach, CA) for the strain gages. The unit has an extremely small form factor, which makes it ideal for data logging in biomechanical applications. Each channel from the DTS unit provides its own 5VDC excitation and a sensitivity value, $mV/V_{ex}/EU$, is defined for each channel measured (Figure 7.5). Data is sampled at a pre-selected rate (0.001-250 kHz), filtered through an anti-aliasing filter configured to 1/5 the sampling rate, passed through an analog-to-digital converter, passed through signal conditioning, and recorded in 32 GB of flash memory. Proprietary software, SliceWare™ (DTS, Seal Beach, CA) is used to configure each channel individually to control the signal conditioning and gain settings based on the desired full scale range (R), in engineering units (EU), and the sensitivity, $S_{i=1,\ldots,8}\left(\frac{mV}{V}EU\right)$.

Prior to recording any data, a diagnostics module performs several diagnostic checks including a shunt calibration and verification of the applied excitation voltage. The each bridge can also be biased during this diagnostic check. After data are collected they are downloaded from the DTS to a personal computer for post-processing in Matlab. They are digitally filtered and the calibration matrix is used to transform the *nx8* bridge response vector into an nx6 force vector, where n is the number of sample collected in a given test.

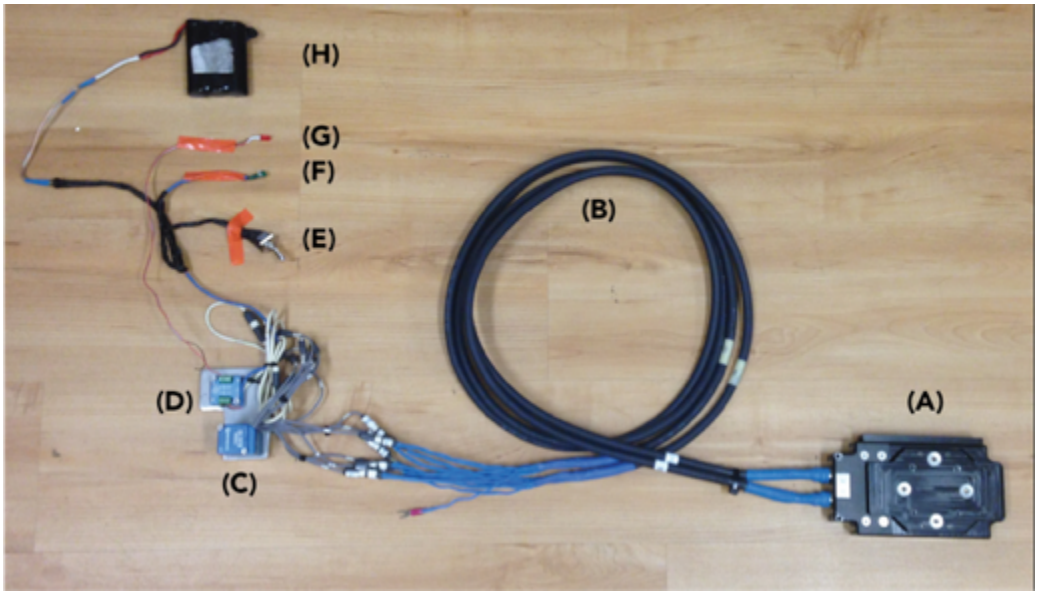

Figure 7.4: The sensor (A) connected by two 14-conductor 7' shielded cables (B) to the DTS Slice NANO DAQ (C). The End of Chain (EOC) (D) supplies power and TTL signals to the DAQ from the 11.1V battery power supply (H) controlled by a power switch (E) and is connected to a power indicator LED (F) and status indicator LED (G).

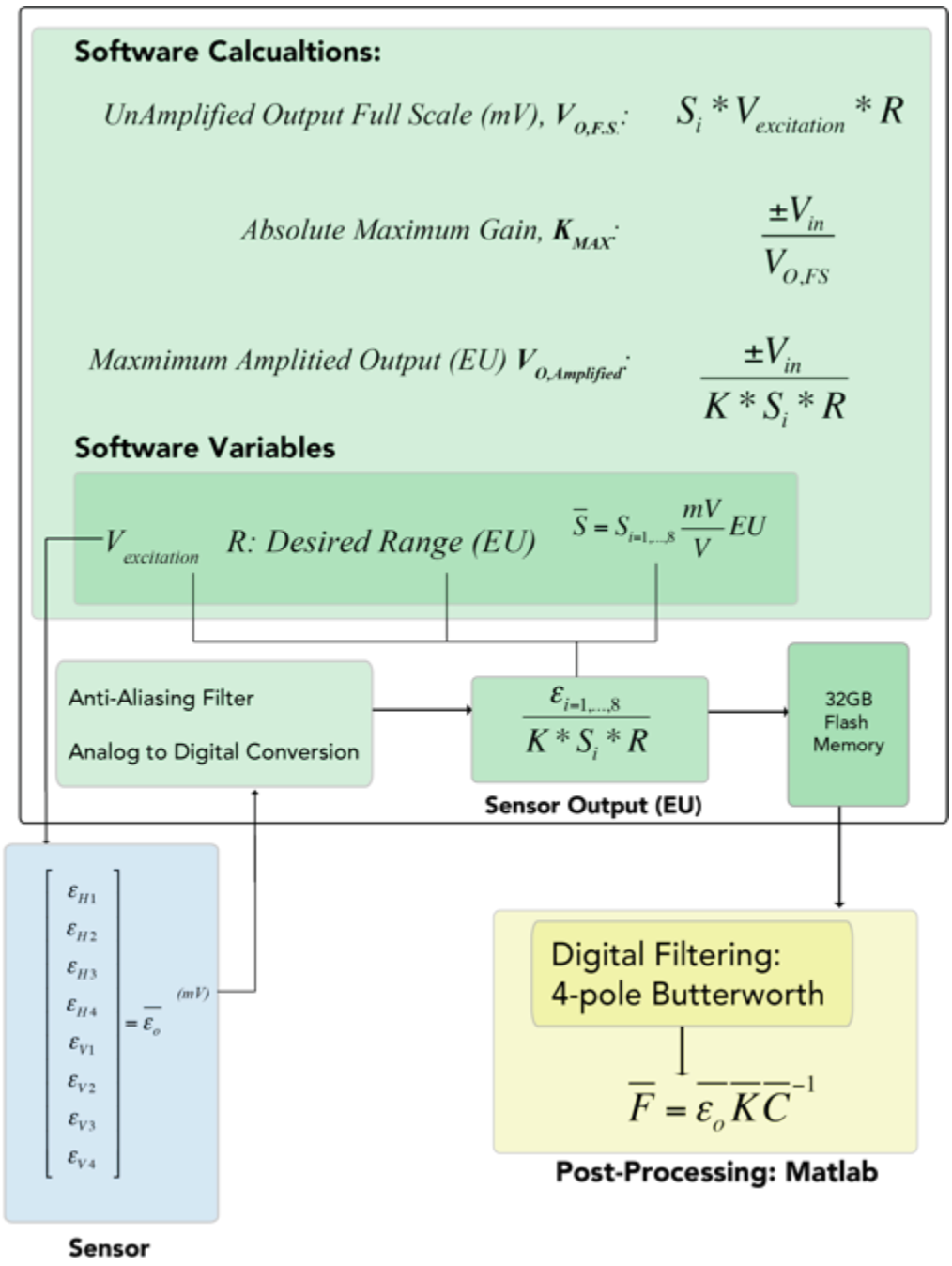

Figure 7.5: The DTS Nano Slice DAQ provides excitation voltage for all eight Wheatstone bridges and signal conditioning, anti-aliasing filtering, A-D conversion, and on-board data logging. Once recording is complete, the raw strain vector is downloaded from the DAQ and post-processed in Matlab where it is digitally filtered and transformed into the nx6 Force vector, where n is the number of samples recorded for a given test.

7.2.2 ***Sensor Calibration***

7.2.2.1 Intra-Bridge Gain Balancing

From Chapter 6.2.2, the transformation matrix, ***K***, performs a summation of the eight individual bridges to convert the raw strain vector from a *1x8* to a *1x6*. If $\mathcal{E}_{Hi}$ and $\mathcal{E}_{Vi}$ represent the response from the horizontal and vertical bridges, respectively, the underlying assumption is that for an applied uniaxial F_Z, M_X, or M_Y, $|\varepsilon_{V1}| = |\varepsilon_{V4}| = |\varepsilon_{V3}| = |\varepsilon_{V4}|$. It follows that for an applied uniaxial F_X, F_X, or M_Z it is assumed that $|\varepsilon_{H1}| = |\varepsilon_{H4}| = |\varepsilon_{H3}| = |\varepsilon_{H4}|$.

In the absence of physical imperfections, as in an FEA model, this is an appropriate assumption. In practice however, the sensitivities of each vertical and horizontal bridge will never be exactly equal to the other bridges due to variation in manufacturing tolerances, imperfections in the material, and gage misalignment, among other factors. To correct for the differences in sensitivities between bridges, the gain applied to each bridge by the signal conditions can be changed to balance the bridges such that the assumptions underlying the transformation matrix *K* will hold for the prototype sensor. The DTS Nano Slice DAQ has software selectable gain settings controlled by the sensitivity, S_i, and the Full-Scale Range, *R*, values that are input into the software during the sensor configuration (Figure 7.6). It was hypothesized that the sensitivity of each bridge, S_i, could be normalized relative to the other bridges with a unique sensitivity value, S_i, which could be used in the Sliceware™ settings to balance the gain between each bridge.

Sensitivity values for the horizontal bridges $S_{H,i}$, were initially set to a nominal value of $S^o_{H,i}$ = 0.005 (mV/V/EU) based on recommendations from DTS engineers. Sensitivity values for the vertical bridges $S_{V,i}$, were initially set to a nominal value of $S^o_{V,i}$ = 0.010 (mV/V/EU).
Following which, a two step loading protocol was performed:

1. A ±500N F_Z load was applied to measure the response $\mathcal{E}_{V1\text{-}V4}$ to an F_Z defined as $C_{V,i}$.

2. A ±50Nm M_Z load was applied to measure the response $\mathcal{E}_{H1\text{-}H4}$ to an Mz, defined as $C_{H,i}$.

Two single axis tension-compression load cells (Model: WNC-500-460, Interface, Scottsdale, AZ, Resolution ±0.008N) were used as reference sensors to measure the applied F_Z and M_Z loads. Data were sampled from the reference sensors and the prototype sensor at 1kHz using the DTS DAQ. Values for $C_{H,i}$ and $C_{V,i}$ and their means, $\overline{C_H}$ and $\overline{C_V}$, were calculated using equations (7.1 & 7.2).

(eqn 7.1) $$C_{H,i} = \frac{\max(\varepsilon_{H,i})}{\max(M_z)}, \quad \text{for } i = 1\text{-}4$$

(eqn 7.2) $$C_{V,i} = \frac{\max(\varepsilon_{V,i})}{\max(F_z)}, \quad \text{for } i = 1\text{-}4$$

The percent deviation of the bridge response from the mean sensitivity of each bridge was calculated (Table 2). To normalize the output of each bridge such that each horizontal and vertical bridge has the same out put for a given load, the sensitivity values used in Sliceware™ were scaled (eqn. 7.3) by the scaling coefficient for a given bridge, γ_{Hi} and γ_{Vi} (eqn. 7.4).

(eqn. 7.3) $$S_{H,i} = \gamma_{H,i} * S^o_{H,i} \quad \text{and} \quad S_{V,i} = \gamma_{V,i} * S^o_{V,i}, \quad \text{for } i = 1\text{-}4$$

where $S^o_{H,i}$ = 0.005 (mV/V/EU) and $S^o_{V,i}$ = 0.010 (mV/V/EU).

(eqn. 7.4) $$\gamma_{H,i} = 1 - \frac{C_{H,i} - \overline{C_H}}{\overline{C_H}} \quad \text{and} \quad \gamma_{V,i} = 1 - \frac{C_{V,i} - \overline{C_V}}{\overline{C_V}}, \quad \text{for } i = 1\text{-}4$$

7.2.3 *Uniaxial Calibration of Prototype Sensor*

Positive and negative uniaxial loads up to 50% of full scale of the aluminum sensor ($F_{X,Y}$ = ±100N, F_Z = ±500N, $M_{X,Y,Z}$ = ±25Nm) were applied to the sensor about it's origin using custom fixtures and a servo-hydraulic tensile load frame (MTS, Eden Prairie, MN). Two single axis tension-compression load cells (Model: WNC-500-460, Interface, Scottsdale, AZ, Resolution ±0.008N) were used as reference sensors to measure the applied loads. Digital calipers (Mitutoyo, Aurora, IL, Resolution ±0.01mm) and a digital inclinometer (Digital Protractor, Pro 360, Resolution ±0.1°) were used to ensure that the custom fixtures applied loads orthogonally to the axes of the six-axis transducer. Data from the eight strain bridges were sampled at 1kHz using the DTS Slice Nano DAQ. Data were filtered using a low-pass 4-pole Butterworth filter with a cutoff frequency of 100 Hz. The voltage response from the sensor was transformed and converted to a force vector in Matlab during post-processing using equations

(1.1)-(1.7), Chapter 6.2.2. Fixtures for applying all six load components and moments are shown in Figure 7.6.

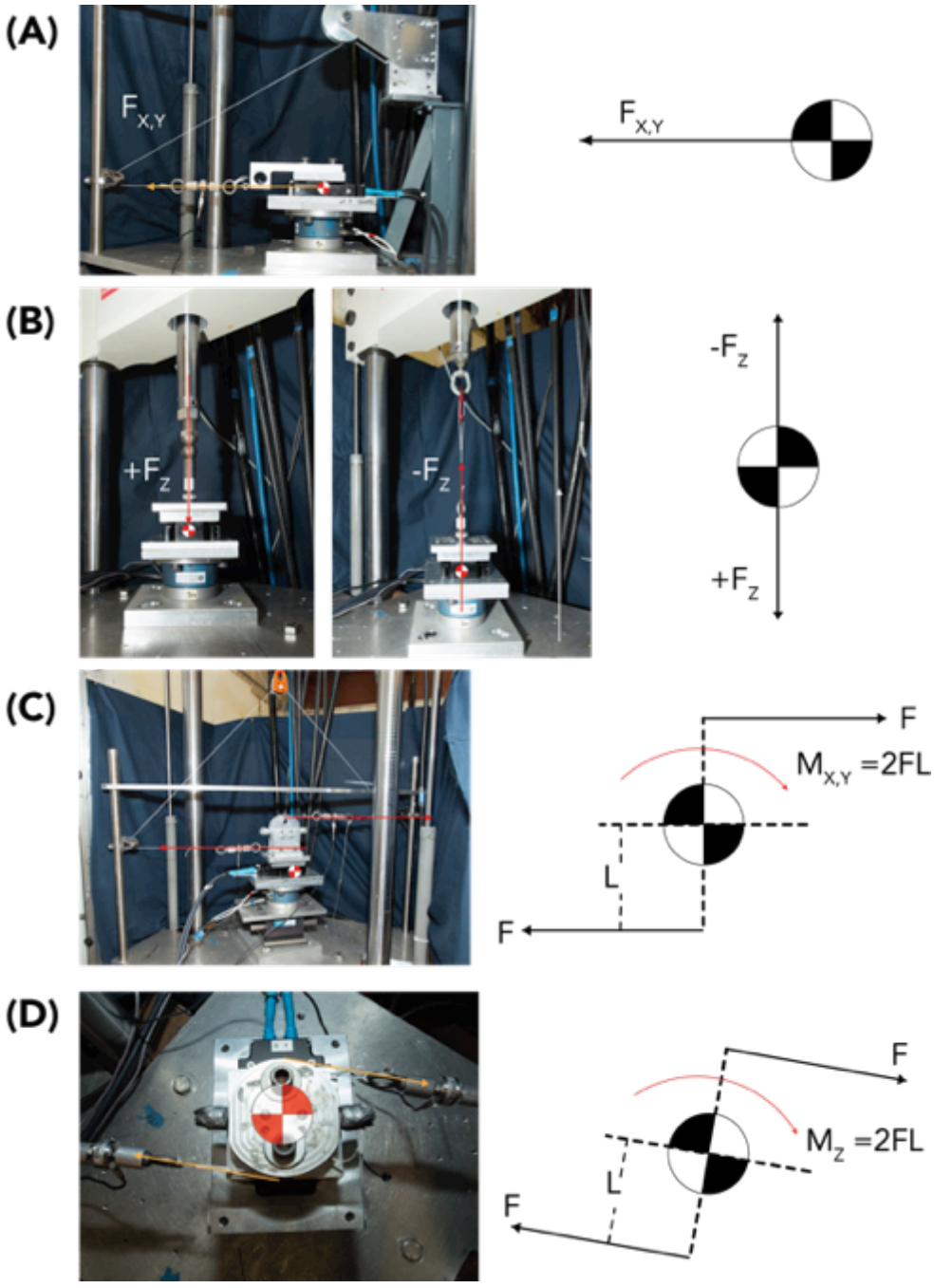

Figure 7.6: Fixtures used for the calibration of the six-axis force-torque transducer. (A) Application of shear loads, $F_{X,Y}$ (B) Application of tension and compression loads F_Z (C) Application of $M_{X,Y}$ moments (D) Application of M_Z moments.

7.2.4 *Combined Loading*

To evaluate the performance of the sensor under combined loading where the loading rates are random and non-orthogonal to the axes of the sensor, a fixture was constructed such that two force vectors could be applied to the sensor and measured using the same reference sensors as those used in the calibration (Figure 7.7). Four configurations of load combinations were tested three times each 1) {+F_1, 0} 2) {0, +F_2}, 3) {+F_1, +F_2}, and 4) {+F_1, -F_2}. The applied loads measured by F_1 and F_2 were used to sum the six-load components (Eqns. 7.5-7.10) about the sensor origin for comparison to loads calculated by the prototype sensor calculated loads.

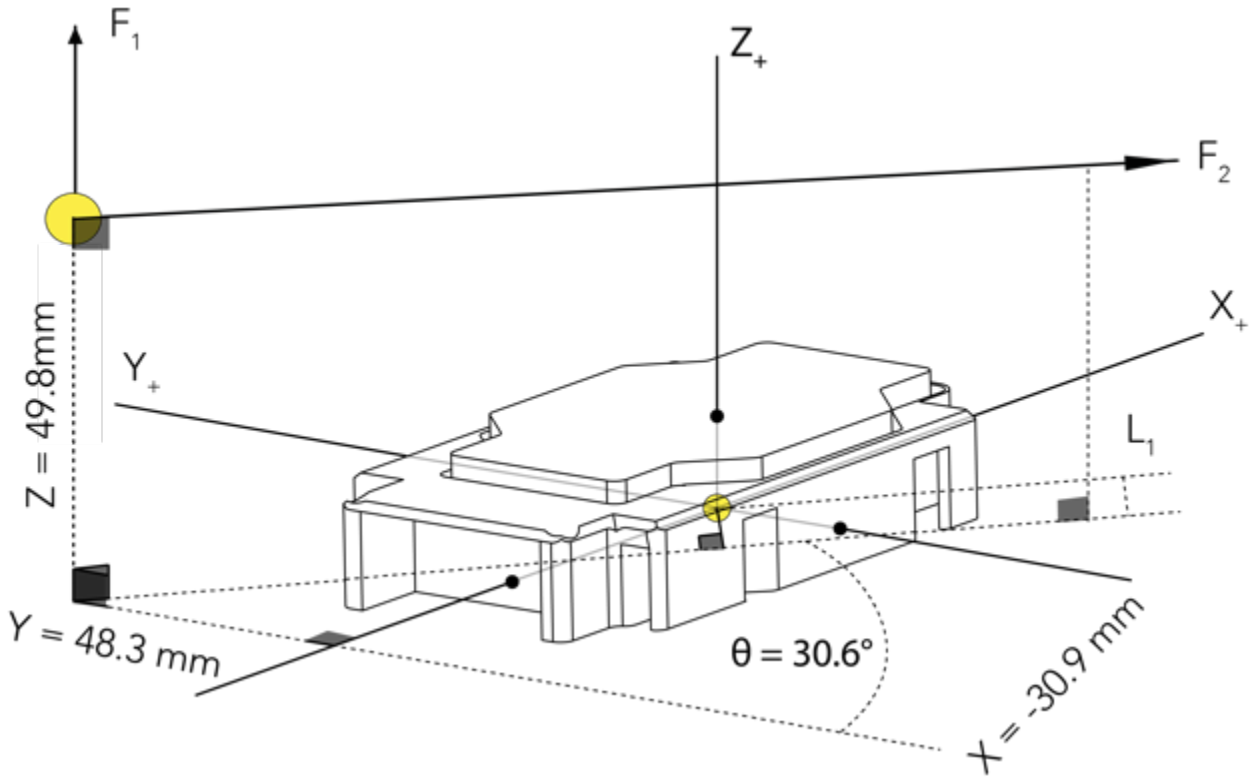

Figure 7.7: Free body diagram of the non-orthogonal combined loads applied to the sensor.

(7.5) $\sum F_X = F_2 \sin\theta$

(7.6) $\sum F_Y = F_2 \cos\theta$

(7.7) $\sum F_Z = F_1$

(7.8) $\sum M_X = F_1 X$

(7.9) $\sum M_Y = F_1 Y$

(7.10) $\sum M_Z = F_2 L_1$

7.3 **Results**

7.3.1 *Geometry of the Prototype Sensor*

The aluminum prototype sensor was constructed using the DMLS process. However, the features shown in Figure 7.1 were slightly skewed resulting from the lack of supporting structures used during construction. For example the hole-B (Figure 7.1) was 0.3mm out of round. The slots A and C (Figure 7.1) were asymmetric; the end of the slot closest to the outside of the arm was within tolerance. However, the end of the slot on the interior part of the arm but deviated from tolerance by up to 0.15mm on the end of the slot. No significant deviations in geometry between arms were measured.

7.3.2 *Strain Gage Placement*

Design variables from the FEA optimization analysis (Chapter 6.3.2) included the optimal location and permissible tolerances for strain gage placement on the sensor. All gages were placed within tolerances with the largest deviation being 0.13mm from the target location (with a maximum allowable deviation of ±0.25mm).

7.3.3 *Intra-Bridge Gain Balancing: Results*

The percent deviation from the mean sensitivity for horizontal and vertical bridges is tabulated in Table 7.1. The vertical bridges required larger scaling coefficients than the horizontal bridges. This was due to the skewed geometry of the sensitivity slots and holes reported in Section 7.3.1.

Table 7.1: Percent deviation and scaling coefficient, [%, $\gamma_{H,V,i}$] $C_{H,i}$ from $\overline{C_H}$ and of $C_{V,i}$ from $\overline{C_V}$ from each arm.

Bridge	**Arm 1**	**Arm 2**	**Arm 3**	**Arm 4**
Horizontal	[0.2%, 1.0]	[0.2%, 1.0]	[0.6%, 0.99]	[0.6%, 0.99]
Vertical	[-2.9%, 1.03]	[10.8%, 0.89]	[-12.5%, 1.12]	[-4.6%, 1.05]

7.3.4 *Uniaxial Calibration of Prototype Sensor: Results*

The response of the prototype sensor to each of the six uniaxial loads was linear (Figure 7.8). A linear regression on the applied loads vs. the calculated loads for each of the six loads had a goodness of fit greater than $R^2 > 0.999$, $p < 0.001$. RMSE between the applied and calculated uniaxial loads did not exceed 0.2% of the applied calibration loads.

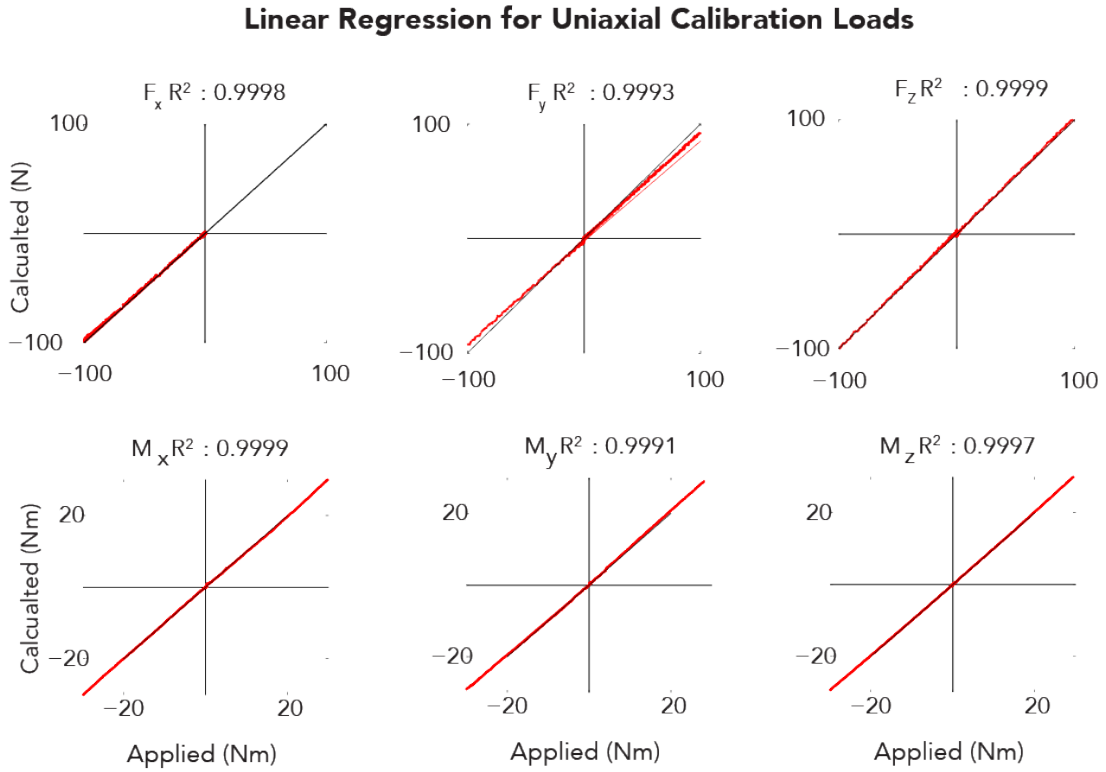

Figure 7.8: Results of a linear regression for uniaxial calibration loads. R2 values reflect the goodness of fit of a regression on the applied uniaxial calibration load to the load predicted by the sensor.

7.3.5 *Combined Loading Trials: Results*

The RMSE for all axes were extremely small for 12 combined loading trials. The average and standard deviation RMSE between the applied loads measured by the reference sensors and the prototype sensor is tabulated in Table 7.2 for 12 trials of combined loads. The maximum absolute RMSE was F_Z =5.69±2.01 N. The addition of F_1 to the combined loading increased the RMSE for F_Z. This is likely a result of the reference load, F_1, not being applied perfectly parallel

to the XY plane of the sensor, producing a small Z component that was not measured by the reference sensors, F_1 and F_2. A linear regression on the applied loads vs. the calculated loads for each of the six loads had a goodness of fit greater than $R^2 > 0.96$, $p < 0.001$. A time history of the relative error between the prototype sensor and the applied loads for an exemplar combined loading trial (Figure 7.9).

Table 7.2: Root Mean Squared Error (RMSE) with Average ± one Standard Deviation in EU & percent of full-scale of Root Mean Squared Error (RMSE) for 12 combinations of non-orthogonal loading with various combinations from the F_1 and F_2 loads.

RMSE	$\mathbf{F_X}$	$\mathbf{F_Y}$	$\mathbf{F_Z}$	$\mathbf{M_X}$	$\mathbf{M_Y}$	$\mathbf{M_Z}$
(EU: N, Nm)	1.47±0.65	1.3±0.35	5.69±2.01	0.2±0.09	0.17±0.13	0.07±0.70
% Full Scale	0.008%	0.007%	0.063%	0.071%	0.061%	0.028%

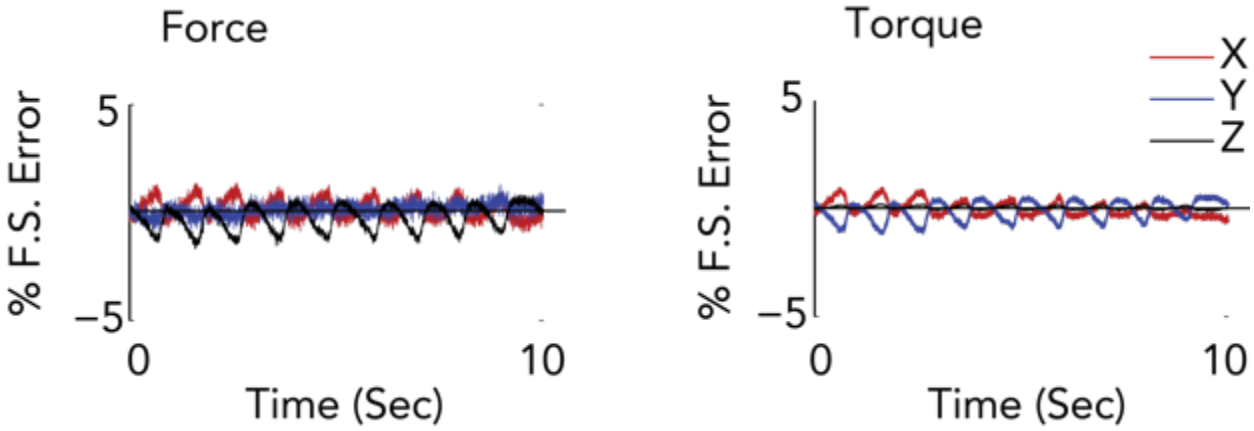

Figure 7.9: The percent full-scale error for an exemplar loading trial for forces (left) and torques (right).

7.3.6 *Comparison of the Prototype and FEA Model*

A comparison of the FEA model to performance of the prototype sensor can be done using several metrics. Each column of $\boldsymbol{C_P}$ and $\boldsymbol{C_{FEA}}$, the calibration matrix from the prototype and FEA model, respectively, was normalized by its diagonal component and the relative magnitude of each element of $\boldsymbol{C_P}$ is plotted against the same element of $\boldsymbol{C_{FEA}}$ (Figure 7.10). The diagonal elements are all significantly larger than the off diagonals, though $\boldsymbol{C_P}$ has off-diagonal

elements that appear to be larger than the same corresponding elements of $\boldsymbol{C_{FEA}}$, namely C_{12}, C_{16}, C_{24}, C_{26}, C_{41}, C_{42}, and C_{51}. The largest of these elements, C_{51}, has a magnitude of 15.5% that of it's corresponding diagonal element, C_{11}. These elements do not appear to affect the accuracy of the sensor calibration.

Several studies have proposed using the condition number of a sensors calibration matrix as measure of sensor performance [57–59]. The condition number of a matrix is the ratio of the largest and smallest values from the singular value decomposition of a matrix[81,83]. It can also be expressed as the product of the *L2* norm of the matrix and the *L2* norm of it's inverse, $Cond(C) = \|C\|\|C^{-1}\|$ where $\|C\|$ is the *L2* norm, or the Euclidian norm, $\|C\|_2 = \sqrt{\sum_{i=1}^{n} x_i^2}$. The smaller the condition number, the more 'well conditioned' the matrix C is for solving a linear system of equations, such as $\boldsymbol{CF = \mathcal{E}}$.

A comparison of the calibration matrices calculated from the prototype sensor, $\boldsymbol{C_P}$, and the FEA model, $\boldsymbol{C_{FEA}}$, with their corresponding condition numbers is shown in Table 7.3. Using the condition number criterion $\boldsymbol{C_P}$, from the prototype sensor, is more well conditioned than $\boldsymbol{C_{FEA}}$ [57–59].

Table 7.3: Comparison of calibration matrices calculated from the prototype sensor and the FEA model.

$$\overline{C_P} = \begin{bmatrix} 0.9649 & -0.1696 & 0.0134 & 0.0022 & -0.0013 & -0.0174 \\ -0.0174 & 0.9449 & 0.0027 & -0.0029 & 0.0000 & 0.0000 \\ -0.0571 & 0.0093 & -0.5243 & 0.0015 & 0.0012 & -0.0004 \\ -0.0827 & -0.0890 & 0.0206 & -0.0186 & 0.0007 & 0.0000 \\ -0.1884 & 0.0705 & -0.0191 & 0.0010 & -0.0173 & -0.0002 \\ -0.0187 & 0.0796 & 0.0023 & -0.0003 & 0.0000 & 0.0101 \end{bmatrix} \frac{mV}{EU} \qquad \overline{C_{FEA}} = \begin{bmatrix} 3.1547 & -0.0522 & 0.0006 & -0.0003 & 0.0004 & -0.0002 \\ 0.0107 & -2.7963 & -0.0007 & 0.0004 & 0.0000 & -0.0002 \\ 0.0113 & -0.0018 & 0.5356 & 0.0001 & -0.0001 & 0.0000 \\ -0.0013 & -0.0014 & 0.0026 & 0.0156 & 0.0003 & 0.0000 \\ 0.047 & -0.0029 & 0.0015 & 0.0001 & -0.0164 & 0.0000 \\ 0.0157 & -0.0011 & -0.0011 & 0.0000 & 0.0000 & -0.0164 \end{bmatrix} \frac{\mu\varepsilon}{EU}$$

$Cond(C_P) = 105.4$ $\qquad$ $Cond(C_{FEA}) = 192.8$

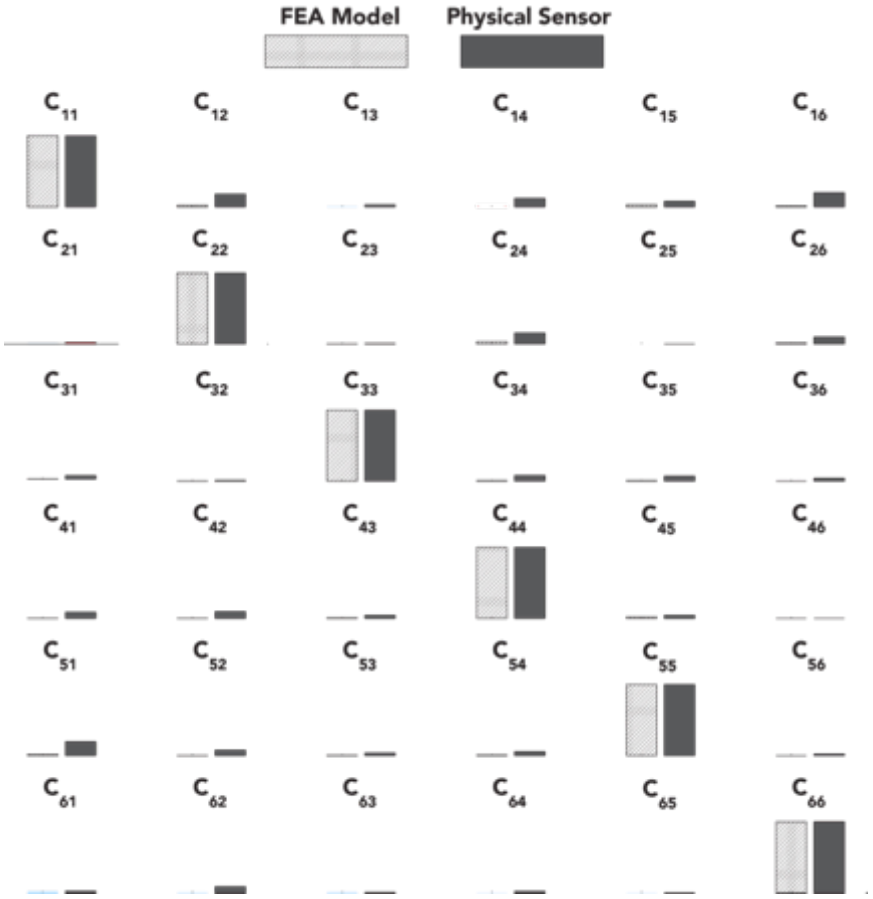

Figure 7.10: Each element of the Calibration Matrices from calculated from the FEA model (Figure 6.7 D) and the physical sensor was normalized by its diagonal component, C_{ij}/C_{ii}. The magnitude of each diagonal component, $C_{ii}/C_{ii} = 1$. The magnitude of each normalized element C_{ij} (unit less) from both calibration matrices is plotted against each other for comparison of the calibration matrices calculated from the FEA model and the prototype sensor.

Both matrices were used calculate loads with RMSE values (comparing the applied vs. calculated loads) less that 0.1% full scale for all axes under uniaxial loading. Under combined loading, $\boldsymbol{C_{FEA}}$ had lower RMSE values than $\boldsymbol{C_P}$, despite having a larger condition number. However, the RMSE values for both $\boldsymbol{C_{FEA}}$ and $\boldsymbol{C_P}$ fall below the maximum permissible values of $RMSE_i < 5\%$, for $i = 1\text{-}6$.

However, a comparison of the RMSE values in Table 6.12 and Table 7.2 is somewhat nebulous because they are not calculated from trials using the same input data. This only provides a measure of the precision between $\boldsymbol{C_{FEA}}$ and $\boldsymbol{C_P}$ but not their accuracy relative to a known reference system.

To quantify their accuracy and allow for a direct comparison of the performance $\boldsymbol{C_{FEA}}$ and $\boldsymbol{C_P}$, an additional analysis was performed. The reference sensor signal from a combined loading trial reported in section 7.3.5 was down sampled from 1000 Hz to 2 Hz. The down sampled signal was comprised of a *50x6* load vector, $\boldsymbol{F=\{F_X, F_Y, F_Z, M_X, M_Y, M_Z\}}$. $\boldsymbol{F}$ was imported into the FEA model was used as a forcing function input to the FEA model and the corresponding strain response from each of the 50 load steps was exported into Matlab and used with $\boldsymbol{C_{FEA}}$ to predict the input loads (Figure 7.11).

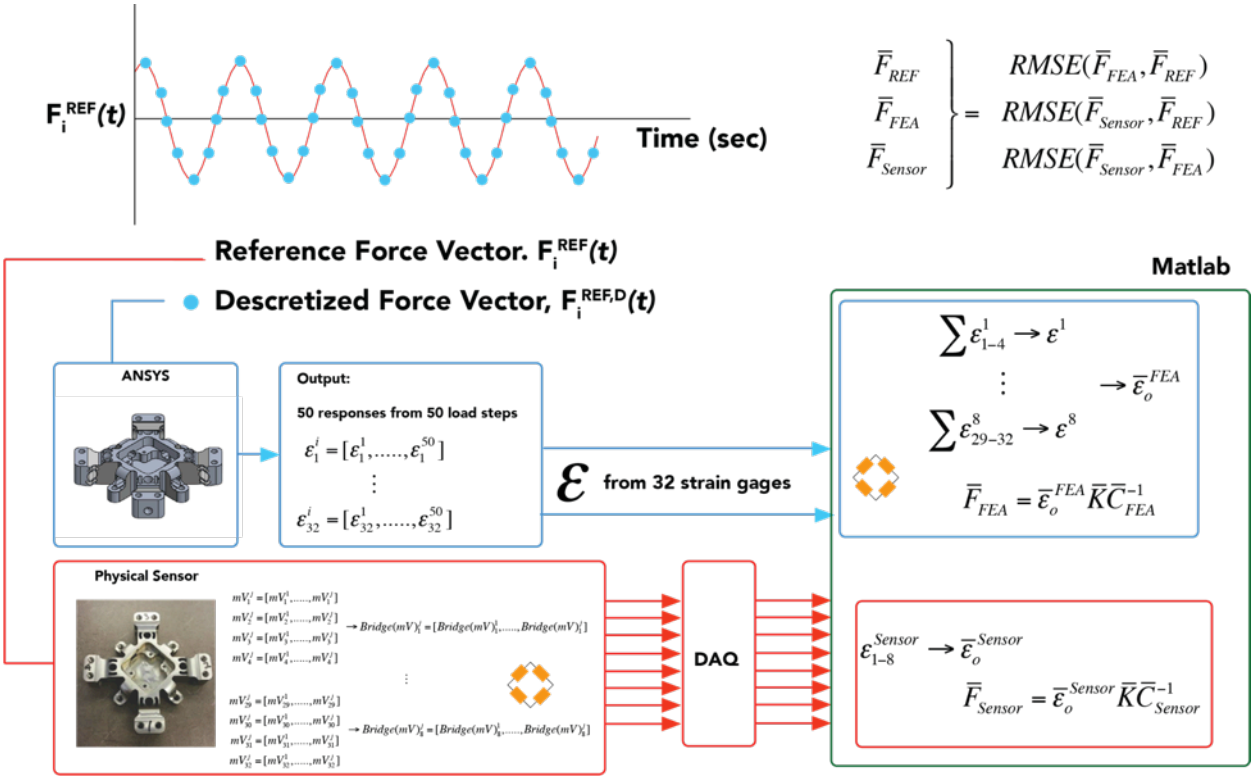

Figure 7.11: A Flow Chart showing how the same load data was applied to the physical sensor, and the FEA model. The strain response from both the FEA model and the sensor were used to calculate the applied loads from the same reference force signal. The RMSE was then calculated.

RMSE values, comparing the loads calculated by the senor to the loads measured by the reference sensors, loads calculated by the FEA model to the applied loads, and loads calculated by the FEA model to loads calculated by the sensor are tabulated in Table 7.4 for the same applied reference load .

The FEA model and prototype sensor were in very good agreement, showing good precision of both $\boldsymbol{C_{FEA}}$ and $\boldsymbol{C_P}$. The FEA model and the prototype sensor were both in very good agreement with the reference applied loads, providing a strong validation of the FEA model and the prototype sensor to the same reference system. A time history of the applied loads compared to the loads predicted by the prototype sensor and by the FEA model is shown in Figure 7.12.

Table 7.4: Comparison of the prototype sensor performance to the FEA model and the reference applied loads. RMSE tabulated in EU and percent of full scale

RMSE	**Sensor vs. Applied**	**FEA vs. Applied**	**FEA vs. Sensor**
F_X [N, % F.S.]	[1.70 N, 0.01%]	[0.24 N, 0.00%]	[1.57 N, 0.01%]
F_Y [N, % F.S.]	[1.11 N, 0.01%]	[0.41 N, 0.00%]	[0.88 N, 0.00%]
F_Z [N, % F.S.]	[3.74 N, 0.04%]	[4.15 N, 0.05%]	[5.06 N, 0.06%]
M_X [N, % F.S.]	[0.13 Nm, 0.05%]	[0.20 Nm, 0.07%]	[0.24 Nm, 0.09%]
M_Y [N, % F.S.]	[0.19 Nm, 0.07%]	[0.13 Nm, 0.05%]	[0.23 Nm, 0.08%]
M_Z [N, % F.S.]	[0.36 Nm, 0.14%]	[0.00 Nm, 0.00%]	[0.04 Nm, 0.02%]

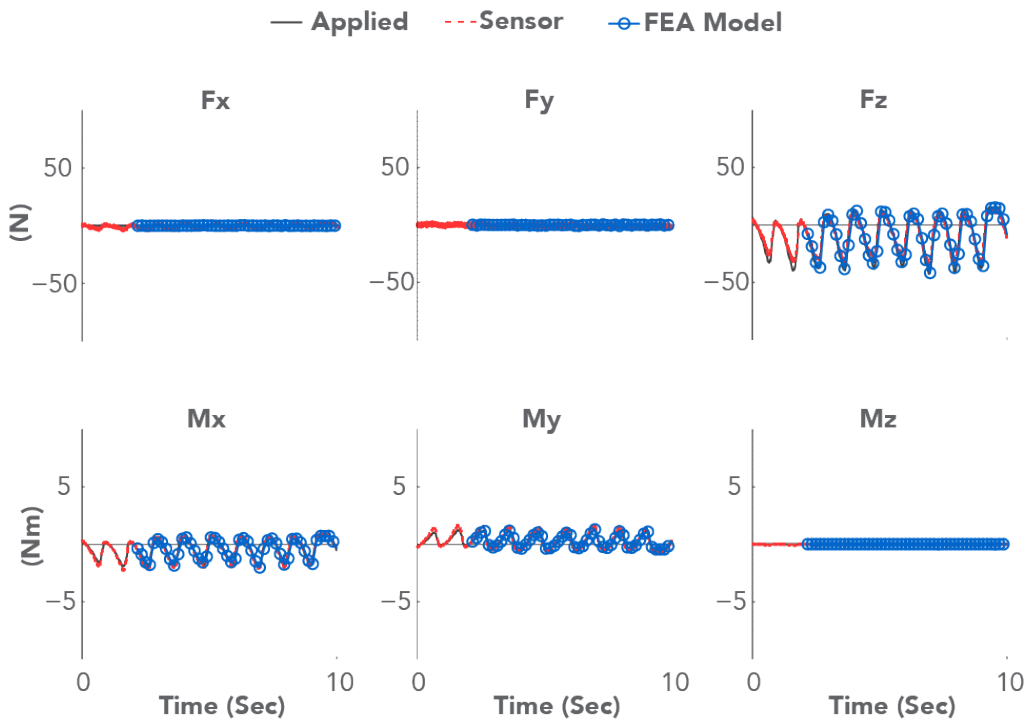

Figure 7.12: Time-history of an exemplar trial of the six load components applied by the reference system, calculated by the physical sensor, and predicted by the FEA model.

7.4 Calibration of Full Scale Sensors

Calibration of two full-scale Inconel six-axis force transducers was performed using the same methodology described in Section 7.2.3. Linearity, accuracy, and hysteresis were all within specified limits. The experimentally determined calibration matrices of both sensors numbers of both sensors are shown in Figure 7.13. The condition number for $C^1 = 96.1$, and $C^2 = 152.6$. An exemplar trial of combined loading is shown in Figure 7.14. Full-scale sensors were also validated for water ingress testing by submerging them in 0.6m of ice water for one hour while recording data to verify no internal leaks or shorts in the circuitry.

$$C^1 = \begin{bmatrix} -9.51 & -2.74 & 0.17 & 0.03 & 0.14 & 0.00 \\ -2.55 & -16.32 & 0.03 & 0.19 & 0.06 & 0.03 \\ -1.38 & -0.52 & 12.07 & 0.01 & 0.06 & 0.00 \\ 0.31 & -0.07 & -0.06 & -0.29 & 0.07 & -0.01 \\ -0.01 & -0.29 & -0.51 & 0.07 & -0.28 & 0.01 \\ -0.02 & 0.00 & -0.12 & 0.01 & -0.00 & 0.18 \end{bmatrix} \quad C^2 = \begin{bmatrix} 9.51 & -1.21 & 0.51 & 0.03 & -0.12 & 0.00 \\ 2.07 & -7.23 & 0.08 & 0.08 & -0.04 & 0.00 \\ -1.08 & 0.53 & 11.87 & 0.00 & 0.00 & 0.00 \\ 0.29 & 0.08 & 0.10 & -0.28 & 0.08 & 0.00 \\ 0.03 & 0.33 & 0.47 & 0.08 & -0.30 & 0.00 \\ 0.00 & 0.00 & -0.08 & 0.00 & -0.00 & 0.09 \end{bmatrix}$$

Figure 7.13: Calibration matrices for both full-scale sensors.

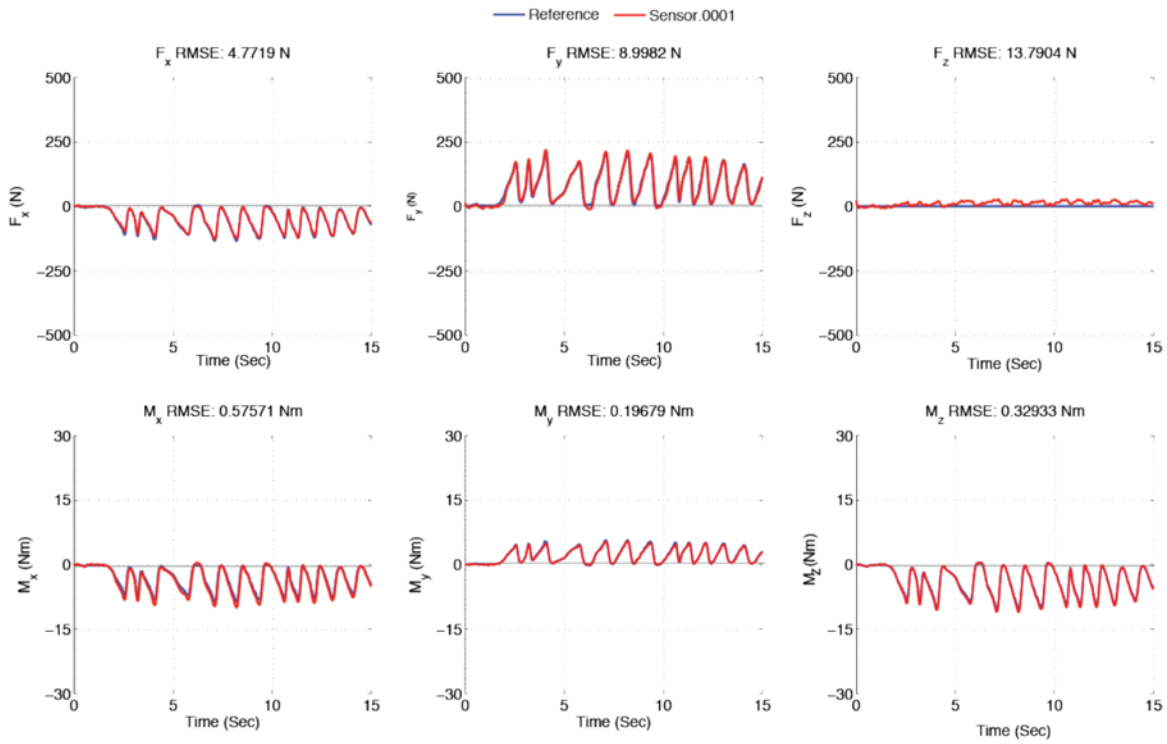

Figure 7.14: An exemplar trial of combined loading of a full-scale Inconel six-axis force transducer. Maximum RMSE was 1.7% of full-scale.

7.5 Discussion

From the studies available that report the accuracy of all six load components of the sensors studied, the errors measured from the FEA model and prototype sensor in the current study are of equal or lesser magnitude[24,59,71,73,90] and also satisfy the performance requirements outlined in Chapter 6.2.1. However, these studies often only report the error of the sensor output relative to the known input load during calibration and do not report on the accuracy of non-orthogonal combined loads applied to the sensor as has been done here. One possible explanation for why the condition number of each matrix was not correlated to the RMSE from the combined loading trials is that studies rarely, if ever, rigorous validations that include combined loading trials.

The bulk of literature on multi-axis transducer design utilizes the condition number criterion as an optimization parameter and a measure of sensor performance[57–59,74,81–83,91]. During the design and optimization of a sensor, it is computationally expensive to use the condition number, as it requires the full calibration matrix to be calculated for every design iteration. When used for the evaluation of multi-axis sensor performance, there was no correlation between the condition numbers of the calibration matrices of the FEA model and the prototype sensor and the RMSE calculated from the model and sensor. Nakamura[92] proposed using strain gage sensitivity, force sensitivity and minimal stiffness as design criteria. Further more, the performance of the FEA model and the sensor design under evaluation reported in the current study confirm that the design criterion first introduced by Kang[73] can be used to effectively optimize sensors without solving for the complete calibration matrix every design iteration.

It was necessary to perform a more rigorous validation of the calibration, using combined loads, than is performed by most studies. In contrast, many studies reporting on the design of multi-axis sensors, perform the optimization routines and derive the calibration matrix using analytical or FEA models, but do not follow through with an analytical or experimental comparison of the model to known applied loads[58,62,64,66]. Some studies perform a uniaxial experimental calibration of their sensor but rely solely on the elements of the calibration matrix to elucidate the accuracy of their sensor design[26,58] or the performance of only a select few axes is reported[62,64,74]. Other studies have reported the precision, the relative error between their experimental sensor and the analytical or FEA model[73], but fail to provide an estimate of accuracy, or the relative error between the experimental sensor performance compared to a

reference system. It has also been observed that several studies do not apply pure couples to calibrate the six axis sensors to torque components[64,75,76] which also will significantly affect the accuracy of the calibration matrix under combined loading.

7.6 **Conclusion**

A six-axis force and torque transducer was designed and optimized using an FEA model and a relatively new optimization criterion. A prototype sensor was constructed and calibrated. The precision and accuracy of the prototype sensor is sufficient to validate both the FEA model and the sensor design as well as satisfy the accuracy requirements for the proposed application of measuring ground reaction forces of skiers on snow.

Chapter 8. The XSENS MVN Biomechanics Motion Capture Suit

8.1 Introduction

The XSENS MVN Biomechanics suit will be used to measure the whole body kinematics of skiers. When used in conjunction with the force sensors described in Chapter 7, the forces transmitted from the snow, through the ski-binding-boot system to the lower leg and knee can be calculated using an inverse dynamics model.

The purpose of this chapter is to introduce how the XSENS MVN Biomechanics Suit (referred to hereafter as MVN) measures three dimensional body motion, it's capabilities, limitations, and why it was selected over other motion capture systems for this research.

8.2 Optical Motion Capture Systems

Optical systems have been the gold standard for 3D motion capture for decades. Optical based systems initially consisted of video cameras tracking markers placed on boney landmarks of interest and tracking the markers position, frame by frame (Figure 8.1).

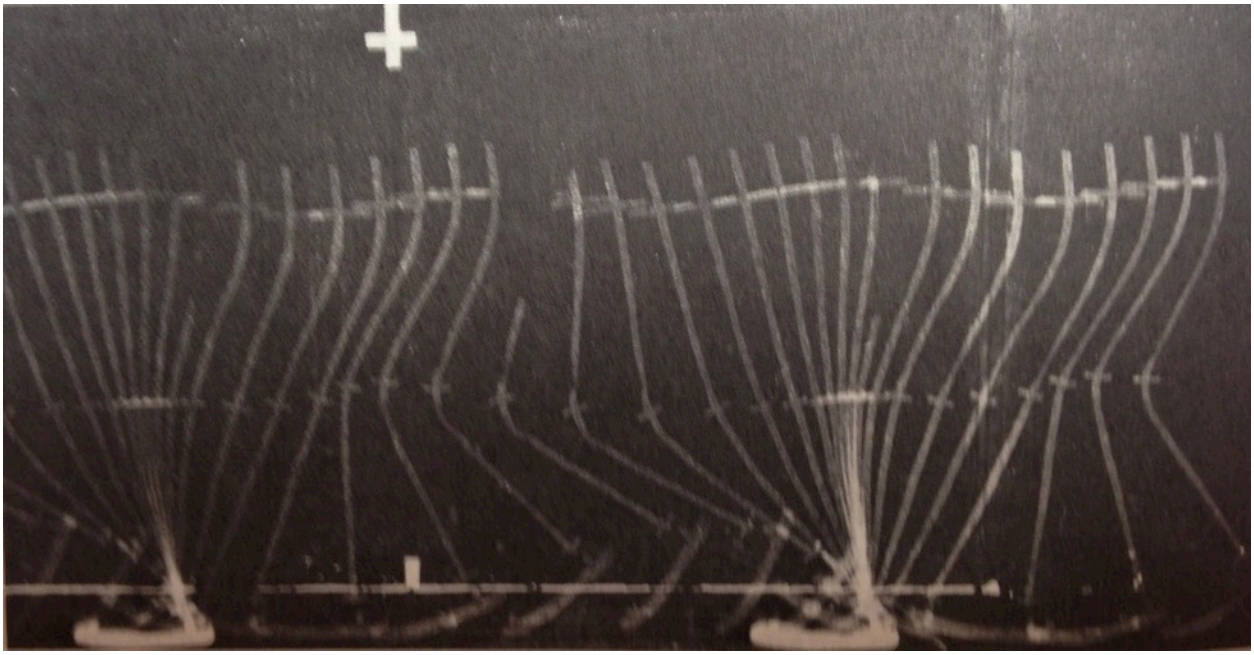

Figure 8.1: Image from David Winter's Textbook[93] on Biomechanics showing early optical methods capturing a single stride using multiple exposures and a strobe light in a dark room.

Multiple cameras can be added to increase the capture volume and measure three dimensional kinematics. Infrared optical systems such as Vicon and Qualysis have become the new gold standard for 3D motion capture in a laboratory setting. These camera systems track reflective markers attached to anatomical landmarks of interest, simplifying data-processing. Optical based systems can achieve extremely high levels of accuracy to the degree of being able to calculate the instantaneous center of rotation and translation of the knee.

However they are not without their limitations. Error can be introduced to the measurement through markers that are placed on clothing and skin that can move relative to the rigid bones they are intended to measure. These systems may be well suited for gait laboratories. However the subject must remain in view of the cameras within the capture volume, making these systems ill-suits for application in the current study.

8.3 XSENS MVN Biomech Suit

The XSENS MVN Biomech Suit utilizes 17 Inertial Measurement Units (IMUs) to track the 3D motion of 23 motion segments of the human body. IMUS consist of nine sensors; tri-axial linear accelerometers, tri-axial rate gyroscopes, and tri-axial magnetometers (Figure 8.2). Using the linear accelerations, measured angular rates, and measurement of the ambient magnetic field, the orientation, position, and 3D motion of the IMU can be calculated using the sensor fusion, where multiple types of sensors are used to estimate a given parameter. Seventeen IMUs are used in the MVN suit (Figure 8.3). are held in specific anatomical locations by a lycra suit worn by the subject to track measure the 3D motion of 23 motion segments. However, the position of each IMU is still somewhat arbitrary and not necessarily in an orientation that is anatomically related to the motion segment it is intended to measure. This problem is overcome by having the subject stand in several static postures from which the MVN Studio software can apply the orientation of each IMU as a baseline orientation for each motion segment.

The length of each motion segment is scaled from anthropometric data using the twelve anatomic measurements taken of the subject (Figure 8.5). The MVN model is constructed using the scaled motion segment lengths and the locations of each IMU (Figure 8.5). The model calculates the 3D motion of each motion segment relative to its own local coordinate system that is directly measured, as well as the global coordinate system (Figure 8.6).

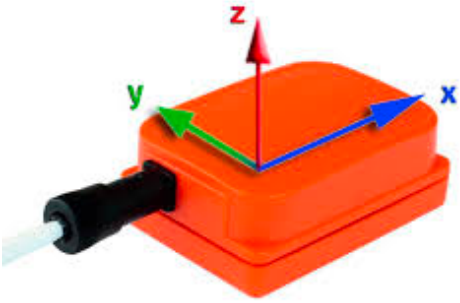

Figure 8.2: One of 17 IMUs used in the MVN (image reproduced from the XSENS MVN Users Manual, Rev. I).

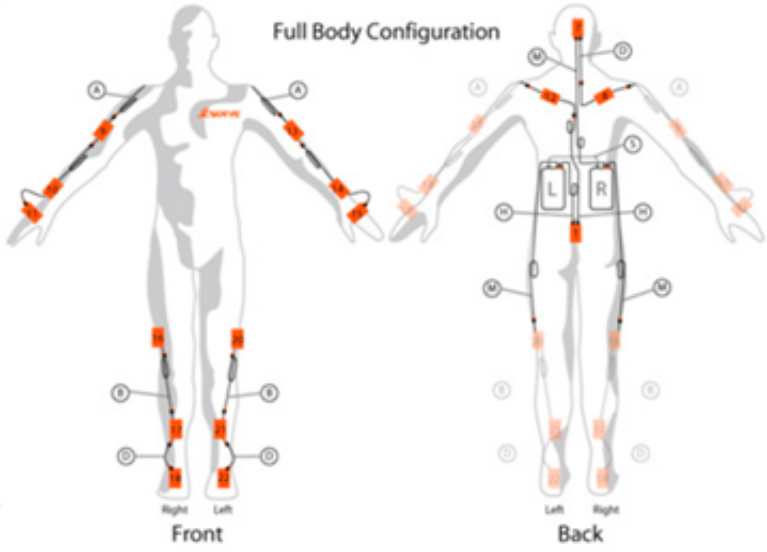

Figure 8.3: Location of the 17 IMRs in the MVN. (image reproduced from the XSENS MVN Users Manual, Rev. I)

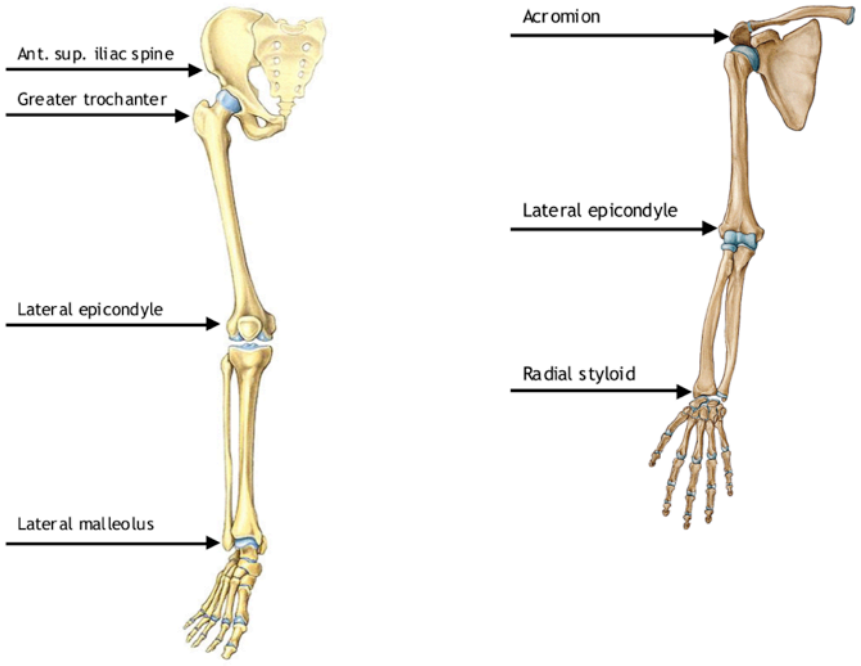

Figure 8.4: Exemplar anatomical measurements used for scaling the MVN model. (image reproduced from the XSENS MVN Users Manual, Rev. I).

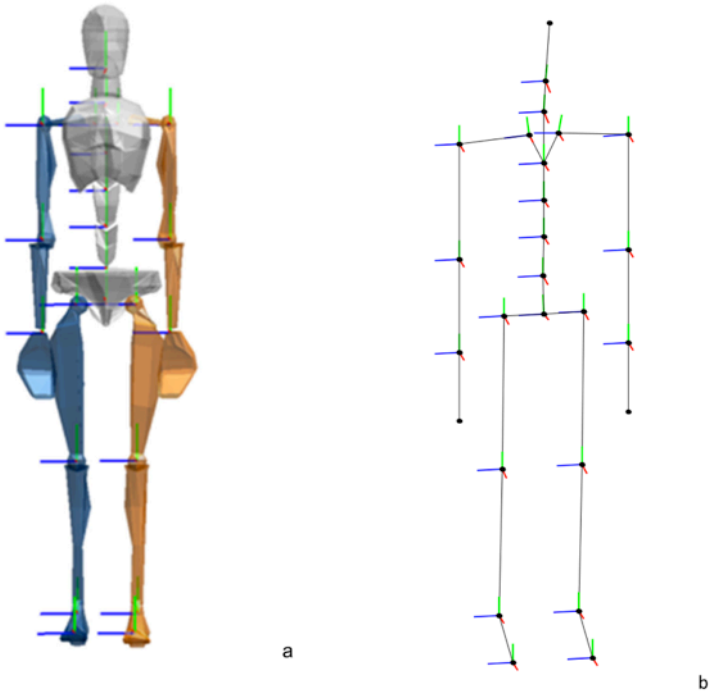

Figure 8.5: The MVN model consisting of 23 motion segments. Each model is scaled from anthropometric data interpolated from subject measurements. (Image reproduced from the XSENS MVN Users Manual, Rev. I)

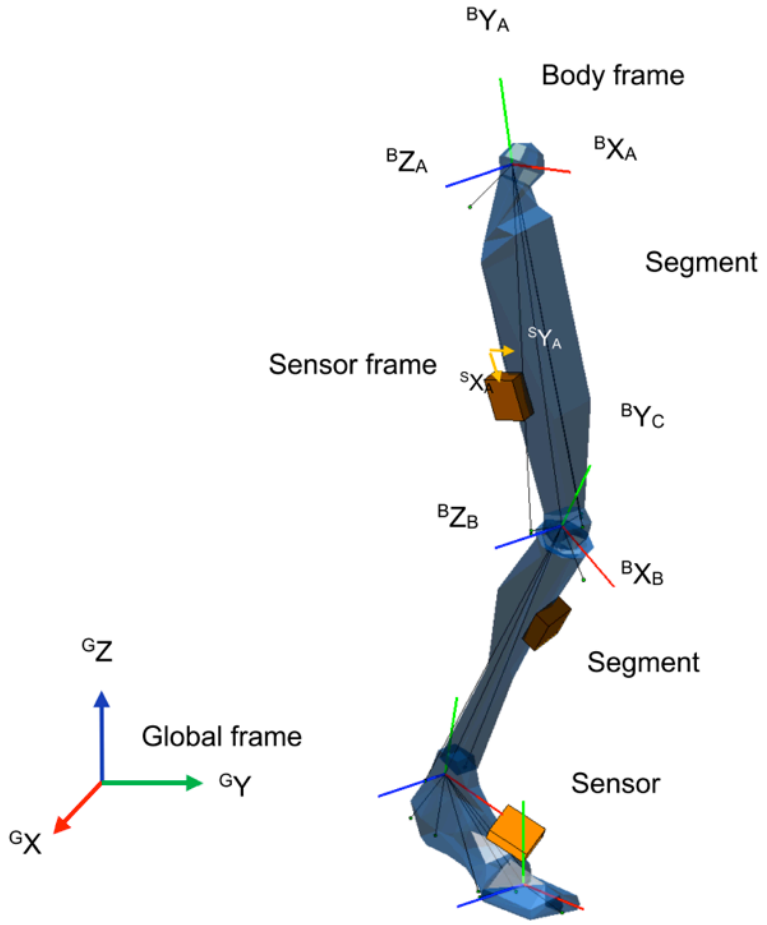

Figure 8.6: The global coordinate system with the coordinate system of each motion segment and the location of the IMUs on the leg. (Image reproduced from the XSENS MVN Users Manual, Rev. I).

The XSENS MVN algorithm assumes each motion segment to be rigid. Each joint connecting the motion segments is modeled as a ball and socket joint with three rotational degrees of freedom and no translational degrees of freedom.

The signals from the seventeen IMUs are compiled by two M-bus units that sit on the lower lumbar spine of the subject. Data can be transmitted wirelessly via Bluetooth 2.0 to a personal computer up to 10m radius, or a PC can be serially connected to the M-buses and placed in a backpack on the subject. This option provides the subject a virtually unlimited capture volume and is the primary reason the XSENS MVN Biomech suit was selected for Study 3 (Figure 8.7).

Figure 8.7: The XSENS MVN Suit allows for 3D kinematics to he measured on skiers outside of a laboratory systems with optical based systems.

8.4 **Limitations**

The XSENS MVN is susceptible to errors associated with differential motion of an IMU relative to the rigid motion segment it is intended to measure. Additionally, the assumptions of ball and socket joints (no relative translation of adjacent motion segments) does not allow for high resolution biomechanical analysis, such as analysis of the center of rotation of joints and predicting strains in ligaments of the joint.

8.5 **Accuracy**

Several studies have utilized the MVN for measuring whole body kinematics of subjects skiing and participating on other recreational activities[75,94,95]. The accuracy of the XSENS MVN claimed by the manufacturer is RMSE of less than ± 3 degrees in dynamic situations[96]. One study by Seel et al.[97] compared the angular displacement of the knee joint on a subject with an above knee amputation and prosthesis on one leg was well as the contralateral leg. Seel et al. reported an RMSE error of 1° in prosthetic knee angle between a ten-camera Vicon Optical Motion Capture system and the XENS system. Measured knee angle of the contralateral l of the single leg amputee an RMSE error of 3°, likely increased by soft tissue artifacts. Other studies have not been able to replicate this value, and estimate the accuracy to be closer to ±5° [95]. For comparison, an analysis of 15 studies utilizing optical methods found an average error of ±5

degrees in joint angles [98]. Other studies have reported inter and intra observer errors using Optical Motion Capture systems also range between 4-5° [99] and 2 cm accuracy in absolute position[100].

8.6 Small-Scale Validation Study of the XSENS MVN Biomech

The accuracy resported by Seel et al.[97] are encouraging; however, there are few other studies that have reported on the accuracy of using IMUs for 3D motion tracking by comparing the XSENS system to an optical based system. To provide additional confidence in the use of the XSENS system for Study 3, a small validation study was initiated to compare the performance of the XSENS MVN Biomechanics suit to a traditional camera-based motion tracking system.

In the Human Motion Analysis Research Lab, Department of Rehabilitation Medicine, University of Washington, a single a human subject was fitted with the XSENS MVN Suit and 33 reflective marker sets on body landmarks (Figure 8.8). A Qualysis infrared camera system (Göteborg, Sweden) measured the position of the reflective marker sets while the XSENS MVN Suit measured kinematics while the subject performed simple quasi-static and dynamic motions. Twelve separate trials were record while the subject performed quasi-static and dynamic motions of the lower extremities, upper extremities, trunk, head, and whole body.

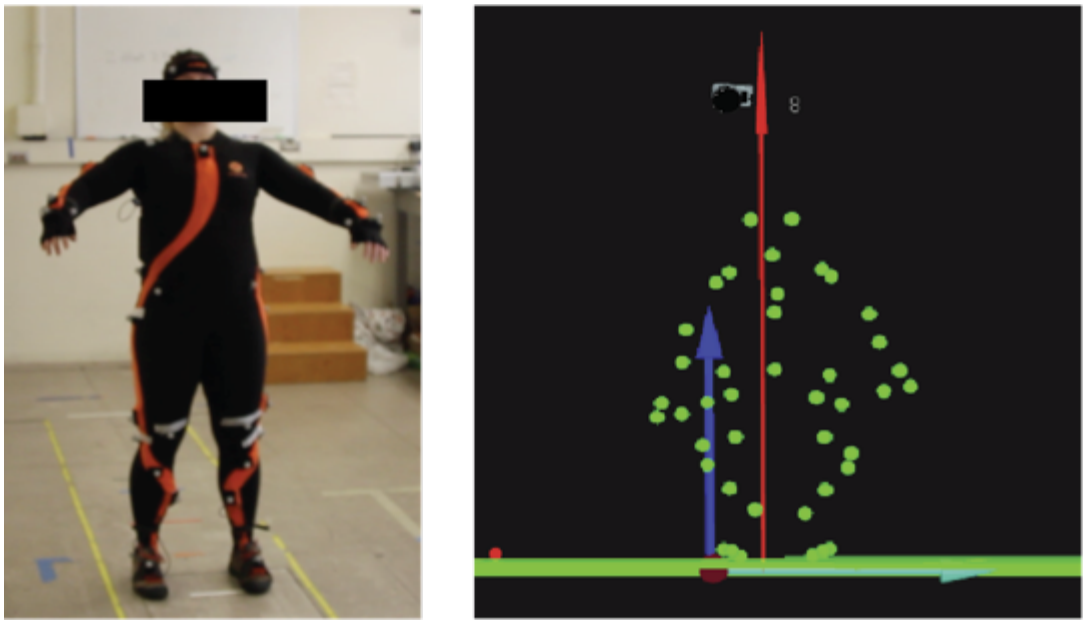

Figure 8.8: *(Left) Subject wearing the XSENS MVN Suit with reflective marker sets attached. (Right) Reflective marker sets tracked by the Qualysis motion capture system.*

There were insufficient markers on each motion segment to allow for tracking of each motion segment for a comparison of joint angles between XSENS and Qualysis. However, several markers were placed close to the anatomical origins of several motion segments of the XSENS system. Therefore a comparison of the displacement of one select Qualysis markers and the origin of the corresponding motion segment in the XSENS system was compared. Figure 8.9 shows how a comparison was performed between the Qualysis marker placed on the olecranon process of the Ulnar bone, and the elbow joint center computed by the XSENS system as the test subject performed various motions of the arm.

As shown in Figure 8.10, there was relatively strong agreement between select Qualysis markers and the XSENS system, with an $RMSE = 0.015m$, and an $R^2 = 0.99$.

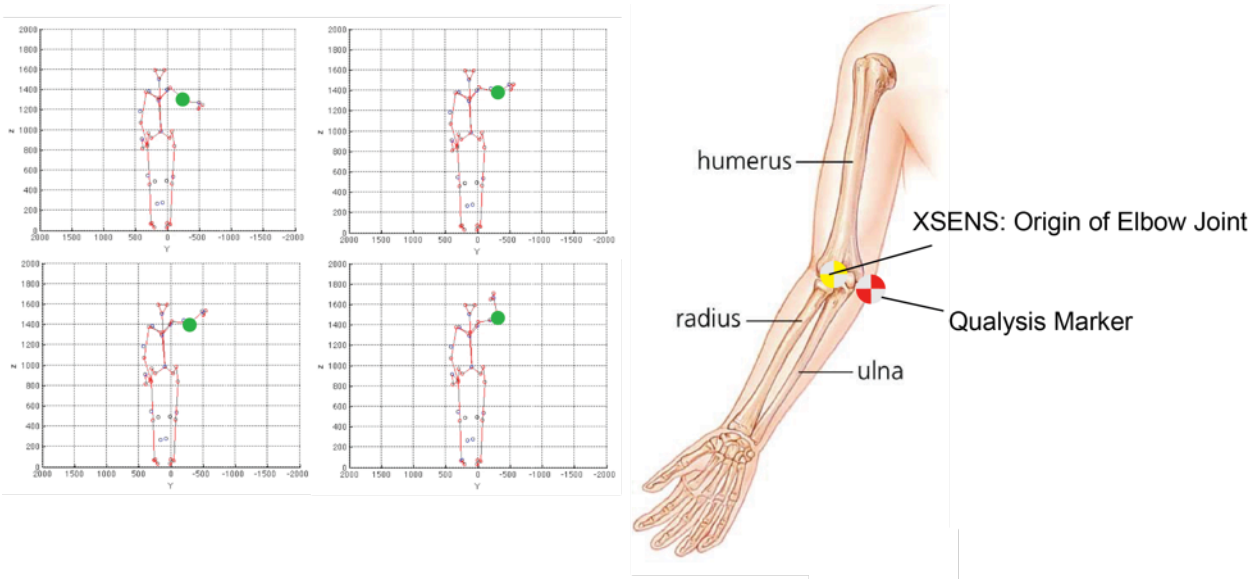

Figure 8.9: Comparison of the resultant displacement of the elbow joint computed in the XSENS system and a Qualysis marker placed on the olecranon process of the Ulnar bone.

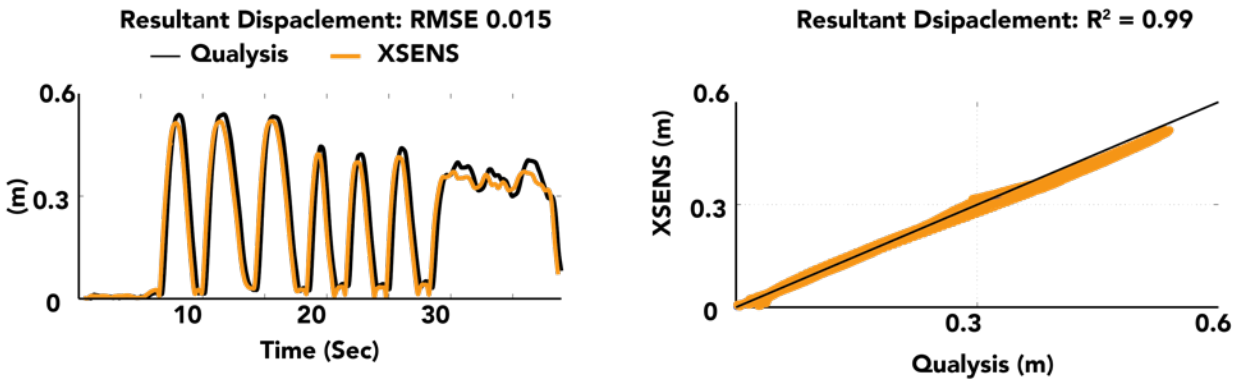

Figure 8.10: Comparison of the resultant displacement of the Qualysis marker and the elbow joint center computed by the XSENS system.

8.7 **Discussion**

The XSENS MVN suit holds several advantages over the other optical motion capture systems, most importantly the ability to measure 3D motion of skiers without the restriction of a capture volume defined by a camera system.

The accuracy of the system has not been well validated, though one preliminary study reports low RMSE errors between the optical systems and the MVN system. Other studies[100,101] have reported position error in the same range as the 2cm position accuracy which corresponded to 1° accuracy in orientation and up to 3.7° accuracy in relative joint angles.

However, a small-scale validation study was been undertaken to better understand the strengths and limitations of the system. Though limited in scope, this study has shown that the XSENS system appears to be capable of the accuracy in the 2cm range for displacements and through inference by the results of other studies, implies that the joint angle measurements will be accurate to within to 3.7°- to 5.0° which is sufficient for this study.

Chapter 9. The On-Snow Performance of Alpine and AT Ski Equipment

9.1 **Overview**

The purpose of this study is to quantify the risk of injury to skiers using modern alpine and AT equipment and identify differences in equipment, gender, snow type, and other risk factors for injuries that may illuminate a strategy for how ACL injuries may reduced or how the reliability of Tech/Pin bindings might be improved.

The preceding nine chapters have described research performed to date that includes:

- Study 1: Laboratory testing of the retention release characteristics of AT boots in Alpine Bindings (Chapters 2-3).
- Study 2: Laboratory testing of the interaction of AT boot inserts with the release characteristics of Tech/Pin bindings (Chapters 4-5).
- Design and calibration of sensors for Study 3 (Chapters 6-7).
- A small-scale validation of the XSENS MVN Biomechanics Suit (Chapter 8).

The results from studies 1 and 2 indicate that the use of AT equipment will not afford skiers the same protection against lower leg fractures as traditional alpine equipment. Studies 1 and 2 have provided valuable insight into the performance of alpine and AT boot binding systems in a controlled laboratory environment. However, ski bindings were designed to prevent the skier who has a considerable effect on the loads that are applied the ski-binding-boot system.

The purpose of performing Study 3 is to quantify the reaction forces at the top of the boot cuff, and the joint reaction forces at the knee for skiers using both alpine and AT equipment while addressing potential injury risk factors such as gender and snow condition. Section 9.2 describes the study design (section 9.2.1), human subject testing (section 9.2.2), equipment used (9.2.3). This chapter also describes the testing protocol (section 9.3), data and data acquisition (section 9.4), statistical analyses (section 9.5). Five analyses from these data are presented including:

- Analysis No. 1: Comparison of Minimum Retention Requirements to Measured Boot Top Loads (Section 9.6)
- Analysis No. 2: Statistical modeling of ground reaction forces and knee flexion angles (Section 9.7)

- Analysis No. 3: Analysis of loads generated during an inadvertent release (Section 9.8), and a comparison of load paths between Alpine and AT Bindings.
- Analysis No. 4: Predicting maximum GRF values from simple anthropometric measurements of skiers (Section 9.9)
- Analysis No. 5: Analysis of Skier Velocity (Section 9.10)

Futhermore, an analysis of the knee kinematics will be performed in Chapter 10 followed by an analysis of knee loads in Chapter 11 estimated from an inverse dynamics model which incorporates kinetic data described in Chapter 9 and kinematic data described in Chapter 10.

9.2 Study 3 - The on-snow performance of alpine and AT equipment

9.2.1 *Study Design*

The purpose of Study 3 is to quantify the performance of alpine and AT equipment by measuring leg and knee loads of skiers using a repeated measures design. Risk factors for injuries such as gender, leg dominance, and snow condition will be included as independent variables. The data collected will allow for the following hypotheses to be tested (previously outlined in Chapter 1.5.2):

- H_4: The minimum release requirements (MRR) values, established by international standards, will not exceed the maximal leg loads generated by skiers using alpine equipment while skiing on groomed maintained slopes.
- H_5: The MRR values, established by international standards, will not exceed the maximal leg loads generated by skiers using AT equipment while skiing on groomed maintained slopes, but may exceed forces generated by skiers using AT equipment off-piste (on non-maintained slopes).
- H_6: The maximal leg loads generated by males will not be different from females.

The following hypothesis will be examined in Chapter 11:

- H_7: The maximal knee loads generated by males will be different from females.

9.2.2 ***Human Subject Testing***

A protocol approved by the University of Washington Internal Review Board (IRB #43735) will be used to recruit human subjects and collect data while subjects ski on instrumented equipment.

9.2.2.1 Subject selection, recruitment, and requirements

Seven male subjects and five female subjects were recruited for testing via social media. Subject selection requirements (inclusion/exclusion criteria) included:

- Weight > 105 lbs. (48 kg)
    - 105 lbs. (48 kg) is the minimum skier weight recommended by Tech/Pin binding manufacturers.
- Height > 60" <
- Skiing Experience > 2 years
- Not currently pregnant and no surgeries, fractures, or head injuries in the last 6 months.
- Provide proof of health insurance.

Each subject was asked to participate in the study for one full day. Subject data was anonymized. Seven males and six females were included in the study. Males were 29.9 ± 4.5 years of age, weighed 114.6 ± 10.2 kg, and measured 177.2 ± 7.4 cm in height. Females were 33.3 ± 5.9 years of age, weighed 86.2 ± 14.8 kg, and measured 164.6 ± 5.513 cm in height. All skiers self identified as a type III skier, except for one female who identified as a type II skier per the skier classification described in ASTM F939-12[32] (Figure 9.1). N = 59 anthropometric measurements were taken of limb lengths, circumferences and relation to overall subject height Figure 9.2. These measurements were used to scale the mass properties of the foot, lower leg, and upper leg [93,102–106] for the inverse dynamics model (Chapter 11).

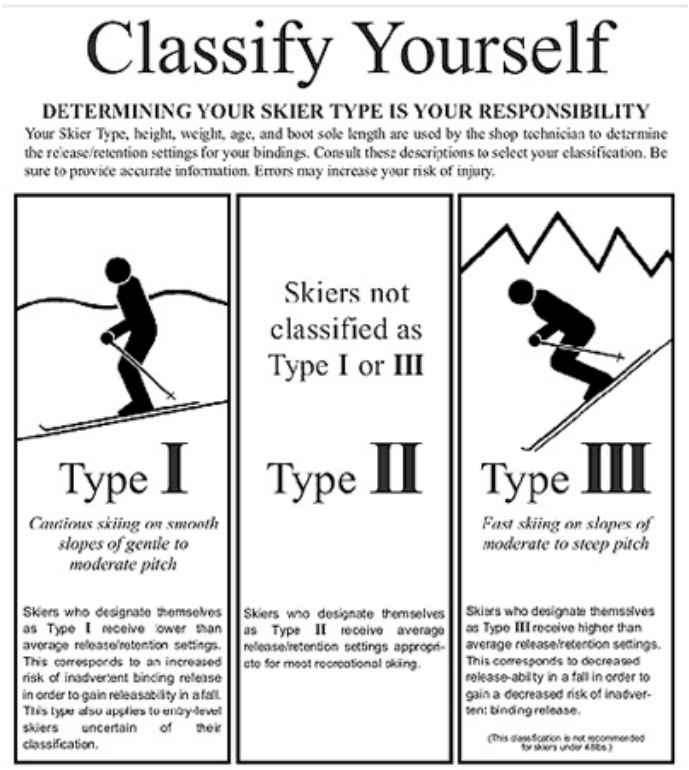

Classify Yourself

DETERMINING YOUR SKIER TYPE IS YOUR RESPONSIBILITY

Your Skier Type, height, weight, age, and boot sole length are used by the shop technician to determine the release/retention settings for your bindings. Consult these descriptions to select your classification. Be sure to provide accurate information. Errors may increase your risk of injury.

Type I

Cautious skiing on smooth slopes of gentle to moderate pitch

Skiers who designate themselves as Type I receive lower than average release/retention settings. This corresponds to an increased risk of inadvertent binding release in order to gain releasability in a fall. This type also applies to entry-level skiers uncertain of their classification.

Skiers not classified as Type I or III

Type II

Skiers who designate themselves as Type II receive average release/retention settings appropriate for most recreational skiing.

Type III

Fast skiing on slopes of moderate to steep pitch

Skiers who designate themselves as Type III receive higher than average release/retention settings. This corresponds to decreased release-ability in a fall in order to gain a decreased risk of inadvertent binding release.

(This classification is not recommended for skiers under 45lbs.)

Figure 9.1 Skier classification chart reproduced from ASTM F939-12[32].

Figure 9.2: N = 59 anthropometric measurements of each subject were taken.

9.2.3 *Equipment*

9.2.3.1 Ski Equipment

9.2.3.1.1 Skis

Skiers were allowed to choose from three lengths of the Dynastar Cham 97 all mountain ski (172cm, 178 cm, or 184cm) Figure 9.3. Females all selected the shortest ski (172 cm) except for the tallest female subject, who selected the longest ski (184 cm). Four males chose the longest skis (184 cm) and three males selected the mid-length skis (178 cm).

The center flexural spring constant, and torsional spring constant of the fore and aft body of the skis were quantified per methods described in ASTM F779-12[107] and ASTM F489-12[108], respectively Figure 9.4. Flexural stiffness decreased with ski length, ($p < 0.001$) (

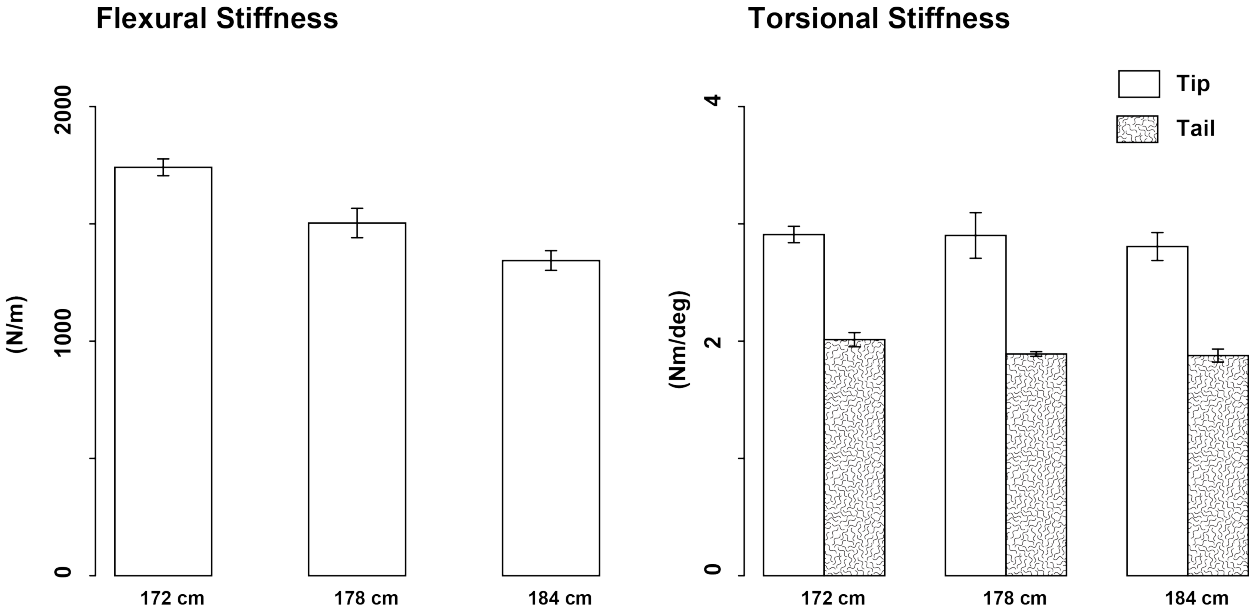

Figure 9.5). Torsional stiffness was not significantly different between ski lengths.

Figure 9.3: Three lengths of the Dynastar Cham 97 ski were used for testing: 172cm (top), 178cm (center), 184cm (bottom)

Figure 9.4: The flexural (left) and torsional (right) spring constants of each ski were measured per ASTM F779-12 and ASTM F489-12.

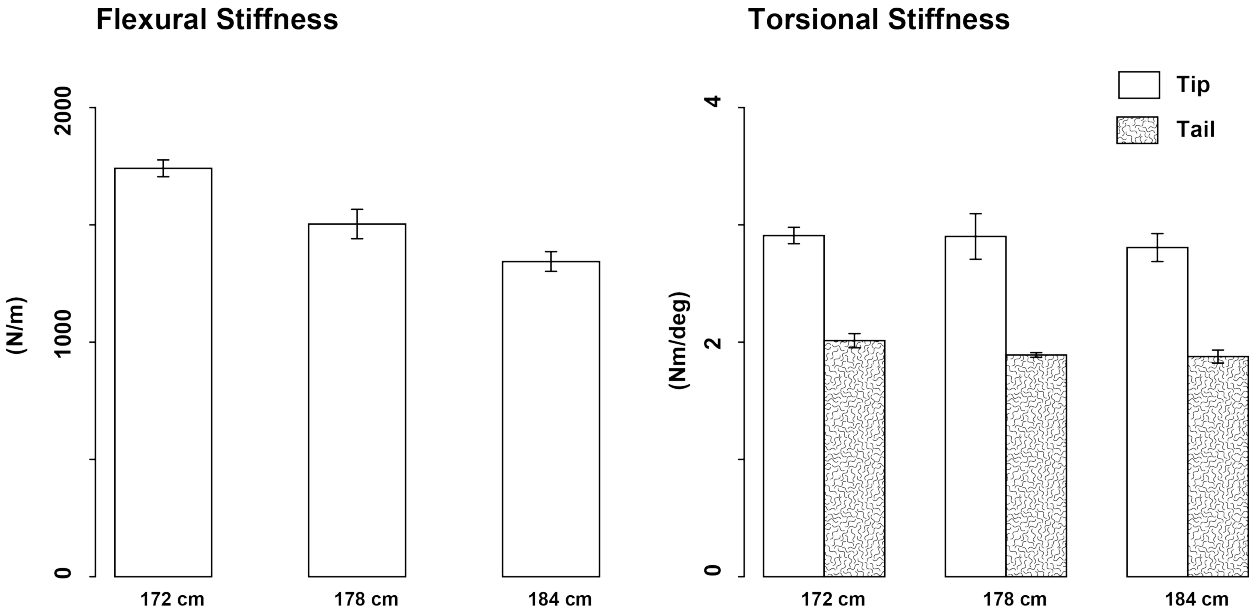

Figure 9.5: Center flexural spring constant, and torsional spring constants of the for-body and after body of the skis.

9.2.3.1.2 Boots

Skiers selected their preferred boot size in a Scarpa Freedom ski boot (Scarpa, Italy). The Scarpa freedom boot utilizes removable soles for use in alpine or AT bindings (Figure 9.6 and Figure 9.7). The same boot shell was used for both Alpine and AT bindings homogenize the

effect of the ski boot between alpine and AT bindings. Females used boot sole lengths ranging from 267-287 mm and males used boot sole lengths ranging from 307-347 mm.

9.2.3.1.1 Bindings

The Rossignol Axial 3 (Isere, France) (indicator setting range: 3.5-10) and Dynafit Radical ST (indicator setting range: 4-10) (Munich, Germany) bindings were selected for testing to provide a comparison between Alpine (Figure 9.8) and AT bindings (Figure 9.9). Bindings were mounted with the custom six axis transducers on the skis (Figure 9.10).

9.2.3.1.1 Ski Poles

Subjects could elect to use their own poles for testing. Poles were provided for upon request.

Figure 9.6: The Scarpa Freedom boot has inter-changeable soles for use in Alpine or AT bindings. This boot was chosen so that the flex of the boot was the same, for both Alpine and AT boots, rather than using two different models of ski boots for Alpine and AT bindings.

Figure 9.7: Alpine boot sole (left) and AT Boot sole (right) attached to the same boot shell model.

Figure 9.8: The Rossignol Axial 3 used for testing as an exemplar Alpine Binding. Indicator setting range: 3.5-10.

Figure 9.9: The Dynafit Radical ST used for testing as an exemplar AT binding. Indicator setting range: 4-10.

9.2.3.2 Testing Equipment

9.2.3.2.1 Kinetics (Six-Axis Force Sensors)

Skis were instrumented with the six-axis force sensors developed in Chapters 6-7. One ski was mounted with two six-axis force sensors mounted at the locations corresponding to the toe and the heelpiece of the recommended mounting position of the boot (Figure 9.10 and Figure 9.11). The force sensors had adapter plates to allow for alpine bindings or Tech/Pin bindings to be attached to the sensors. The adapter plates were manufactured such that PointO (Figure 9.10 and Figure 9.11) remained in a fixed position relative to the ski when different bindings are mounted onto the six-axis sensors.

Figure 9.10: Two six-axis force transducers mounted under the toe and heelpieces of an Alpine ski binding.

Figure 9.11: Two six-axis force transducers mounted under the toe and heelpieces of an AT ski binding. The XSENS IMU for each boot can be seen on the boot toe.

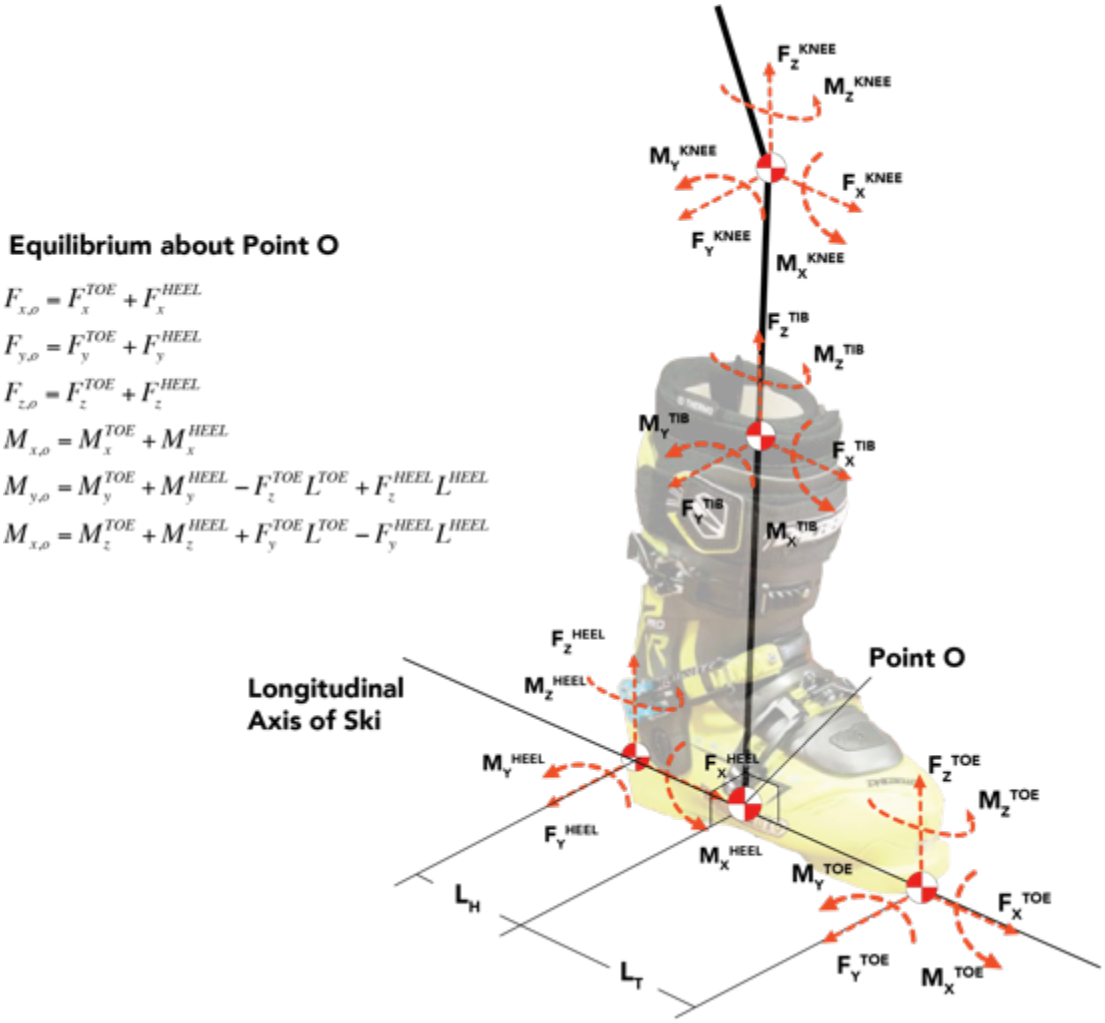

Figure 9.12: Force equilibrium between toe, heel, and Point O. L^H is equal to 35% of the total boot sole length (BSL).

It was cost prohibitive to instrument both skis simultaneously as this would require two more custom force transducers and 16 additional data-acquisition channels. Therefore on the other ski, dummy sensor blocks of the same height, weight, and shape as the six-axis sensors were mounted in the same fashion as the instrumented ski, to equalize the mounting height and weight of both skis. This configuration allowed for ground reaction forces at the toe and heelpiece of the ski binding on the instrumented leg were recorded. The both legs were measured during separate runs. The order of which leg is tested first, dominant or non-dominant, was randomized. Data from the force sensors was acquired using the DTS Nano Slice Unit (Chapter 7). Sensors had a mass of 0.75 kg, a thickness of 29.1 mm thickness for the ski transducer. Sensors had a full-scale range is 19 kN (Resolution: 0.5 N) in shear [Fx, Fy], 12 kN (Resolution:

0.3 N) in tension/compression [Fz]; torque range was 280 Nm (Resolution: 0.008 Nm) in all three axes [Mx, My, Mz] (Figure 9.12). The maximum RMSE from the six axes of both sensors was 1.7%. Ground reaction forces were acquired at 2.4 kHz using 16-bit data acquisition system (Slice Nano, Diversified Technical Systems, Seal Beach, CA) with an anti-aliasing filter.

9.2.3.2.2 Kinematics

The XSENS MVN Biomechanics suit was used to measure body kinematics using 17 IMU and a common filter algorithm to calculate the kinematics of 17 motion segments and 23 joints Figure 9.13. Data from the XSENS MVN Biomechanics suit was collected using a Microsoft Surface Pro 3 Tablet connected serially to the MVN M-Bus (Redmond, WA) running MVN Studio (XSENS, Culver City, CA). Data were sampled at 120 Hz and digitally filtered using a low-pass zero-phase shift, 4-pole Butterworth Filter with a cutoff frequency of 10 Hz. The XSENS system was connected to a Microsoft Surface Pro 3 Tablet (Microsoft, Redmond, WA) placed in the backpack of the subject that was used to record the kinematic data. Magnetic fields from mechanized chair lifts can cause the IMU sensors of the MVN suit to drift over time. After the subject rides a chair lift to return to the top of the course, the MVN suit was recalibrated before the start of each recording trial.

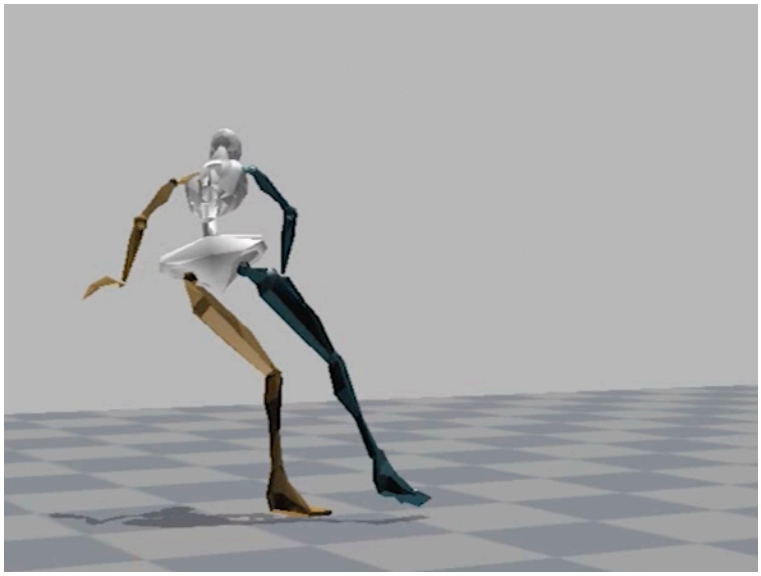

Figure 9.13: An exemplar avatar shown in MVN Studio using data collected from a skier in the XSENS MVN Biomech Suit.

9.2.3.2.3 Skier Position, Speed, and Heading

A Racepak G2K Global Positioning System (GPS) unit was used to collect skier position and speed at 100 Hz (Accuracy: ±0.21 m, ±0.1 kmh, Rancho Santa Margarita, CA,). The GPS antennae affixed the subjects' helmet measured the global position, speed, and heading of the skier.

9.2.3.2.1 Data Synchronization

To record a trial, the XSENS MVN Biomech suit was initialized, following which, the data acquisition system for the force plates and GPS were initialized by a manual switch closure. With all three systems recording, the skier stomped three times on the force plates to produce three corresponding spikes in the force plate data and the linear accelerometer channels in the XSENS sensors mounted on the ski boot to be aligned in post processing (Figure 9.14).

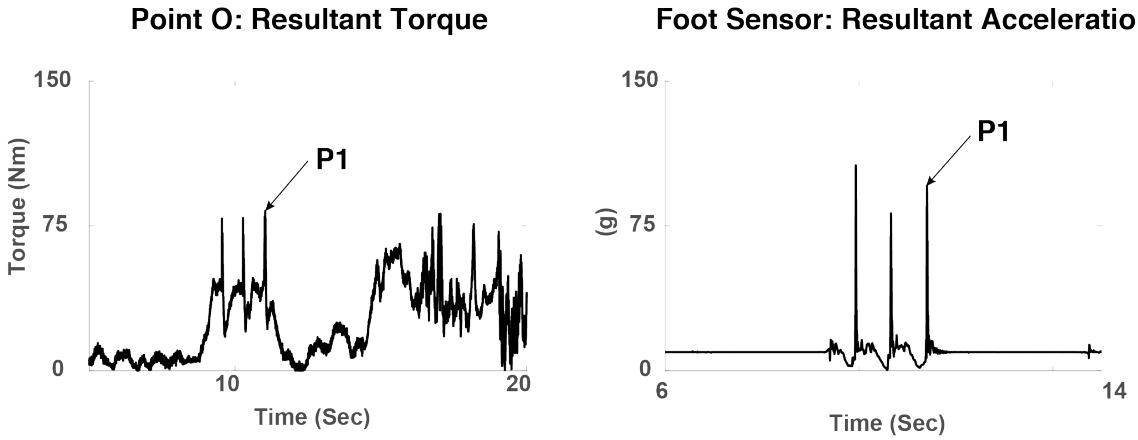

Figure 9.14: Force plate data (left) and XSENS Biomech data (right) synchronization was performed by aligning the peaks labeled P1 from three stomps performed by subjects at the start of each test.

Figure 9.15: A female subject on skis with force plates mounted under the bindings. The cable from the ski extends to the backpack where the data acquisition unit and other electronics were housed. The XSENS MVN Biomech suit is under the subject's outerwear.

The DTS, Surface Pro 3, and GPS unit were housed in a small backpack worn by the subject. Cables from the force sensors will run up the back of the instrumented leg and strain relieved before entering the backpack and connecting to the DTS (Figure 9.15). The total mass of skiers wearing a helmet, clothing, ski boots, the XSENS MVN Biomech suit, and backpack with electronics was approximately 29-30 lbs.

9.2.3.2.1 Video

Video recording of each trial will be performed at 30 fps and 1080p resolution to allow for visual review of any anomalies, skier falls, and skier motions during each trial.

9.2.3.2.2 Snow Characterization

Snow conditions were quantified by measuring foot indentation, air temperature, and snow surface temperature with a digital snow thermometer after each run [109] (Figure 9.16).

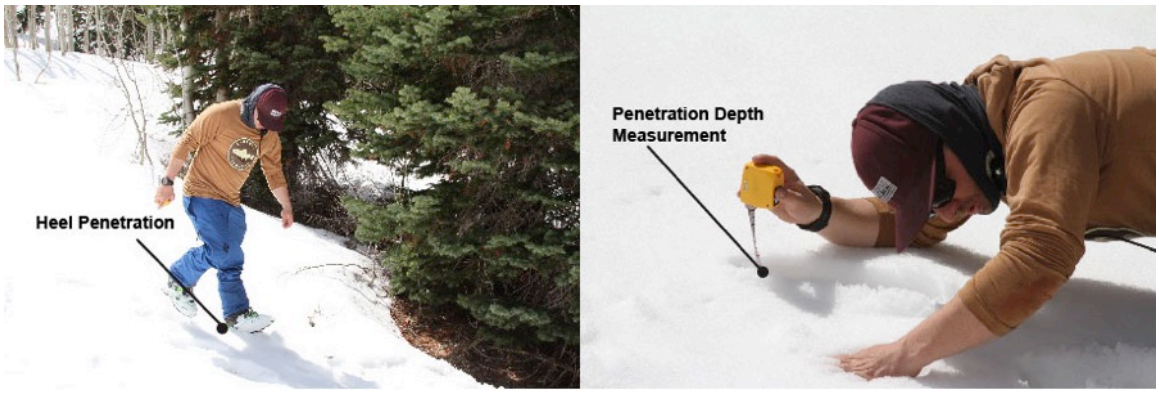

Figure 9.16: Snow characterization was performed using heel penetration tests by the same observer each day.

9.3 Testing Protocol

Subjects were required to use a helmet but were allowed to use their own or one provided by the study. Subjects were fitted for in the XSENS MVN Biomechanics suit and were allowed to wear their skiing outerwear over the suit while outside in the snow. Prior to each day of testing, each Alpine and AT binding was installed and adjusted for the each subject per ISO 8061:2015[33]. Proper binding function and settings was verified using a Vermont Safety Release Calibrator (Vermont Ski Safety Research, Underhill Center, VT) to measure the release torque in twist and forward lean. Subjects were not allowed to lock the toe-piece of the Tech/Pin bindings while skiing.

Each subject skied down an expert slope at a North American ski resort (Snowbird Ski and Summer Resort). Skiers also performed non-skiing maneuvers including five sidesteps. Trials were conducted on a ski run with a North East (NE) aspect and a starting elevation of 8,600' above sea level with 800 feet of vertical relief and an average slope angle of 32° (Figure 9.17). The slope had groomed and non-maintained (off-piste) surfaces such that leg and knee loads can be measured on both snow surfaces in the same run (Figure 9.17Figure 9.17, Figure 9.18).

Subjects skied in eight different configurations of ski equipment (Table 9.1). One subject was tested per day for 13 days in April 2016. Of these 13 days, nine days had snow conditions that were considered corn, which is snow that refreezes overnight, and slowly softened under the heat of the sun throughout the day. Four other trials involved snow conditions considered to be powder with approximately 7-10" of fresh snow that fell overnight.

Table 9.1: Each subject skied a minimum of one run in each of the testing configurations tabulated below. The testing order of each configuration was randomized.

Configuration	Run	Boot	Binding	MVN Suit	Binding Sensors	Instrumented Leg
A	1	Alpine	Alpine	✔	⃠	⃠
	2	Alpine	Alpine	✔	⃠	⃠
B	1	Alpine	Alpine	✔	✔	Dominant Leg
	2	Alpine	Alpine	✔	✔	Non-Dominant
C	1	AT	Tech/Pin	✔	✔	Dominant Leg
	2	AT	Tech/Pin	✔	✔	Non-Dominant

Subjects skied in alpine boots and bindings mounted directly on skis (i.e. without force sensors), configuration A. The purpose of these two runs (A1-A2, Table 9.1) was to allow the subject to become accustomed to the boot-binding-ski system, snow conditions, and the MVN Biomechanics suit. These runs also allowed for a comparison of the kinematics of each subject skiing with and without sensors mounted under the bindings to elucidate the effect, if any, the added height and weight of the force plates had on skiers.

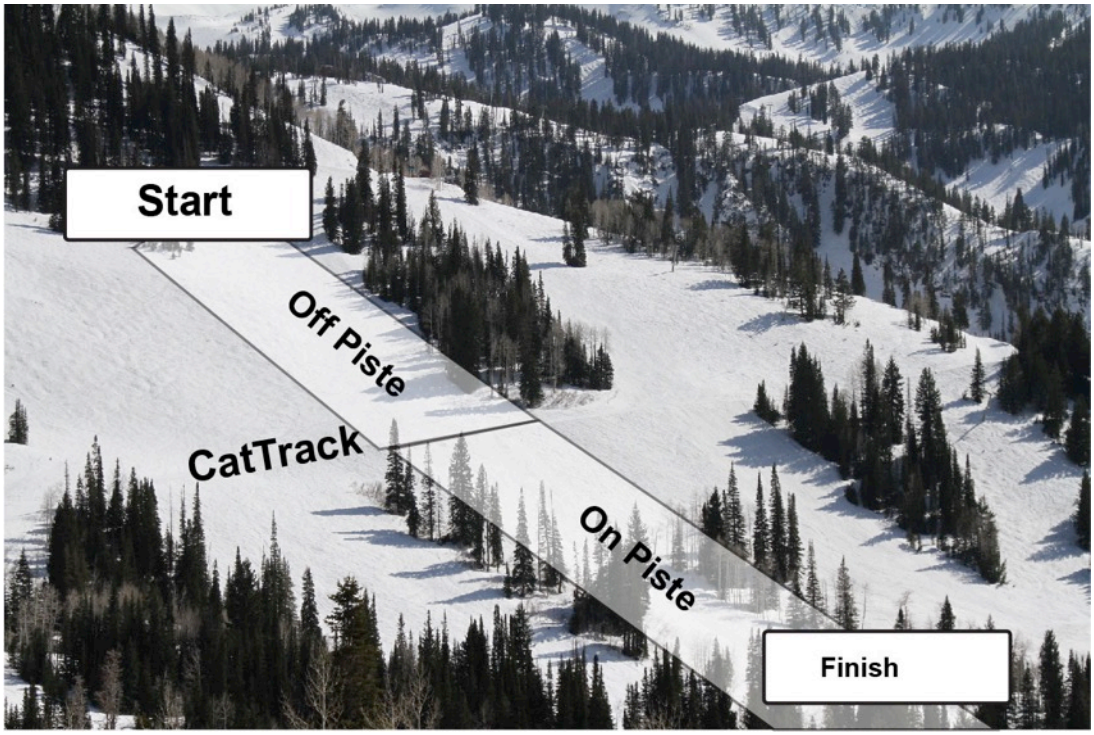

Figure 9.17: Test slope used for on-snow data collection. The off-piste section was demarcated from the on-piste section by a cat track that subjects were instructed to stop for 3 seconds on to simplify the data analysis between the two slopes.

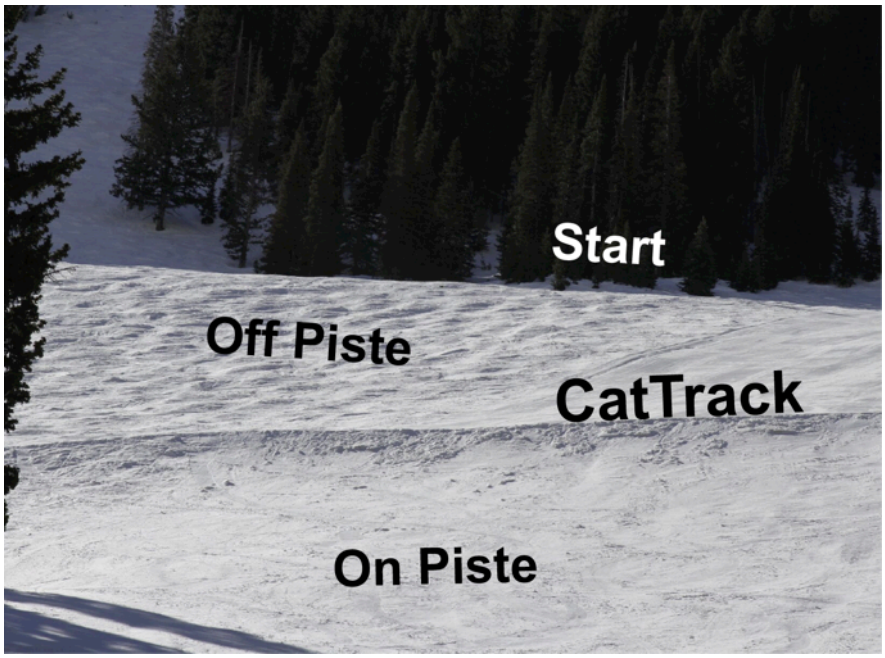

Figure 9.18: A detailed photo of the off-piste slope and on-piste slope, taken from bottom of the slope at the finish area.

9.4 Data Processing and Analysis

9.4.1 *Kinetics*

Raw voltage data from the two six-axis force sensors were transformed into six components for force and torque using the calibration matrices experimentally determined in Section 7.4. Each channel was digitally filtered using a low-pass zero-phase shift, 4-pole Butterworth Filter using Matlab (Natick, MA). The cutoff frequency for each channel was selected using a residual analysis method described by Winter [93] (Figure 9.19) for each channel and ranged between 150 and 210 Hz.

Using data from the toe and heel sensors, and equations shown in Figure 9.20, the force and torque were summed about Point O. The forward lean, M_Y, and twist, M_Z, load components were also transformed from Point O to the top of the Boot Top for further analysis (Figure 9.20).

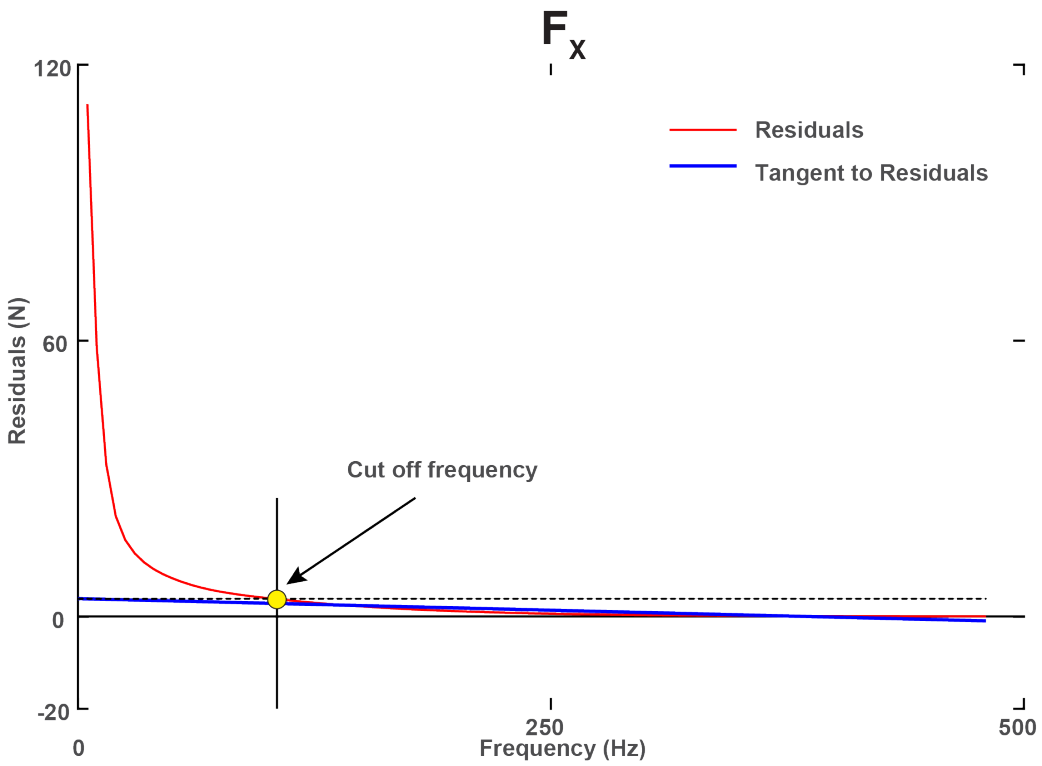

Figure 9.19: Cut off frequencies were chosen by selecting the frequency corresponding to the intercept of a tangent line fit to the residuals of the frequency content the signal.

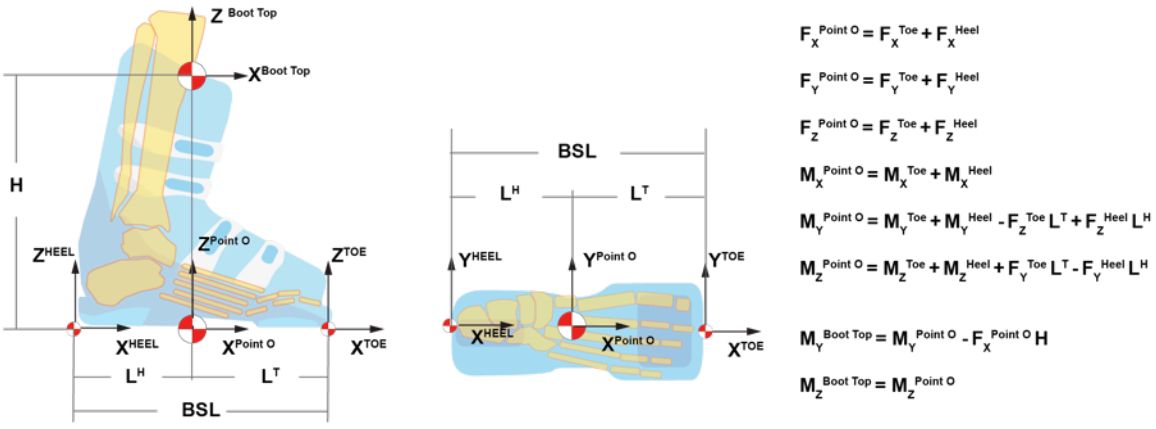

Figure 9.20: Two six-axis of force and torque transducers measured loads at the toe and heel. The loads from the toe and heel were summed about Point O and the boot top using the equations presented above. L^H is equal to 35% of the total boot sole length (BSL).

9.4.2 *Kinematics*

The XSENS MVN Biomech system utilizes 17 inertial measurement units (IMU) to estimate body kinematics. Each IMU incorporates nine channels of data including tri-axial linear accelerometers, tri-axial rate gyroscopes, and tri-axial magnetometers. The XSENS MVN Biomech system incorporates three types of fusion engines, or algorithms to combine the 153 channels of data into full body kinematics for 23 motion segments and 17 joints.

According to the XSENS MVN Biomech support documentation[96] a brief summary of each fusion engine follows.

- **XKF3:** The default fusion engine that utilizes the magnetometers to determine the global heading of the subject. The joint angles computed are not as accurate as the KiC Fusion Engines.
- **KiC (Kinematic Coupling) without Magnetometers:** Recommended fusion engine for more accurate joint angles and segment orientations when the subject is moving continuously. This fusion engine ignores magnetometer data, and requires the position of the IMUs relative to the hip, knee and angle joints to manually measured (Figure 9.21).
- **KiC (Kinematic Coupling):** Recommended for trials where the subject is stationary for long periods of time, and occasionally utilizes magnetometer data.

Based on the recommendations in the XSENS MVN Biomech documentation, the fusion engine, *KiC without magnetometers*, would appear to be the most appropriate fusion engine for processing the skiing data from this study. The XSENS MVN Studio software records kinematic data in an .mvn file which can be post-processed using any of the three fusion engines. The knee joint angle output from each of the three fusion engines is graphically compared in Figure 9.22 for one trial. The fusion engine *KiC without magnetometers* appears to output knee joint angles that are closest to *in vivo* values from the literature[94,110–113]. The *KiC* fusion engine slightly overestimates joint angles compared to the *KiC without magnetometers*, and the *XKF3* fusion over-predicts the adduction and rotation knee joint angles relative to reported maximal joint angle values from the literature. Based on this comparison, the raw kinematic data was processed using the *KiC without magnetometers* fusion engine, with the pelvis fixed. Data were filtered using a 4-pole low pass Butterworth filter, with a cut off frequency determined using the residual analysis method described in 9.4.1 before further analysis described in Chapter 10.

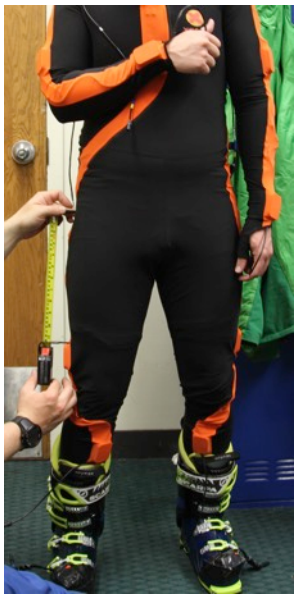

Figure 9.21: Measurement of the upper leg IMU to the hip joint for the KiC (Kinematic Coupling) Fusion Engine.

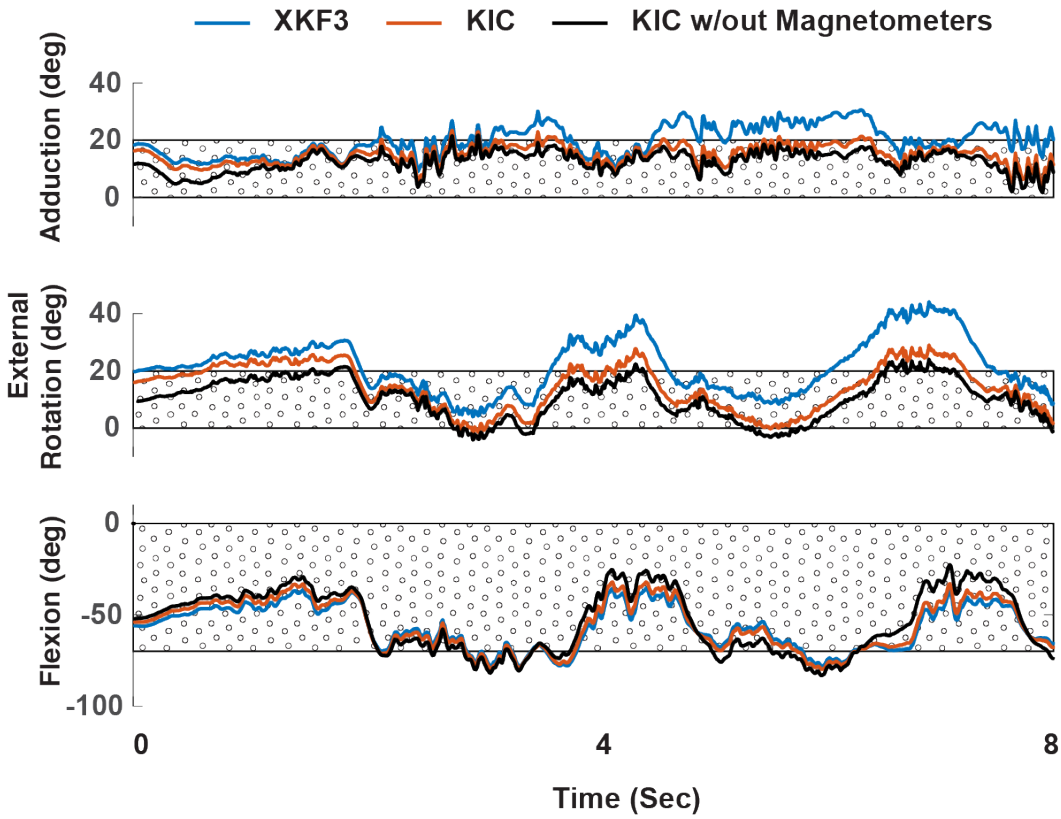

Figure 9.22: A comparison of the knee joint angles output by the three fusion engines the XSENS MVN Suit utilizes to calculate joint angles, XKF3, KiC, and KiC without magnetometers. The textured boundary represents the measured in vivo range from the literature [94,110–112,114].

9.5 Statistical Analyses

The load path of forces and torques transmitted through the toe and heelpiece are of particular interest for comparing the effectiveness of alpine and AT bindings to lower the likelihood of a lower leg fracture by operating within the retention-release envelope defined by ISO 8061:2015 for forward lean and twisting releases (Figure 9.23).

Four separate analyses were performed on the ground reaction forces, kinematics, and GPS data measured:

1. A comparison of the M_Y and M_Z loads measured and transformed to the boot top, to permissible loads boot-top loads per ISO 0462_2012[35](Section 9.6).
2. An examination of all loads measured at the toe and heel, and calculated at Point O, of each binding, as well as the knee flexion joint angles, to identify relationships between various covariates designed into the study (Section 9.7).
3. Examine how well general anthropometric measurements used in ISO 9462:2012[35] predict loads generated during skiing (Section 9.8).
4. Analysis of skier velocity using GPS data (Section9.10).

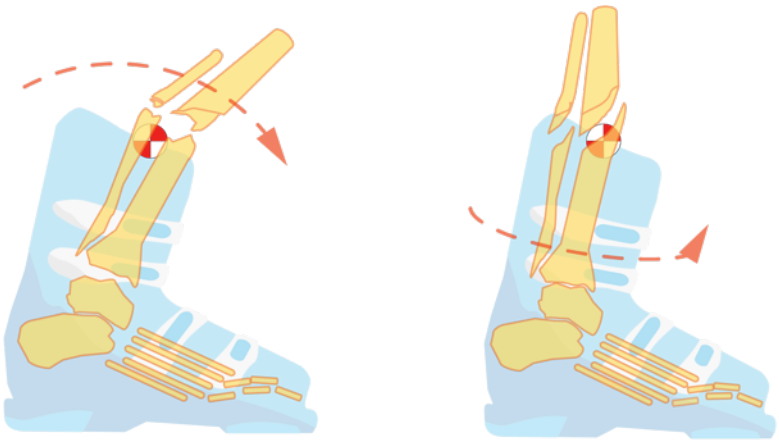

Figure 9.23: The forward lean and twisting torque measured at the boot top can induce bending (left) and spiral fractures (right) if the torque exceeds the injury threshold.

9.6 Analysis No. 1: Comparison of Minimum Retention Requirements to Measured Boot Top Loads

The purpose of this analysis is to compare the retention-release values recommended by international standards [115] to the loads measured at the ski boot top. Recent epidemiological studies have proposed lowering binding settings for female skiers[14] to prevent knee injuries. The potential effect of this proposal on knee injuries will be addressed in Chapter 11, however, one potential adverse effect of lowering binding settings is the risk of inadvertent release. The purpose of this analysis is to measures if the boot top loads generated by male and female skiers exceed to the minimum retention requirements (MRR) values specified by international standards in alpine and AT bindings.

9.6.1 *Methods*

The forward lean [M_Y] and twisting torques [M_Z] transformed to the boot top were normalized using the forward lean and twisting release torques measured on each binding prior to testing using a Vermont Calibrator (Vermont Ski Safety Research, Underhill Center, VT). A 99% confidence interval was calculated by fitting a Gaussian probability density function to a scatter plot of measured twisting and bending torque and compared to the retention-release envelope for forward lean and twist specified by ISO 8061:2015[115]. For comparison across subjects, the M_Y and M_Z values measured for each subject were normalized by the M_Y and M_Z release values measured using the Vermont Calibrator (Figure 9.24 and Figure 9.25). Therefore the units for the axes in Figure 9.24 - Figure 9.29 are (Nm/Nm), where the bending (y-axis) or twisting (x-axis) torque measured at the boot top was normalized by the bending and twisting release torque the binding was set to for a given test subject.

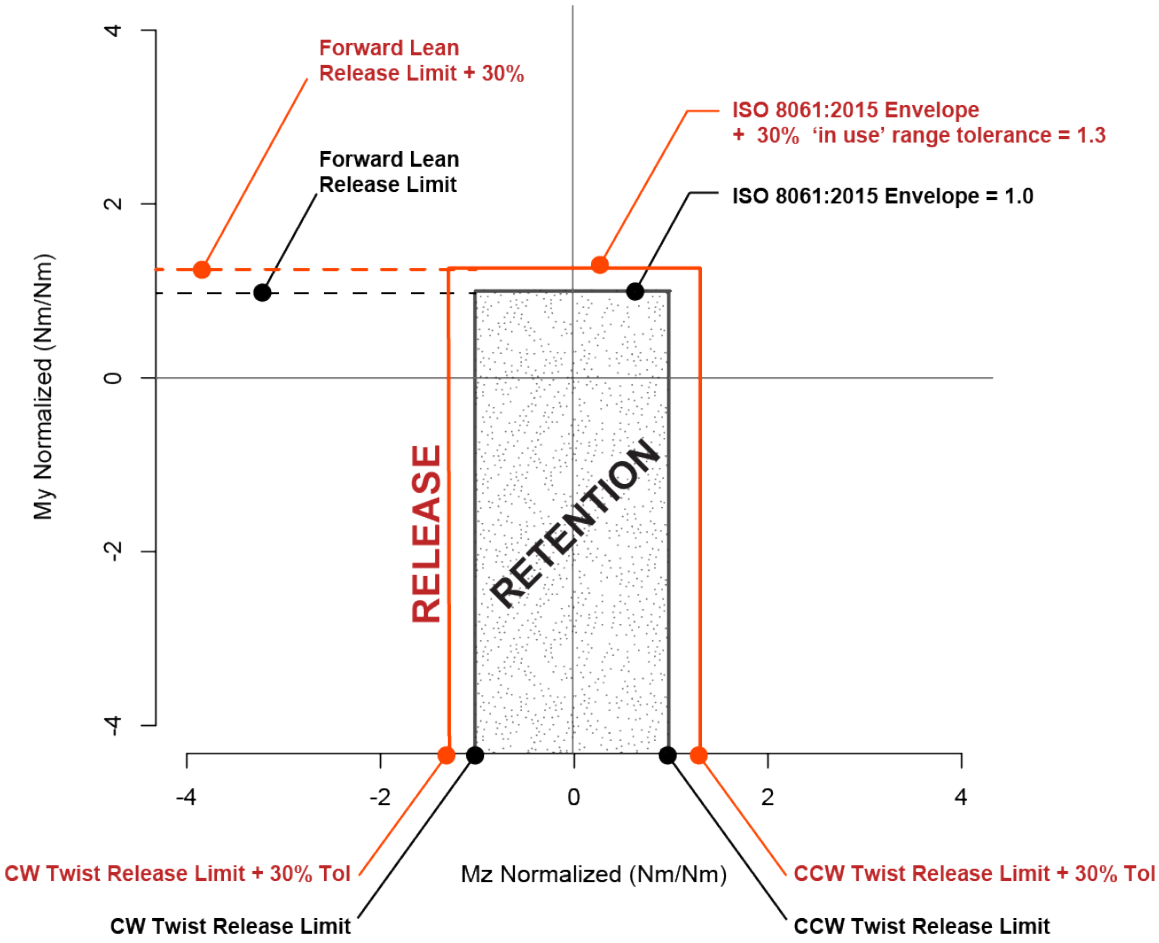

Figure 9.24: Axes showing the retention envelope for normalized twist [M_Z] and forward lean release torque values [M_Y]. The maximum release envelope is 30% greater than the retention envelope.

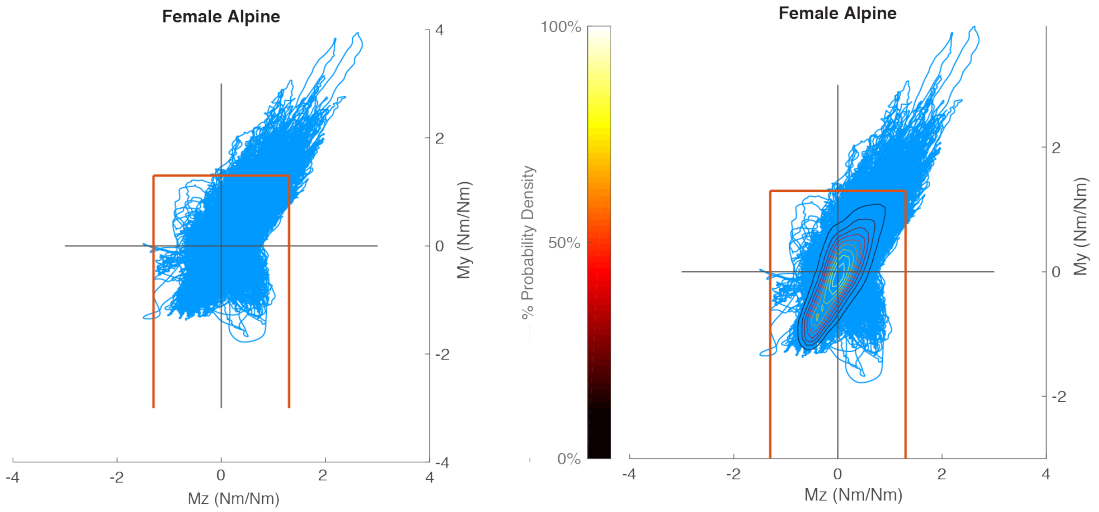

Figure 9.25: An example of a scatter plots of the forward lean [M_Y] and twisting torques [M_Z] (left) from all females. The Gaussian probability distribution function overlaid with the outer contour indicating the 99% probability density function boundary.

9.6.2 ***Results***

A total of 147 trial runs were recorded. Of these trials, one male fell twice (one binding release, one non-release), a second male fell twice (no release), a third male fell three times (one inadvertent release, two non-releases), and one female fell (double release of both bindings. Two falls occurred on the groomed on-piste trail. The other four falls occurred on the off-piste trails. During non-skiing maneuvers, the alpine and AT bindings both inadvertently released one time each. These releases did not cause the subjects to fall. No injuries were reported during testing.

The distribution of forward lean [M_Y] and twisting torques [M_Z] at the boot top were significantly different between covariates including binding [AT, Alpine], gender [Male, Female], and piste [On, Off]. However, the effect size for binding and piste were less than 0.001, so these statistical differences have little practical importance. However, the differences in distributions for men and women were more consequential.

The differences between males and females for M_Y were significant with a large effect size ($\beta = 0.006$, $SE = 0.0007$, $\boldsymbol{\eta^2 = 0.09}$). The differences between males and females for M_Z were significant with the largest effect size ($\beta = 0.04$, $SE = 0.003$, $\boldsymbol{\eta^2 = 0.17}$). These effect sizes indicate that the differences in loads measured at the boot top

between males and females are significantly different and large enough to be of practical significance. Examination of the female distributions, shows that females appear to use a narrower range of M_Z than Males, which is confirmed by the larger effect size for MZ, $\boldsymbol{\eta^2 = 0.17}$, than M_Y, $\boldsymbol{\eta^2 = 0.09}$, (Figure 9.27 and Figure 9.29).

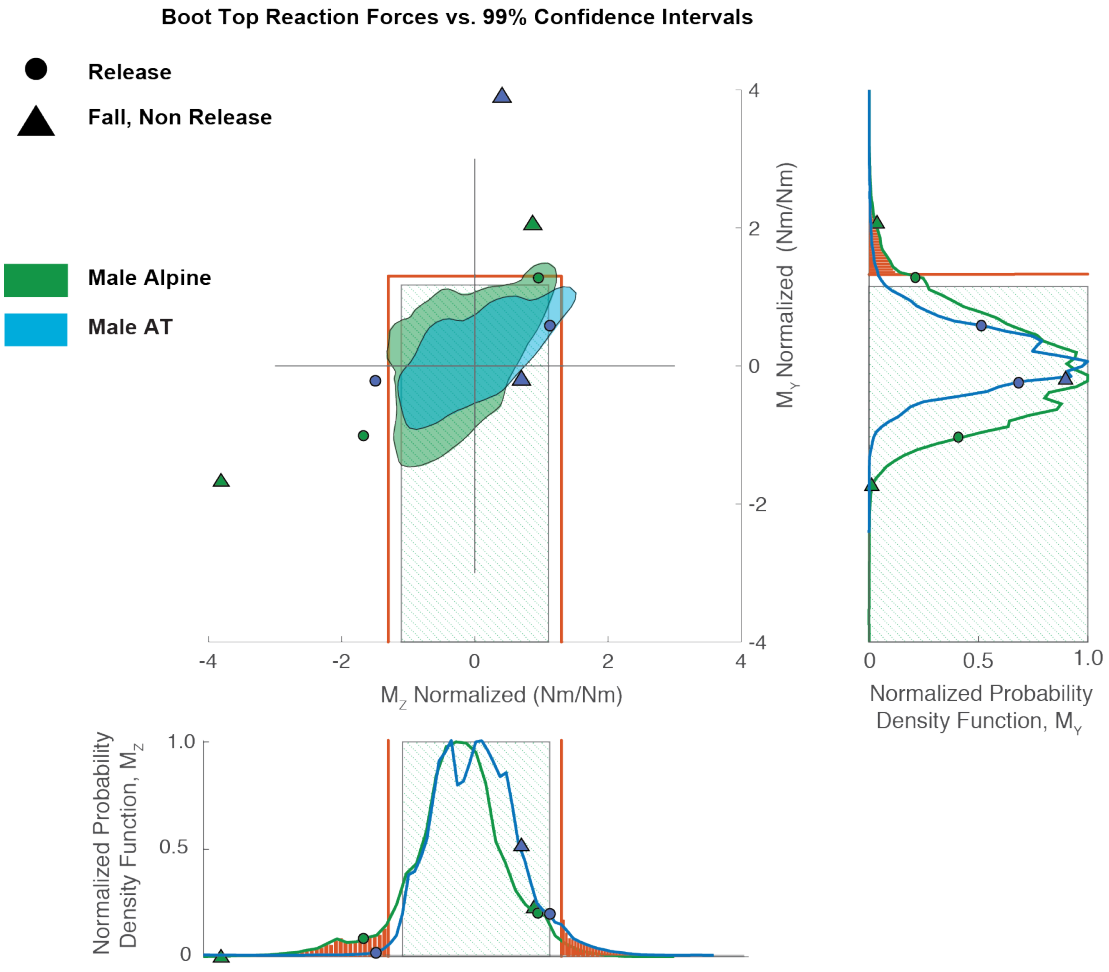

Figure 9.26: The 99% probability density function boundary for [M_Y] and [M_Z] for all males in Alpine and AT bindings. Triangles indicate falls with no binding release. Circles indicate falls with a binding release.

The 99% boundary of the probability density function rarely exceeded the prescribed retention-release envelope for both the Alpine and Tech/Pin bindings. For Alpine bindings, males slightly exceeded the 30% in use range in Forward Lean. In falls with alpine binding releases (No. 6 & 7, Figure 9.26 and Figure 9.28), loads did not exceed 150% of the release envelope. However, two falls with alpine bindings that did not release exceeded the release envelope in twist by approximately 200% and 400%, respectively (No. 5 & 8, Figure 9.26 and Figure 9.28).

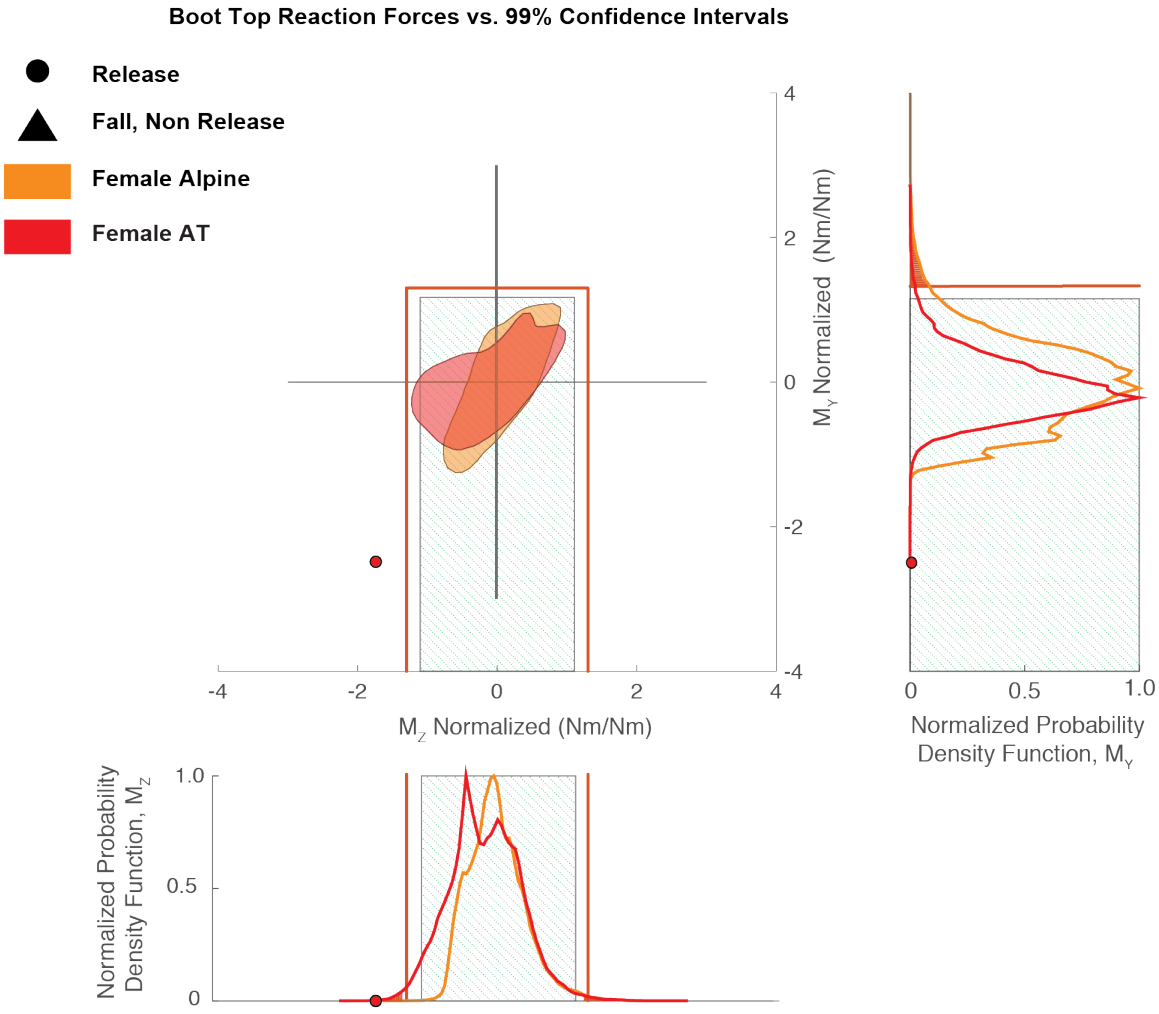

Figure 9.27: The 99% probability density function boundary for [M_Y] and [M_Z] for all females in Alpine and AT bindings. Triangles indicate falls with no binding release. Circles indicate falls with a binding release.

For AT bindings, males slightly exceeded the 30% in use range in Twist. One fall with AT bindings that did not release exceeded the release envelope by approximately 400% in forward lean (No. 1, Figure 9.26 and Figure 9.29). Two releases (No. 3 & 4, Figure 9.26 and Figure 9.29) were classified as inadvertent releases that either did not cause the subject to fall, or the release of the binding is thought to have caused the fall. One fall from a female subject produced a double release of both bindings (No. 9, Figure 9.27 and Figure 9.29).

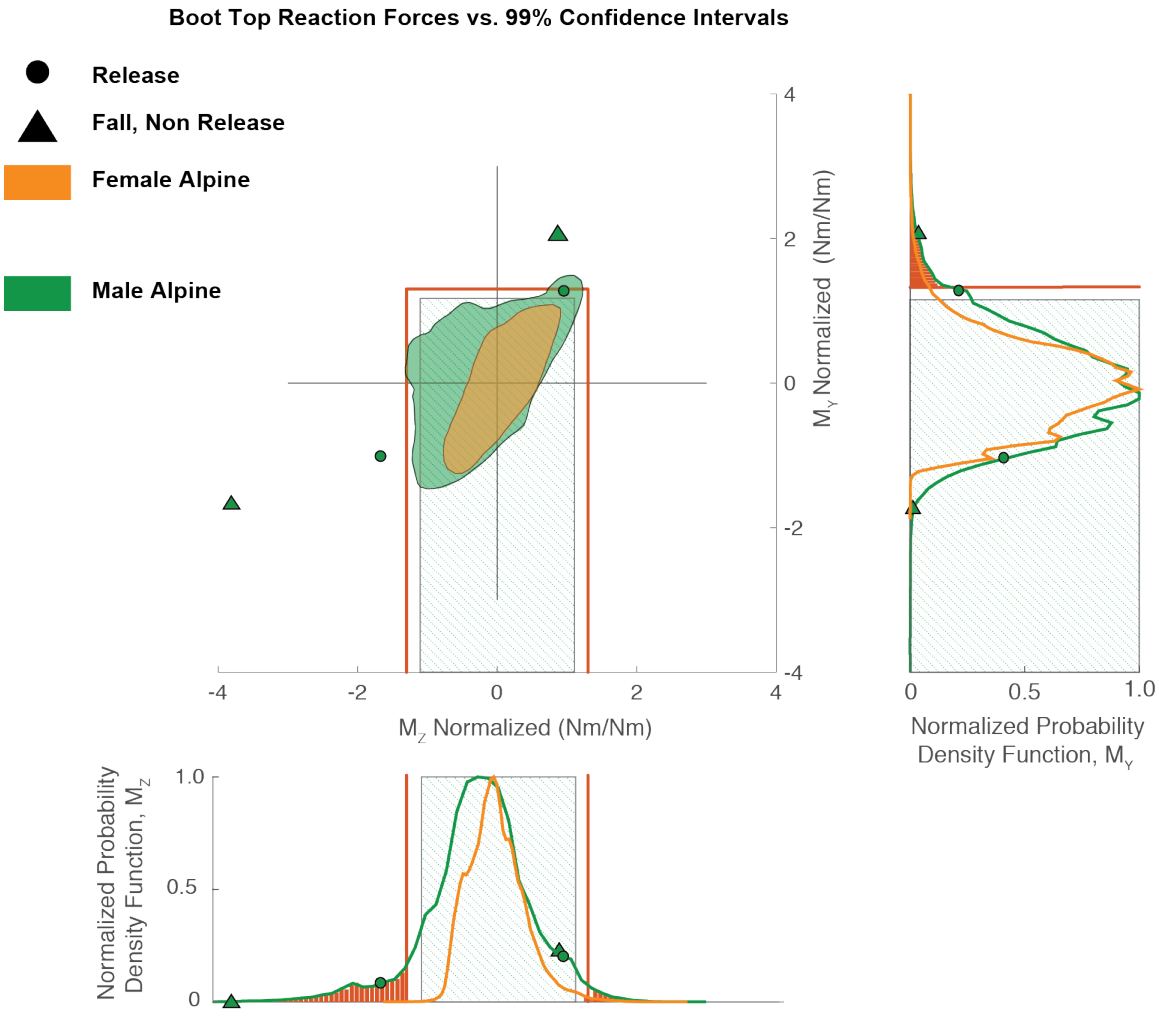

Figure 9.28: The 99% probability density function boundary for [M_Y] and [M_Z] for all males and all females in Alpine bindings. Triangles indicate falls with no binding release. Circles indicate falls with a binding release.

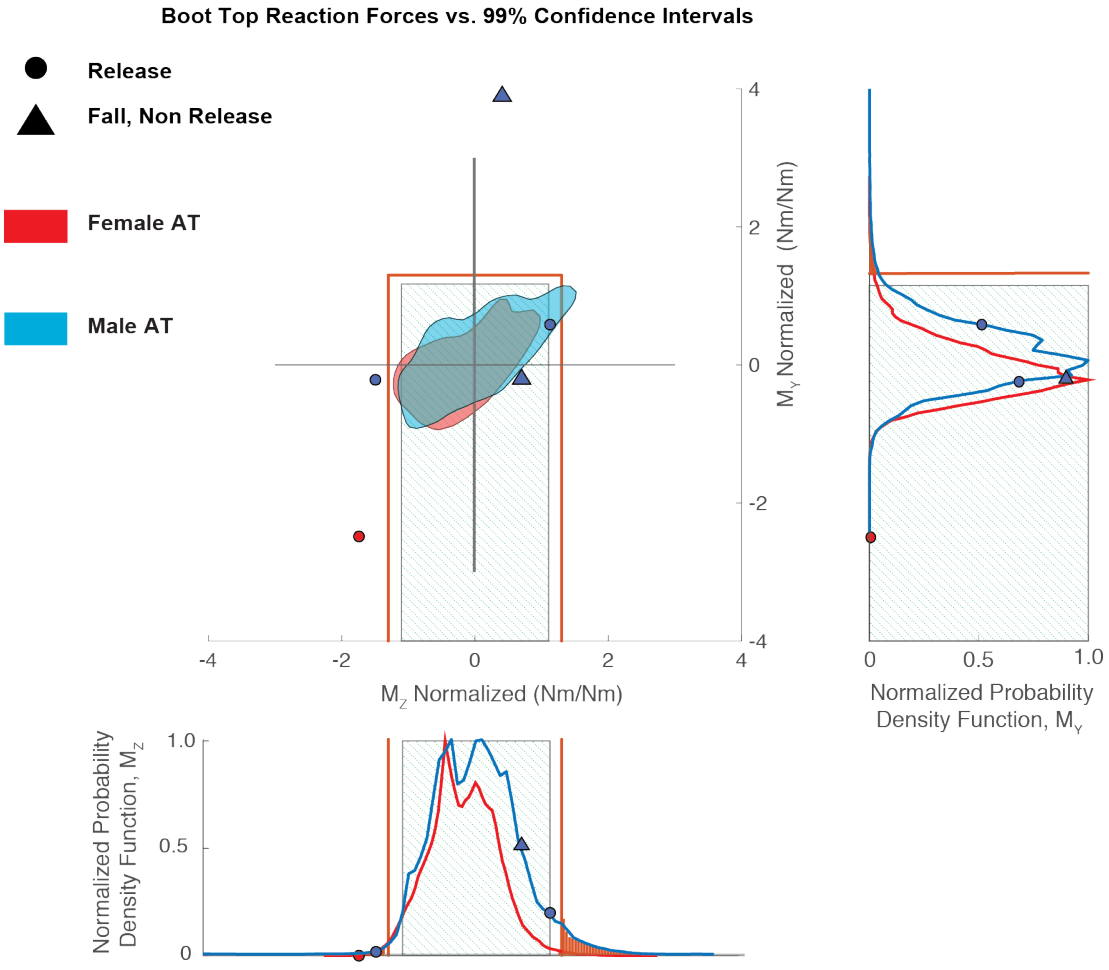

Figure 9.29: The 99% probability density function boundary for [M_Y] and [M_Z] for all males and all females AT bindings. Triangles indicate falls with no binding release. Circles indicate falls with a binding release.

9.6.3 ***Discussion***

Shealy et. al. examined the ability of ski bindings to detect the point at which a binding should release using 'Signal Detection Theory'[8]. In this study, Shealy et. al. defined injuries attributed to an inadvertent release as a *false-alarm*, implying the binding should not have released. Injuries attributed to a non-release were defined as a *miss*, meaning bindings should have released to prevent the injury, but did not. Bindings were

less precise for males than females, and males were 36% more likely to experience a *false-alarm* than a *miss*.

In the current study, no injuries were reported so no comparison is possible to the rates of 'false alarms' or 'misses' reported by Shealy et. al.[8] in the context of injury rates. However, using Equations 9.1-9.3 a comparison can be made on

However, the loads measured during falls or binding releases can be compared to international standards to evaluate binding performance on the snow. Let the measured loads shown in Figure 9.26 - Figure 9.29 define if a fall with a release is a *miss* or a *false alarm*, using the normalized boundaries for release shown in Figure 9.24. Equations 9.1-9.3 can be used to describe a *miss*, a *false alarm*, or an appropriate 'Target Release'. This criterion counts a release outside the envelope as a *miss*.

Equation 9.1
$$Miss = \begin{cases} 1.3 > M_Y \\ 1.3 > M_Z \end{cases}$$

Equation 9.2
$$False\ Alarm = \begin{cases} M_Y < 1.0 \\ M_Z < 1.0 \end{cases}$$

Equation 9.3
$$Target\ Release = \begin{cases} 1.3 > M_Y > 1.0 \\ 1.3 > M_Z < 1.0 \end{cases}$$

Using this criterion, Alpine bindings released appropriately in one fall, and three of the four falls, or 75%, were *misses*. AT bindings released appropriately in two falls and three of the five falls, or 60%, were misses (Table 9.2). Analyzing the number of falls by gender, eight of the nine falls occurred to in males. The one fall from a female occurred when the female lost control and fell forward with both bindings releasing, but according to the measured loads was defined as a *miss* because the binding did not release before loads exceeded the envelope limit.

Table 9.2 Number of releases or non-releases categorized according to Equations 9.1-9.3 and re-categorized based on whether the skier felt the release, or non-release was appropriate.

Alpine, N = 643 Turns			**AT, N = 728 Turns**		
Miss	**False Alarm**	**OK**	**Miss**	**False Alarm**	**OK**
3	0	1	3	0	2
0.47%	0.00%	0.16%	0.41%	0.00%	0.27%

In the 1990s before wider skis, Scher[27] found that these loads rarely exceeded the envelope criteria. It is possible that wider skis, stiffer boots, and the inclusion of off-piste slopes to the data set have cause the loads measured in the current study to be larger than those previously reported by Mote[12], Quinn[39], and Scher[27].

In conclusion results show that under normal skiing, male and female skiers generate loads that reach the release envelope limit but to not exceed it except in the event of a fall. Alpine and AT bindings had similar rates of failing to release before loads exceeded the MRR values. Males fell more frequently than females. If binding settings were lowered for female skiers, the risk of an inadvertent release could increase.

9.7 Analysis No. 2: Statistical modeling of ground reaction forces and knee flexion angles.

Previous studies shown in **Error! Reference source not found.** have demonstrated that the retention characteristics of AT bindings are not as reliable as alpine bindings. Anecdotally, skiers have responded to this uncertainty by locking the release mechanism of their ski bindings out. If the release function is locked out, this can significantly increase the risk of a lower leg injury to skiers. Conversely, an inadvertent release can also cause serious injuries to the upper extremities, head, and neck[9,11]. Before the retention and release characteristics of AT bindings can be optimized, it is critical to understand how the loads are transferred from the ski to the skier through AT bindings, how that differs from Alpine bindings, and define what the performance parameters of AT bindings should be. The objective of this analysis is to measure what factors such as gender, binding, or piste drive cause higher or lower loads (1) at the toe and heel pieces and (2) at Point O.

9.7.1 *Methods*

This analysis was performed on the maximum loads and joint angles for each turn performed. When skiers transition from one edge to another while skiing, an MX torque is produced to hold the ski on edge (Figure 9.30). The transition point between each turn was defined as the M_X signal changing sense as shown in Figure 9.31. From 147 runs, 1364 turns were identified. Figure 9.32 shows how these points were chosen over an entire run and in more detail in Figure 9.33. Each turn was labeled as an inside or outside turn depending on whether the instrumented foot was on the inside or outside foot of the turn (Figure 9.31). The time of the M_X crossing zero was used to differentiate between inside and outside turns in the kinematics data from the XSENS suit.

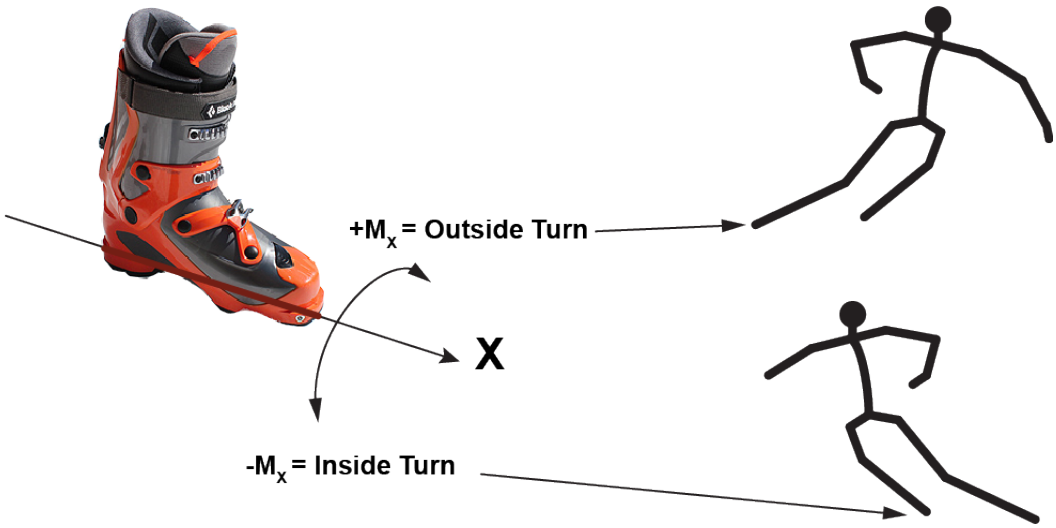

Figure 9.30: Orientation of the X-axis along the longitudinal axis of the ski, and the edge-to-edge torque, MX, used to define the transmission between turns.

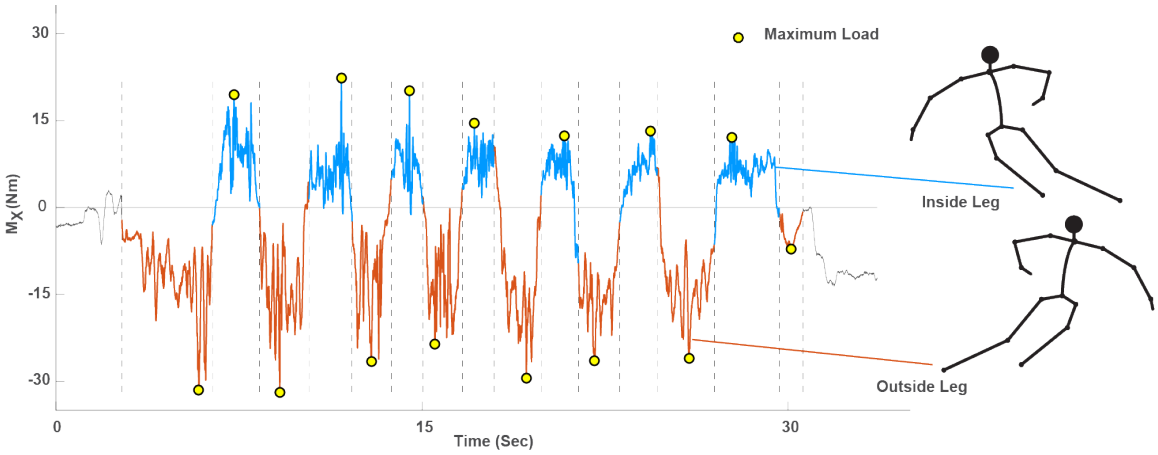

Figure 9.31: Turns with the instrumented leg on the inside or outside leg of the turn were differentiated using the criterion of when the applied M_X at Point O changed sense. The maximum load measured during each turn is designated by the yellow dot.

Linear mixed effects models were selected as an appropriate statistical method to analyze six-axes of peak loads from 1,364 turns. Mixed models allow for investigation of relationships between response variables and independent variables, or covariates that are observed or measured with the response variable. Reproducible covariates are defined as *fixed-effects*. Covariates that cannot be observed, quantified, or reproduced are defined as *random-effects*[116–118].

Mixed effects models perform a multiple linear regression utilizing both fixed and random effects. In a repeated-measures study, data is considered to be unbalanced if the data is incomplete. For example, during data collection, weather conditions did not always allow for measurements to be taken on both on and off-piste slopes. Therefore there are some subjects for which only off-piste measurements were taken. Furthermore, each subject would have to have taken precisely the same number of turns on a given run to produce a balanced dataset. If a traditional analysis of variance (ANOVA) were to be employed for this analysis, incomplete data could not be included in the analysis.

However, mixed effects models can accommodate for an unbalanced dataset; for this analysis the *lmer* package in R [119] was used.

Furthermore, it is likely that a certain degree of variability will be inherent between subjects due snow conditions varying day to day, as well as the variability inherent in-between subjects. Certain covariates of interest, such as differences in loads and kinematics between inside and outside turns (Figure 9.33), may differ between turns.

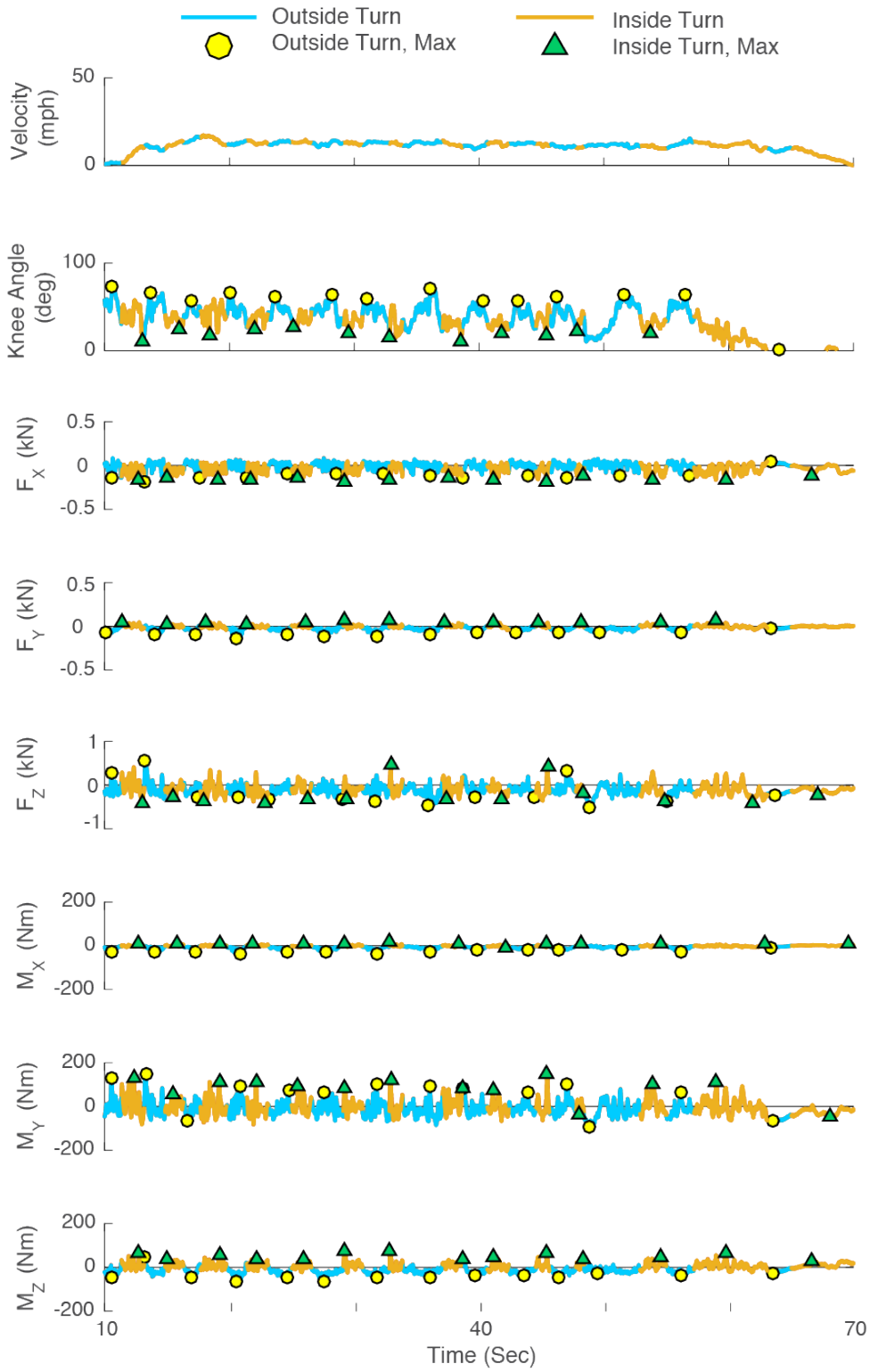

Figure 9.32: Skier Velocity (Top), Knee Flexion Angle, and six load components measured for an entire trial are plotted. Time durations for inside turns (blue) and outside turns (orange) are plotted, along with the maximum for inside and outside turns off piste.

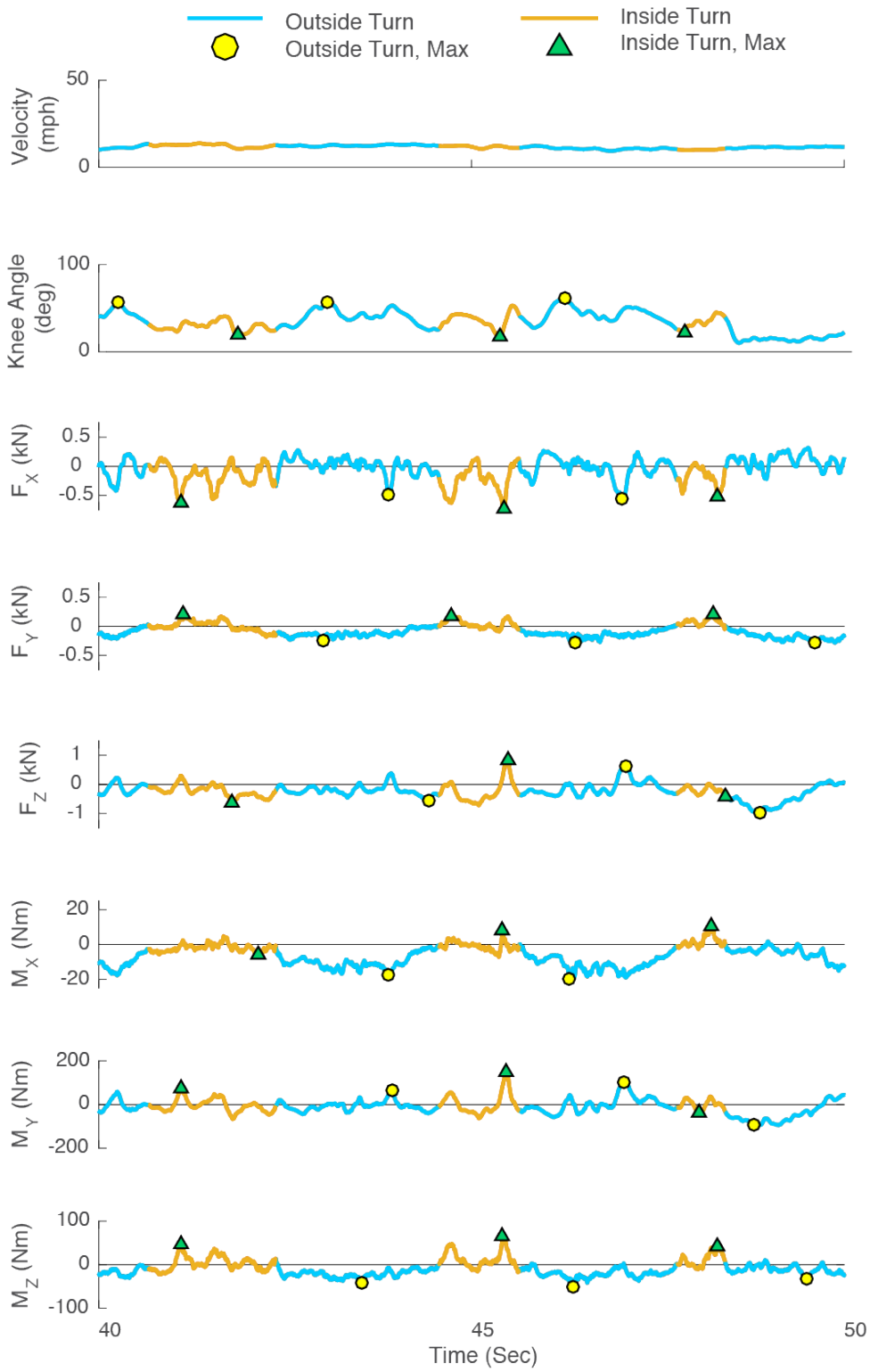

Figure 9.33: Skier Velocity (Top), Knee Flexion Angle, and six load components measured for a ten second portion of the off-piste trial shown in Figure 9.32 (with limits changed for each axis).

The ability of treating each subject, and each turn made by each subject as a *random-effect* in a mixed effects model will allow for a repeated measures analysis that will significantly increase the sample size and power of the analysis. Rather than analyzing one maximum value from the each of the 12 subjects in each condition, multiple turns can be analyzed.

Random-effects can be defined in three ways: 1) allowing a slope for each level, 2) allowing a random intercept, and 3) allowing random slopes and intercepts (Figure 9.34). In this way, the random variance induced by each subject, changes in snow condition, and each turn, are accounted for in each model.

With the aim of analyzing kinetics and kinematics of each turn, and their relation to the covariates built into this study, linear mixed effects modes were developed to address the following response variables:

1. Six linear mixed effect models were developed to analyze the relationship of each load components summed about Point O from the loads measured at the toe and heelpiece. These models included all covariates listed in Table 9.3with the exception of ***Location***.
2. Six linear mixed effects models were developed to analyze the relationship of each load component measured at the toe and heelpieces, with the goal to differentiate how covariates affect load transfer through the toe and heelpiece of the binding. These models included all covariates listed in Table 9.4.
3. Two linear mixed effects models were developed to analyze the relationship of knee flexion joint angles to covariates built into the experimental design.
    a. The first model was developed to evaluate the effect the force plate sensors had on knee flexion angles. Knee angles from 2428 turns made with force plates under alpine bindings were compared to knee angles from 386 turns made without force plates under alpine bindings. This model included all covariates in Table 9.3 except for ***Binding*.**
    b. A second joint angle model was developed that only included data from the 147 runs with force plates under the ski bindings. This model included all covariates in Table 9.4 except for ***Sensor*.**

Response variables were normalized about their mean, and transformed using a Box-Cox power transformation to achieve a normal distribution (Figure 9.35).

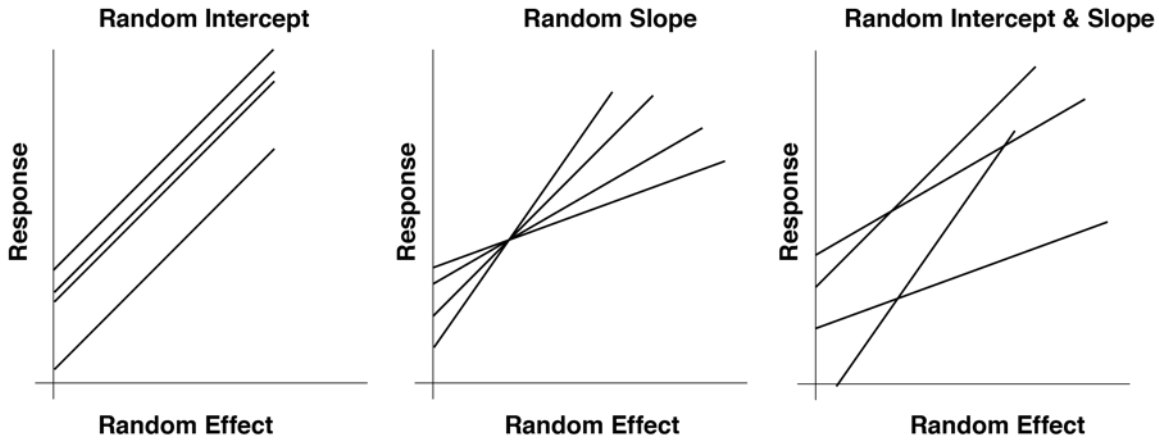

Figure 9.34: Mixed effect models can utilize random intercepts and constant slopes (left), a constant intercept and random slopes (center), or random intercepts and slopes for each subject (right). Figure adapted from Gelman 2007 [117].

Table 9.3: Level -1 covariate factors used as fixed-effects in the mixed effects models for GRF response variables.

Factor	**Levels**	
Gender	Female	Male
Binding	Alpine	AT
Piste	Off	On
Turn Direction	In	Out
Location	Toe piece	Heel piece
Snow Depth (in.)	Continuous: Min 1", Max = 9.75"	
Ski Stiffness (ft/lbs)	410, 460, 530	
Leg	Dominant	Non-Dominant

Table 9.4: Level -1 covariate factors used as fixed-effects in the mixed effects models for joint angle response variables.

Factor	**Levels**	
Sensor	No	Yes
Gender	Female	Male
Binding	Alpine	AT
Piste	Off	On
Turn Direction	In	Out

Fixed-effects, or covariates, were defined as factors of interest built into the design of the study and are tabulated in Table 9.3. Collinearity among *fixed-effects* was checked using variation inflation factors, (VIF) < 2 [54]. After each covariate was added to the mixed effects model, it was tested for r interactions using the least likelihood ratio test.

Random-effects were also added using the least likelihood ratio test; if they were not a significant source of variance to the model, they were removed and the model was simplified to a linear fixed effects model. The *random-effects* of subject and turn were crossed, and defined to allow intercepts. Turns were nested within each subject.

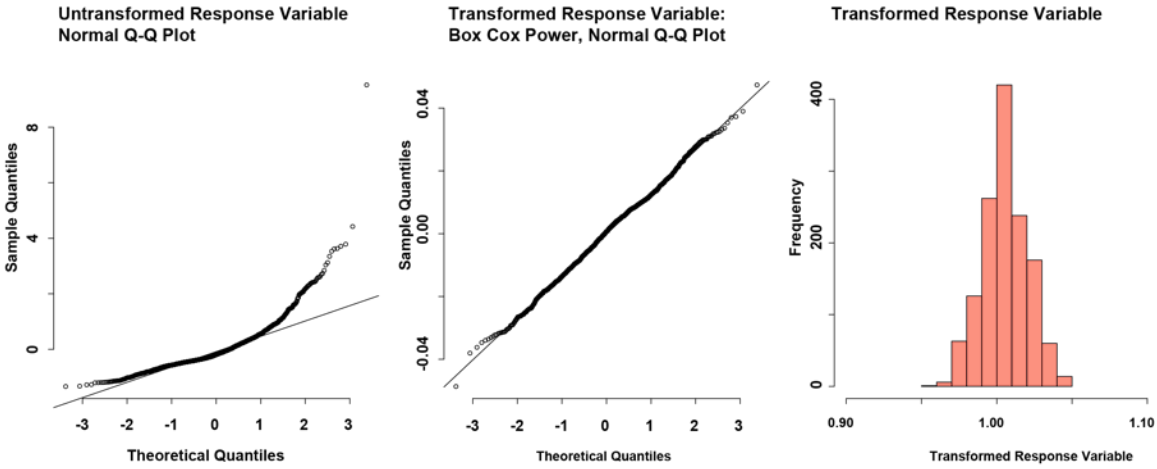

Figure 9.35: Response variables whose distribution that did not pass Kolmogorov-Smirnov tests of normality (left) were transformed using a Box-Cox power transformation to achieve a normal distribution (center & right).

9.7.2 ***Results***

For the purposes of these analyses, plotting the results of each model separately does not allow for comparison of how each covariate of interest affects various load components. Therefore, the 'standardized coefficient' metric was chosen to allow a comparison across different models and different covariates. Standardized coefficients are normalized to describe the portion of standard deviations of the response variable that will be caused by one standard deviation change in the *fixed-effect* or *independent variable*. When categorical variables are used as *fixed-effects,* standardized coefficients describe the portion the of standard deviations of the response variable that will change when the categorical variable changes from one level to

another, say, from male to female. Ski stiffness was considered as a predictor variable but was not a significant contributor to variation in any of the six loads modeled.

Extended results from each model will be provided in an appendix. For clarity, the standardized coefficients from each model have been compiled and organized by covariate. Six linear mixed effects models were developed to analyze each respective load component resolved about Point O for a relationship to each covariate such as gender, binding, or piste.

9.7.2.1 Interpreting Linear Mixed Effect Results

Linear mixed effects models are significantly more complicated to interpret when many are accustomed to only looking for p-values to indicate differences. To aid in the interpretation of the linear mixed effects model results, a brief example is given here.

A linear mixed effects model is developed to compare the how forces at PointO varied by fixed effect. In the present example, the covariate gender has two levels, male and female. The purpose of the analysis is to examine how binding loads differ between males and females. The linear mixed effect model will output the standardized effect, in other words, how much the loads at PointO will change between males and females. Figure 9.36 shows how the standard estimate can be displayed graphically, which not only allows for differences to be shown, but the magnitude of those differences. Since all six loads are of interest but will have different standard deviations, the x-axis is normalized between ±1 standard deviation, represented by the symbol σ. Each of the six loads is listed on the vertical y-axis, with the standard deviation for each load in square brackets. For example, the standard deviation for F_X measured at PointO was $\sigma^{Fx} = 914$ N, and for M_Z at PointO, $\sigma^{Mz} = 106.8$ Nm. If F_X were plotted alone, then the ±1 limits on the x-axis of Figure 9.36 could be replaced with ±914.

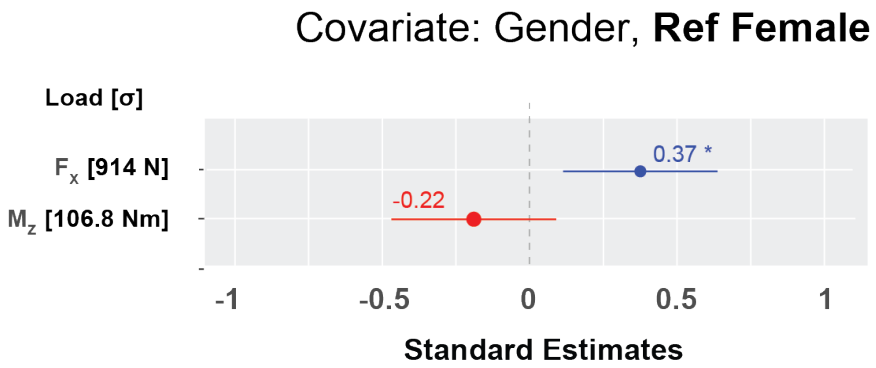

*Figure 9.36: Exemplar plot showing the standard estimate values. Asterisks indicates that there is a significant difference with a * for $p \leq 0.05$, ** for $p \leq 0.01$, or *** for $p \leq 0.001$.*

If one is examining the difference between males and females, the x-axis limits of ±1 are equal to σ^{Fx} = 914 N for F_X and σ^{Mz} = 106.8 Nm for M_Z. The standard estimate plotted is the difference between the levels of the covariate (Males vs. Females) in units of σ. The reference level is listed in the plot title, in this case, females. The standard estimate value for F_X of 0.37, shown by the blue dot, shows that males generate σ^{Fx}*0.37 = 338N more F_X than the reference level, in this case females. Asterisks represent a significant difference with a $p \leq 0.05$ for *, $p \leq 0.01$ for **, or $p \leq 0.001$ for ***. The blue indicates that the difference in the predictor variable, F_X, is lower for the reference level of the covariate (females) than males.

Following this pattern it can be noted that for PointO, the standard estimate of -0.22 for M_Z value indicates that the mean M_Z for males is -0.22* σ^{Mz} = 23.4 Nm less than the females, shown by the red. This difference is not significant indicated by the absence of asterisks, and the 95% Confidence Intervals (error bars) that cross the 0 value of the standard error axis.

9.7.2.2 Dependent Variable: GRFs at Point O, Covariate: Gender

A comparison of maximal loads between male and female skiers is summarized in Figure 9.37. Significantly lower lateral loads [F_Y] to the ski bindings were identified in males, a difference of $-0.59\sigma^F_y$, or 362N, than females. No significant difference was found between males and females for torsion [M_Z]. Significantly higher loads were identified in males compared to females for the other four loads measured (Figure 9.37).

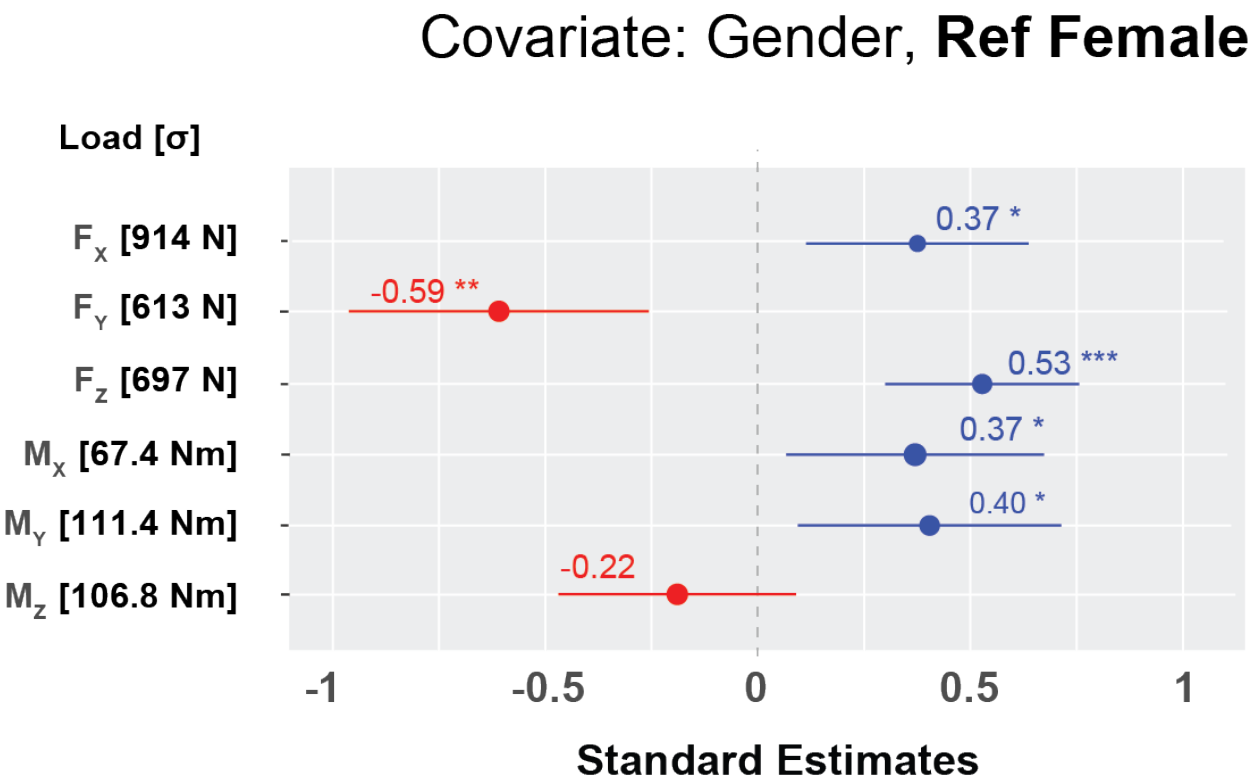

*Figure 9.37: Standardized estimates from the Linear Mixed Effects Models for the independent variable **Gender**. A model for each respective load produces estimates for the fixed effect of **Gender** for each load. The numerical value given in square brackets is the standard deviation for each load. The plotted values indicate the change in load in units of standard deviation measured on males, relative to females.*

9.7.2.3 Dependent Variable: GRFs at Point O, Covariate: Binding

M_X was lower for AT bindings, $-0.52\sigma^F_y$ than Alpine Bindings (Figure 9.38). M_X was higher for AT bindings, $0.24\sigma^M_x$ than Alpine Bindings. No significant differences were found in the principal binding axes M_Y or M_Z between either binding at Point O.

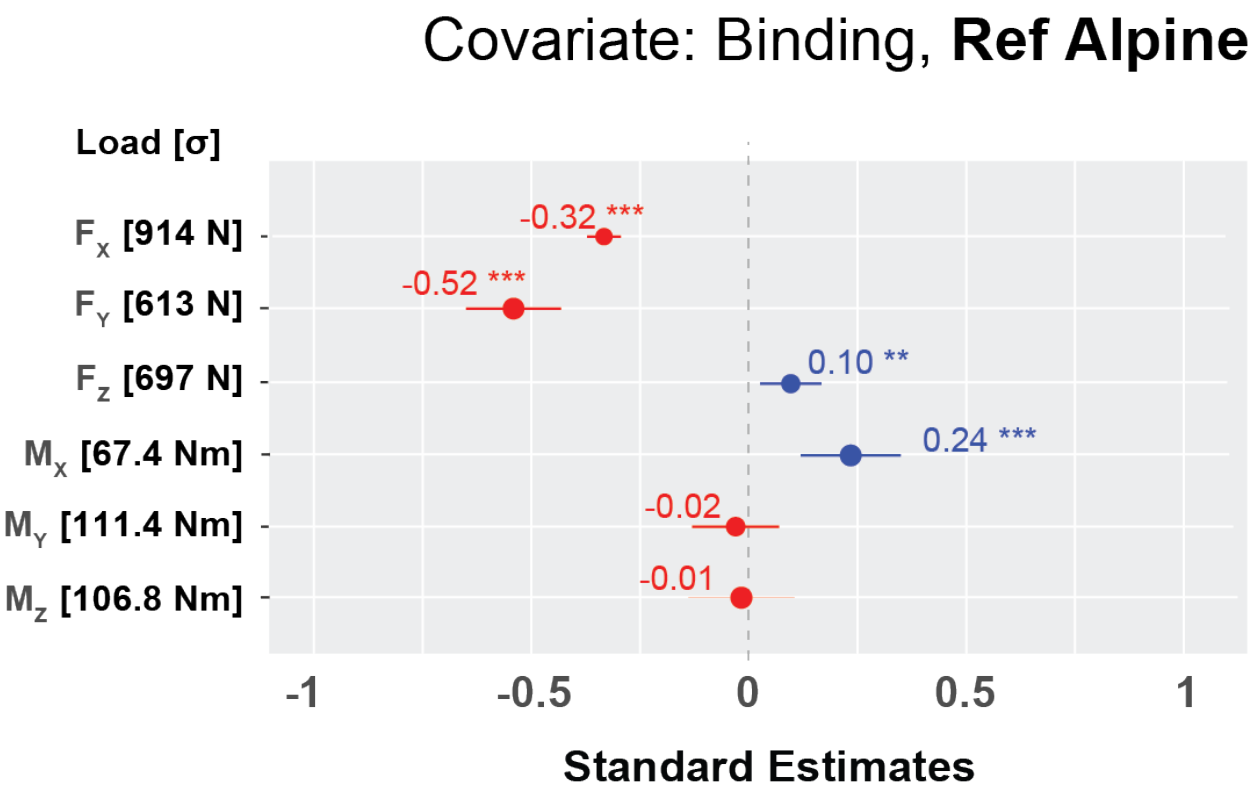

*Figure 9.38: Standardized estimates the independent variable **Binding**. The plotted values indicate the change in load in units of standard deviation measured for AT bindings, relative to Alpine bindings.*

9.7.2.4 Dependent Variable: GRFs at Point O, Covariate: Turn Direction

No significant difference in shear loads [F_X, F_Y] was measured at Point O between the inside and outside turns (Figure 9.39). Outside turns were significantly higher than inside turns for all other loads. This indicates skiers weight the outside foot more than the inside foot.

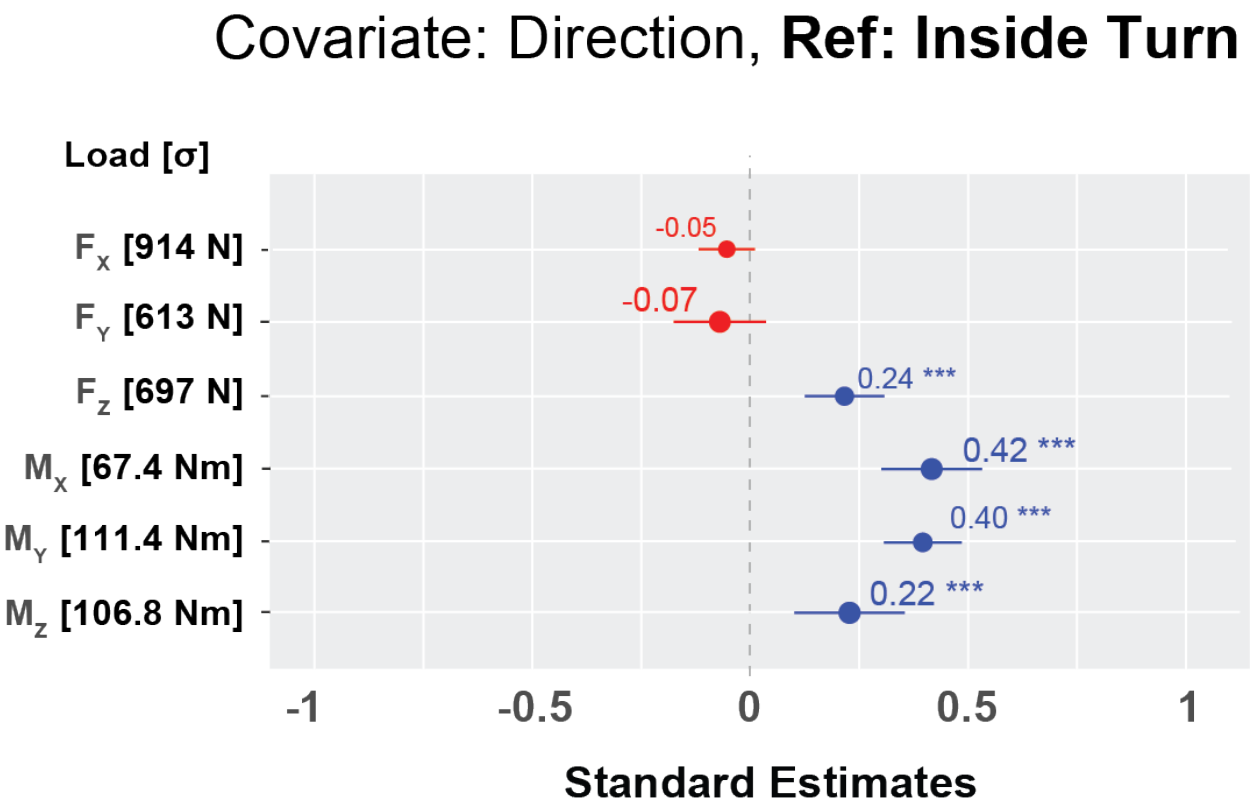

*Figure 9.39: Standardized estimates for the independent variable **Direction**. The plotted values indicate the change in load in units of standard deviation measured on the inside foot of turns, relative to the outside foot of turns.*

9.7.2.5 Dependent Variable: GRFs at Point O, Covariate: Piste

Lower bending torque, $-0.20\sigma^{M}_{y}$, was measured at Point O, on compared to off-piste, indicating skiers are not pressing the boot cuff through the turn as hard off-piste compared to turns on-piste. Other load components were not significantly different (Figure 9.40).

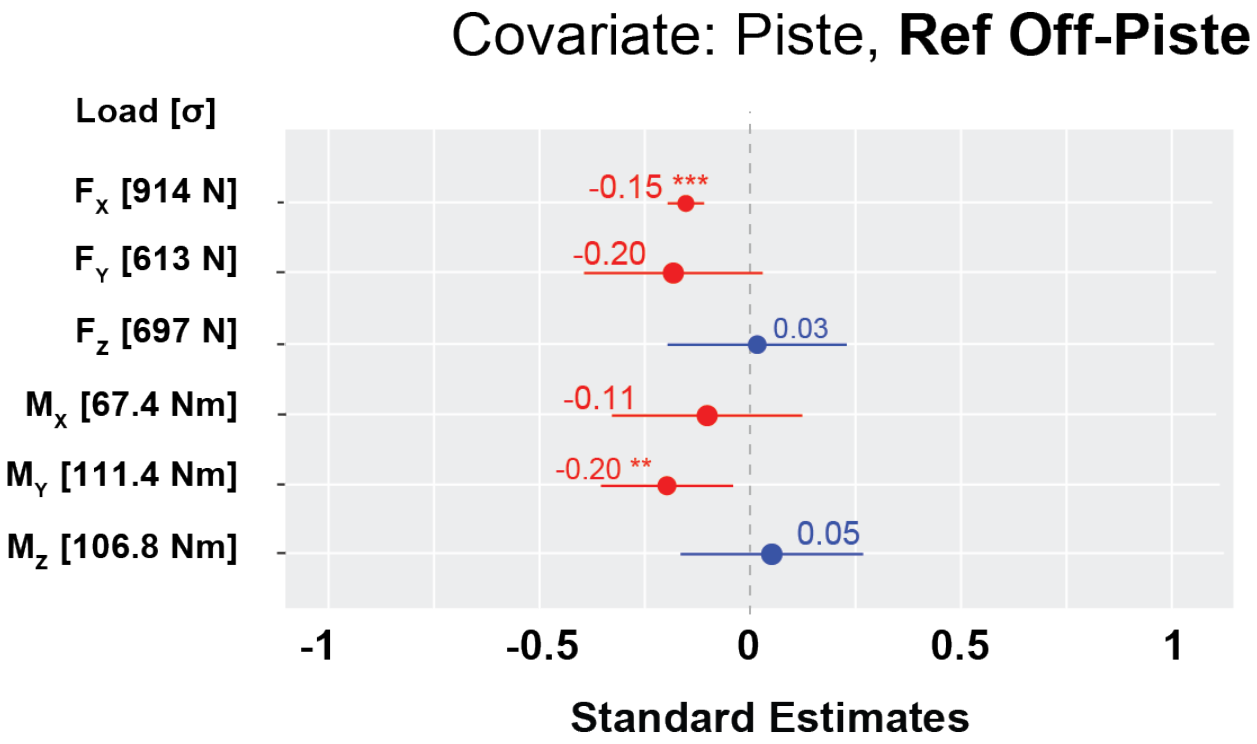

*Figure 9.40: Standardized estimates from the independent variable **Piste**. The plotted values indicate the change in load in units of standard deviation measured on the On Piste slopes, relative to the Off-Piste slopes.*

9.7.2.6 Dependent Variable: GRFs at Point O, Covariate: Piste | Turn Direction

The significant interaction term between Piste and Turn Direction indicates skiers weight their inside and outside feet differently depending on the piste they are skiing on. With the interaction term, it is evident that the slope affects how skiers weight their outside foot. Skiers apply less bending torque to the boot, $-0.34\sigma^{M}_{y}$, than on-piste (Figure 9.41). No significant difference is found in the rolling torque, M_X, on either piste, but skiers still apply more rolling torque to their outside foot, $0.34\sigma^{M}_{x}$, regardless of the piste they are skiing on. Skiers weight their outside foot more, regardless of piste, 0.24^{F}_{z}.

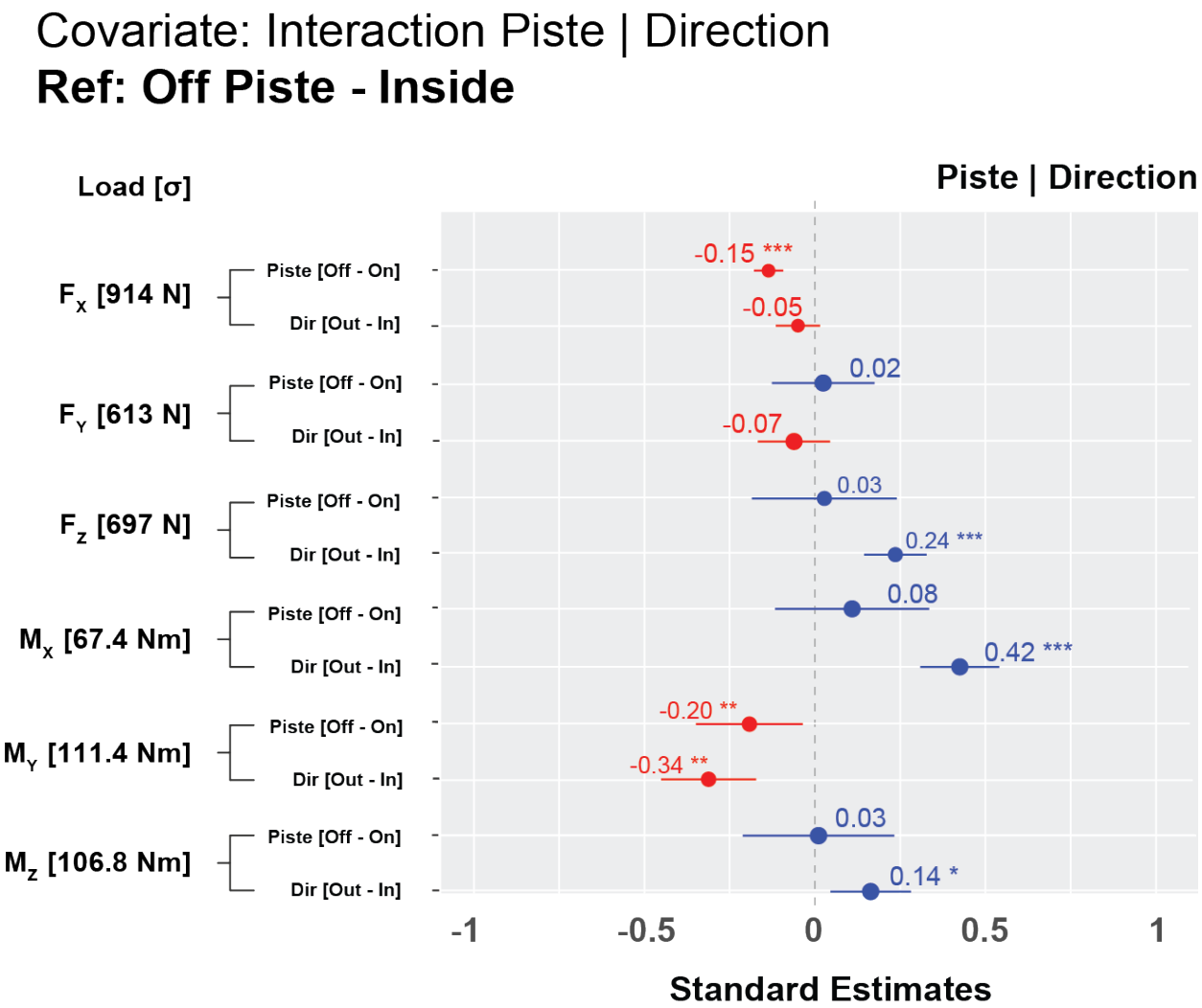

*Figure 9.41: Standardized estimates for the interaction of the independent variable **Piste** and **Direction**. The plotted values indicate the change in load in units of standard deviation measured on the On Piste slopes and the Inside foot of ski turns, relative to the Off Piste slopes and the Outside foot of ski turns.*

9.7.2.7 *Dependent Variable: GRFs at Point O, Covariate: Leg Dominance*

Slightly higher loads were measured at Point on non-dominant legs for M_X and M_Z, $0.21\sigma^M{}_x$ and $0.22\sigma^M{}_x$, respectively (Figure 9.42). Non-dominant legs might use poor technique, resulting in higher loads.

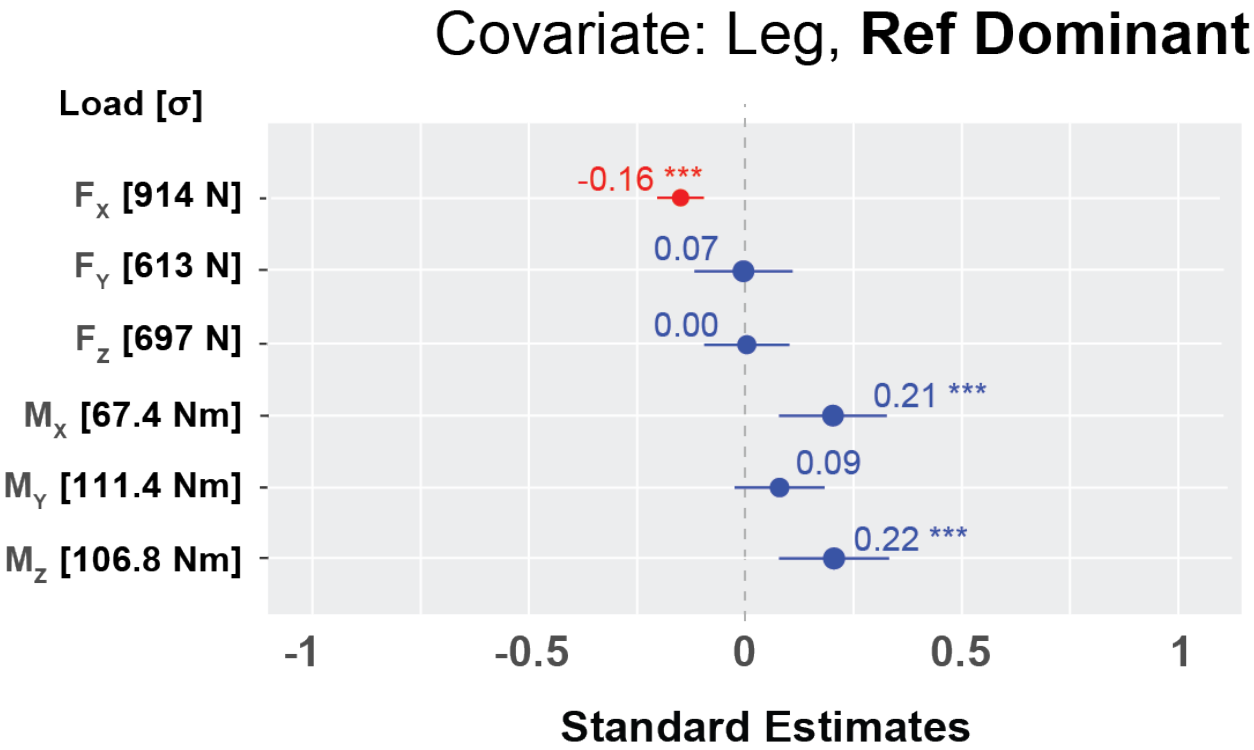

*Figure 9.42: Standardized estimates for the independent variable **Leg**. The plotted values indicate the change in load in units of standard deviation measured on the non-dominant legs, relative to the dominant legs of subjects.*

9.7.2.8 *Dependent Variable: GRFs at Toe and Heel, Covariate: Location | Binding Interaction*

A significant interaction term was found between Binding [Alpine vs. AT] and Location [Heel vs. Toe] for all six-load components. In Figure 9.43, the standardized coefficients are given from each model. The standard deviation is given in square brackets next to each load component. The numbers in each graph give the proportion of the standard deviation needed to change between levels of a given covariate. Skiers appear to weight the alpine bindings differently, since alpine binding toe pieces transmit $.43\sigma^F{}_z$ F_Z compared toe $.12\sigma^F{}_z$ for AT bindings. For alpine bindings, the toe piece transmits $.13\sigma^M{}_x$ of M_X more than the heelpiece while there is no difference in the amount of M_X applied through the toe and heelpieces for AT

bindings. This implies that the heelpiece of AT bindings is transferring more load. This trend is nearly identical for M_Z. Under M_Y however, Alpine binding heelpieces transfer $-0.17\sigma^{M}_{y}$ than Alpine toe pieces. AT binding toe pieces however, transfer $0.19\sigma^{M}_{y}$ more load than AT binding heelpieces.

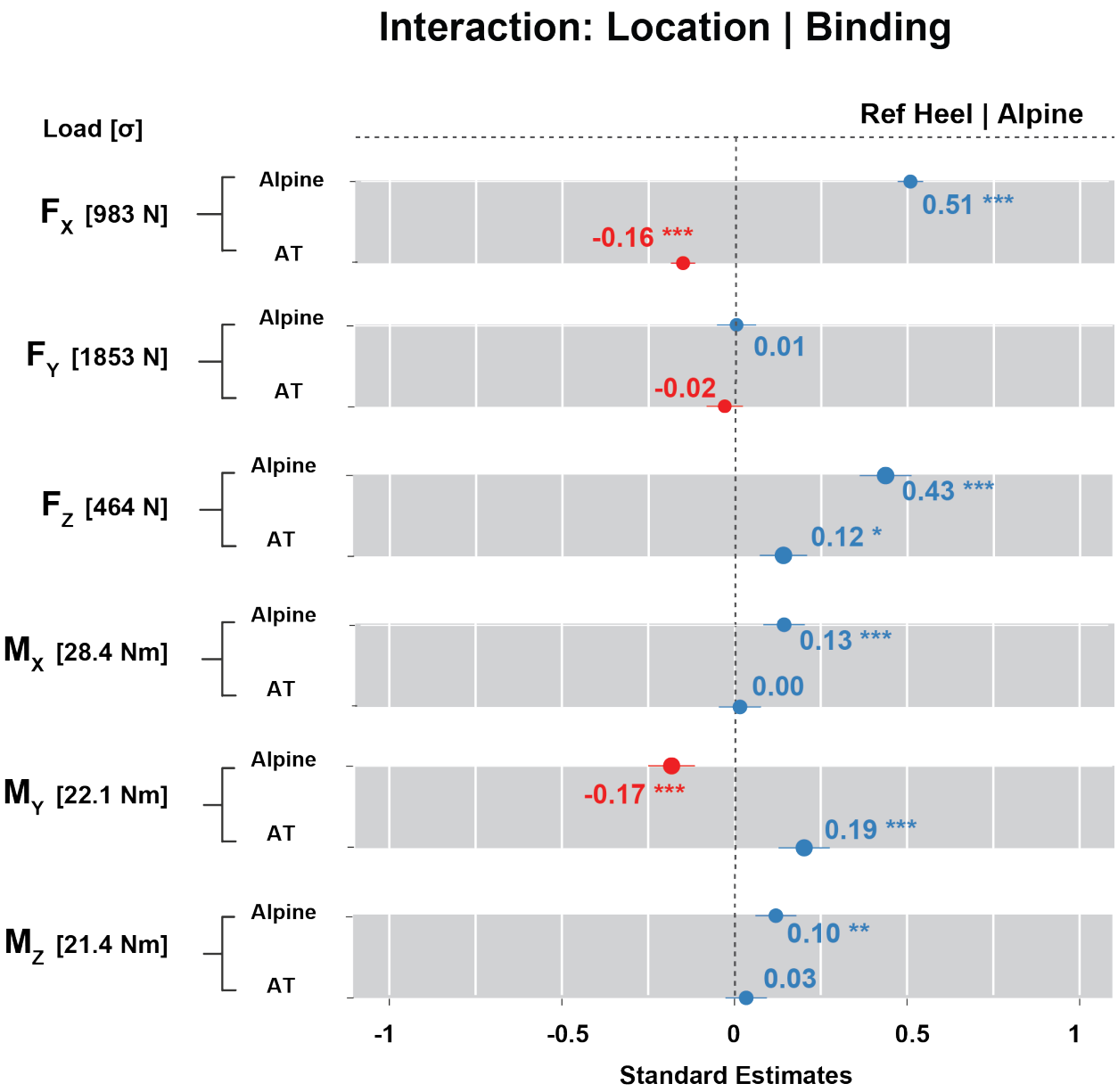

Figure 9.43: Standardized estimates for the interaction of the independent variables Location and Binding. A model for each respective load produces estimates for the fixed effect of Piste and Direction for each load. The plotted values indicate the change in load in units of standard deviation measured on the toe, relative to the heelpiece.

9.7.2.9 Dependent Variable: GRFs at Point O, Covariate: Snow Penetration Depth

Efforts to quantify snow conditions included making temperature measurements of the air 1m off the snow surface, snow surface temperature, and snow penetration measurements. These penetration measurements were taken by having the same observer step with a ski boot heel into the snow after each run on both on-piste and off-piste snow. The depth of penetration of the boot heel was recorded [109].

Snow depth was only a significant contributor to variation in F_Y and M_X. Figure 9.44shows a linear regression on all six load components. R^2 values were extremely low for all six axis force components, but F_X and M_Y were significant contributors to the linear mixed effects models for Point O. Figure 9.45depicts amount F_X and M_Y will change, in units of one standard deviation, σ^F_X and σ^M_Y, for each change in snow depth equal to one standard deviation, $\sigma^{snow} = 3.02$".

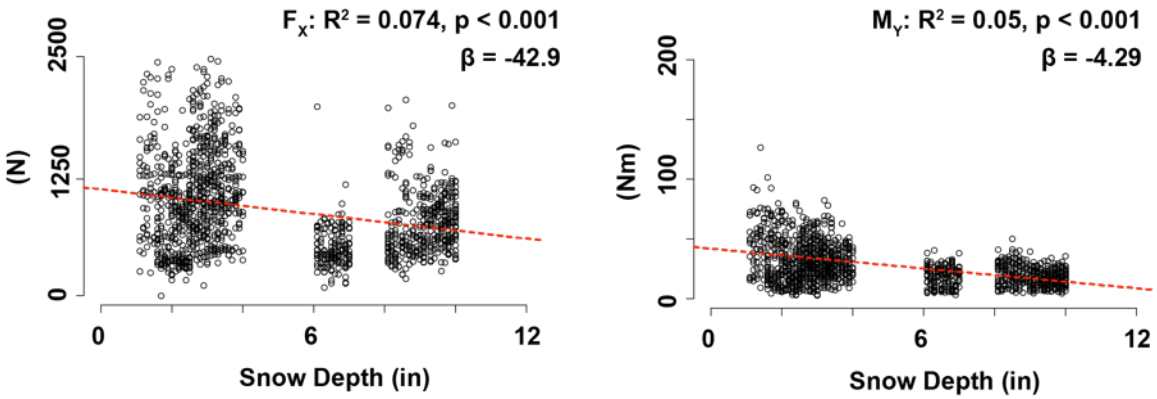

Figure 9.44: Linear regression of FX and MY on snow depth. R2 values were extremely low for all six-axis force components.

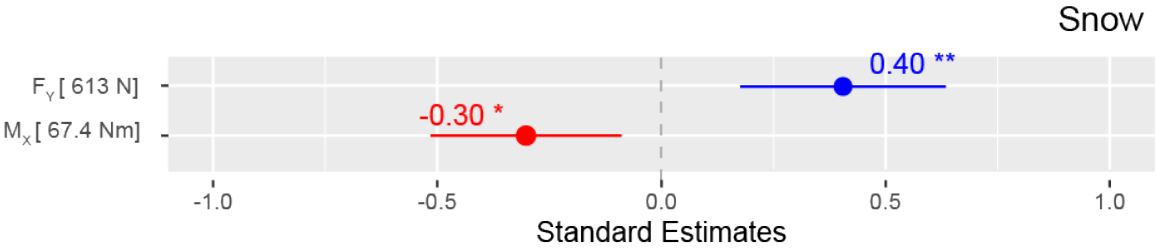

*Figure 9.45: Standardized estimates for the covariate **Snow**. The plotted values indicate the change in load in units of standard deviation measured at Point O. The standardized estimate depicts how much each load will change for each change in standard deviation in snow, $\sigma^{snow} = 3.02$".*

9.7.2.10 Dependent Variable: Knee Flexion Angle

Knee flexion angle was significantly different depending on if the knee was on the inside or outside foot of a turn. Knees on the outside of the turn were straighter, and had a smaller angle, than on the inside of the turn (Figure 9.46).

Males had 6.8° more knee flexion than females. Overall, skiers off-piste had smaller flexion angles, -12.7°, than on-piste. Significant interactions between Gender and Turn Direction shows that the outside knee for males is more straight, -4.7° than females.

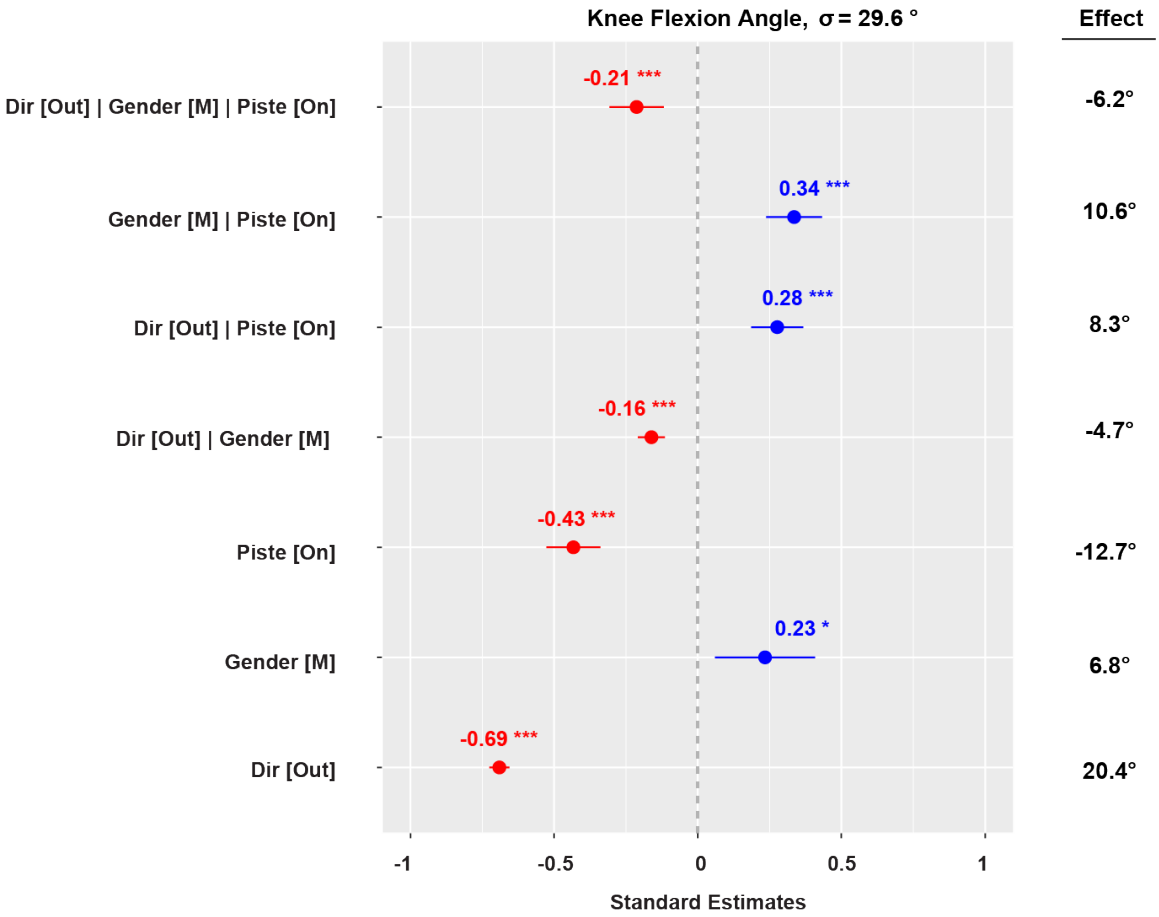

Figure 9.46: Standardized estimates for the Knee Flexion Angle. Covariates with significant effects are shown. The 'Effect' column transforms the standard estimate from units of σ to degrees for covariates with significant affects.

9.7.2.11 Dependent Variable: Knee Flexion Angle, Covariate: Force plate

Knee flexion angle was not significantly different with and without force plates alone (Figure 9.47). Knee flexion angle was not affected by differences in piste alone either. A significant interaction of Force Plates and Piste shows a 6.5° effect on knee flexion angle for on-piste slopes. Other three-way interactions were smaller in magnitude and had an effect of causing lower flexion angles. Overall, the effect of skiing with force plates under the binding force plates appears to be very small on skier kinematics.

An exemplar time history of knee joint angles, and skier speed, during off-piste and on-piste trials is shown in Figure 9.48 for the same subject during subsequent runs with and without sensors under the ski bindings. Sensors did not significantly affect knee adduction-abduction and internal-external. The difference in knee flexion between the trials with and without sensors can be observed in the on-piste trial in Figure 9.48.

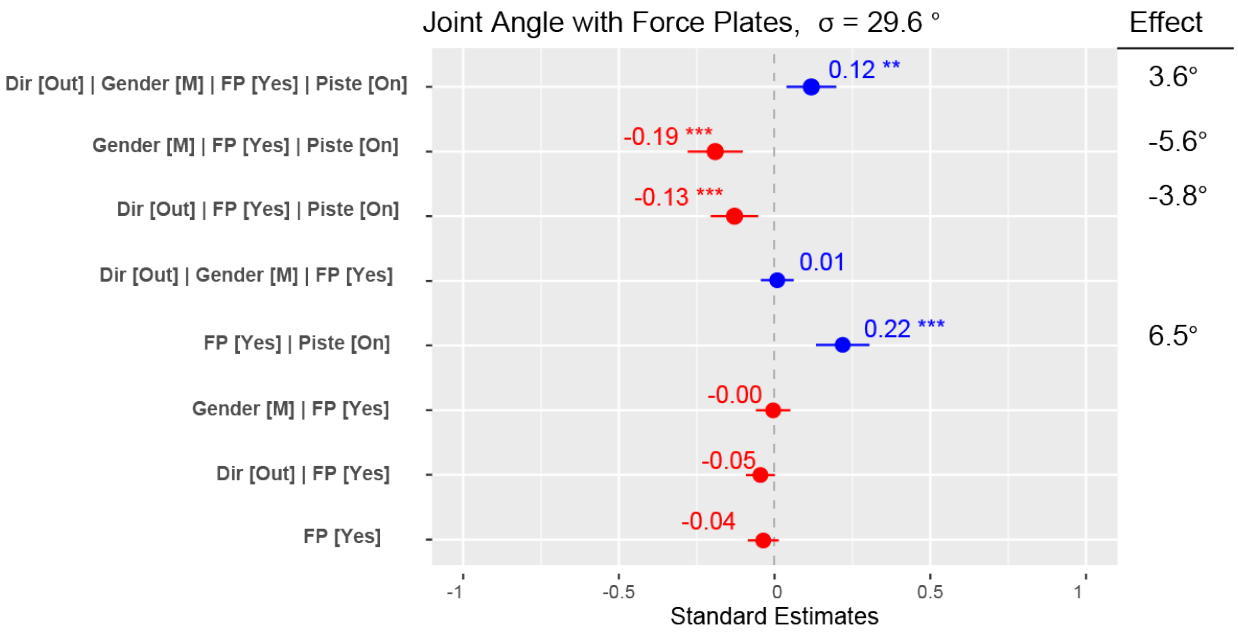

Figure 9.47: Standardized estimates for the Knee Flexion Angle comparing the effect of skiing with force plates under the ski binding, and without force plates (designated as FP). The 'Effect' column transforms the standard estimate from units of σ to degrees for covariates with significant affects.

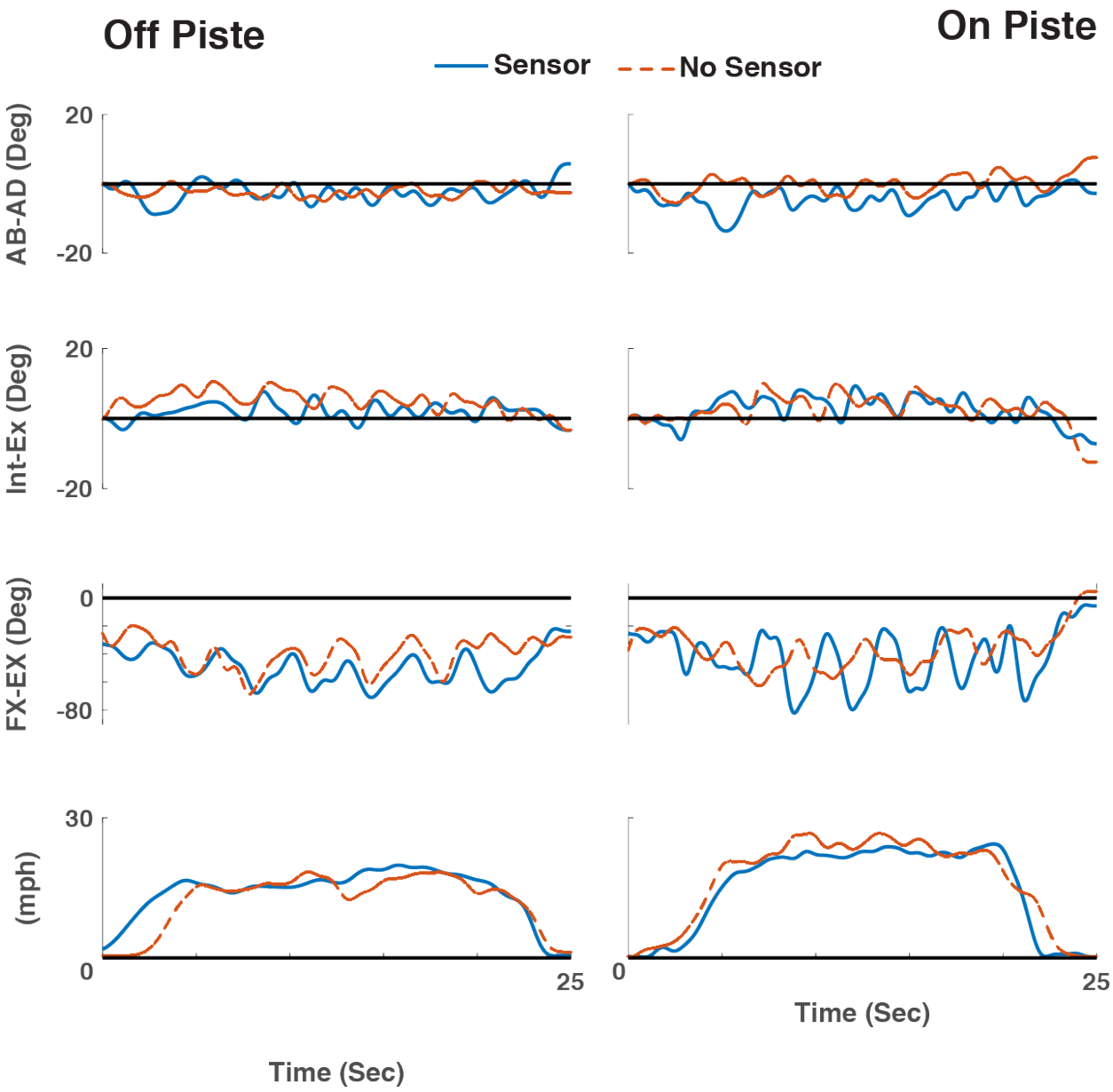

Figure 9.48: *Exemplar time history of two runs off piste (Left) and on-piste (right) from one subject with and without sensors mounted under the binding. The addition of sensors had no significant affect on abduction | adduction and internal | external rotation joint angles. The addition of sensors under the bindings resulted in ~6.5° greater flexion than without sensors during on-piste trials. No significant difference in joint angle was observed during off-piste trials.*

9.7.3 *Discussion*

The purpose of Analysis No. 2 was to elucidate what covariates, or independent variables, contribute the most to variation in the six load components passing through the toe and heel piece of ski bindings to the skier. The statistical analysis presented falls into a class of inferential statistics that attempts to reach conclusions beyond the immediate data collected.

The large number of covariates analyzed increases the degrees of freedom of the analysis and can significantly complicate the analysis. Therefore selection of the appropriate statistical methods was heavily driven by the central purpose of this analysis: to determine which covariates affect the ground reaction forces the most.

Gender, binding, and turn direction all contributed significantly to variation in most if not all six-load components. One surprising result was the relatively small effect piste, when considered by itself, had on ground reaction forces. However, when considered with other covariates, its effect on ground reaction forces was significantly amplified.

Many of the linear mixed effects models had interaction terms that were 3-way or 4-way. These produce upwards of 40 coefficients and effect turns that can be extremely difficult to interpret. This illustrates one benefit of the current analysis: if the 1-way and 2-way effects are examined, they are more easily digested and provide valuable insight. For example, the 2-way interaction between Piste and Turn direction quantified the amount that the six load components change based on the piste, and if the ski being measured is on the inside or outside foot of the turn. Skiers weight their outside foot more heavily on-piste. However, on the variable and uneven surface of off-piste slopes, skiers weight their inside, uphill, leg more proportionally to their downhill leg. Under certain snow conditions such as breakable crust, or heavy thick powder snow, this could pose a greater injury risk than on-piste skiing[5].

The proportion of load transmitted through the toe and heelpiece of Alpine and AT bindings was of particular interest in this analysis. The total amount of load transferred through Alpine and AT bindings was not significantly different for M_Y and M_Z loads (Figure 9.38). However, the difference in load path between the Alpine and AT bindings (Figure 9.43) confirms that while the sum total of certain load components being transferred to the skier through the ski binding does not change based on binding, the path that those load components take as they are transmitted to the skier does.

Previous chapters have discussed the limitations of AT binding toe pieces (Chapter 4) and their limited ability to absorb energy and be adjusted for varying styles and size of skiers. The inferior energy absorption and sensitivity of AT bindings to M_Y and M_Z loads, coupled with the fact that the toe piece must transmit more load, despite being the weakest link in toe piece – heelpiece chain is likely a significant contributor to the perception that AT bindings are susceptible to inadvertent release. Indeed, the previous section 9.6.3, highlighted this very fact, that the release envelopes are likely too conservative for modern ski equipment, and that most binding releases were perceived by skiers to be *false-alarms*.

Finally, this analysis also examined the raw kinematic data to quantify the effect the force plates mounted under the bindings had on skiers, as well as understand which covariates effect knee flexion angles the most. The force plates had a small effect on knee flexion angle (less than 6 degrees) that was most pronounced when females changed between on-off piste. The kinematic data confirmed the importance of analyzing inside and outside turns separately as the magnitude of knee flexion angle changes significantly between each part of the turn.

In conclusion, gender, binding, and turn direction significantly affected the magnitude of binding forces. AT and alpine binding toe and heel pieces transfer the same net load but through different paths. The sensors mounted between the ski and binding affected the knee flexion angle during on-piste trials.

9.8 Analysis No. 3: Loads generated during an inadvertent release in an AT binding, and a comparison of load paths between Alpine and AT bindings

During one data trial, a male was skiing off-piste on an AT binding, which released when the skier was turning down an icy slope at a slow rate of speed. The binding release did not cause the skier to fall and was considered to be an inadvertent release (Figure 9.49). The release occurred on the first run of the day and it is possible that ice or snow was packed into the boot-binding interface. However, this type of inadvertent release is hypothesized to cause skiers to ski with the toe piece of their bindings "locked out" in response to the perception among skiers that inadvertent releases are common when using AT bindings. The objective of Analysis No. 3, is to use this case study to analyze the load components acting on the toe piece, the heel piece, and about Point O to understand what load components contribute to the inadvertent release phenomenon, and if the inadvertent release could be driven by a frequency content.

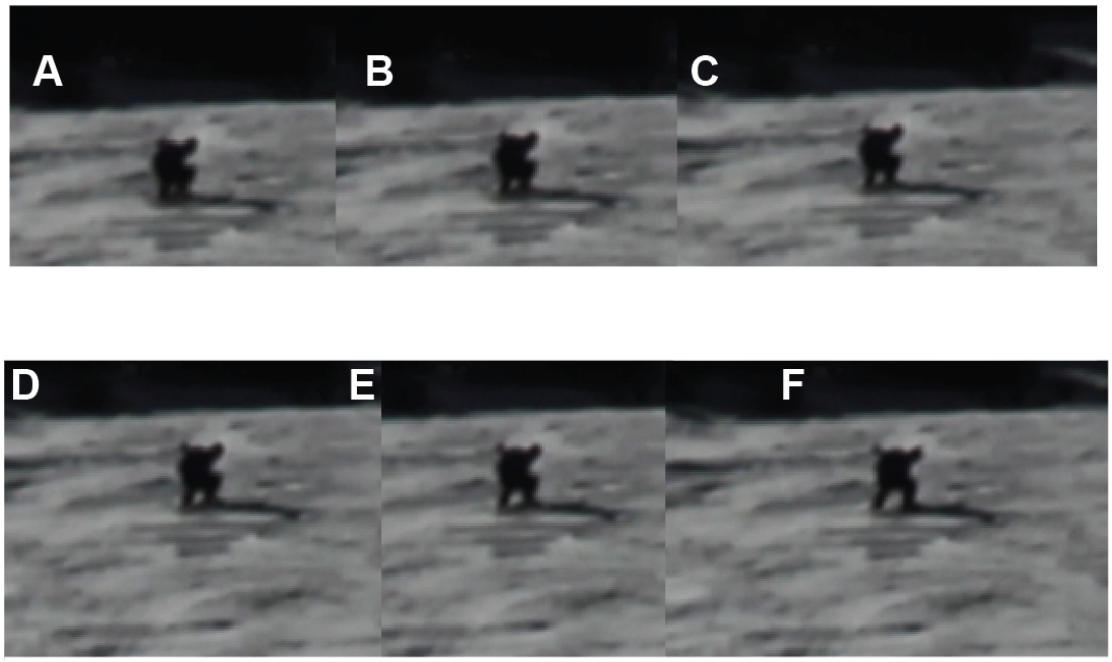

Figure 9.49: Video frames showing the 1 second leading up to the release of the binding, during which the skier did not fall, as shown in the final frame (F).

9.8.1 *Methods*

The ground reaction forces from the trial in which the inadvertent release occurred were analyzed at two levels: 1) Boot Top and 2) Toe and Heel Piece. For comparative purposes, a second trial was selected from the same subject, piste, and leg but measured with an alpine boot. Comparisons between the loads each binding component, toe and heelpiece were analyzed. The load signals were filtered as described in Section 9.4.

9.8.2 *Results*

9.8.2.1 Boot top loads

The loads transformed from Point O to the top of the boot cuff are shown in Figure 9.50. The M_Y and M_Z release limits are shown for comparison of the loads generated during the inadvertent release. The M_Y loads never reach magnitudes that should cause a release. The M_Z loads cross the limit initial limit but stay with in the permissible deviation of 30% for in-use range. Per ISO 8061:2015, the loads generated in the turns leading up to and at the release at the time of the binding release were on the release threshold of the boot.

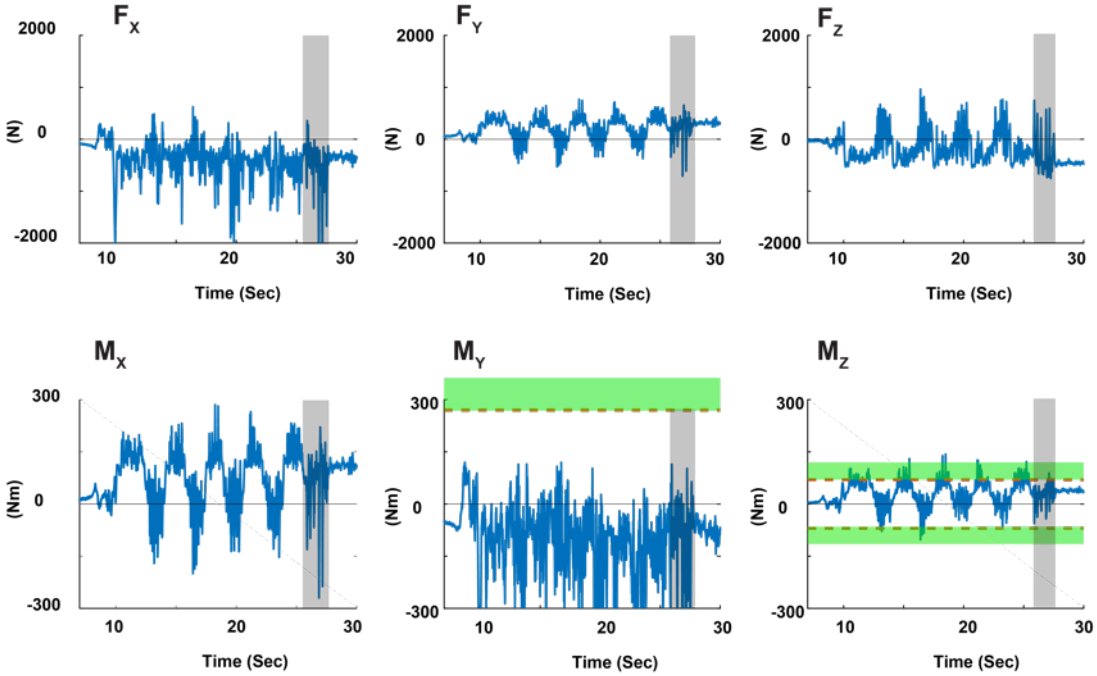

Figure 9.50: Loads transformed from Point O to the boot top. The release values specified by international standards for the M_Y and M_Z release limits are demarcated by the green rectangles which denote the release limit and the additional 30% in-use range limit. The grey zone marks the time range of the sliding turn during which the inadvertent release occurred.

9.8.2.2 Toe and Heelpiece Loads

A comparison of the loads transferred by the toe and heelpieces to the skier is shown in Figure 9.51 and Figure 9.52. The grey shaded region marks the turn during which the inadvertent release occurred. A time history of the entire run is shown in Figure 9.51. During the course of the run, the load sharing of the edge-to-edge rolling torque (Figure 9.30), M_X, and lateral shear loads, F_Y, were born predominantly by the toe piece. This is supported by the results from statistical analysis in Section 9.7.2.8 that showed that AT binding toe pieces transferred more load than the heelpiece. A time history of the turn that produced the inadvertent release, and the turn preceding it, are shown in Figure 9.52.

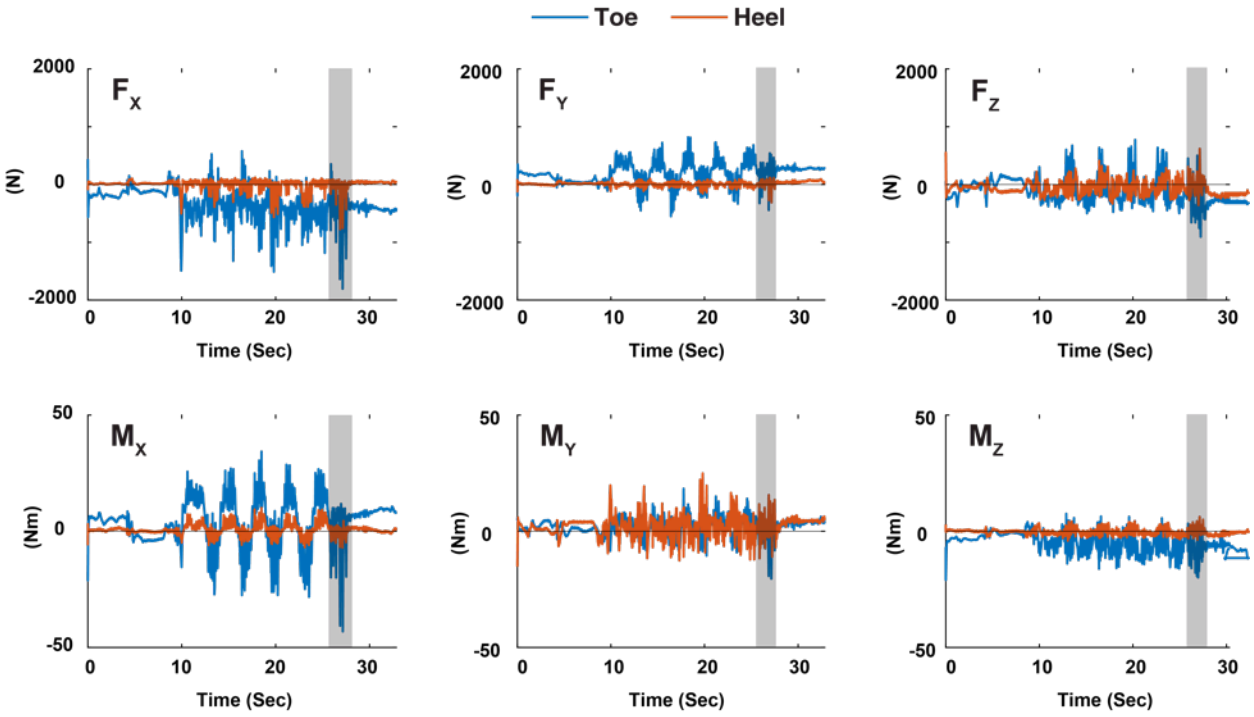

Figure 9.51: A Time history of the six load components measured at the toe and heelpiece. The shaded region is the turn during which the inadvertent release occurred.

The load component that appears to be dominating the toe and heelpieces during the turn that resulted in the inadvertent release is M_X. Several high-frequency peaks are seen in the toe piece leading up to the release. Little response is seen from the heelpiece. This is hypothesized to be a limiting function of the boot-binding interface for AT Bindings. For applying the edge-to-edge rolling torque, M_X, the toe piece has significantly greater mechanical advantage than the heelpiece (Figure 9.53).

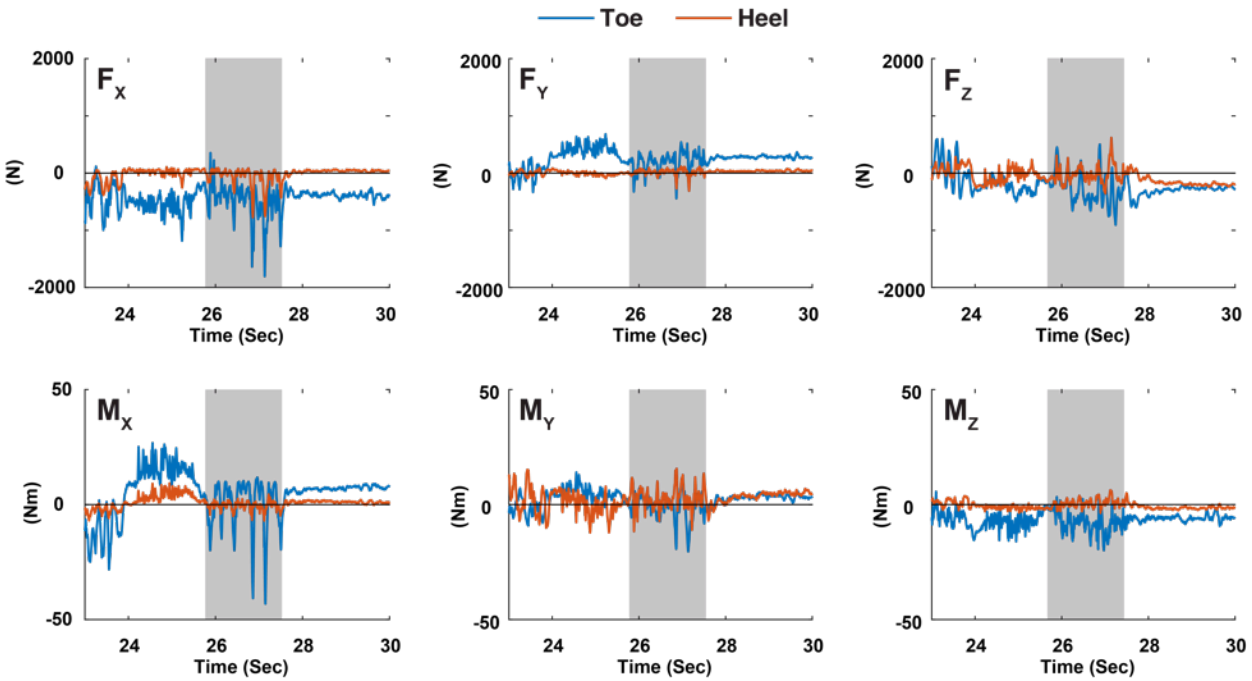

Figure 9.52: A Time history of the six load components measured at the toe and heelpiece. The shaded region is the turn during which the inadvertent release occurred.

However, as shown in Chapter 4.2.2, the force-displacement relationship of the toe piece places this binding at a disadvantage. As shown in Figure 9.54, the clamping constraint force applied to the boot by the binding decreases as the toe piece opens.

One possible mechanism driving the pre-release of AT bindings is the high frequency peaks shown in Figure 9.52 incrementally force the toe piece open before it can return to center at it's equilibrium position, shown in Figure 9.54. As the magnitude and frequency of the loading increases, the binding is less likely and capable of returning to its equilibrium position.

Alpine bindings do not suffer from the same mechanism of inadvertent release, rather large deformations are thought to release the heel of the boot during inadvertent release in alpine bindings. To compare the loads between the toe and heelpieces under the conditions that generated the inadvertent release being considered in this section, loads from the run with the inadvertent release were plotted along side data from a trial for the same subject, piste, and leg using Alpine bindings (Figure 9.55). No significant differences between the toe and heelpieces can be observed in the Alpine bindings while, significant differences can be observed in F_Y, M_X, and M_Z between the toe and heelpieces of AT bindings.

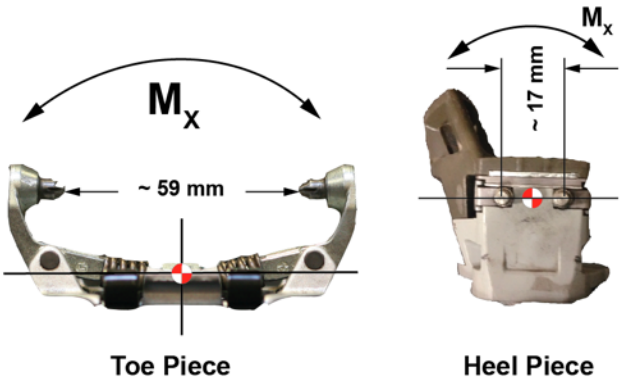

Figure 9.53: The mechanical advantage of the binding toe piece (left) is significantly larger than the mechanical advantage of the heelpiece interface with the AT Boot (right).

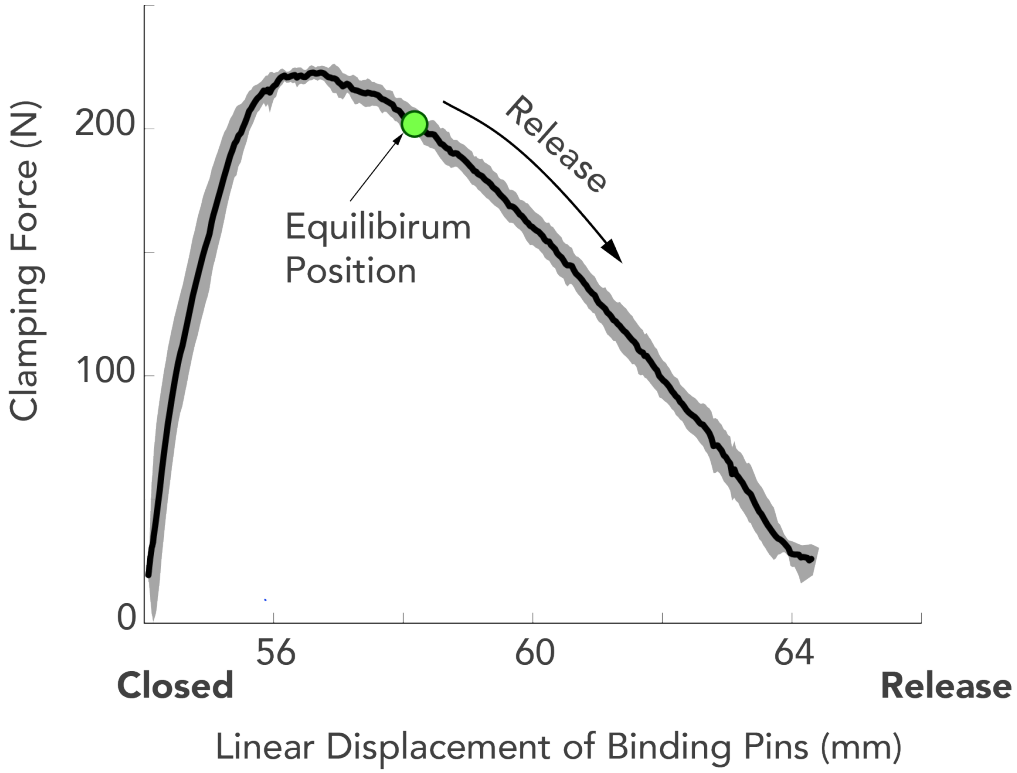

Figure 9.54: Clamping force of the toe piece decreases as the toe piece is forced open. As magnitude and frequency of the loading increase, the binding is unable to return to the equilibrium position.

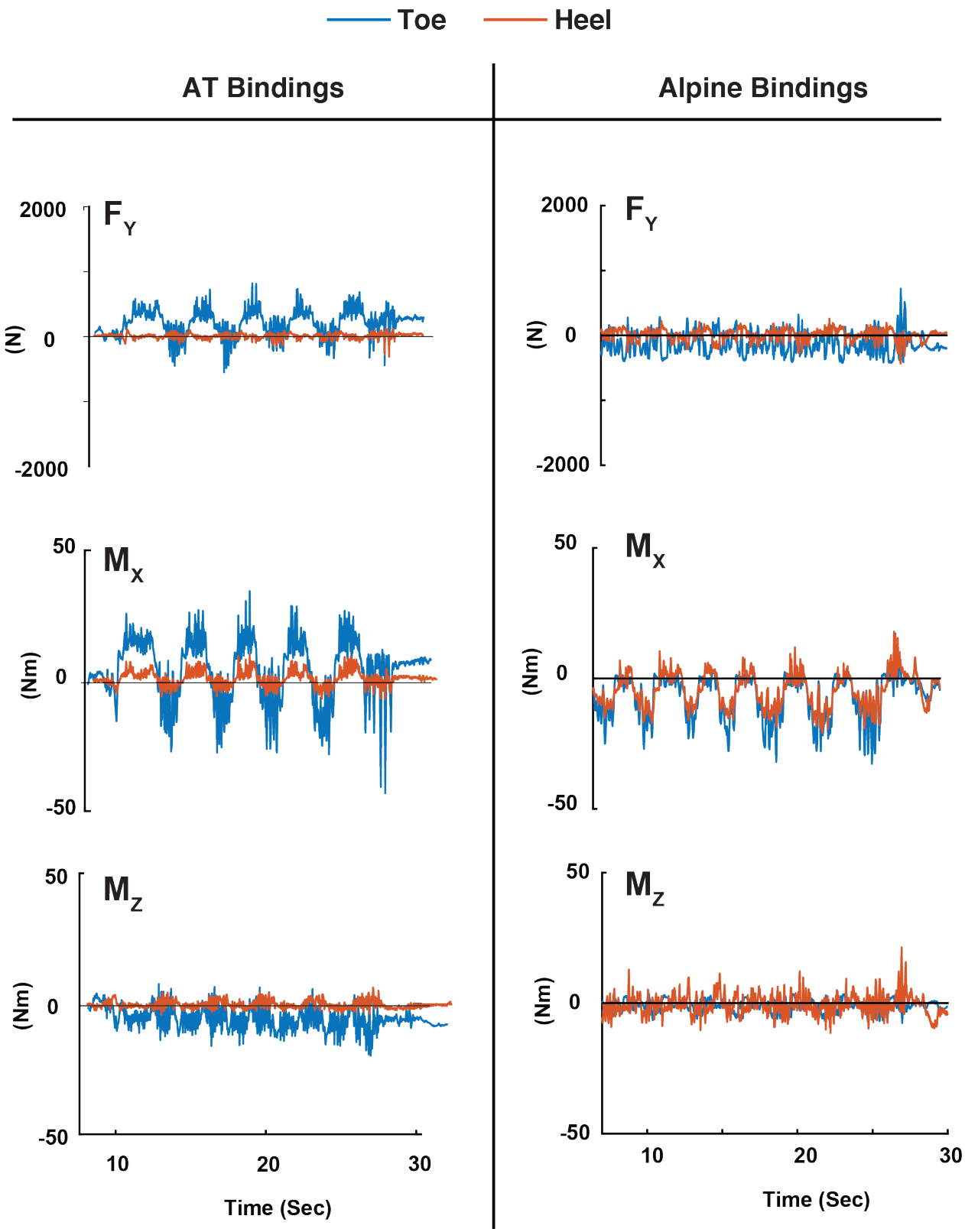

Figure 9.55: Differences in the load path through the toe and heelpieces of AT bindings (left) and Alpine bindings (right).

Figure 9.56 uses results from a Fast Fourier Transform (FFT) to show the frequency content of the turn with the inadvertent release sign and compare it to other turns on AT bindings and Alpine bindings under the same subject, piste, and leg conditions. The frequency content from the turn with the inadvertent release is significantly different from the turns from both bindings without a release. The nominal frequency of the turn analyzed from the Alpine binding, and AT binding without a release was 4.1 Hz. However, the turn that resulted in the inadvertent release contained several peaks in frequency at 2.8 Hz, 6.7 Hz, 10.8 Hz, and 13.5 Hz.

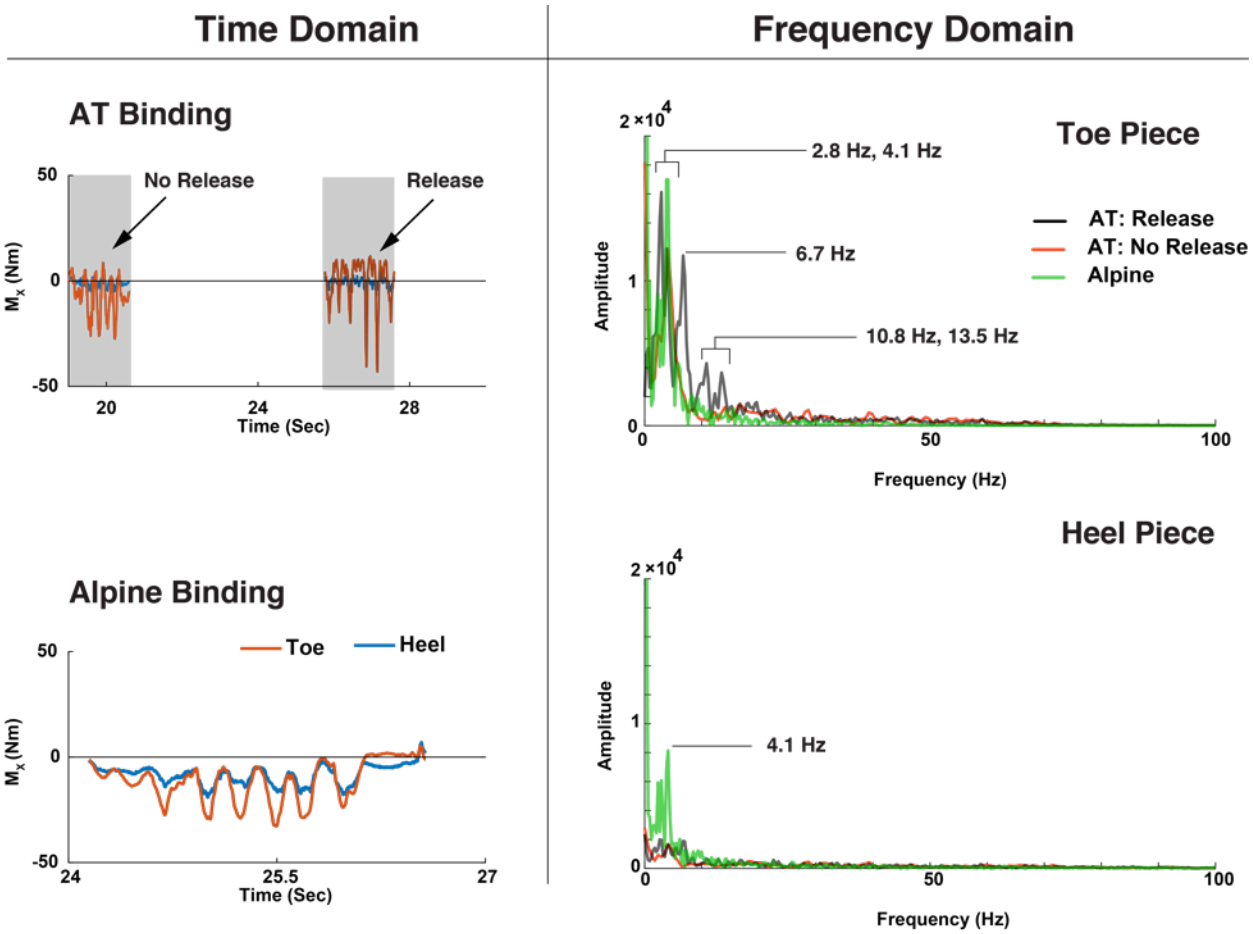

Figure 9.56: A comparison of the frequency content using an FFT on the M_X loads for 1) AT binding during a during with no release, 2) a turn that produced the inadvertent release, and 3) one turn from alpine bindings for the same subject, leg, and piste as what produced the inadvertent release.

9.8.1 *Discussion*

The toe piece of AT bindings transfers a significantly larger portion of loads to the skier than the heelpiece. This differs significantly from Alpine bindings where the differences between toe and heelpiece are nearly indistinguishable for certain loads. AT bindings transfer loads to the skier through different pathways than Alpine bindings, relying heavily on the toe piece which as been shown to be very limited in it's ability to absorb energy (Section 4.3.3). The data presented in this analysis show that the pre-release mechanism could be a function high-frequency loads that when applied at lower frequencies, do not cause the pre-release to occur. As the magnitude and frequency of the loading increases, the binding is less likely and capable of returning to its equilibrium position.

The release occurred on the first run of the day and it is possible that ice or snow was packed into the boot-binding interface. The loads generated during the inadvertent release were not significantly large, but the repeated peaks of from the hard icy conditions are unmistakably different from the previous turns in the trial (Figure 9.51). This example of an inadvertent release is likely the only sample that exists of an inadvertent release in an AT binding that has been measured by recording all six load components at the toe and heel individually. Out of 147 runs, this is the only instance that was observed and recorded. However, future studies could record longer ski runs in firm and icy conditions to attempt to reproduce these phenomena and obtain a greater sample size than the one instance explored in this chapter.

The natural frequency of skis has been shown to range between 10-150 Hz depending on geometry and materials used in construction[120] . Given the different peaks on frequency from the turn that induced the inadvertent release, one potential mechanism of an inadvertent release could be resonance of the AT binding toe piece. Future laboratory studies could examine the interaction between the natural frequency of the AT binding toe piece, the natural frequency of the ski, and the frequency of the forces acting on the skis to examine the plausibility or likelihood of the AT binding toe piece resonating if ski conditions produce an appropriate forcing function.

It is important to note that this case study examines the hypothesized prerelease mechanism from one event. While providing valuable insight into the possibilities of the mechanism driving the pre-release phenomena, it imperative to measure more instances of these phenomena before drawing absolute conclusions, and developing proposed solutions.

9.9 Analysis No. 4: Predicting maximum GRF values from simple anthropometric measurements of skiers

International standards currently use common anthropometric measurements such as height and weight to determine binding settings for an individual skier. A recent prospective epidemiological study by Ruedl et. al[14] proposed including gender as a factor to determine binding settings. There is some evidence that shorter skis may have caused ACL injuries to decline[15,16,121]. The purpose of this analysis is to determine if gender or ski length are reliable factors that could be used to more appropriately determine ski binding indicator settings for individuals.

9.9.1 *Methods*

Using the maximum forces at Point O from Analysis No 2, a multiple linear regression analysis was performed on each of the six load components. The ratio of the ski length relative to skier height skier height (labeled Ski_Ratio), skier height, weight and gender were used as covaraites [15]. The contribution to the overall variation described by each linear regression, R^2, for each of these predictors was calculated using the *relaimpo* package in R[55].

9.9.2 *Results*

Skier height and weight represented 19.6% and 18.2% of the variation in M_Y and M_Z loads measured at Point O, respectively (Table 9.5). A regression on each covariate is shown in Figure 9.57.

Ski-Ratio and gender improved the R^2 correlation coefficient from 20.5% and 25.6% of the variation in M_Y and M_Z loads measured at Point O, respectively (Table 9.5).

Ski-Ratio and gender improved slightly increased the overall correlation coefficient to $R^2 = 0.225$ and $R^2 = 0.254$ for M_Y and M_Z, respectively. Although very low, the p value $p < 0.001$ indicates a significant correlation, though regressors, only account for 25.4% of the variance explained by the model. Overall, Ski-Ratio and gender only improved the ability to predict maximum M_Y and M_Z, loads by 3.0% and 7.3%, respectively. The greatest predictors for M_Y for M_Z loads are weight, and height, respectively (Table 9.5).

Table 9.5: Parameters from linear regression models for covariates to predict M_Y and M_Z. β represents the slope, or strength of the effect each parameter had on the loads, while the p-value represents the probability that the β is not equal to zero (has no effect).

Model No.	Parameter	β	S.E.	t	p	% σ^2	η^2	Model Fit
M_{Y1}	**Intercept**	311	32.9	9.5	< 0.001	-	-	F(2,1368) = 166.2
	Height	-3	0.3	-10.3	< 0.001	4.3%	0.06	**R^2 = 0.1948**
	Weight	1	0.1	17.1	< 0.001	15.3%	0.17	*p < 0.0001*
M_{Y2}	**Intercept**	-885	177	-5.0	< 0.001	-	-	F(2,1367) = 130.6
	Height	0	0.4	-0.2	0.838	3.2%	0.00	**R^2 = 0.221**
	Weight	1	0.1	15.5	< 0.001	15.6%	0.14	*p < 0.0001*
	Ratio	754	110	6.9	< 0.001	3.5%	0.03	
M_{Y3}	**Intercept**	368	35.6	10.3	< 0.001	-	-	F(2,1367) = 117.8
	Height	-3	0.3	-10.9	< 0.0001	4.4%	0.07	**R^2 = 0.2054**
	Weight	1	0.1	11.9	< 0.001	10.5%	0.08	*p < 0.0001*
	Gender	19	4.7	4.0	< 0.001	5.7%	0.01	
M_{Y4}	**Intercept**	-750	183	-4.1	< 0.001	-	-	F(2,1367) = 100.5
	Height	0	0.5	-0.9	0.377	2.6%	0.00	**R^2 = 0.2251**
	Weight	1	0.1	11.5	< 0.001	11.2%	0.08	*p < 0.0001*
	Ratio	694	112	6.2	< 0.001	3.3%	0.02	
	Gender	13	4.7	2.8	0.00453	5.6%	0.00	
M_{Z1}	**Intercept**	-1148	237	-4.8	< 0.001	-	-	F(2,1355) = 151.2
	Height	7.7	1.4	5.4	< 0.001	13.8%	0.11	
	Weight	3.3	1.4	2.5	0.014	4.4%	0.01	**R^2 = 0.1812**
	Height |Weight	0.0	0.0	-2.8	0.006	0.5%	0.00	*p < 0.0001*
M_{Z2}	**Intercept**	-1572	297	-5.3	< 0.001	-	-	F(2,1355) = 151.2
	Height	8.4	1.5	5.8	< 0.001	11.0%	0.06	
	Weight	3.0	1.4	2.2	0.027	3.5%	0.01	**R^2 =0.1812**
	Ratio	297	125	2.4	0.018	4.1%	0.00	*p < 0.0001*
	Height |Weight	0.0	0.0	-2.6	0.01	0.4%	0.00	
M_{Z3}	**Intercept**	-684	231	-3.0	0.003	-	-	F(2,1355) = 155
	Height	5.5	1.4	4.0	< 0.001	11.4%	0.08	
	Weight	0.9	1.3	0.7	0.494	4.7%	0.06	**R^2 =0.254**
	Gender	56.7	5.0	11.3	< 0.001	9.3%	0.07	*p < 0.0001*
	Height |Weight	0.0	0.0	-1.6	0.115	0.2%	0.00	
M_{Z4}	**Intercept**	-765	293	-2.6	0.009	-	-	F(2,1355) = 116.3
	Height	5.6	1.4	4.0	< 0.001	9.1%	0.03	
	Weight	0.9	1.3	0.7	0.515	4.3%	0.06	**R^2 =0.254**
	Ratio	54.6	122	0.4	0.654	3.4%	0.00	*p < 0.0001*
	Gender	56.3	5.1	11.0	< 0.001	8.7%	0.07	
	Height |Weight	0.0	0.0	-1.5	0.124	0.2%	0.00	

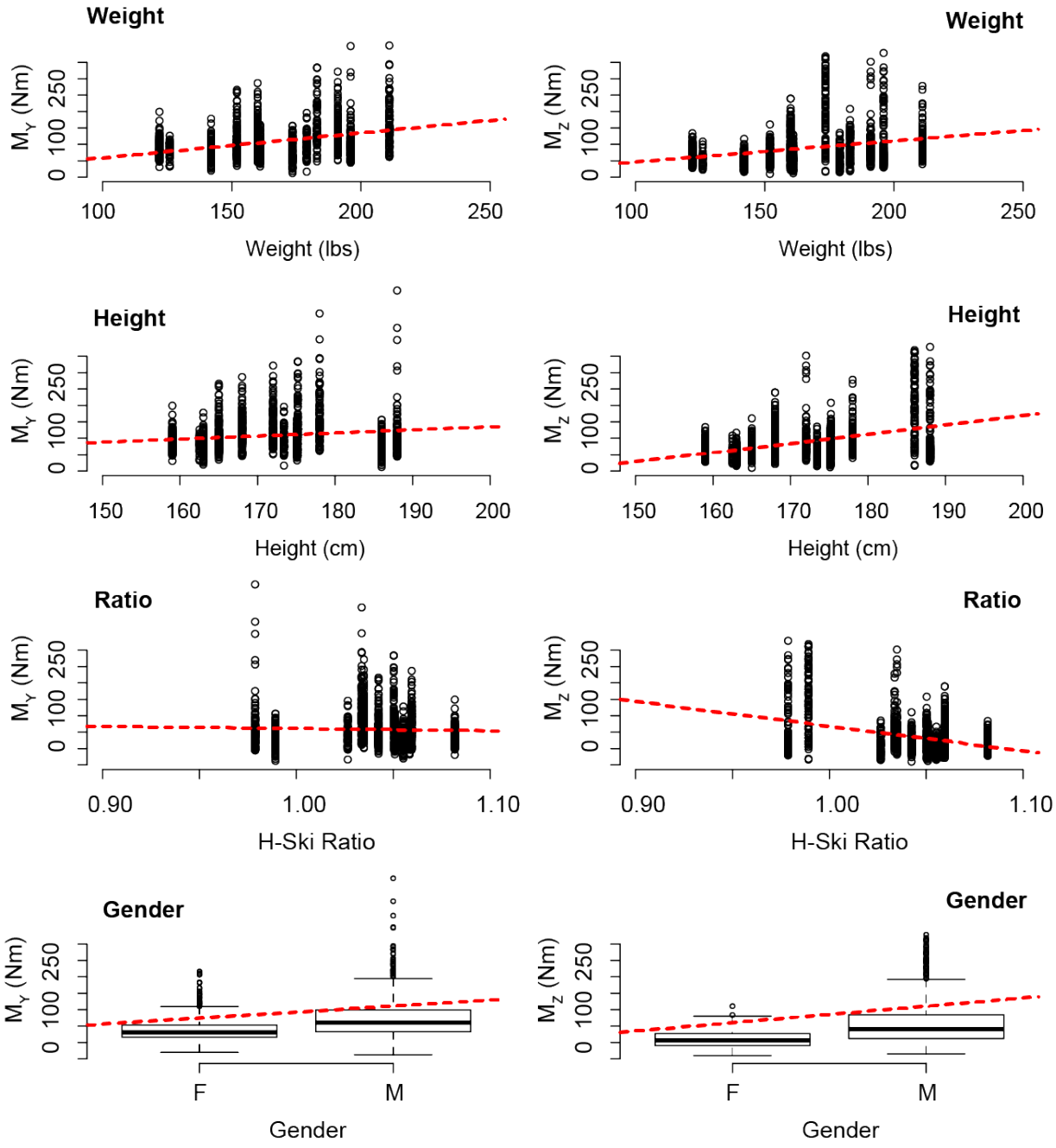

Figure 9.57: Multiple linear regression for M_Y and M_Z on skier weight, height, and the ratio of ski length to skier height, and Gender.

9.9.3 *Discussion*

Shealy et. al. reported that during the development of standards for release values, skier weight was the single best predictor of the Minimum Retention Required (MRR)[4]. Current standards utilize skier weight along with other parameters such as height and age to select the appropriate release value for a given skier[32,33]. However, Scher reported skier weight was a poor predictor of a MRR for a particular skier[27]. Crawford also reported poor correlation with skier weight and MRR, typically less than $R^2 = 0.3$.

In the present study, a regression on the maximum M_Y and M_Z loads generated during skiing, and the weight of each skier is also poorly correlated (Table 9.5). Other studies have reported lower injury rates with shorter skis[15], or have proposed including gender as a factor for lower release values[14].

When the ratio of ski length to skier height, and gender are included in a linear model, ski length ratio has little effect on the strength of the correlation. Gender has a stronger effect but overall it only improves the fit of the model by 6% (Table 9.5). Even though including Gender as a covariate in the linear regression slightly improves the model fit, this does not imply that release values that are determined by considering gender will reduce the incidence of knee injuries[4,13].

In conclusion, gender is not a strong predictor of the MRR values for an individual skier and would not likely improve binding performance for males and females.

9.10 Analysis No. 5: Analysis of Skier Velocity

Skier binding settings are in part, determined by a classification that skiers select that describes how aggressively they ski (Figure 9.1). Ruedl et. al. hypothesized that women over-estimate how fast they ski and thereby inadvertently self-select a higher binding setting than necessary[14]. Speed can also have significant ramifications in the event of an inadvertent release[8,11]. In this section, skier speeds and the corresponding ground reaction forces for men and women are compared for on and off piste runs to evaluate if there are drastic differences in speed between genders.

9.10.1 *Methods*

Figure 9.58 shows the trial used for testing and the track that male and female skiers utilized to descent the slope. Ground reaction forces were down sampled to 100 Hz to match the GPS data sampling rate, and a linear regression analysis was performed to compare how well skier speed predicted ground reaction forces summed about point O. Maximal speeds from each turn analyzed in the previous chapter were compared using a linear mixed effect model to compare skier speed across gender and piste (Figure 9.59).

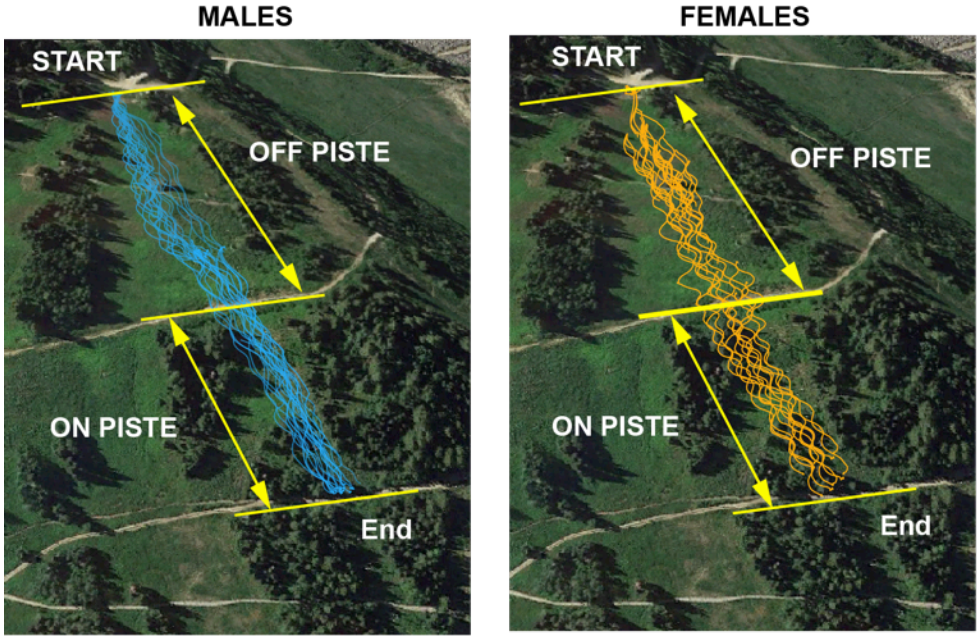

Figure 9.58: GPS tracks male (blue), and female orange) overlaid on a satellite map of the test slope. Note the orange track runs through shadows from the satellite image, and not through trees.

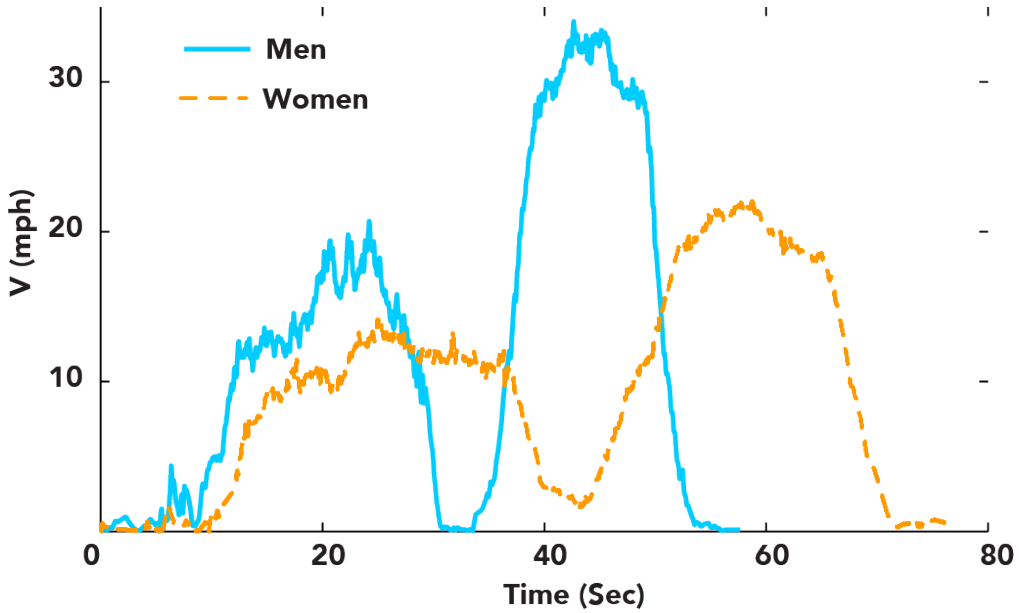

Figure 9.59: Skier velocity for an exemplar male and female skier. The two humps correspond to skiers pausing between the off-piste (first hump) and on-piste (second hump) slopes.

9.10.2 ***Results***

A significant linear regression was found for predicting skier speed using gender and piste as regressors but it only predicted 3% of the variation in skier speed ($F(2,254,118) = 2566$, $R^2 = 0.03$, $p < 0.001$. Skier speed was significantly different between off and on-piste slopes $p < 0.001$ (Figure 9.60). Skier speeds for men and women were significantly different off piste $p < 0.001$ but the effect size for piste was small, $\eta^2 = 0.014$ (Figure 9.60 and Figure 9.61). Men skied approximately 7 mph faster than women on-piste ($\beta = 7.41$, SE = 0.156, $p < 0.001$). No significant difference in skier speed was found between bindings. Skier speed was not significantly correlated to any of the six ground reaction force components summed about PointO (Figure 9.62).

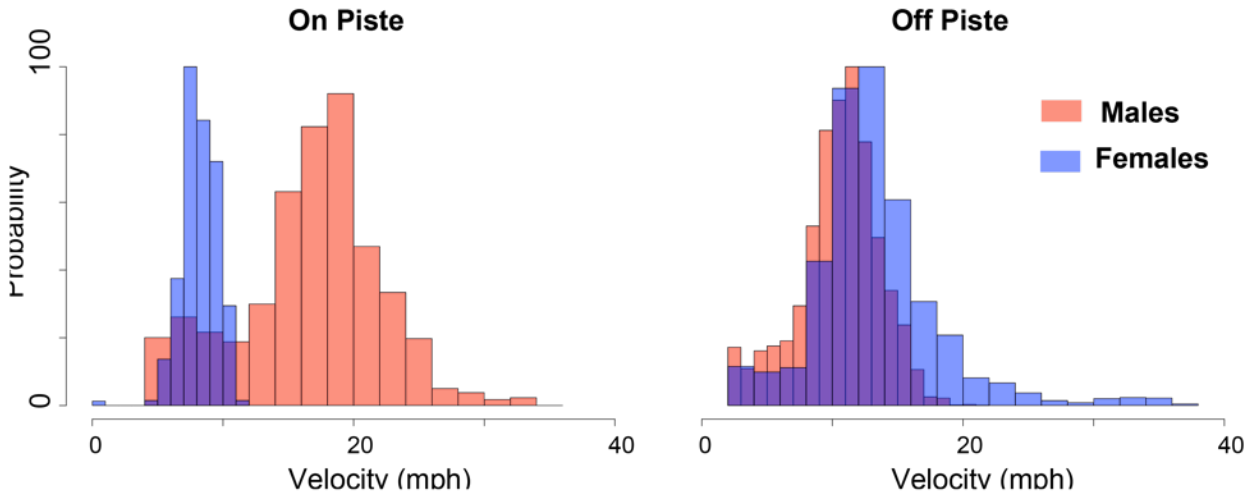

Figure 9.60: Distribution of male and female skier velocities on and off piste.

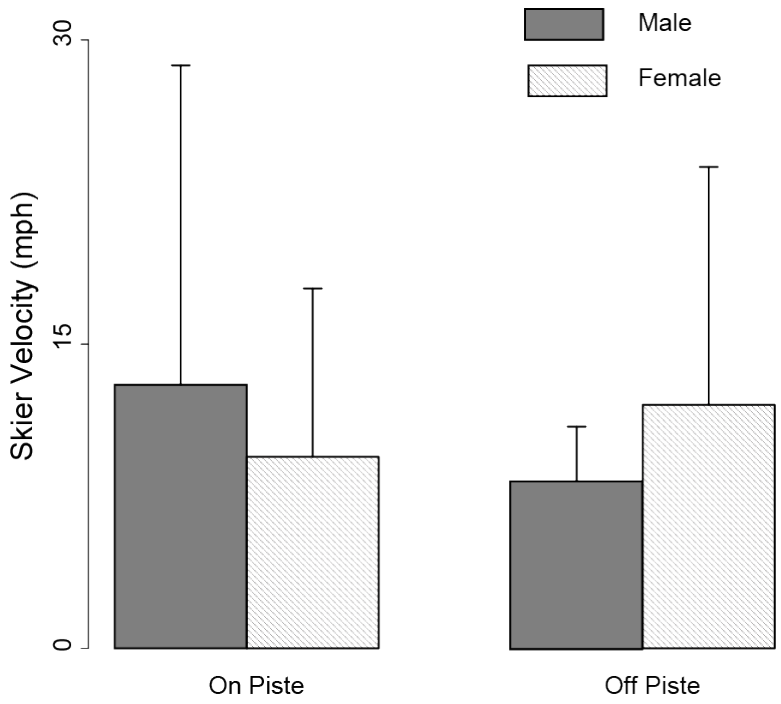

Figure 9.61: Mean skier velocity for male and female skiers for On-Piste and Off-Piste slopes.

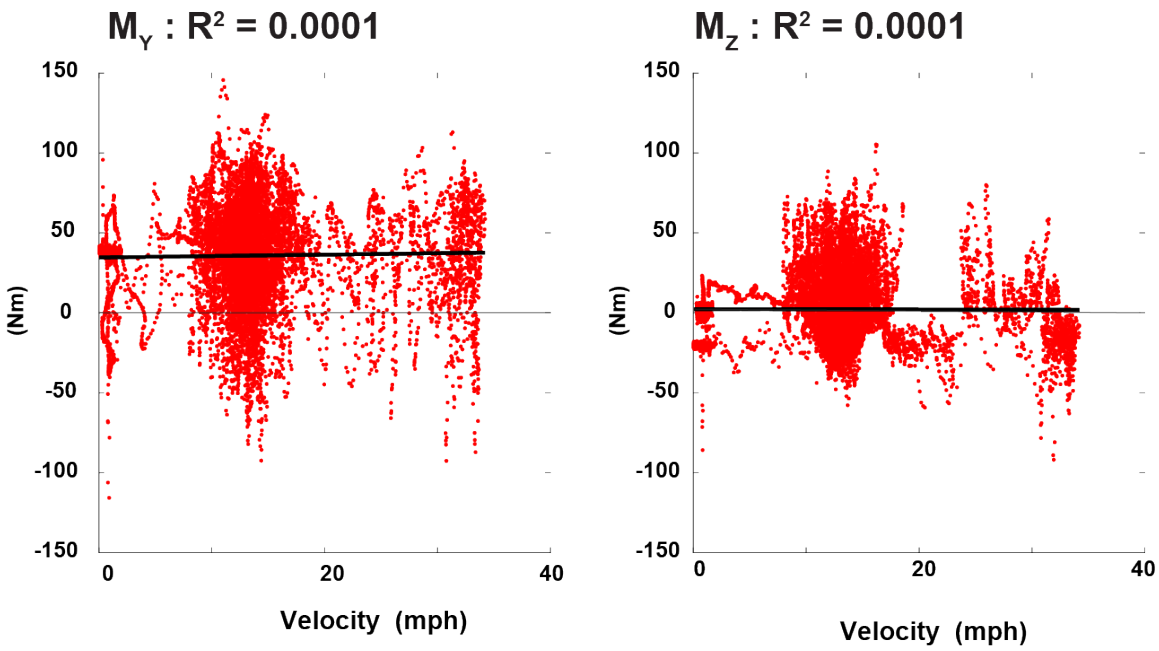

Figure 9.62: Exemplar linear regression from one run demonstrating how skier velocity was not correlated to ground reaction forces, M_Y and M_Z.

9.10.3 ***Discussion***

Males skied faster than females on piste, and tended to initiate fewer turns. However, off-piste there was little difference between skier speed and number of turns initiated between gender. No relationship between skier speed and bindings was found. However, it should be noted that skiers did not ski the exact same course, but were allowed to choose their own path down the test slope (Figure 9.58). This is more representative of the self-selected speed skiers inherently choose, and not a representation of their maximum speeds. Ruedl et. al. [14] hypothesized that females underestimated their velocity and thereby incorrectly select a higher skier type than would be appropriate for their skiing ability. Contrary to this hypothesis, females skied the same speed as their male counterparts, or slower. It is the opinion of those who ran the study that each male and female skier selected the appropriate skier type that corresponded to their aggressiveness and skiing ability.

9.11 **Conclusions**

In the 1980s and 1990s, Mote[12], Quinn[39], and Scher[27] measured the ground reaction forces on the toe and heel piece of ski bindings. Since then ski equipment and injury patterns have changed dramatically. ACL injuries are the most prevalent among skiers, and females account for 70% of all skier ACL injuries, though they represent far less than 50% of the skiing population[7,14–16]. Ruedl et. al.[14] proposed several hypotheses for why female skiers are at greater risk of knee injuries and has proposed gender-specific release values. After an exhaustive review of literature and current technological advances, Senner et. al. [121] conceded that no binding technology currently exists, or 'is on the horizon', that has a plausible ability to address the large number of ACL injuries affecting skiers each year, particularly among female skiers[15]. Senner et. al. hypothesized that mechatronic ski bindings, capable of measuring more than M_Y and M_Z, and capable of providing feedback between the toe and heelpiece had the greatest potential for reducing knee injuries.

An additional injury concern that has evolved since the early 2005's is the limited functionality of AT bindings, and the anecdotal behavior of skiers locking the toe piece during skiing in response to a perception that Tech/Pin bindings are more prone to inadvertent releases.

Before any proposals for reducing knee injuries, or improving the retention performance of Tech/Pin bindings can be seriously considered, it is important to quantify the ground reaction forces transmitted from the ski to the skier, and what parameters affect those loads.

The analyses presented in this chapter have reported on the performance of Alpine and AT bindings on-snow. The objectives and results of the five analyses reported here are summarized in Table 9.6. These analyses have shown that the retention-release envelopes specified by international standards are still sufficient, and that lowering them could expose skiers to a greater risk of injury from inadvertent releases. Alpine and AT bindings both had similar rates of 'misses', or not releasing before loads at the boot top exceeded the retention release envelope. AT and alpine bindings transmit loads to the skier through different paths, but the net loads transmitted to the skier are not drastically different. Other metrics that have been proposed as criteria for the selection of binding release limits were poor predictors of binding loads.

In conclusion, the results from this analysis indicate that the release values, and criteria used for selecting them specified by international standards, are sufficient for MRR values.

Table 9.6: Summary of each of the five analyses, their objectives, and conclusions.

Analysis	Title
No. 1	**Comparison of Minimum Retention Requirements to Measured Boot Top Loads**
Q1.	Do the boot top loads generated by male and female skiers exceed the release requirements of international standards? Do these loads differ between Alpine and AT bindings?
R1.	Male and Female skiers both generated loads that reached the retention-release envelope. Alpine and AT bindings had similar rates of 'misses', or failure to release before loads exceeded the release envelope.
No. 2	**Statistical modeling of ground reaction forces and knee flexion angles.**
Q2.	What covariates are risk factors for higher binding forces?
R2.	Females had significantly higher lateral shear loads, while males had higher edge-edge torque and bending torque. AT bindings transmitted slightly more edge-edge torque than alpine bindings. Skiers applied more load to their outside foot than their inside foot. Bending torque was the only significant load different between on-off piste slopes. AT binding toe piece transmitted more edge-edge torque than the AT heel piece. Alpine binding toe-heel pieces transmitted equal amounts of edge-edge torque Snow penetration depth caused overall binding forces to decrease. The additional height and weight of the sensors caused skiers to increase their knee flexion by 6.5° during on-piste trials. The sensors had no effect on knee kinematics during off-piste trials.
No. 3	**Loads generated during an inadvertent release in an AT binding, and a comparison of load paths between Alpine and AT bindings**
Q3.	What is the mechanism of pre-release in AT Bindings?
R3.	A combined high shear and edge-edge torque appears to have overwhelmed the toe piece. Only one event was measured, more are necessary to confirm these findings.
No. 4	**Predicting maximum GRF values from simple anthropometric measurements of skiers**
Q4.	Do additional covariates such as Gender and Ski Length improve the correlation between binding loads?
R4.	Gender and Ski Length were not well correlated with ski binding loads
No. 5	**Analysis of Skier Velocity**
Q5.	Does skier velocity correlate to binding force?
R5.	Male and female skier velocity was not different during off-piste trials. Males skied faster during on-piste trials than females. Skier speed was not correlated with binding loads.

Chapter 10. Knee Kinematics

10.1 **Introduction**

Kinematic data was collected on male and female skiers as described in section 9.4.2. Gender based differences in knee kinematics has been well studied in gait laboratories[112,122] but not in studies specific to skiing. The purpose of this analysis was to determine if knee joint angles differ between male and female skiers using kinematic data recorded using the XSENS MVN Biomech suit.

10.2 **Methods**

Section 9.4.2 describes the methods used for collecting and signal-processing the kinematic data. Using the criterion described in 9.7.1 for differentiating between turns, the time points of each turn were used to segment the kinematic data into outside and inside turns for statistical analysis.

10.3 **Results**

General descriptive statistics for adduction-abduction, internal-external rotation, and flexion-extesion knee angles for males vs. females and inside vs. outside turns are tabulated in Table 10.1

Table 10.1: Descriptive statistics for knee joint angles for males vs. females, and inside vs. outside turns.

MN [Lower CI, Upper CI]		**Adduction (-) | Abduction (+)**	**Internal (-) | External (+) Rotation**	**Flexion (-) | Extension (+)**
Outside Turns	Male	-2.69° [-4.56°, -0.82°]	3.48° [1.22°, 5.74°]	-36.3° [-39.53°, -33.07°]
	Female	-5.66° [-8.78°, -2.54°]	10.08° [6.25°, 13.91°]	-37.3° [-44.34°, -30.26°]
Inside Turns	Male	6.73° [4.98°, 8.48°]	-8.37° [-10.49°, -6.25°]	-41.3° [-45°, -37.6°]
	Female	6.72° [4.8°, 8.64°]	-4.44° [-6.05°, -2.83°]	-31.5° [-35.43°, -27.57°]

10.3.1 *Adduction | Abduction Knee Angles*

Gender had no significant effect on variation in adduction – abduction angles. A significant linear model ($F(3,725) = 33.12, R^2 = 0.12, p < 0.001$) predicted turn direction to change the adduction – abduction angle by 6.18° between inside and outside turns ($\beta = 6.18, SE = 0.86, p < 0.001$) (Figure 10.1).

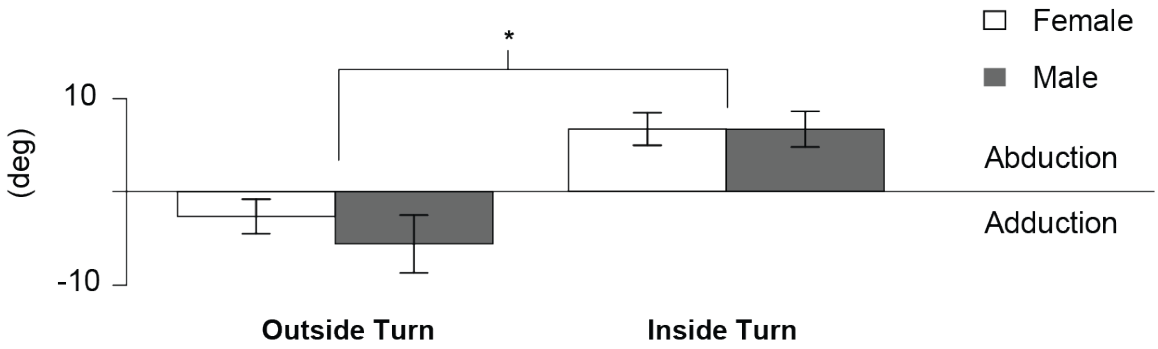

*Figure 10.1: Males had significantly larger adduction angles in outside turns than females. There was no significant difference between male and female skiers in abduction in inside turns. Adduction | Abduction angles were significantly different between outside and inside turns. * indicates $p < 0.05$.*

10.3.2 *Internal | External Rotation Knee Angles*

A significant linear model ($F(3,725) = 40.12, R^2 = 0.14, p < 0.001$) predicted external - internal rotation to vary by 5.3° between males and females, with females having significantly larger internal rotation knee angles ($\beta = -5.3, SE = 1.3, p < 0.001$). The model also identified a significant interaction term between turn direction and gender; this indicates that females have larger internal rotation during inside turns, and males have larger external rotation during outside turns ($\beta = -7.3, SE = 1.03, p < 0.001$) (Figure 10.2). The effect of turn direction, $\beta = -7.3$, is slightly larger than the effect for gender, $\beta = -5.3$.

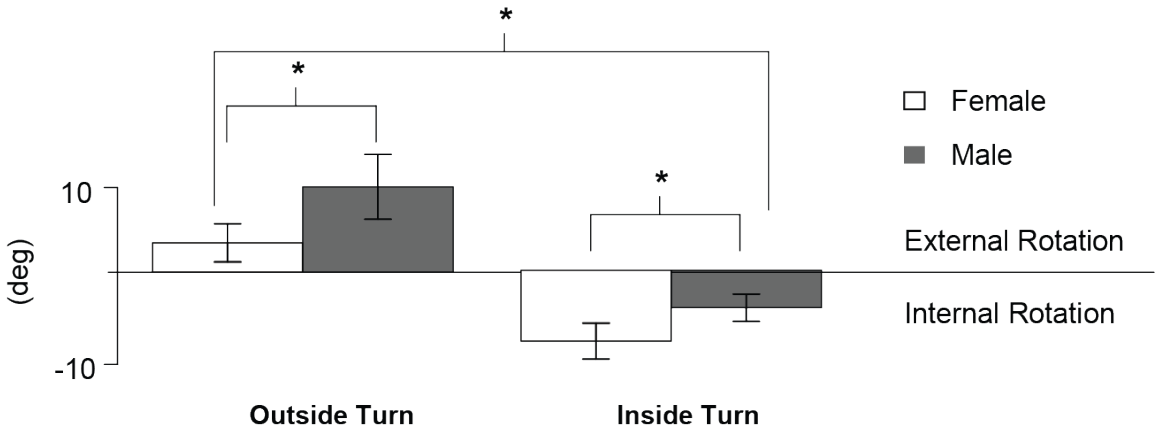

*Figure 10.2: Males had significantly larger external rotation angles in outside turns than females. Females had significantly larger internal rotation angles than males in inside turns. There was no significant difference between male and female skiers in abduction in inside turns. Internal | External rotation angles were significantly different between outside and inside turns. * indicates $p < 0.05$.*

10.3.3 ***Flexion | Extension Knee Angles***

A significant linear model (*$F(3,725) = 3.148$, $R^2 = 0.08$, $p < 0.001$*) predicted flexion - extension rotation to vary between males and females depending on the turn direction. For outside turns, flexion angle is not significantly different between males and females. For inside turns, flexion angle increases with females while it decreases for males (*$\beta = -5.4$, $SE = 2.27$, $p < 0.001$*) (Figure 10.3).

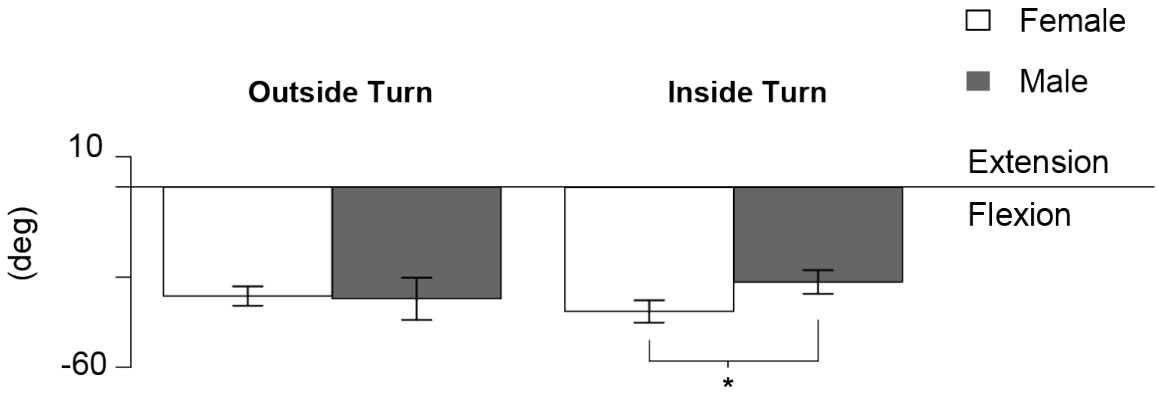

*Figure 10.3: No significant difference between males and females was found in flexion angle for outside turns. Females had significantly greater flexion angles during inside turns than males. * indicates $p < 0.05$.*

10.4 **Discussion**

The purpose of this analysis was to determine if knee joint kinematics differ between male and female skiers. This analysis demonstrated that gender-specific kinematics are a function whether the joint is performing an inside or outside turn. Males and female knee adduction (valgus) angles only differ in outside turns while knee flexion angles only differ when the knee is executing an inside turn. Females had lower adduction angles (outside turns) and greater flexion angles (inside turns). Smaller flexion angles and greater adduction (valgus) angles increase tension and strain in the ACL[123]. Sigward et. al.[112] found that females had larger adduction and valgus angles than males during running-cutting activities. The difference between the results presented in this study and Sigward et. al. could be a function of how different activities (skiing vs. cutting) are executed, as well as constraints imposed on the ankle joint by the ski boot.

In conclusion, differences in knee kinematics were found between males and female skiers. These differences do not follow patterns reported by other studies, which may be explained by the specific activity of skiing being studied here.

Chapter 11. Estimating Knee Loads on Skiers

11.1 **Introduction**

Knee injuries, including ruptures of the anterior cruciate ligament, are the most prevalent injury among skiers. A 9% decline over the past decade has been attributed to the introduction of shorter skis[13,15–17]. However, female skiers injure their ACL at significantly higher rates than male skiers[4,14]. The primary function of the ACL is to constrain anterior tibial translation of the tibia relative to the femoral condyles[112]. It is also believed to assist in stabilizing the knee under internal rotation[124]. Sigward et. al.[112] reported that a sharp deceleration and change of direction during landing, cutting, or for the purposes of the present study, skiing, produced the appropriate conditions for a non-contact ACL rupture. The exact mechanism of injury for non-contact ACL injuries is hypothesized to include anterior translation of the tibia[125] (Demorat, 2004) as well as valgus and internal rotation torque components[113]. Ettingler et. al.[29] described what is now commonly referred to as the 'Phantom Foot' in which a skier suffers a backwards twisting fall that induces a combined valgus-internal rotation to rupture the ACL. Combined loading has been shown to increase ACL strain and tension in *in vitro* testing using cadaveric specimens[123,124,126]. The force in the ACL was shown to be a function of flexion angle, internal rotation torque, and valgus moment[124]. Durselen et al.[112] reported females had lower knee flexion angles during athletic activities, producing larger anterior forces on the tibia.

Releasable ski bindings were developed to prevent twisting and bending fractures of the tibia-fibula at the ski boot top, unlike ACL injuries where the ACL and other ligaments are strained or ruptured. To this end, ski bindings respond to a lateral force at the toe of the boot to prevent twisting fractures of the tibia-fibula, and a vertical force at the heel of the boot to prevent tibia-fibula fractures at the boot top. A small number of binding incorporate a third degree of freedom that allows the toe piece to respond to an upwards vertical force at the toe, but this response is not standardized, or adjustable.

In recent years, a young company has developed a ski binding with a third degree of freedom that allows the boot to release laterally from the heel of the binding in adduction, and has claimed that this mechanism can prevent ACL injuries (KneeBinding, Stowe, VT). Other

proposals for reducing ACL injuries among female skiers have included reducing their binding settings relative to males[14].

The purpose of this study is to test the hypothesis that knee loads do differ between male and female skiers, and that specific loads measured at the toe and heel piece can be used to predict when peak knee loads will occur.

11.2 Methods

Inverse dynamics is a method used to determine the generalized forces and torques at a joint provided the kinematics of the system and the external forces acting on the system are known. For a generic mechanical system, the classical equations of motion can be written as shown in Equation 11.1,

Equation 11.1 : $M(s)\ddot{s} + C(s,\dot{s}) + F(s) = \bar{\boldsymbol{T}}$

where $s, \dot{s}, \ddot{s} \in R^N$ are the generalized positions, velocities, and accelerations, respectively. The mass matrix is represented as $M(s) \in R^N$; the Coriolis and centrifugal forces are presented by the vector $C(s,\dot{s}) \in R^N$, and gravitational forces are represented by the vector $G(s) \in R^N$, where N represents the number of the degrees of freedom. $\bar{T}$ represents the vector of generalized forces at a specific joint that are unknown.

11.2.1 *Model Construction*

An inverse dynamics model was developed using OpenSim (PaloAlto, CA). OpenSim is an open-source software system designed for the construction and analysis of human motion using musculoskeletal human models. Many open-source models have been developed to analyze gait kinematics, performance of ankle-foot-orthoses, among others. For the present study, kinematics of the lower leg were measured using the XSENS MVN Biomech (Chapter 10). External forces acting on the skier were quantified by force transducers mounted between the ski and the ski binding (Chapter 9).

Most analyses performed using models in OpenSim utilize data from a controlled setting in a gait laboratory. The window the time of interest during the gait cycle includes the time between the heel-strike and toe off where most of the weight is born by one foot, or the reaction forces from both feet during the gait cycle is captured by two individual force plates. These studies often utilize models that have been heavily validated such as the *gait2354*[127–130] (Figure

11.1). Studies such as Ford and McLean[131] have performed inverse dynamics on bipedal models without the torso included in the model. Dempsey et. al.[133] utilized a single leg model but explicitly investigated single leg landing.

For the present analysis, only one foot was instrumented and the generalized forces on the other leg are unknown. Hence, the model cannot include the non-instrumented leg and one assumption required for this model is that external forces the acting on the non-instrumented leg were decoupled from the instrumented leg. This limitation in the model may affect the accuracy of the model. However, since all subjects, male and female, are modeled in the same manner, the relative differences are assumed to be preserved.

The model incorporated eight rigid bodies including the pelvis, femur, tibia-fibula, talus, calcaneus, and metatarsals, and the boot-binding-sensor-ski assembly connected by four seven joints (Figure 11.2 and Figure 11.3). The joints and constraints are tabulated in Table 11.1. The *gait2354* model was adapted for the current analysis by removing the torso and non-instrumented leg (Figure 11.1 and Figure 11.3).

*Table 11.1: Degrees of freedom defined in each joint. All fixed degrees of freedom were constrained at zero translation or rotation except for those denoted by * indicating a fixed initial offset ranging between 10-20°.*

Joint	**Parent**	**Child**	**DoF**	**R_X**	**R_Y**	**R_Z**	**T_X**	**T_Y**	**T_Z**
Pelvis Ground	Ground	Pelvis	3	*Free*	*Free*	*Free*	*Fixed*	*Fixed*	*Fixed*
Hip	Pelvis	Femur	3	*Free*	*Free*	*Free*	*Fixed*	*Fixed*	*Fixed*
Knee	Femur	Tibia	6	*Free*	*Free*	*Free*	*$f(R_Z)$*	*Free*	*$f(R_Z)$*
Ankle	Tibia	Talus	0	*Fixed*	*Fixed*	*Fixed**	*Fixed*	*Fixed*	*Fixed*
Talo-calcaneal	Talus	Calcaneus	0	*Fixed*	*Fixed*	*Fixed*	*Fixed*	*Fixed*	*Fixed*
Calc-Meta	Calcaneus	Meta	0	*Fixed*	*Fixed*	*Fixed*	*Fixed*	*Fixed*	*Fixed*
Calcaneal-Metatarsophalangeal	Calcaneus	Ski	0	*Fixed*	*Fixed*	*Fixed*	*Fixed*	*Fixed*	*Fixed*

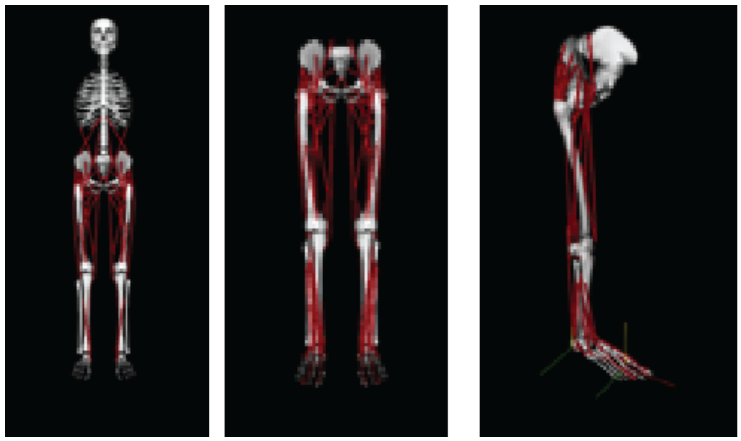

Figure 11.1: The gait2354 model (left) was modified for the current analysis by removing the head and torso (center) and the non-instrumented leg (right).

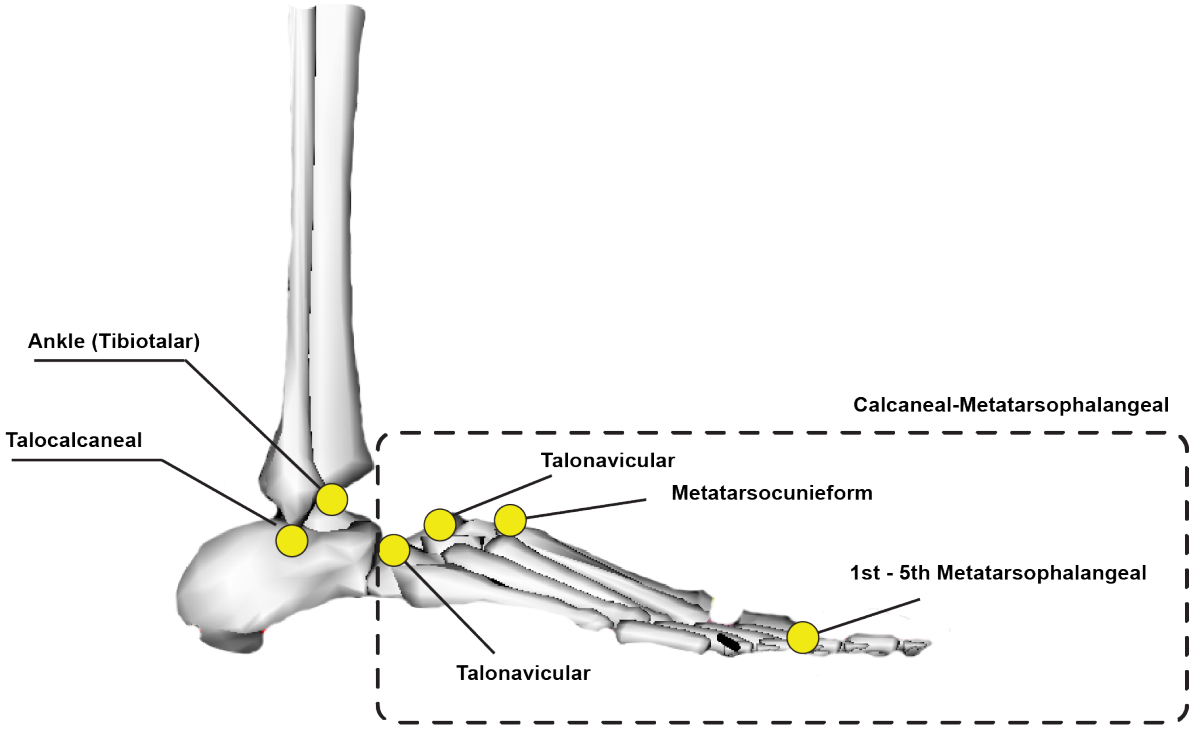

Figure 11.2: Construction of the foot bones and joints incorporated into the model. The foot was modeled as a rigid body enclosed in a ski boot. Therefore a custom joint defined as the Calcaneal Metatarsophalangeal joint was created to combine the joints shown above into one single rigid body.

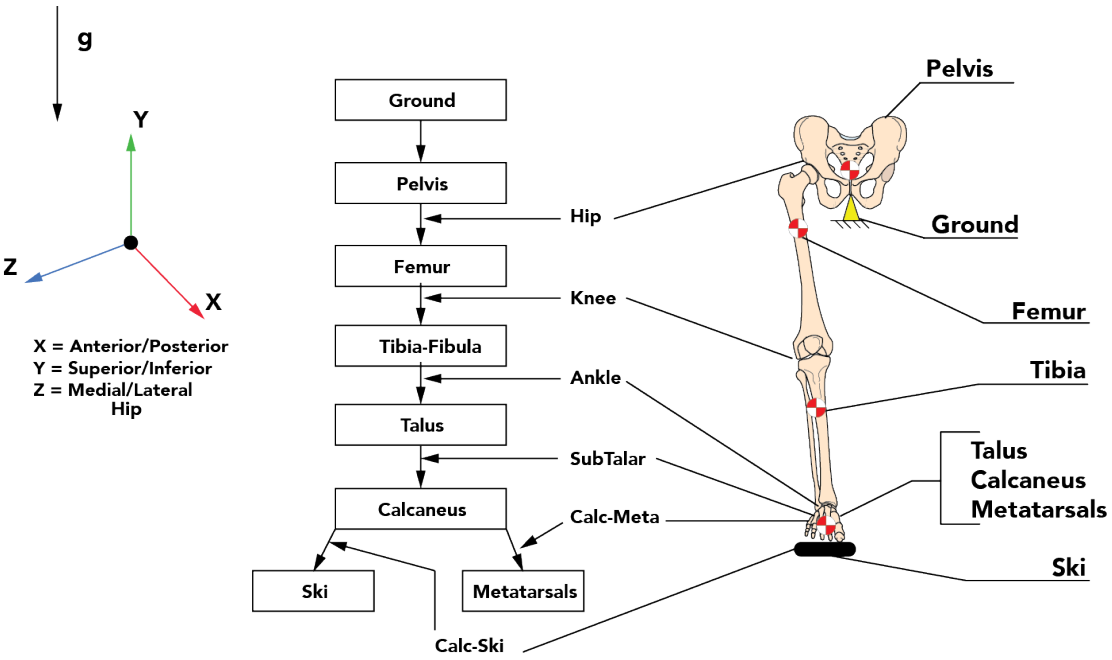

Figure 11.3: *Rigid bodies and their parent-child relationship in the model.*

The mass properties including the mass, mass moments of inertia, and location of the center of mass were determined for each of the rigid bodies by using anthropometric measurements specified by Young[102], Chandler[105], and Yeadon[134] for male and female subjects. The mass properties for the boot-binding-sensor-ski assembly were determined from a computer aided design (CAD) model of the assembly (Solidworks, Walthan, MA) (Figure 11.4).

Past studies have modeled the ankle as a frictionless joint. However, because the ankle is constrained within a ski boot, the ankle was modeled as a fixed joint with all six degrees of freedom constrained, and a fixed flexion angle to represent more accurately the constraints imposed by the high ski boot cuff. On average the boot cuff supported 79.2%±14.3% of the length of the lower leg, causing a portion of the external loads to bypass the ankle joint and be transmitted directly to the tibia. The fixed flexion angle was determined for each subject by averaging the flexion angle for each subject during a static trial often ranging between 11.1-19.3°.

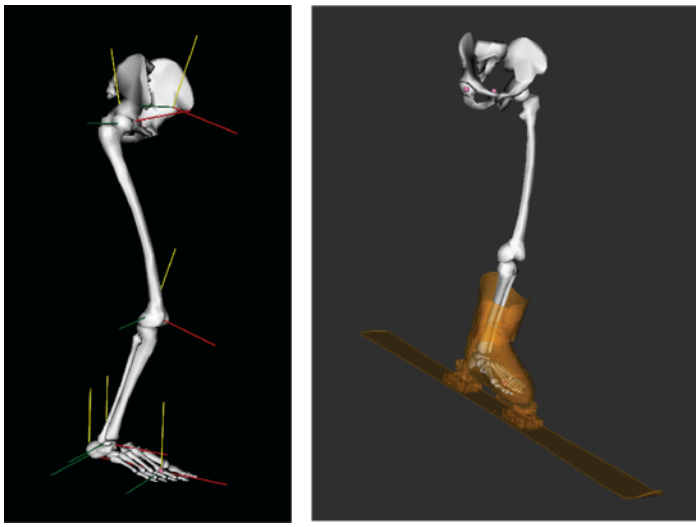

Figure 11.4: Coordinate system of each joint modeled (Left) and the total model including the boot-binding-ski-sensor assembly (Right).

11.2.2 ***Model Scaling***

Two subject-specific models were developed for the left and right leg for each subject. Each model was geometrically scaled using anthropometric measurements and the location of specific joint centers computed by the XSENS MVN Biomech System using the same convention as defined by the International Society of Biomechanics (ISB). The markers for the center of mass of the pelvis, left and right acetabulum, knee joint center, ankle joint center, and the custom calcaneo-metatarso-phalangeal joint were used for scaling. Using these markers, the origins of each motion segment were placed in the model for anthropometric scaling (Figure 11.5). Maximum RMSE error of the markers defined by the XSENS MVN system relative to the OpenSim model reported by OpenSim was 1.53cm.

Figure 11.5: The origins of each motion segment were used as marker sets for anthropometric scaling of a model in OpenSim. The scaled models for the largest subject (Left) and smallest subject (Right) are shown. The bone models have been made translucent to indicate the locations of the markers used for scaling.

11.2.3 *Inverse Dynamics Model*

Once a subject specific model was scaled appropriately, the model could be used to predict the generalized forces at the knee. The inputs for the inverse dynamics model include: 1) Generalized Reaction Forces and 2) Generalized coordinates or kinematics of each motion segment (Figure 11.6).

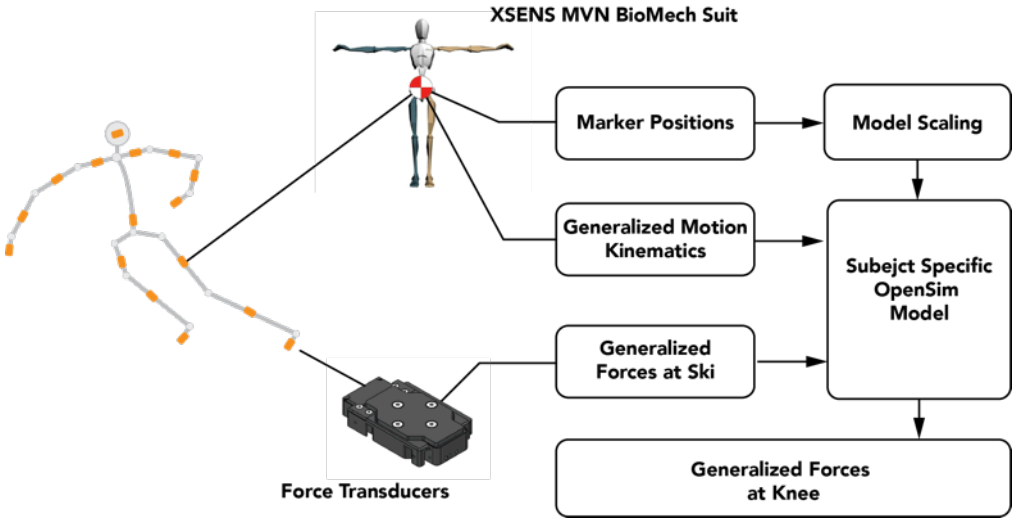

Figure 11.6: The workflow and inputs into the inverse dynamics model to output the generalized forces at the knee.

1. **External Forces:** Forces from the two force plates at the toe and heelpiece of the ski binding were summed about Point O. The external forces were applied to the model as a point load at this point (Figure 11.6). This point corresponded to a point 15% of the total foot length, located anterior of the origin of the calcaneus in the sagittal plane as defined by OpenSim, and 7.8 cm interior of the calcaneus in the horizontal plane of the sensors. Because the external reaction forces were recorded in a different coordinate system than what is defined in OpenSim, this required a 90° transform about the X-Axis, or longitudinal axis of the ski to match the coordinate system in the OpenSim model. Motion between the sensors-binding-boot and calcaneus was assumed to be negligible, and the external forces were transformed to align with the orientation of the calcaneus throughout the duration of the trial. External forces were down sampled from 2400 Hz to 120 Hz to match the sampling rate of the kinematic data and filtered with a 4-pole, zero shift low pass Butterworth filter. The cut off frequency was determined for each load and trial using the Residuals Analysis described in Section 9.4.1.

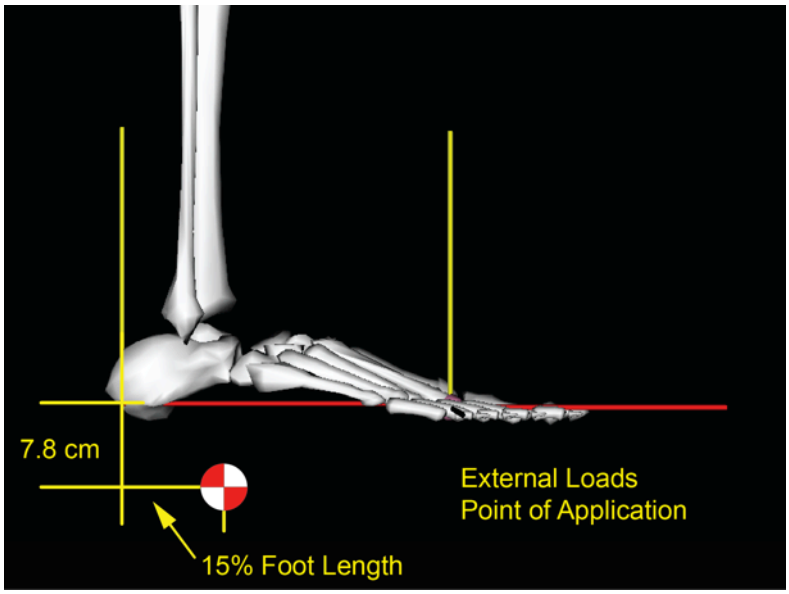

Figure 11.7: The point of application of the external loads lays 15% of the total foot length, anterior of the origin of the calcaneus in the sagittal plane, and 7.8 cm inferior, in the plane of the force transducers on the ski.

2. **Kinematics:** Generalized coordinates, or kinematics were imported into OpenSim from the output of the XSENS MVN Biomech suit. The orientation of the Pelvis relative to ground, or the acceleration of gravity was calculated by converting the orientation of the Pelvis, output of the XSENS MVN Suit (recorded in quaternion data), to the ***ZYX*** Euler angle sequence to match the tilt, list, and rotation of the pelvis.

   The XSENS MVN Biomech system models each joint as a ball and socket joint with three revolute degrees of freedom, and no translational degrees of freedom. Therefore, all translational degrees of freedom for all joints were fixed were except for the knee joint. In the *gait2354* model developed by Delp et. al.[127], the anterior-posterior and superior-inferior translation of the knee is defined as a function of knee flexion ankle, θ_{Flex}, (Equation 11.2 and Equation 11.3) as reported by Walker et. al.[135] These small translations were calculated and imported as generalized coordinates as well.

Equation 11.2 $$Superior\ Translation = -3.75e^{-6}\theta_{Flex}^{3} + 8..8e^{-4}\theta_{Flex}^{2} - 0.068\theta_{Flex}$$

Equation 11.3 $$Anterior\ Translation = 4.796e^{-4}\theta_{Flex}^{2} - 0.1283\theta_{Flex}$$

11.2.4 *Data Analysis*

As described in Section 9.7.1, trials were divided into individual turns for inside and outside turns. Due to technical issues related to the XSENS MVN Biomech suit, a significant portion of the kinematic data was not useable due to signal drift or fatigued connectors within the chain of IMUs in the suit. These were often difficult to identify in the field and were often not apparent until reviewing and processing the data after the end of the testing day.

The kinematic data for 47 trials, or 31.7%, from four female subjects and 6 male subjects not corrupt and was acceptable for this analysis. A total of 874 turns were extracted from these 47 trials, and each turn was used to identify the maximum net joint loads acting on the knee. General descriptive statistics for the maximum load components at the knee are reported.

To identify whether either of these concepts proposed by KneeBinding, or Ruedl[14] may reduce the loads on the knee, a linear regression analysis was performed on the loads measured at either the toe or the heelpiece to predict the loads at the knee.

For new binding concepts such as the KneeBinding to be able to reduce knee injuries, there must be a relationship between the additional degree of freedom, measured as lateral F_Z force at the heelpiece, and loads at the knee. In order for other proposals such as those from Ruedl[14], lowering traditional binding settings for females, to reduce knee injuries, there must also be a relationship, or correlation, between the forces traditional bindings respond to (lateral force at the toe, vertical force at the heel), and loads on the knee.

To quantify these relationships, a linear regression was performed on all six-load components at the toe and heelpiece to predict the six load components at the knee. Further more, the time at which each peak occurred at the knee relative to peak loads at the toe and heelpiece was calculated to quantify the dynamic response necessary for a binding to respond to injurious loads, before they progress up to the knee.

11.3 **Results**

To assess the validity of inverse dynamics model, the magnitude of the net joint loads were compared to values reported from previously published studies investigating knee loads during skiing and snowboarding as well as studies reporting knee loads from gait kinematics[38,75,95,122,131,136]. The output from the OpenSim model for an exemplar time history from one trial is shown in Figure 11.8. The hashed rectangle represents the average knee loads reported from the literature for skiing and snowboarding[38,75,95]. The shaded region represents the average knee loads from the literature reporting walking, running, and cutting studies in gait laboratories[122,131,136]. The results from the model yielded predicted net knee loads within one standard deviation of the snow-sports literature and other gait laboratory studies. Few studies report all six-load components at the knee, and therefore only one study reported values for F_Z, the medial-lateral force at the knee[136]. The values predicted by the OpenSim model in the current study exceed the reported values for F_Z but are not exceptionally large relative to other force components. Based on these comparisons, the model output was considered to be in relative agreement with other studies.

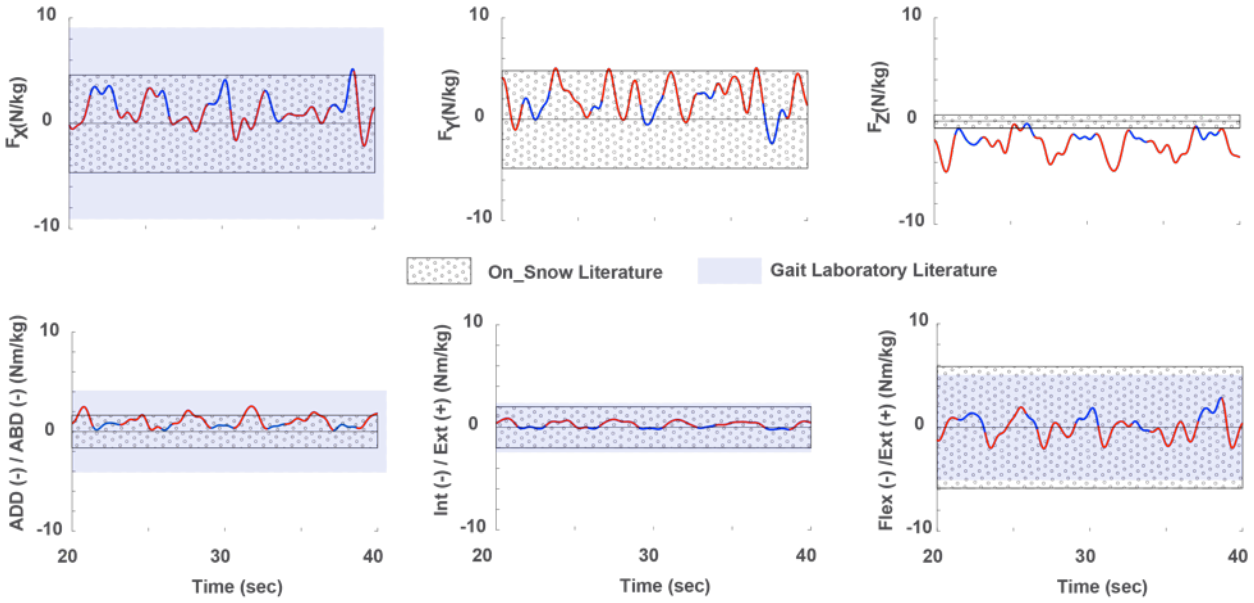

Figure 11.8: Exemplar Time History of the net knee joint forces and torques predicted by the OpenSim model fell within one standard deviation of other values reported by the literature[122,131,136].

11.3.1 *Maximal Forces*

A significant linear model ($F(3,725) = 40.12$, $R^2 = 0.14$, $p < 0.001$) predicted external - internal rotation to vary by 5.3° between males and females, with females having significantly larger internal rotation knee angles ($\beta = -5.3$, $SE = 1.3$, $p < 0.001$).

Descriptive statistics such as the mean and 95% confidence intervals for the six load components at the knee predicted by the OpenSim model are tabulated in Table 11.2. Figure 11.9 and Figure 11.10 show the relationships between males and females for forces and torques normalized by body weight. Males had significantly larger peak anterior forces (F_X/kg) than angles ($\beta = 227$, $SE = 35$, $p < 0.001$). While females had significantly larger superior-interior (F_Y/kg) forces in outside turns ($\beta = -103.9$, $SE = 46.4$, $p < 0.001$). Peak abduction moments (M_X/kg) were significantly larger in females than males ($\beta = -93.1$, $SE = 13.1$, $p < 0.001$). The mean M_X moment for males was 33.3 ± 19.3 Nm (abduction) in contrast to the mean M_X moment for females, -60.1 ± 13.5 Nm (Table 11.2). These gender-based differences Figure 11.10 are similar to values reported by Sigward[112] who investigated knee loads during cutting in a gait laboratory.

Cadaveric studies have demonstrated that combinations of valgus and internal rotation torque increase ACL tension or strain[123,126,137]. The peak resultant knee torque using the adduction/abduction and rotation al torque was found to be significantly greater in males than females (Figure 11.11).

Table 11.2: Average Peak Net loads on the knee for male and female skiers, not normalized to body weight.

		F_X (N)	F_Y (N)	F_Z (N)	M_X (Nm)	M_Y (Nm)	M_Z (Nm)
Females	**Mean**	37.8	227.7	-2.3	-60.1	8.2-	-14.3
	Upper 95% CI	92.3	329.1	29.3	-73.6	15.3	-8.2
	Lower 95% CI	-16.6	126.4	-33.9	-46.6	1.0	-36.9
Males	**Mean**	263.8	130.6	2.9	33.3	8.0	93.3
	Upper 95% CI	308.4	169.6	42.3	14.0	15.5	118.8
	Lower 95% CI	219.3	91.5	-36.5	52.5	0.6	67.8

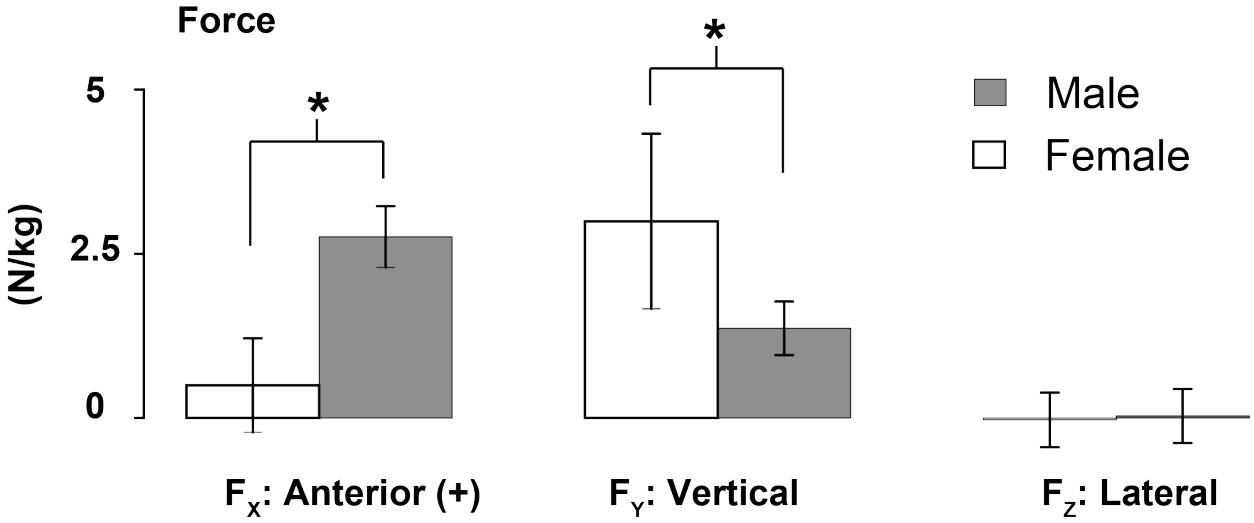

*Figure 11.9: Net peak knee loads, normalized by body weight for F_X (Anterior | Posterior), F_Y (Superior | Inferior), F_Z (Medial | Lateral) for males and females. * denotes a statistically significant difference.*

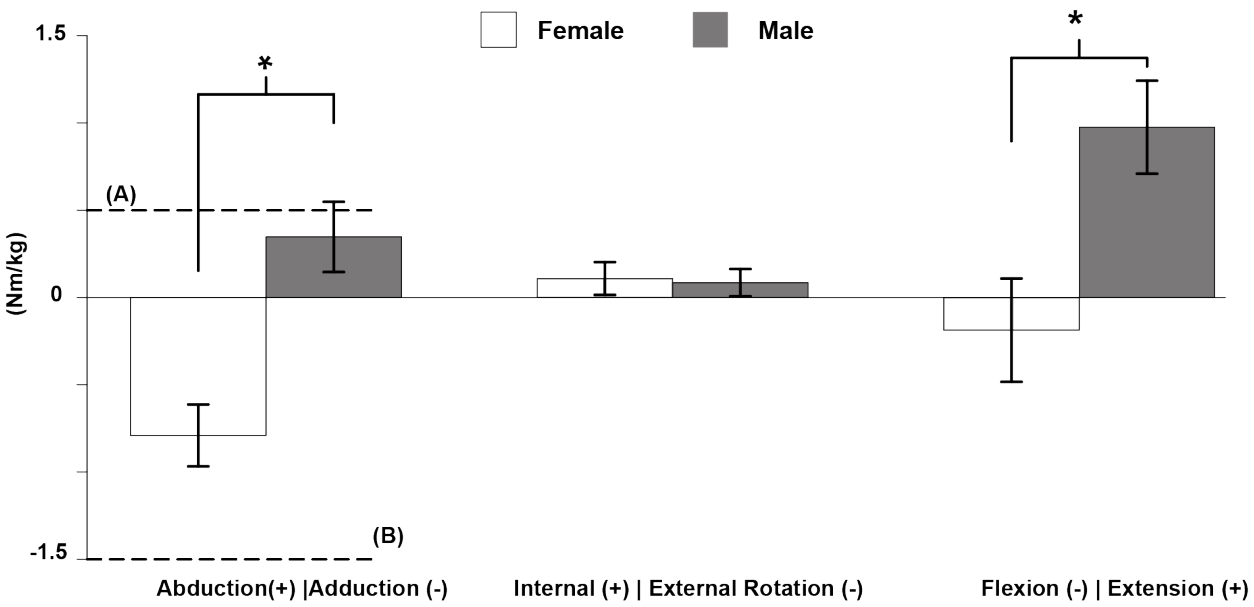

*Figure 11.10: Net peak knee loads, normalized by body weight (kg) for M_X (Adduction | Abduction), M_Y (Internal | External Rotation), and M_Z (Flexion | Extension) for males and females. * denotes a statistically significant difference. Line (A) is the maximum abduction torque reported by Sigward[112] for males. Line (B) is the maximum adduction torque reported by Sigward[112] for females.*

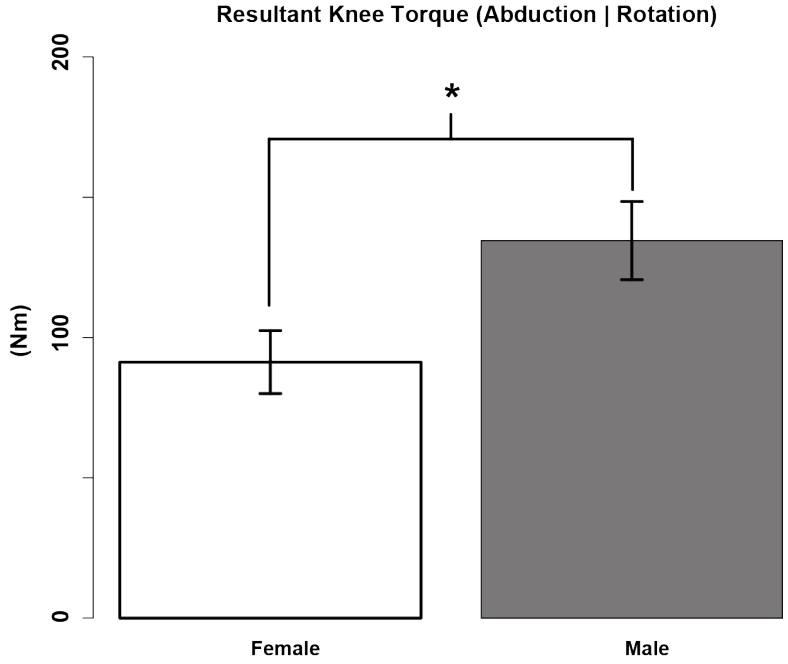

Figure 11.11: Net peak resultant torque computed from the internal/external rotation torque and adduction/abduction torque.

11.3.2 *Binding loads to knee loads*

No strong correlations were found between binding loads and knee loads that were not controlled by gender. When gender is considered, the peak lateral force, F_Z, at the toe and heelpiece was moderately correlated with the lateral force at the knee, and the adduction torque at the knee in females but not males (Table 11.5). A significant correlation was found between the peak lateral force at the toe piece and the peak adduction torque, internal rotation, and flexion torque at the knee in females (Figure 11.12) ($\beta = 0.47$, $SE = 0.11$, $p < 0.001$). However the strongest correlations were found between the peak longitudinal force (F_X) and the peak flexion-extension torque at the knee among females (Table 11.5).

The peak lateral force at the toe and vertical force at the heel are graphically shown in Figure 11.13 with the time history of the net knee torque. The time at which the peak lateral toe force and vertical heel force occur for each turn are graphically overlaid on the curves of the knee torques to illustrate the short time duration between peak loads at the binding and peak loads at the knee. The mean and 95% confidence interval are tabulated in Table 11.3 and Table 11.4. Figure 11.14 and Figure 11.15 show each of the knee torques in detail with the time of peak binding loads. The relationship between peak binding loads and the peak knee loads (dt^{TOEn} and dt^{HEELn}) is shown in Figure 11.16.

The peaks at the binding and the knee occur very close together. For example, Figure 11.16 shows the range of values for time between peak loads between the binding and knee. For females, the peak lateral force at the toe piece and heelpiece occur 0.138 ± 0.11 seconds and 0.152 ± 0.71 seconds before the peak adduction knee torque, respectively. For males, the peak lateral force at the heelpiece occurs 0.05 ± 0.08 seconds after the peak adduction knee torque.

Table 11.3: Mean and 95% Confidence intervals for dt^{TOEn} for peak six load components at the toe piece and the knee while skiing.

dt^{TOEn}	**Toe Forces**		
Knee Loads	**F_X**	**F_Y**	**F_Z**
F_X	0.014 [-0.066,0.08]	0.028 [-0.054,0.082]	-0.005 [-0.072,0.067]
F_Y	-0.048 [-0.127,0.079]	-0.034 [-0.11,0.076]	-0.067 [-0.136,0.069]
F_Z	0.156 [0.085,0.071]	0.17 [0.093,0.077]	0.137 [0.075,0.062]
M_X	0.107 [0.038,0.069]	0.121 [0.045,0.076]	0.0877 [0.0287,0.059]
M_Y	0.059 [-0.014,0.073]	0.073 [-0.002,0.075]	0.04 [-0.019,0.059]
M_Z	-0.11 [-0.178,0.068]	-0.096 [-0.175,0.079]	-0.129 [-0.191,0.062]

dt^{TOEn}	**Toe Moments**		
Knee Loads	**M_X**	**M_Y**	**M_Z**
F_X	-0.057 [-0.124,0.067]	0.169 [0.083,0.086]	0.0238 [-0.0512,0.075]
F_Y	-0.118 [-0.186,0.068]	0.107 [0.021,0.086]	-0.038 [-0.11,0.072]
F_Z	0.086 [0.0246,0.0614]	0.311 [0.228,0.083]	0.166 [0.091,0.075]
M_X	0.036 [-0.024,0.06]	0.262 [0.182,0.08]	0.117 [0.043,0.074]
M_Y	-0.0118 [-0.0728,0.061]	0.214 [0.133,0.081]	0.069 [0.002,0.067]
M_Z	-0.18 [-0.246,0.066]	0.0456 [-0.0334,0.079]	-0.01 [-0.08,0.07]

Table 11.4: Mean and 95% Confidence intervals for dt^{HEELn} for peak the six load components at the heelpiece and the knee while skiing.

dt^{HEELn}	Heel Forces		
Knee Loads	**F_X**	**F_Y**	**F_Z**
F_X	-0.025 [-0.105,0.08]	-0.038 [-0.124,0.086]	-0.161 [-0.244,0.083]
F_Y	-0.087 [-0.163,0.076]	-0.01 [-0.096,0.086]	-0.223 [-0.299,0.076]
F_Z	0.117 [0.037,0.08]	0.104 [0.027,0.077]	-0.019 [-0.097,0.078]
M_X	0.068 [-0.001,0.077]	0.055 [-0.024,0.079]	-0.07 [-0.147,0.077]
M_Y	0.0195 [-0.056,0.073]	0.007 [-0.072,0.079]	-0.116 [-0.189,0.073]
M_Z	-0.149 [-0.221,0.072]	-0.162 [-0.247,0.085]	-0.285 [-0.362,0.077]

dt^{HEELn}	**Heel Torques**		
Knee Loads	**M_X**	**M_Y**	**M_Z**
F_X	-0.195 [-0.271,0.076]	0.016 [-0.07,0.086]	-0.122 [-0.201,0.079]
F_Y	-0.257 [-0.332,0.075]	-0.046 [-0.124,0.078]	-0.184 [-0.263,0.079]
F_Z	-0.053 [-0.121,0.068]	0.158 [0.082,0.076]	0.02 [-0.054,0.074]
M_X	-0.103 [-0.168,0.065]	0.108 [0.034,0.074]	-0.029 [-0.103,0.074]
M_Y	-0.151 [-0.219,0.068]	0.06 [-0.017,0.077]	-0.077 [-0.149,0.072]
M_Z	-0.319 [-0.391,0.072]	-0.108 [-0.187,0.079]	-0.25 [-0.324,0.074]

Table 11.5: Correlation coefficients, R^2, of linear regression on binding loads measured at the toe and heelpiece against the peak knee loads from each turn . Bold values represent $R^2 > 0.5$.

R^2			Binding Loads											
			Males						Females					
			F_X	F_Y	F_Z	M_X	M_Y	M_Z	F_X	F_Y	F_Z	M_X	M_Y	M_Z
Knee Loads	F_X	Toe	0.28	0.01	0.24	0.11	0.12	0.04	0.37	0.12	0.43	0.25	0.28	0.20
		Heel	0.18	0.01	0.03	0.01	0.04	0.03	0.03	0.03	0.01	0.10	0.03	0.01
	F_Y	Toe	0.04	0.28	0.04	0.02	0.00	0.12	0.08	0.00	0.06	0.01	0.03	0.08
		Heel	0.16	0.07	0.09	0.08	0.12	0.00	0.01	0.02	0.00	0.01	0.00	0.00
	F_Z	Toe	0.06	0.00	0.19	0.01	0.03	0.12	**0.51**	0.17	**0.74**	**0.63**	0.27	0.33
		Heel	0.29	0.00	0.29	0.24	0.25	0.03	0.08	0.03	0.02	0.26	0.03	0.08
	M_X	Toe	0.06	0.00	0.22	0.02	0.03	0.14	0.48	0.16	**0.71**	**0.61**	0.22	0.30
		Heel	0.32	0.00	0.36	0.28	0.31	0.02	0.03	0.08	0.03	0.28	0.02	0.06
	M_Y	Toe	0.30	0.01	0.42	0.26	0.23	0.04	**0.58**	0.06	**0.60**	0.37	0.18	0.37
		Heel	0.00	0.03	0.08	0.14	0.00	0.00	0.10	0.03	0.14	0.24	0.02	0.07
	M_Z	Toe	0.43	0.15	0.37	0.07	0.08	0.22	**0.80**	0.00	**0.58**	0.26	0.34	**0.60**
		Heel	0.26	0.01	0.02	0.01	0.06	0.05	0.21	0.01	0.13	0.29	0.03	0.08

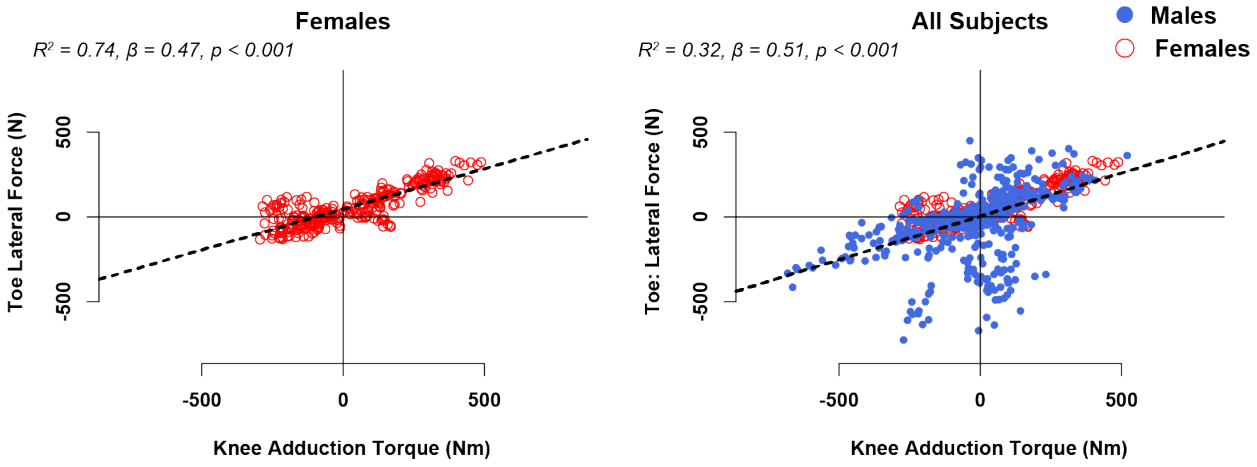

Figure 11.12: Several significant correlations were found in knee loads with females that were not significant when gender was not considered a factor, for example lateral force at the toe piece and knee adduction torque. Each point plotted represents the peak load from a given turn.

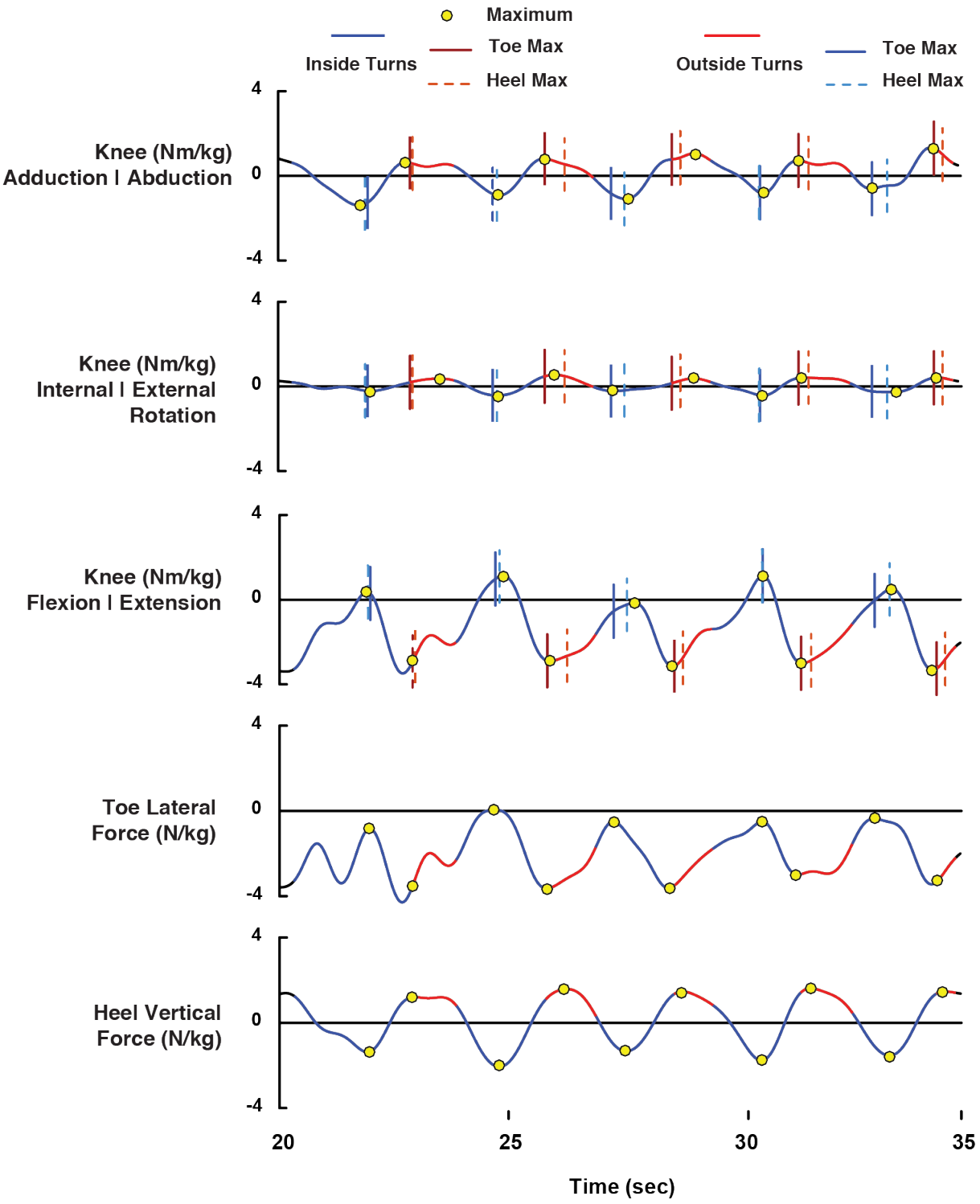

Figure 11.13: An exemplar time-history of the vertical force at the heel, lateral force at the toe, and the three net torques at the knee. The maximum for each trace is denoted. The time points at which the maximum loads were measured at the toe and heelpiece of the binding are overlaid on each axis of knee torque.

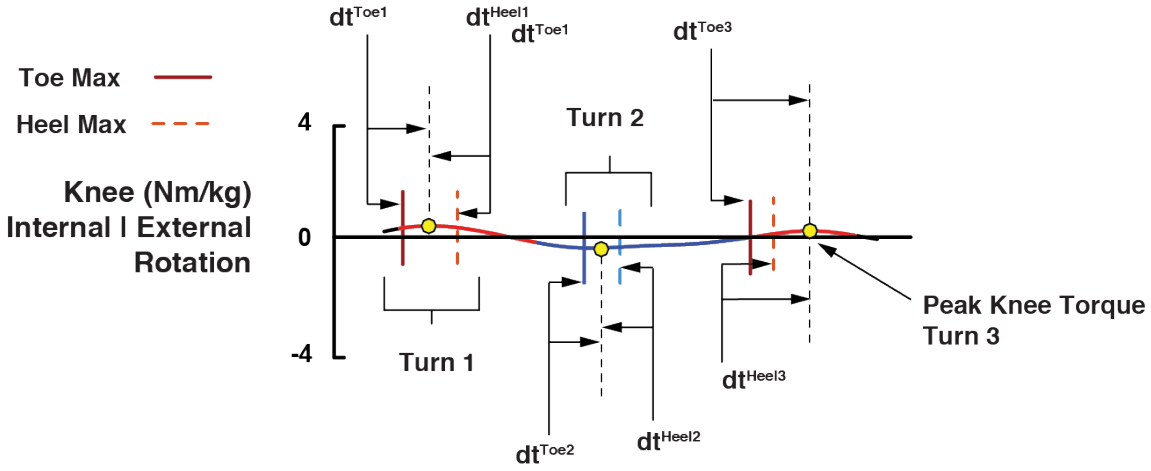

Figure 11.14: Exemplar time history of knee torque with peak knee torques identified with the time of the peak binding loads labeled.

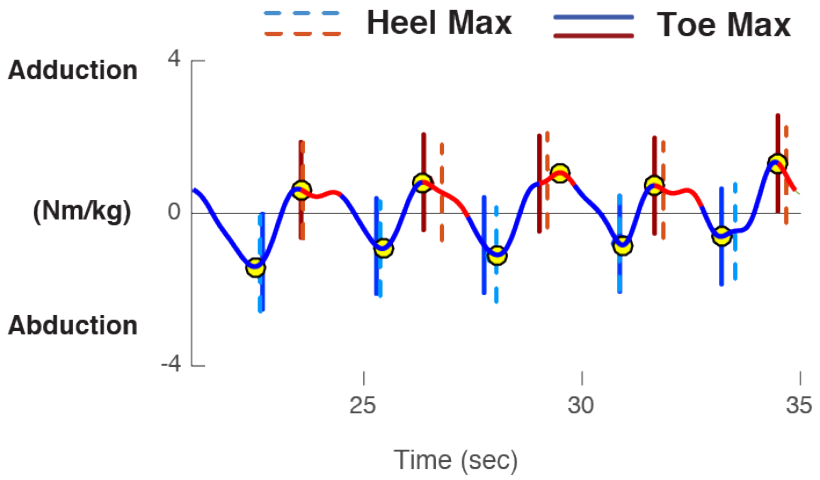

Figure 11.15: Net Adduction | Abduction knee torque. The times of maximum vertical heel and lateral toe forces are imposed on the curve.

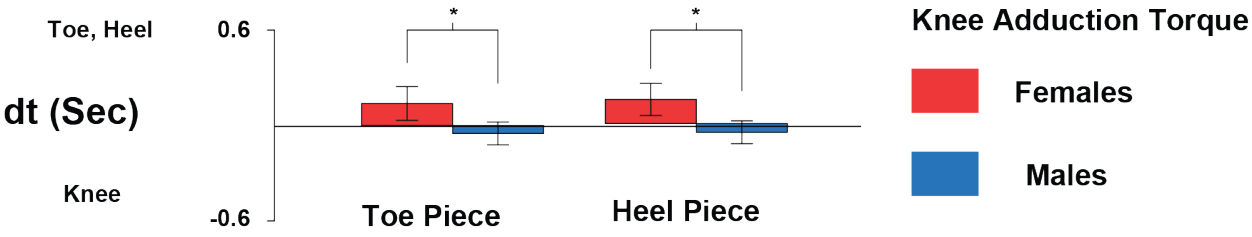

*Figure 11.16: The timing of the peak binding loads to peak knee loads dt^{TOE} and dt^{HEEL} are shown for the knee adduction torque that was moderately correlated with the lateral force at the toe piece and heelpiece of the binding. * indicates a significant difference with $p < 0.05$.*

11.4 **Discussion**

The objective of the present study was to quantify the loads transferred from the ski binding to the skier through the heel and toe piece to assess the risk of knee injury between male and female skiers. Significant differences in net peak knee loads were found; of particular interest were differences in peak knee adduction torques. Significant differences in the adduction torque at the knee were correlated with the lateral force acting on the toe of the binding.

One ski binding currently on the market, KneeBinding, has designed an additional degree of freedom to allow for a lateral release of the heel in response to a lateral force that has been hypothesized to produce an adduction torque capable of rupturing an ACL. However, in the present study, the correlation between the lateral force at the heel, and knee adduction torque was very low, $R^2 = 0.14$, under normal skiing loads. Therefore it may be unlikely that the mechanism incorporated by KneeBinding will be beneficial in mitigating knee injuries. However, this conclusion is limited in scope since no knee injuries were actually measured during testing.

The results from this study indicate that the response of a binding to such loads would need to be extremely quick as peak loads are transferred from the ski to the knee in approximately 0.15-0.25 seconds in females. Provided a binding could respond this fast, loads at the toe piece binding were well correlated with internal rotation torques at the knee. The times between peak load at the binding, and peak load at the knee are reported under normal skiing. These times will likely be shorter in the event of a fall.

Many studies have reported that combined loading is significantly more injurious than applying single components of load to the knee. Therefore, there is no indication that the KneeBinding, or any other binding, could adequately respond to the combined adduction and internal rotation torques at the knee to prevent ACL injuries in females. In males, the lateral force at the binding is not correlated with adduction torque at the knee, and the force is transmitted significantly faster than females, therefore, such a mechanism would not likely prevent ACL injuries in males.

Traditional alpine bindings only respond to lateral forces at the toe, and vertical forces at the heel. Lateral forces at the toe were reasonably well correlated with internal rotation torque ($R^2 = 0.71$) and adduction torque ($R^2 = 0.6$) at the knee for females, but vertical forces at the heel were not correlated with any load components at the knee. Ruedl et. al.[14] recently proposed lowering the binding settings for traditional alpine binding for females to reduce the risk of ACL

injuries. Therefore, it may be possible that lowering the release value at the toe could lower the peak knee torque, but not with out compromising the retention requirements necessary for female skiers. The results from Chapter 9 indicate that skier generate loads up to the minimum required retention values (MRR). Lowering settings for females would also lower the MRR values at which their bindings would release and in turn potentially increase their risk of injury from an inadvertent release.

During the course of this testing, no subjects suffered an ACL injury during the course of collecting data for this study. Therefore it cannot be concluded whether or not a correlation between specific load components at the toe or heelpiece of the binding, and internal rotation torque of the knee exists during a fall in which a skier suffers an ACL rupture. In such instances it is difficult to quantify the loading conditions present at the bindings during an event in which a skier suffers an ACL injury without having directly measured such an event. Without such data, it is necessary to make inferences from the results in this study and the literature.

The gender-based differences in adduction knee torque reported in the study agree with other studies[112], and indicate that the adduction torques generated by females are certainly more of a risk factor than abduction torque generated by male skiers. However, if such a binding cannot respond to specific load components that generate injurious magnitudes of internal torque, then it likely cannot mitigate the classic phantom-foot ACL injury[29]. It should be noted that one limitation of this model was assumption that loads acting on the non-instrumented leg were decoupled from the instrumented leg. This could affect the absolute accuracy of the values estimated from the inverse dynamics model. However, the relative differences between male and females are likely preserved. Future work should include solving for the theoretical reaction forces acting on the acetabulum corresponding to the non-instrumented leg to satisfy the equations of motion.

Future work could include a validation of the single-leg inverse dynamics model, evaluation of ski width as a risk factor for knee injuries[110], and improving the inverse dynamics model to allow for the boot stiffness to apply reaction forces across the ankle joint, rather than fully constraining the ankle joint to evaluate the effect of ski boot stiffness on knee loads. In conclusion, this study has demonstrated differences in net knee joint loads between male and female skiers, possibly explaining the high rate of ACL injuries among female skiers[15]. Several

key loads measured at the binding toe piece have also been shown to correlate well with peak knee loads in females.

Chapter 12. Conclusions

This research was motivated by the need to (1) understand the potential risks of skiers using new types of alpine touring (AT) and (2) understand more fully why female skiers injure their ACL at significantly higher rates than male skiers. Specifically the aims of this research were to:

- Quantify the performance of AT boot-binding systems.
- Quantify the performance requirements AT boot-binding systems, i.e. the loads these systems must transmit from the ski to the skier.
- Quantify and compare net knee joint loads between male and female skiers.

The following sections of this chapter summarize the salient findings from each study included in this dissertation, and whether those findings support the hypotheses under study.

For better or worse, there has been little change in ski injury rates over the last two decades. Alpine boots and bindings are well suited for protecting skiers from lower leg injuries but were not specifically design to protect skiers' knees from forces and torques known to cause ACL injuries. Alpine touring is growing rapidly and many skiers are mixing their alpine boots and bindings with AT equipment.

At the present time, Study 1 and Study 2 have been completed and showed in a laboratory setting, that AT equipment will not provide the same release characteristics as skiers have come to expect from traditional alpine equipment. When AT boots and alpine bindings are used together, the likelihood of a binding releasing in a fall is low, resulting in a higher risk of a lower leg injury. When AT boots are used in Tech/Pin bindings, the retention-release performance varies significantly by which brand of boot is used. This finding agrees with anecdotal reports by skiers that the retention function of Tech/Pin boot-binding system is unreliable which causes some skiers to lock out the release function of their Tech/Pin bindings. This also increases the risk of a lower leg injury.

Therefore, two significant challenges currently facing the ski industry are reducing the number of knee injuries, and improving the retention-release function of AT equipment. The loads transferred to the knee from modern ski equipment must be quantified before novel equipment designs can be introduced to protect the knee. The functional performance

requirements of AT equipment must also be quantified before the retention-release performance can be improved.

Study 3 measured the whole body kinematics and reaction forces generated by male and female subjects skiing on various combinations of alpine and AT ski equipment in various snow conditions. A custom low-profile six-axis force transducer was been designed, optimized, and built to perform this measurement. The loads transmitted to the lower leg and knees were calculated to assess the likelihood of injury to the lower leg and knee from skiing on alpine and AT ski equipment.

12.1 Laboratory Testing of Alpine Touring Equipment

The objective of Study 1 was to use laboratory test equipment to investigate the risk of skiers using AT boots in alpine bindings. It was hypothesized that using AT boots in alpine bindings would significantly alter the release characteristics of alpine bindings.

The significant findings include:

1. AT boots cannot reliably be used in alpine bindings without the increased risk of a lower leg fracture.
2. Several binding manufacturers include mechanical AFDs in binding intended for use with AT boots. Under specific loading conditions, mechanical AFDs create adverse release behavior and render the spring-cam release mechanism unable to control the release torque of the boot from the binding (Figure 2.6).

In summary, the hypothesis was accepted and it was shown that AT boots significantly increase the load of alpine bindings, subsequently increasing the risk of injury.

The objectives of Study 2 were to use laboratory test equipment to quantify the variation in release torque in a new type of AT binding, called a Tech/Pin binding. It was hypothesized that variations between binding design and boot geometry would cause significant variation in release characteristics.

The significant findings include:

1. Small variations in boot geometry less than 0.25mm can cause the release torque of AT bindings to vary by more than 50% (Figure 4.9).

2. The sensitivity of a binding to changes in boot geometry is a function of the indicator settings of the binding, which significantly complicates the effort to identify an optimal boot geometry that manufactures could standardize (Figure 5.6).

In summary, the initial hypothesis, that variations in boot geometry would cause significant variation in release characteristics, was accepted. The results indicated that standardization of the boot-binding interface would reduce variability in retention-release characteristics of AT bindings.

12.2 On-Snow Characterization of Alpine and AT Bindings

The results from studies 1 and 2 demonstrated that in order to optimize and improve the retention and release characteristics of AT boots and bindings, it is necessary to understand what load they must transmit from the skier to the ski, and how those loads may increase, or decrease, the risk of injury.

In addition to the need to quantify the performance requirements for AT bindings, it was of particular interest to also measure how loads are transferred to both male and female skiers, to help better understand why female skiers are at significantly higher risk of an ACL injury.

Therefore, the objectives of this Study 3 were:

- Quantify the loads that the toe and heel piece of alpine and AT Bindings transfer to the skier. The hypothesis for this objective was that the net loads that both bindings transfer to the skier are the same, but the path that the loads take (toe vs. heel loading) would be significantly different.
- Quantify the loads transferred to male and female skiers knees, and identify specific load components at the binding that are correlated with high loads at the knee. It was hypothesized that significant differences in knee loads would be found between male and female skiers and that loads on the binding would be well correlated to both male and female skiers.

To achieve these objectives, a custom low-profile six-axis force transducer was designed (Figure 6.7) and fabricated (Figure 7.3). The final sensor design had a lower stack height, and greater range, than other sensors designs found in the literature. Furthermore, an XSENS MVN Biomech suit was utilized to measure skier joint kinematics. A small-scale validation study

found that the position accuracy of the suit was similar to other published values and acceptable for use for the present study (Figure 8.10).

The study was conducted in the spring of the 2016 ski season at Snowbird, UT. The binding loads and body kinematics of N = 13 skiers (N = 7 males, N = 6 females) were measured as they skied down an expert slope (Figure 9.58). Using the binding loads and body kinematics, an inverse dynamics model was developed to estimate the loads at the knee of each skier.

Significant findings from this study include:

1. The minimum required retention values for male and female skiers is sufficient for over 99% of the loads generated during normal skiing (Figure 9.26).
2. Both alpine and AT bindings had similar rates of 'misses', not releasing before loads on the tibia-fibula exceed the recommended release values (Table 9.2).
3. The toe and heelpiece of alpine bindings transfer the same amount of load to the skier, while the toe piece of AT bindings transfers significantly more load than the heel piece (Figure 9.41).
4. One inadvertent release of a tech binding was measured in which the binding released when it was perceived to not be necessary. Upon investigation, high frequency lateral force and rolling torque at the toe piece likely overwhelmed the toe piece until it released (Figure 9.56).
5. Gender and ski length were not significantly correlated with binding loads.
6. Skier speed was not correlated with binding loads, but has significant ramifications in the event of an inadvertent release.
7. Knee joint kinematics were significantly different between male and female skiers, depending on if the knee was performing an inside or outside turn.
8. Normalized peak knee adduction loads were found to be significantly larger for female skiers than male skiers.
9. Peak lateral force at the toe piece was well correlated with adduction torque and internal rotation for female skiers. However, this correlation did not hold up for male skiers.

In summary, AT and alpine bindings did not differ in the net force transferred to skiers, and the MRR values for skiers was sufficient, but skiers frequency reached the minimum required limit under normal skiing. The path that loads take from the ski to the skier, via the toe piece or

heelpiece, was significantly different, and therefore the initial hypothesis was accepted. This has significant implications to for the design and optimization of AT bindings.

Furthermore, male and female skier knee loads were found to be significantly different. However significant correlations between loads measured at the binding and the knee were only found for females and not males. Therefore the initial hypotheses is only partially accepted.

12.3 **Implications for Equipment Design**

There are several critical implications for the design of ski bindings that can be gleaned from these results. The results from Study 1 demonstrate that binding technology and test methods that have worked well for alpine bindings and that have been grandfathered into the design and testing of AT equipment do not function the same way. In Study 1, the ASTM F504 test method was used to evaluate boot-binding systems. However many systems are designed to explicitly pass the test method ISO 9462 utilized by the Technischer Überwachungsverein (TÜV) (Munich, GER). Therefore, many AT boot-binding combinations that have been certified by the TÜV using the ISO 9462 test method do not release appropriately using the ASTM F504 test method. The results from this study demonstrate the importance of the ISO 9462 test method to incorporate several key tests from the ASTM F504 test method.

The results from Study 2 demonstrate similar complications of differences between international standards. In particular, several of the bindings tested in Study 2, had been certified by the TÜV but did not perform appropriately in simple twisting tests in this study (Figure 5.2).

From the results of Study 3, it is unlikely that several interventions that have been proposed to mitigate ACL injuries, namely lowering binding settings for females[14] and, a novel binding design by KneeBinding, will not prove effective in mitigating knee injuries. The novel release mechanism incorporated in the design of KneeBinding does not correlate well with loads at the knee. The proposal by Ruedl et. al. to lower release values for females could potentially have some merit in lowering the peak internal torque and adduction torque in female skiers. However there are two complications with this proposal:

1. The settings could only be lower on the toe piece in response to a lateral force, since the vertical force at the heel was not correlated with any female knee loads.
2. By lowering the settings for females, the risk of an inadvertent release would significantly increase. Figure 9.26 through Figure 9.29 demonstrate that females reach

the twisting release torque retention limit under normal skiing. Therefore by lowering the lateral force at the toe requiring release, the risk of an inadvertent release, and the subsequent injuries associated with them will increase.

12.4 Limitations and Recommendations

Several recommendations and improvements to the methods could be performed to improve future testing. First, a designated static trial from the XSENS MVN Biomech suit would significantly simplify the scaling of the OpenSim model and trouble shooting. After the drift and data drop out issues with the XSENS MVN Suit, new connectors were installed which significantly improved the robustness of the suit.

Another factor that was not quantified in the analysis was the surface roughness of the snow. The penetration tests were a measure of how soft the snow was, but the surface roughness is hypothesized to have played a significant role in the forces generated during skiing. Future studies could use LiDar to map out and scan a test slope to quantify the surface roughness.

Several improvements could also be made to the cable assembly of the sensors and how they attached to the data acquisition system in the backpack. Significant time was spent testing non-skiing maneuvers such as side stepping, duck walking, and kick turning. However the mass of the ski-sensor-binding system along with the cables, and cable restrain system had a significant affect on the subjects and how they performed these maneuvers.

Future testing could also instrument both feet to evaluate how skiers execute turns, the timing of edge pressure between the inside and outside foot, etc. Subjects were allowed to ski down the test slope in any manner they chose and were free to make as many turns as they wanted. From a logistical standpoint, this was easier on the front end. However, this also complicated the analysis and it was too cumbersome to attempt to examine how loads change as a function of the phase of the turn.

The sensor design described in Chapter 6 has proven to be very versatile and a second version of them was design and manufactured for used with snowboarding (Figure 12.1). In later testing using the weight that the snowboarders needed to carry was reduced from 30 lbs to 15 lbs by having a tester follow the subject with the XSENS kinematic data streaming over Bluetooth to a tablet in the testers backpack. This reduction in weight could significantly change how some skiers perform. For the purpose of evaluating AT bindings, the heavy backpack was considered

typical of the weight backcountry skiers are carrying. However, reducing the weight skiers carry during testing could significantly affect the results.

Future studies could benefit from having subjects ski a closed course with gates to allow for more precise comparisons of the phase of each turn, skier speeds, and other variables. Further more the sensors developed for this testing and the inverse dynamics model could be used to explore several other important factors associated with skier safety including:

- The effect of wider skis on knee loads.
- Other activities including jumping, or hiking in AT bindings.
- How new AT Bindings released on the market can absorb energy and transfer load?
- How do knee loads between recreational skiers and ski racers differ?
- Improving the OpenSim model to allow for constrained motion of the ankle.

Figure 12.1: Two custom sensors were developed using the same design described in Chapter 6.

12.5 **Summary**

This study evaluated the performance of alpine and AT bindings using laboratory tests and field measurements on the snow. The laboratory testing demonstrated that AT bindings do not provide skiers the same protection against lower leg injuries when the bindings should release. The field measurements demonstrated that both Alpine and AT bindings release at values greater than the target release value. These results have now quantified the amount of force and energy AT bindings must transmit to the skier and can be utilized by manufacturers of ski bindings and ski boots to improve the retention-release performance of their systems.

Bibliography

1. Sørensen M, Rankama T, Kankaanpää J, et al. The First Eastern Migrations of People and Knowledge into Scandinavia: Evidence from Studies of Mesolithic Technology, 9th-8th Millennium BC. *Nor Archaeol Rev*. 2013;46(1):19-56. doi:10.1080/00293652.2013.770416.
2. Formenti F, Ardigò LP, Minetti AE. Human locomotion on snow: determinants of economy and speed of skiing across the ages. *Proc R Soc B Biol Sci*. 2005;272(1572):1561-1569. doi:10.1098/rspb.2005.3121.
3. Eriksson E, Johnson RJ. The etiology of downhill ski injuries. *Exerc Sport Sci Rev*. 1980;8:1-17. http://www.ncbi.nlm.nih.gov/entrez/query.fcgi?cmd=Retrieve&db=PubMed&dopt=Citation&list_uids=6786894.
4. Shealy JE, Ettlinger CF, Johnson RJ. What Do We Know About Ski Injury Research that Relates Binding Function to Knee and Lower Leg Injuries? *ASTM Spec Tech Publ*. 2003;1440:36-52.
5. Earle A, Moritz J, Saviers G, Ball J. Ski Injuries. *J Am Med Assoc*. 1962;180(4):285-288. doi:10.1038/2091178c0.
6. Johnson R, Pope M EC. Ski Injuries Johnson.
7. Johnson RJ, Ettlinger CF, Shealy JE. Update on Injury Trends in Alpine Skiing. *Ski trauma Saf*. 2007;5(10):11-22.
8. Shealy JE, Ettlinger CF, Johnson RJ. Using Signal Detection Theory as a Model to Evaluate Release / Retention Criteria in Alpine Skiing. *J ASTM Int*. 2005;2(7):1-12.
9. Finch CF, Kelsall HL. The effectiveness of ski bindings and their professional adjustment for preventing alpine skiing injuries. *Sport Med*. 1998;25(6):407-416.
10. Natri A, Beynnon BD, Ettlinger CF, Johnson RJ, Shealy JE. Alpine Ski Bindings and Injuries, Current Findings. *Sport Med*. 1999;28(1):35-48.
11. Ettlinger CF, Dodge D, Johnson RJ, Shealy JE, Sargent M. Retention Requirements for Alpine Ski Bindings. *J ASTM Int*. 2010;7(6):1-22. doi:10.1520/JAI102978.
12. Mote CD. The Forces of Skiing and Their Implication to Injury. *Int J Sport Biomech*. 1987;3:309-325.
13. Johnson RJ, Ettlinger CF, Shealy JE. Myths Concerning Alpine Skiing Injuries. *Sport Heal A Multidiscip Approach*. 2009;1(6):486-492. doi:10.1177/1941738109347964.
14. Ruedl G, Helle K, Tecklenburg K, Schranz A, Fink C, Burtscher M. Factors associated with self-reported failure of binding release among ACL injured male and female recreational skiers: a catalyst to change ISO binding standards? *Br J Sports Med*. 2016;50(1):37-40. doi:10.1136/bjsports-2015-095482.
15. Burtscher M, Gatterer H, Flatz M, et al. Effects of modern ski equipment on the overall injury rate and the pattern of injury location in Alpine skiing. *Clin J Sport Med*. 2008;18(4):355-357. doi:10.1097/MJT.0b013e31815fd0fe.
16. Ruedl G, Webhofer M, Linortner I, et al. ACL injury mechanisms and related factors in male and female carving skiers: A retrospective study. *Int J Sports Med*. 2011;32(10):801-806. doi:10.1055/s-0031-1279719.
17. Ruedl G, Kopp M, Sommersacher R, Woldrich T, Burtscher M. Factors associated with injuries occurred on slope intersections and in snow parks compared to on-slope injuries. *Accid Anal Prev*. 2013;50:1221-1225. doi:10.1016/j.aap.2012.09.019.

18. Deibert MC, Aronsson DD, Johnson RJ, Ettlinger CF, Shealy JE. Skiing injuries in children, adolescents, and adults. *J Bone Jt Surg Am*. 1998;80(1):25-32.
19. Asang E. A Basis for Interpreting Typical Skiing Injury Mechanisms. *Orthpedic Clin North Am*. 1976;7(1):63-73.
20. Asang E. Experimental biomechanics of the human leg. A basis for interpreting typical skiing mechanisms. *Orthop Clin North Am*. 1976;7(1):63-73.
21. Hauser W. New IAS-Adjusted Specification 80 Based on Tibia Method. *Ski trauma Saf*. 8AD;4:79-85.
22. Outwater J, Woodard M. Skiing Forces and Fractures. *Mech Eng*. 1967:26-30.
23. Kuo CY, Louie JK, Mote CD. Field measurements in snow skiing injury research. *J Biomech*. 1983;16(8):609-624. doi:10.1016/0021-9290(83)90168-9.
24. Hull ML, Mote CD. Leg loading in snow skiing: computer analyses. *J Biomech*. 1980;13(6):481-491. doi:10.1115/1.3426365.
25. Maxwell SM, Hull ML. Measurement of strength and loading variables on the knee during Alpine skiing. *J Biomech*. 1989;22(6-7):609-624. doi:10.1016/0021-9290(89)90012-2.
26. Wunderly GS, Hull ML, Maxwell SM. A Second Generatin Microcomputer Controlled Binding System for Alpine Skiing Research. *J Biomech*. 1988;21(4):299-318.
27. Scher IS, Engineering E. P REDICTING SNOW SKI BINDING by. *Thesis*. 2000.
28. Hull ML, Swanstrom M, Wade B. Electromechanical Ski Release Binding with Mechanical Backup. *J ASTM Int*. 1997;11:81-92.
29. Ettlinger C, Johnson R, Shealy JE. A method to help reduce the risk of serious knee sprains incurred in alpine skiing. *Am J Sports Med*. 1995;23:5310537.
30. Shealy JE, Ettlinger C. An Investigation of Ski Binding Settings Based on Minimum Retention Requirements. *Ski Trauma Ski Saf*. 1982;4:1130121.
31. Crawford R, Binding S, Retention M. Ski Binding Minimum Retention Requirements. *J ASTM Int*. 1997;11:93-108.
32. ASTM F- 939-12: Selection of Release Torque Values for Alpine Ski Bindings. *Am Soc Test Mater*. 2012.
33. ISO 8061:2015 Alpine ski-bindings -- Selection of release torque values. *Int Stand Organiztion*. 2015:1-15.
34. ISO 5355:2005 Alpine ski-boots -Requirements and test methods. *Int Stand Organiztion*. 2014.
35. ISO 9462:2014 Alpine ski-bindings - Requirements and test methods. *Int Stand Organiztion*. 2014.
36. ISO 9523:2015 Touring ski-boots for adults - Interface with touring ski-bindings - Requirements and test methods. *Int Stand Organiztion*. 2015.
37. ISO 13992:2014 Alpine touring ski-bindings - Requirements and test methods. *Int Stand Organiztion*. 2014.
38. Quinn TP, Mote CD. Optimal design of an uncoupled six degree of freedom dynamometer. *Exp Mech*. 1990;30(1):40-48. doi:10.1007/BF02322701.
39. Quinn T, Jr CM. Prediction of the loading along the leg during snow skiing. *J Biomech*. 1992;25(6):609-625.
40. Nakazato K, Scheiber P, Müller E. Comparison between the force application point determined by portable force plate system and the center of pressure determined by pressure insole system during alpine skiing. *Sport Eng*. 2013;16(4):297-307. doi:10.1007/s12283-013-0119-x.

41. Stricker G, Scheiber P, Lindenhofer E, Müller E. Determination of forces in alpine skiing and snowboarding: Validation of a mobile data acquisition system. *Eur J Sport Sci*. 2010;10(1):31-41. doi:10.1080/17461390903108141.
42. Klous M, Müller E, Schwameder H. Three-dimensional knee joint loading in alpine skiing: a comparison between a carved and a skidded turn. *J Appl Biomech*. 2012;28(6):655-664. http://www.ncbi.nlm.nih.gov/pubmed/22660886.
43. Warme, WJ, Feagin, JA, King, P, Lambert, KL, Cunningham R. A. G. Vredenburgh, & H. H. Cohen, Proceedings of the Human Factors and Ergonomics Society 39th Annual Meeting - 1995, pp. 1015-1019. *J Safety Res*. 1993;27(4):272-273.
44. Hauser W. Experimental Prospective skiing injury study (1989). *Skiing*. 1989;7:18-24.
45. Bouter, LM, Knipschild, PG, Volovics A. Binding Function in relation to injury risk in downhill skiing.pdf. *Am J Sports Med*. 1989;17(2):226-233.
46. Ekeland, A, Holtmoen, A, Lystad H. Lower extremity equipment-related injuries in recreational skiers. *Am J Sports Med*. 1993;21(August):201-205.
47. ASTM F-504-05 (2012) Standard Test Method for Measuring the Quasi-Static Release Moments of Alpine Ski. *Am Socity Test Mater*. 2012:1-6.
48. Senner V, Michel FI, Lehner S. Technical possibilities for optimising the ski-binding-boot functional unit to reduce knee injuries in recreational alpine skiing. 2013:211-228. doi:10.1007/s12283-013-0138-7.
49. Colonna M, Nicotra M, Moncalero M. Materials, Designs and Standards Used in Ski-Boots for Alpine Skiing. *Sports*. 2013;1(4):78-113. doi:10.3390/sports1040078.
50. ASTM. ASTM D2240-05: Standard Test Method for Rubber Property-Durometer Hardness. 2015.
51. Liggins, Surry K, Finlay JB. Sealing Fuji Prescale pressure sensitive film for protection against fluid damage: the effect on its response. *Strain*. 1995.
52. Liggins a. B, Finlay JB. Image-Averaging in the Analysis of Data From Pressure-Sensitive Film. *Exp Tech*. 1997;21(3):19-22. doi:10.1111/j.1747-1567.1997.tb00518.x.
53. Alhalki MM, Howell SM, Hull ML. How three methods for fixing a medial meniscal autograft affect tibial contact mechanics. *Am J Sports Med*. 1999;27(3):320-328. http://www.ncbi.nlm.nih.gov/pubmed/10352767.
54. O'Brien RM. A Caution Regarding Rules of Thumb for Variance Inflation Factors. *Qual Quant*. 2007;41(5):673-690. doi:10.1007/s11135-006-9018-6.
55. Grömping U. Relative Importance for Linear Regression in R: The Package relaimpo. *J Stat Softw*. 2006;17(1):1-27.
56. TohmOlofsson P, Andersson M. *Probability Statistics and Stochastic Processes*. Vol XXXIII.; 2012. doi:10.1007/s13398-014-0173-7.2.
57. Chao L-P, Chen K-T. Shape optimal design and force sensitivity evaluation of six-axis force sensors. *Sensors Actuators A Phys*. 1997;63(2):105-112. doi:10.1016/S0924-4247(97)01534-3.
58. Liu S a., Tzo HL. A novel six-component force sensor of good measurement isotropy and sensitivities. *Sensors Actuators, A Phys*. 2002;100(2-3):223-230. doi:10.1016/S0924-4247(02)00135-8.
59. Bicchi A. A criterion for optimal design of multi-axis force sensors. *Rob Auton Syst*. 1992;10(4):269-286. doi:10.1016/0921-8890(92)90005-J.
60. Bicchi A, Canepa G. Optimal design of multivariate sensors. *Meas Sci Technol*. 1994;319(5):319-332. http://iopscience.iop.org/0957-0233/5/4/001. Accessed November

19, 2014.
61. Howard CQ, Hansen CH. Six-Axis Vibrational Power Transducer for Active Vibration Isolation. *Proc Acoust*. 2005;2(November):1-8.
62. Park Y-K, Kumme R, Roeske D, Kang D-I. Column-type multi-component force transducers and their evaluation for dynamic measurement. *Meas Sci Technol*. 2008;19(11):115205. doi:10.1088/0957-0233/19/11/115205.
63. Mastinu G, Gobbi M, Previati G. A New Six-axis Load Cell. Part I: Design. *Exp Mech*. 2011;51(3):373-388. doi:10.1007/s11340-010-9355-1.
64. Ballo F, Gobbi M, Mastinu G, Previati G. Advances in Force and Moments Measurements by an Innovative Six-axis Load Cell. *Exp Mech*. 2014;54(4):571-592. doi:10.1007/s11340-013-9824-4.
65. Sanders JE, Miller R a, Berglund DN, Zachariah SG. A modular six-directional force sensor for prosthetic assessment: a technical note. *J Rehabil Res Dev*. 1997;34(2):195-202.
66. Wu B, Cai P. Decoupling Analysis of a Sliding Structure Six-axis Force/Torque Sensor. *Meas Sci Rev*. 2013;13(4):187-193.
67. Cappa P, Jackson JL, Patan F. Moment Measurement Accuracy of a Parallel Spherical Robot for Dynamic Posturography. 2010;57(5):1198-1208.
68. Liu T, Inoue Y, Shibata K. Wearable force sensor with parallel structure for measurement of ground-reaction force. *Meas J Int Meas Confed*. 2007;40(6):644-653. doi:10.1016/j.measurement.2006.08.008.
69. Davis RR, Hull ML. Measurement of pedal loading in bicycling: II. Analysis and results. *J Biomech*. 1981;14(12):857-872. doi:10.1016/0021-9290(81)90145-7.
70. Kang C-G. Maximum Structural Error Propagation of Multi-Axis Force Sensors. *Japan Soc Mech Eng*. 2001;44(3):676-681.
71. Chen D, Song A, Li A. Design and Calibration of a Six-axis Force/torque Sensor with Large Measurement Range Used for the Space Manipulator. *Procedia Eng*. 2015;99:1164-1170. doi:10.1016/j.proeng.2014.12.699.
72. Liang Q, Zhang D, Wang Y, Ge Y. Design and Analysis of a Novel Six-Component F/T Sensor based on CPM for Passive Compliant Assembly. *Meas Sci Rev*. 2013;13(5):253-264. doi:10.2478/msr-2013-0038.
73. Kang M-K, Lee S, Kim J-H. Optimal design of a mechanically decoupled six-axis force/torque sensor based on the principal cross coupling minimization. *Sensors Smart Struct Civil, Mech Aerosp Syst*. 2014;9061(90612N):90612N. doi:10.1117/12.2044744.
74. Kang C. Performance improvement of a 6-axis force-torque sensor via novel electronics and cross-shaped double-hole structure. *Int J Control Autom Syst*. 2005;3(3):469-476. http://ijcas.com/admin/paper/files/IJCAS_v3_n3_pp.469-476.pdf.
75. Kruger a., McAlpine P, Borrani F, Edelmann-Nusser J. Determination of three-dimensional joint loading within the lower extremities in snowboarding. *Proc Inst Mech Eng Part H J Eng Med*. 2011;226(2):170-175. doi:10.1177/0954411911426938.
76. Nakazato K, Scheiber P, Müller E. A comparison of ground reaction forces determined by portable force-plate and pressure-insole systems in alpine skiing. *J Sport Sci Med*. 2011;10(4):754-762.
77. Systems EO. Material data sheet EOS Aluminium AlSi10Mg for EOSINT M 270 Material data sheet Technical data. 2011:5.
78. Systems EO. Material data sheet EOS NickelAlloy IN718 Material data sheet Technical data. 2011:5.

79. Systems EO. Material data sheet EOS Titanium Ti64 Material data sheet Technical data. 2011:5.
80. Statnikov R, Matusov J, Statnikov A. Multicriteria Engineering Optimization Problems: Statement, Solution and Applications. *J Optim Theory Appl*. 2012;155(2):355-375. doi:10.1007/s10957-012-0083-9.
81. Bayo E, Stubbe JR. Six-axis force sensor evaluation and a new type of optimal frame truss design for robotic applications. *J Robot Syst*. 1989;6(2):191-208. doi:10.1002/rob.4620060206.
82. Svinin MM, Uchiyama M. Optimal Geometric Structures of Force/Torque Sensors. *Int J Rob Res*. 1995;14(6):560-573. doi:10.1177/027836499501400603.
83. Uchiyama M, Nakamura Y, Hakomori K. Evaluation of the robot force sensor structure using singular value decomposition. *Adv Robot*. 1990;5(1):39–52. http://www.ingentaconnect.com/content/vsp/arb/1990/00000005/00000001/art00005.
84. International S. Nickel Alloy, Corrosion and Heat Resistant, Bars, Forgings, and Rings, 52.5Ni - 19Cr - 3.0Mo - 5.1Cb - 0.90Ti - 0.50Al - 18Fe, Consumable Electrode or Vacuum Induction Melted, 1950 °F (1066 °C) Solution Heat Treated, Precipitation Hardenable. 2001:3.
85. Baufeld B. Mechanical properties of INCONEL 718 parts manufactured by shaped metal deposition (SMD). *J Mater Eng Perform*. 2012;21(7):1416-1421. doi:10.1007/s11665-011-0009-y.
86. Ning Y, Fuh JYH, Wong YS, Loh HT. An intelligent parameter selection system for the direct metal laser sintering process. *Int J Prod Res*. 2004;42(1):183-199. doi:10.1080/00207540310001595873.
87. Sochalski-Kolbus LM, Payzant EA, Cornwell PA, et al. Comparison of Residual Stresses in Inconel 718 Simple Parts Made by Electron Beam Melting and Direct Laser Metal Sintering. *Metall Mater Trans A Phys Metall Mater Sci*. 2015;46(3):1419-1432. doi:10.1007/s11661-014-2722-2.
88. Strondl a, Palm M, Gnauk J, Frommeyer G. Microstructure and mechanical properties of nickel based superalloy IN718 produced by rapid prototyping with electron beam melting (EBM). *Mater Sci Technol*. 2011;27(5):876-883. doi:10.1179/026708309X12468927349451.
89. Sanz C, García Navas V. Structural integrity of direct metal laser sintered parts subjected to thermal and finishing treatments. *J Mater Process Technol*. 2013;213(12):2126-2136. doi:10.1016/j.jmatprotec.2013.06.013.
90. Brookhuis R a, Droogendijk H, de Boer MJ, et al. Six-axis force–torque sensor with a large range for biomechanical applications. *J Micromechanics Microengineering*. 2014;24(3):35015. doi:10.1088/0960-1317/24/3/035015.
91. Bicchi a, Canepa G. Optimal design of multivariate sensors. *Meas Sci Technol*. 1999;5(4):319-332. doi:10.1088/0957-0233/5/4/001.
92. Nakamura Y, Yoshikawa T, Futamata I. Design and signal processing of six-axis force sensors. In: *4th International Symposium of Robotics Research*. ; 1988:75-81. http://dl.acm.org/citation.cfm?id=57425.57433.
93. Winter DA. *Biomechanics and Motor Control of Human Movement*.; 1990.
94. Supej M. 3D measurements of alpine skiing with an inertial sensor motion capture suit and GNSS RTK system. *J Sports Sci*. 2010;28(7):759-769.
95. Brodie M, Walmsley A, Page W. Fusion motion capture: a prototype system using inertial

measurement units and GPS for the biomechanical analysis of ski racing. *Sport Technol*. 2008;1(1):17-28. doi:10.1002/jst.6.
96. Mvn UG, Biomech MVN, Link MVN, Awinda MVN. MVN User Manual. 2015;(March).
97. Seel T, Raisch J, Schauer T. IMU-Based Joint Angle Measurement for Gait Analysis. *Sensors*. 2014;14(4):6891-6909. doi:10.3390/s140406891.
98. McGinley JL, Baker R, Wolfe R, Morris ME. The reliability of three-dimensional kinematic gait measurements: A systematic review. *Gait Posture*. 2009;29(3):360-369. doi:10.1016/j.gaitpost.2008.09.003.
99. Schwartz MH, Trost JP, Wervey RA. Measurement and management of errors in quantitative gait data. *Gait Posture*. 2004;20(2):196-203. doi:10.1016/j.gaitpost.2003.09.011.
100. Hol JD, Schön TB, Luinge H, Slycke PJ, Gustafsson F. Robust real-time tracking by fusing measurements from inertial and vision sensors. *J Real-Time Image Process*. 2007;2(2-3):149-160. doi:10.1007/s11554-007-0040-2.
101. Brodie MA, Walmsley A, Page W. The static accuracy and calibration of inertial measurement units for 3D orientation. *Comput Methods Biomech Biomed Engin*. 2008;11(6):641-648. doi:10.1080/10255840802326736.
102. Young, JW, Chandler, RF, Snow C. *Anthropometric and Mass Distribution Characteristics of the Adult Female*. Oklahoma City, Oklahoma; 1983.
103. McConville JT, Churchill T, Kaleps I, Clauser CE, Cuzzi J. Anthropometric relationships of body and body segment moments of inertia. *Tech Rep AFAMRL-TR-80-119, Wright patterson Air Force Base, Ohio*. 1980:1-113.
104. Hartono M, Gunawan LH. Drillis and Contini Revisited Using Correlation Analysis for Indonesian Adults Anthropometry. 2015:1138-1141.
105. Chandler, RF, Clauser, CE, McConville, JT, Reynolds, HM, Young J. *Investigation of Inertial Properties of the Human Body*. Vol 53.; 1975. doi:10.1017/CBO9781107415324.004.
106. Park SJ, Kim CB, Park SC. Anthropometric and biomechanical characteristics on body segments of Koreans. *Appl Human Sci*. 1999;18(3):91-99. doi:10.2114/jpa.18.91.
107. ASTM F779 - 12 Standard Test Method for Torsion Characteristic of Alpine Skis. *Am Soc Test Mater*. 2012.
108. ASTM F498 - 12 Standard Test Method for Center Spring Constant and Spring Constant Balance of Alpine Skis. *Am Soc Test Mater*. 2012.
109. Fierz C, Armstrong RL, Durand Y, et al. The international classification for seasonal snow on the ground. *IHP-VII Tech Doc Hydrol*. 2009;83(1):90. doi:http://www.cosis.net/abstracts/EGU05/09775/EGU05-J-09775.pdf.
110. Zorko M, Nemec B, Babič J, Lešnik B, Supej M. The waist width of skis influences the kinematics of the knee joint in alpine skiing. *J Sport Sci Med*. 2015;14(3):606-619.
111. Supej M. 3D measurements of alpine skiing with an inertial sensor motion capture suit and GNSS RTK system. *J Sports Sci*. 2010;28(7):759-769. doi:10.1080/02640411003716934.
112. Sigward SM, Powers CM. The influence of gender on knee kinematics, kinetics and muscle activation patterns during side-step cutting. *Clin Biomech*. 2006;21(1):41-48. doi:10.1016/j.clinbiomech.2005.08.001.
113. Dempsey AR, Lloyd DG, Elliott BC, Steele JR, Munro BJ, Russo KA. The effect of technique change on knee loads during sidestep cutting. *Med Sci Sports Exerc*.

2007;39(10):1765-1773. doi:10.1249/mss.0b013e31812f56d1.
114. Hébert-Losier K, Supej M, Holmberg HC. Biomechanical factors influencing the performance of elite alpine ski racers. *Sport Med*. 2014;44(4):519-533. doi:10.1007/s40279-013-0132-z.
115. ISO 8061:2015 - Alpine ski-bindings -- Selection of release torque values. *Int Stand Organiztion*. 2015.
116. Bates D. Fitting Mixed-Effects Models Using the lme4 Package in R. *Int Meet Psychom Soc*. 2008. http://www.stat.wisc.edu/~bates/IMPS2008/lme4D.pdf.
117. Gelman Andrew HJ. *Gelman Andrew, Hill Jennifer*. 1st ed. Cambridge University Press; 2007.
118. Seltman HJ. Chapter 15 Mixed Models. *Exp Des Anal*. 2014:357-378.
119. Douglas Bates, Martin Maechler, Ben Bolker SW. Bates LMER. *J Stat Softw*. 2015;67(1):1-48. doi:10.18637/jss.v067.i01.
120. Foss GC, Glenne B. Reducing On-Snow Vibrations of Skis and Snowboards. *Sound Vib*. 2007;41(12):22-26.
121. Senner V, Michel FI, Lehner S, Brügger O. Technical possibilities for optimising the ski-binding-boot functional unit to reduce knee injuries in recreational alpine skiing. *Sport Eng*. 2013;16(4):211-228. doi:10.1007/s12283-013-0138-7.
122. McLean SG, Lipfert SW, Van Den Bogert AJ. Effect of gender and defensive opponent on the biomechanics of sidestep cutting. *Med Sci Sports Exerc*. 2004;36(6):1008-1016. doi:10.1249/01.MSS.0000128180.51443.83.
123. Shin CS, Chaudhari AM, Andriacchi TP. The effect of isolated valgus moments on ACL strain during single-leg landing: A simulation study. *J Biomech*. 2009;42(3):280-285. doi:10.1016/j.jbiomech.2008.10.031.
124. Markolf, KL, Burchfield, DM, Shapiro, MM, Shepard, MF, Finerman, G, Slauterbeck J. Combined Knee Loading States that Generate High Anterior Cruciate Ligament Forces. *J Orthop Res*. 1995;13:930-935.
125. DeMorat G, Weinhold P, Blackbur T, Chudik S, Garrett W. Aggressive Quadriceps Loading Can Induce Noncontact Anterior Cruciate Ligament Injury. *Am J Sports Med*. 2004;32(2):477-483. doi:10.1177/0363546503258928.
126. Shin CS, Chaudhari AM, Andriacchi TP. Valgus plus internal rotation moments increase anterior cruciate ligament strain more than either alone. *Med Sci Sports Exerc*. 2011;43(8):1484-1491. doi:10.1249/MSS.0b013e31820f8395.
127. Delp SL, Loan JP, Hoy MG, Zajac FE, Topp EL, Rosen JM. An Interactive Graphics-Based Model of the Lower Extremity to Study Orthopaedic Surgical Procedures. *IEEE Trans Biomed Eng*. 1990;37(8):757-767. doi:10.1109/10.102791.
128. Yamaguchi GT, Zajac FE. A planar model of the knee joint to characterize the knee extensor mechanism. *J Biomech*. 1989;22(1):1-10. doi:10.1016/0021-9290(89)90179-6.
129. Anderson FC, Pandy MG. A Dynamic Optimization Solution for Vertical Jumping in Three Dimensions. *Comput Methods Biomech Biomed Engin*. 1999;2(3):201-231. doi:10.1080/10255849908907988.
130. Anderson FC, Pandy MG. Dynamic optimization of human walking. *J Biomech Eng*. 2001;123(October 2001):381-390. doi:10.1115/1.1392310.
131. Ford KR, Mclean SG. Biomechanical Measures of Neuromuscular Control and Valgus Loading of the Knee Predict Anterior Cruciate Ligament Injury Risk in Female Athletes A Prospective Study Biomechanical Measures of Neuromuscular Control and Valgus

Loading of the Knee Predict Ant. *Am Orthop Soc Sport Med*. 2005;33(4):1-10. doi:10.1177/0363546504269591.
132. Scheiber P, Seifert J, Müller E. Relationships between biomechanics and physiology in older, recreational alpine skiers. *Scand J Med Sci Sport*. 2012;22(1):49-57. doi:10.1111/j.1600-0838.2010.01146.x.
133. Dempsey AR, Elliott BC, Munro BJ, Steele JR, Lloyd DG. Whole body kinematics and knee moments that occur during an overhead catch and landing task in sport. *Clin Biomech*. 2012;27(5):466-474. doi:10.1016/j.clinbiomech.2011.12.001.
134. Yeadon MR, Morlock M. The Appropriate Use of Regression Equations Inertia for the Estimation of Segmental Parameters. *J Biomech*. 1989;22(617):683-689.
135. Walker PS, Rovick JS, Robertson DD. The effects of knee brace hinge design and placement on joint mechanics. *J Biomech*. 1988;21(11). doi:10.1016/0021-9290(88)90135-2.
136. McLean SG, Huang X, Su A, Van Den Bogert AJ. Sagittal plane biomechanics cannot injure the ACL during sidestep cutting. *Clin Biomech*. 2004;19(8):828-838. doi:10.1016/j.clinbiomech.2004.06.006.
137. Meyer EG, Haut RC. Anterior cruciate ligament injury induced by internal tibial torsion or tibiofemoral compression. *J Biomech*. 2008;41(16):3377-3383. doi:10.1016/j.jbiomech.2008.09.023.

Appendix A: Angular Displacement of Bindings Relative to Boots

The desired angular displacement at release for AT boots was defined as 300% of the angular displacement at release of the reference alpine boot for each specific binding and load case. Because the angular displacement at release for the reference alpine boot varied by binding model and load scenario, the desired range for angular displacement at release for AT boots also varied by binding model and load scenario; see Table A1.

Table A1. Upper bounds for the desired ranges of angular displacement at release and the range of desired torque at release for each alpine binding and load scenario. The desired angular displacement at release for AT boots was defined as 300% of the angular displacement at release of the reference alpine boot for each specific binding and load case. Because the angular displacement at release for the reference alpine boot varied by binding model and load scenario, the desired range for angular displacement at release for AT boots also varied by binding model and load scenario.

		Load Scenario			
	Binding	**Forward Lean**	**Pure Twist**	**Front Preload Twist**	**Rear Preload Twist**
300% of the Angular Displacement at Release	1	12.6	5.1	2.4	7.5
	2	6.1	9.8	7.2	14.3
	3	9.7	7.4	5.6	6.5
	4	7.8	6.7	5.3	10.2
	5	10.4	7.3	4.6	7.9
	6	14.3	5.9	3.5	8.6
	7	10.4	7.2	5.2	6.6
	8	7.4	4.8	2.1	4.1
Torque (*Nm*)	Min (Nm)	248	60	60	60
	Max (Nm)	305	75.4	94.3	101.8

Appendix B: Multiple Linear Regression Tables

Table B1: Multiple Regression Results for Release Torque of alpine boots as the dependent variable for Pure Twist, Front Preload Twist, and Rear Preload Twist releases. Note: X|Y notation indicates a significant interaction between independent variables X and Y.

Alpine Boots	Pure Twist			Front Preload Twist			Rear Preload Twist		
	βn	**SE**	***p***	**βn**	**SE**	***p***	**βn**	**SE**	***p***
Intercept	0	0.066	*1.0*	0	0.05	*1.0*	0.011	0.042	*0.79*
AFD	-	-	-	0.278	0.074	*<.001*	-	-	-
AFD Pressure	0.244	0.077	*<.001*	-0.633	0.084	*<.001*	-	-	-
DoF	-	-	-	-	-	-	-0.579	0.05	*<.001*
EI	0.202	0.069	*<.001*	-	-	-	0.261	0.066	*<.001*
FP	0.191	0.074	*0.01*	-0.103	0.056	*0.07*	-0.503	0.045	*<.001*
FP|EI	-	-	-	-0.422	0.064	*<.001*	-0.421	0.073	*<.001*
Hardness	0.65	0.066	*<.001*	0.589	0.05	*<.001*	-	-	-
Toe	-	-	-	-0.234	0.085	*0.01*	0.267	0.052	*<.001*
AFD P| Hardness	-0.137	0.067	*0.04*	-	-	-	-	-	-

Table B2: Standardized coefficients (β_n), standard errors (SE), and p-values for the null hypothesis, $\beta_n = 0$, from MLR models for Pure Twist, Front Preload Twist, and Rear Preload Twist release torque.

		Pure Twist			Front Preload Twist			Rear Preload Twist		
	Regressors	**β_n**	**SE**	***p***	**βn**	**SE**	***p***	**βn**	**SE**	***p***
Alpine and AT Boots	AFD	-0.056	0.074	*0.45*	0.286	0.043	*<.001*	0.127	0.05	*0.01*
	AFD Area	-	-	-	-	-	-	0.379	0.047	*<.001*
	AFD Force	0.449	0.102	*<.001*	-0.112	0.091	*0.22*	-	-	-
	AFD Pressure	-0.21	0.085	*0.01*	-0.003	0.073	*0.97*	-0.31	0.072	*<.001*
	AFD | AFD P	0.266	0.046	*<.001*	-0.126	0.034	*<.001*	-	-	-
	DoF	0.169	0.053	*<.001*	-	-	-	-0.215	0.041	*<.001*
	DoF| AFD F	0.136	0.033	*<.001*	-	-	-	-	-	-
	EI	0.059	0.061	*0.33*	-0.052	0.054	*0.33*	0.353	0.045	*<.001*
	FP	0.171	0.048	*<.001*	-0.185	0.036	*<.001*	-0.504	0.033	*<.001*
	EI|FP	0.242	0.073	*<.001*	-0.39	0.055	*<.001*	-0.719	0.055	*<.001*
	Hardness	0.64	0.085	*<.001*	-0.663	0.062	*<.001*	-0.261	0.071	*<.001*
	Hardness|AFDF	0.5	0.115	*<.001*	-0.434	0.085	*<.001*	-	-	-
	Hardness | AFD	-	-	-	-	-	-	0.203	0.031	*<.001*
	Tech	0.154	0.053	*<.001*	-0.34	0.042	*<.001*	-0.018	0.038	*0.63*
	Tech|FP	-0.093	0.041	*0.02*	-	-	-	-	-	-
	Toe	0.139	0.058	*0.02*	-	-	-	0.209	0.042	*<.001*
	Tech|Toe	-	-	-	-	-	-	-0.042	0.03	*0.16*

Appendix C: Multiple Linear Regression Tables

Table C.1: MLR Fit Metrics for release torque from 10 bindings.

Binding	F(4,10)	***Multiple R^2***	***Adjusted R^2***	***P***
1	645.1	0.996	0.995	< 0.001
2	143	0.983	0.976	< 0.001
3	47.3	0.950	0.930	< 0.001
4	892.5	0.997	0.996	< 0.001
5	19.57	0.887	0.841	< 0.001
6	86.41	0.972	0.961	< 0.001
7	27.84	0.736	0.709	< 0.001
8	693.1	0.996	0.995	< 0.001
9	6.247	0.714	0.600	< 0.001
10	4.066	0.619	0.467	< 0.001

Table C.2: Scaled MLR coefficients (β_n), standard errors (SE), and fit metrics for independent variables: Dim A, Dim C, the interaction of Dim A & Dim C (Dim A | Dim C), and the Clamping Force (CF).

MLR: Independent Variables

Bindings		Intcpt.	*Dim A*	*Dim C*	*DimA | Dim C*	*CF*	R^2	*p*
	β_n	-0.29	***0.44***	***1.11***	***-0.32***	***-0.08***		
All	SE	0.10	***0.06***	***0.15***	***0.14***	***0.09***	0.325	< 0.001
	p	*< 0.001*	*< 0.001*	*< 0.001*	*< 0.001*	*0.182*		
	β_n	-0.25	-0.58	-0.20	-0.28	-0.76		
1	SE	0.04	0.09	0.06	0.05	0.05	0.996	< 0.001
	p	*< 0.001*	*< 0.001*	*< 0.001*	*< 0.001*	*< 0.001*		
	β_n	-0.52	-0.20	1.06	-0.59	-0.09		
2	SE	0.09	0.11	0.19	0.14	0.10	0.976	< 0.001
	p	*< 0.001*	*0.31*	*< 0.001*	*< 0.001*	*0.43*		
	β_n	-0.28	0.98	1.83	-0.32	-0.24		
3	SE	0.16	0.32	0.23	0.1642	0.18	0.930	< 0.001
	p	*0.109*	*0.0124*	*< 0.001*	*0.080*	*0.211*		
	β_n	-0.43	2.12	2.78	-0.49	-0.14		
4	SE	0.04	0.08	0.05	0.04	0.04	0.996	< 0.001
	p	*< 0.001*	*< 0.001*	*< 0.001*	*< 0.001*	*< 0.001*		
	β_n	-0.98	-2.20	0.31	-1.18	1.26		
5	SE	0.30	0.52	0.24	0.34	0.28	0.841	< 0.001
	P	*0.009*	*0.002*	*0.226*	*0.006*	*0.001*		
	β_n	-1.83	-4.09	-1.0647	-2.0661	1.85		
6	SE	0.12	0.24	0.17	0.12	0.14	0.961	< 0.001
	P	*< 0.001*	*< 0.001*	*< 0.001*	*< 0.001*	*< 0.001*		
	β_n	-0.37	3.02	3.77	-0.40	-0.55		
7	SE	0.14	0.36	0.40	0.12	0.11	0.709	< 0.001
	P	*< 0.001*	*< 0.001*	*< 0.001*	*< 0.001*	*< 0.001*		
	β_n	-0.43	3.26	4.20	-0.48	-0.49		
8	SE	0.03	0.08	0.09	0.03	0.03	0.995	< 0.001
	P	*< 0.001*	*< 0.001*	*< 0.001*	*< 0.001*	*< 0.001*		
	β_n	-0.42	1.82	2.86	-0.49	-0.48		
9	SE	0.03	0.03	0.06	0.06	0.03	0.600	< 0.001
	P	*< 0.001*	*< 0.001*	*< 0.001*	*< 0.001*	*< 0.001*		
	β_n	-0.62	1.32	1.79	-0.72	0.44		
10	SE	0.33	0.49	0.57	0.32	0.24	0.467	< 0.001
	p	*0.090*	*0.023*	*0.010*	*0.050*	*0.099*		

Appendix D: Additional Statistical Tables

Table D.1: Linear regression of Indicator Values on Release torque for test configurations 2-3 corresponding to tests with the heelpiece settings at the minimum, median, and maximum indicator values. One linear regression was performed for each binding model tested. The reference slope of the Indicator Value-Release torque curve prescribed by ISO 13992:2006 is 10 Nm/IV.

Binding	Slope (Nm/IV)	F		Mult. R^2	Adj. R^2	*p*
1	3.54	F(1,58)	374	0.8657	0.8634	*< 0.001*
2	5.59	F(1,46)	138.3	0.7504	0.745	*< 0.001*
3	8.47	F(1,58)	284.2	0.8305	0.8276	*< 0.001*

Table D.2: MLR metrics with standardized coefficients.

	Config	Interc.	βn β_F	$\beta_{Dim\ A}$	$\beta_{Dim\ C}$	$\beta_{Dim\ A \mid Dim\ C}$	Adj.R^2	p
Binding 1	**C1**	0.00	0.12	1.02	1.83	0.00	0.90	*<0.001*
	C2	0.39	-0.24	2.31	2.13	0.47	0.91	*<0.001*
	C3	0.92	0.24	0.11	-0.24	1.10	0.90	*<0.001*
	C4	0.77	0.45	-0.85	-0.69	0.92	0.84	*<0.001*
Binding 2	**C1**	-0.20	0.44	-0.79	0.66	-0.24	0.88	*<0.001*
	C2	-0.46	1.37	-0.61	1.41	-0.55	0.84	*<0.001*
	C3	-0.62	1.63	-2.37	-0.89	-0.74	0.68	*0.003*
	C4	-0.65	0.15	0.18	-0.06	-0.77	0.70	*0.002*
Binding 3	**C1**	0.00	0.92	-0.07	1.07	0.00	0.98	*<0.001*
	C2	0.00	0.80	-0.14	1.08	0.00	0.96	*<0.001*
	C3	0.00	2.02	-2.17	-0.24	0.00	0.80	*0.001*
	C4	0.00	2.15	-2.17	-0.23	0.00	0.92	*<0.001*

Table D.3: Percent relative contribution and the 95% CIs [LL, UL] of boot-binding constraints to release torque variation for Pure Twist releases.

	Config	Clamping Force	Dim A	Dim C	Dim A | Dim C
Binding 1	C1	15.7% [14.35, 18.83]	33.2% [28.2, 40.2]	39.2% [32.9, 48.0]	3.1% [0.1, 10.1]
	C2	18.7% [11.8, 29.0]	13.1% [10.3, 17.6]	41.8% [31.1, 53.6]	15.3% [5.5, 29.5]
	C3	23.7% [10.9, 40.8]	12.7% [7.1, 22.0]	13.0% [3.5, 28.2]	28.0% [9.2, 50.9]
	C4	4.5% [3.2,13.8]	24.9% [13.6, 41.6]	15.9% [8.7, 28.8]	33.4% [15.7, 54.7]
Binding 2	C1	27.0% [22.7, 32.4]	14.6% [14.1, 15.4]	57.0% [51.2, 61.8]	0% [0, 0]
	C2	18.5% [13.8, 24.4]	14.7% [13.7, 16.9]	63.8% [58.2, 70.1]	0% [0, 0]
	C3	43.5% [33.7,57.1]	32.3% [25.6, 43.6]	9.5% [5.7, 19.6]	0% [0, 0]
	C4	53.0% [46.8, 60.0]	31.8% [27.6, 38.3]	9.1% [6.8, 15]	0% [0, 0]
Binding 3	C1	7.8% [6.6,10.5]	19.3% [18.3, 21.6]	65.4% [61.7, 69.8]	0% [0, 0]
	C2	5.8% [4.5, 9.8]	24.0% [19.6, 30.0]	53.2% [45.4, 60.3]	10.2% [3.9, 19.1]
	C3	17.6% [10.8, 26.5]	7.9% [5.0, 12.3]	2.2% [1.4, 5.8]	65.0% [54.7, 76.8]
	C4	14.8% [8.2, 26.0]	20.3% [13.2, 29.7]	6.0% [3.3, 11.7]	47.7% [33.3, 63.9]